Engineering Acoustic Protein Nanostructures for Non-Invasive Molecular Imaging using Ultrasound

Thesis by

Anupama Lakshmanan

In Partial Fulfillment of the Requirements for
the degree of
Doctor of Philosophy in Bioengineering

Caltech

CALIFORNIA INSTITUTE OF TECHNOLOGY
Pasadena, California

2019
(Defended May 31, 2019)

Anupama Lakshmanan
ORCID: 0000-0002-6702-837X

ACKNOWLEDGEMENTS

The research work presented in this thesis would not have been possible without the invaluable and timely advice, help and encouragement that I have received from my mentors, colleagues, friends and family. First and foremost, I would like to convey my heartfelt gratitude to my thesis advisor - Professor Mikhail Shapiro, for his unwavering support, mentorship and guidance during my time at Caltech. I am constantly amazed and inspired by Mikhail's creativity, focus and relentless drive to conduct breakthrough research. I joined Mikhail's group when he had just moved to Caltech as an Assistant Professor. It has been an incredible learning experience to witness him establish and expand the lab to its current state through sheer hard work, and more importantly, his fearless belief and pursuit of his grand scientific vision despite the risks and challenges along the way. Mikhail's infectious optimism, confidence, as well as his timely feedback and suggestions, have helped me successfully navigate the tough patches of my graduate journey. I have learnt a lot from him on how to conceive, implement and communicate scientific ideas in an efficient and effective manner, and will always cherish these learnings.

Second, I am immensely indebted to my thesis committee - Professors David Tirrell, Viviana Gradinaru and Changhuei Yang, for their precious time, helpful discussions and advice. I worked with Dave and Viviana during my initial rotations, and am fortunate to receive their continued guidance as members of my thesis committee. I also benefited from Yang's extensive knowledge of optical and acoustic imaging, and signal processing techniques.

Next, I am extremely grateful to Professor Frances Arnold, with whom I also rotated during my first year, and still remain her mentee through the Biotechnology Leadership Program (BLP). The BLP gave me valuable exposure as to how scientific research and innovations happen outside academia, an opportunity that I am very thankful for. The BLP also allowed me to closely interact with Dr. Kim Mayer and Dr. Julie Kelly, who have been truly outstanding in their role as program directors and always been there for us when we needed them. I will always cherish the enriching, warm and friendly conversations that I have had with Kim and Julie and thank them for all their help. I would also like to thank Prof. Henry Lester, who has always had kind words of praise and encouragement for me, as well as given me invaluable and candid feedback for personal and professional success, right from the time when I was a student and TA for his Neuroscience class back in 2013-2014.

Beyond Caltech faculty, I have had the pleasure of working with exceptionally talented and motivated students and colleagues on campus and in the Shapiro lab. They have constantly inspired me to do better and aim higher through invigorating scientific discussions, strong work-ethics, and an appetite for challenging research problems. I have especially enjoyed working with Suchita Nety, Teresa Tran and Zhiyang Jin. Mentoring them has been a very rewarding experience, and their contributions have been critical to the research work presented in this thesis. Special thanks to lab colleagues Dr. Dan Piraner and Dr. Ray Bourdeau for their dependable dose of wisdom and humor – these kept me sane and smiling during the long and sometimes arduous lab work hours. I would also like to thank Audrey Lee-Gosselin, Danny Sawyer, Mohamad Abedi, Dr. Pradeep Ramesh, Dr. David Maresca,

Dr. George Lu, Dr. Arnab Mukherjee, Dr. Avinoam Bar-Zion, Di Wu, Bill Ling, Arash Farhadi, Rob Hurt, Hunter Davis, Gabrielle Ho, Dina Malounda and Paulene Abundo, for numerous enriching and memorable moments in the Shapiro lab.

I consider Caltech to be a monastery for science, where students, staff and faculty are supported in every possible way to help them realize their true potential as scientists. The unsung heroes are the administrative staff working behind the scenes to ensure our productivity and keep things running smoothly. In this regard, I would especially like to acknowledge the timely and generous help provided by Linda Scott, Felicia Hunt and Irina Meininger in navigating administrative tasks and hurdles.

I would like to sincerely thank my previous mentor Professor Charlotte Hauser, who played an instrumental role in me coming to Caltech for graduate school. Charlotte was my mentor for 3 years before I started graduate school, and built a solid foundation for my research career by encouraging me to ask bold and meaningful scientific questions, perform critical and rigorous experimental validation of hypotheses and follow my curiosity and passion for science.

Friends and social circles have been an integral component of my graduate student life in Pasadena. I had the good fortune of getting wonderful and caring friends who have enhanced my graduate school experience and contributed to my personal development outside of lab. I will especially cherish the memorable and fun times with my roommate - Sripriya Ravindra Kumar, whose help, friendship, composure and common sense infused the feeling of having a home away from home. I would also like to thank Poorna Subramaniam, Prachi Parihar, Siddharth Jain, Neel Nadkarni, Saransh Sharma, Sisir Yalamanchili and Pushkar Kopparla for their enjoyable company and solid friendship over the years. In addition, I am very thankful for the valuable personal guidance and support that I have received from Professor Palghat. P. Vaidyanathan, Suresha Guptha and Geetha Suresh.

I am deeply grateful for having a wonderful and supportive family who have always believed in me and encouraged me to reach for the skies while staying grounded to my roots. Special thanks to my brother Anand, sister-in-law Niralee and my aunts – Annapoorni S. and Dr. Indira V., for everything that they have done for me over the years. I also feel blessed to have found a wonderful, loving and caring husband in Dr. Vivek Nandakumar, who shares my passion for science, and has been my pillar of strength and support during the final phase of my PhD.

Finally, none of this would have been possible without the unconditional and selfless love, support and guidance of my parents – Lakshmanan Sahasranaman and Reva Lakshmanan. They have always placed my happiness above everything else, and let me travel across the world to pursue my dreams. I will always strive to uphold the high values and ideals that they have instilled in me, and dedicate my PhD thesis to them as a tiny acknowledgement for everything that they have done and continue to do for me.

ABSTRACT

Visualizing biomolecular and cellular processes in real time within deep tissues is fundamental to our understanding of the normal and pathological activity underlying health and disease. Ultrasound provides the ability to non-invasively image deep inside biological tissues with high spatial and temporal resolution. However, this technology has limited capacity to monitor molecular and cellular processes, due to the lack of appropriate intra-cellular and endogenously producible nanoscale contrast agents, which can directly couple sound waves to the activity or concentration of physiologically relevant molecules. This problem could in principle be solved by developing genetically encodable ultrasound sensors – biomolecules that can get illuminated in ultrasound imaging in response to specific cellular or molecular activity. This thesis describes the engineering and characterization of acoustic protein nanostructures called 'gas vesicles', or 'GVs', to accomplish this task.

GVs are protein-shelled gas-filled nanostructures produced by buoyant microbes, and were recently shown to be capable of scattering sound waves to produce ultrasound contrast. Owing to this property, they were initially conceptualized as a new class of ultrasound contrast agents. However, little was known about their tunability to enable molecular ultrasound imaging for a wide range of applications. In this thesis, we leveraged the genetic encodability of GVs to modify them at the level of their DNA sequence and constituent proteins, and thereby tune their mechanical, acoustic, surface and targeting properties. We accomplished this by establishing a facile and modular molecular engineering platform, to produce GVs that provide enhanced nonlinear signals for sensitive and specific detection in deep tissues, target specific cell types such as cancer and immune cells, and also provide distinct acoustic collapse spectra for multiplexed imaging. We then extended this platform to build GV-based biosensors that modulate their nonlinear ultrasound signals in response to changes in the activity or concentration of specific molecules in their environment. Specifically, we engineered acoustic sensors for three different types of enzymes and for calcium – whose activity or flux underlie a wide range of important cellular processes. Furthermore, we succeeded in transferring the genetic code of gas vesicles from their species of origin into a variety of other microbes that do not naturally produce them, in order to unlock their potential as ultrasound reporter genes. Our results establish GVs as reliable acoustic biomolecules, and thereby extend the capabilities of ultrasound for molecular and cellular imaging in a manner analogous to green fluorescent protein (GFP) and its derivatives in optical microscopy. When combined with the advantages of ultrasound for non-invasive imaging, this work facilitates novel technology to significantly enhance our understanding of molecular and cellular processes in basic biology, as well as enable improved diagnosis, monitoring and treatment of diseases.

PUBLISHED CONTENT AND CONTRIBUTIONS

D. Maresca*, **A. Lakshmanan***, M. Abedi, A. Bar-Zion, A. Farhadi, G.J. Lu, J.O. Szablowski, D. Wu, S. Yoo and M.G. Shapiro (2018). Biomolecular ultrasound and sonogenetics. *Annual Reviews in Chemical and Biomolecular Engineering*, 9, 229-252. ***Equal contribution**. doi: 10.1146/annurev-chembioeng-060817-084034

A.L. participated in writing and editing of the manuscript, and preparation of figures.

R. W. Bourdeau, A. L-Gosselin, **A. Lakshmanan**, A. Farhadi, S.R. Kumar, S. P. Nety and M.G. Shapiro (2018). Acoustic reporter genes for non-invasive imaging of microbes in mammalian hosts. *Nature*, 553, 86-90. doi: 10.1038/nature25021

A.L. participated in the preparation and testing of the genetic constructs in *E.Coli* and other heterologous microbial hosts, assisted with the *in vitro* ultrasound experiments, obtained TEM images, and conducted metabolic burden experiments in *E. coli* Nissle 1917 cells.

A. Farhadi, G. Ho, M. Kunth, B. Ling, **A. Lakshmanan**, G.J. Lu, R.W. Bourdeau, L. Schröder and M.G. Shapiro (2018). Recombinantly expressed gas vesicles as nanoscale contrast agents for ultrasound and hyperpolarized MRI. *AIChE Journal*, 64(8), 2927-2933. doi: 10.1002/aic.16138

A.L. participated in the image processing and data analysis of TEM images.

G. J. Lu, A. Farhadi, J.O. Szablowski, S. R. Barnes, **A. Lakshmanan**, R. W. Bourdeau and M. G. Shapiro (2018). Acoustically modulated magnetic resonance imaging of gas-filled protein nanostructures. *Nature Materials*, 17, 456-463. doi: 10.1038/s41563-018-0023-7

A.L. participated in the preparation of samples for *in vitro* and *in vivo* experiments.

A. Lakshmanan*, G. J. Lu*, A. Farhadi*, S. P. Nety*, M. Kunth, A. L-Gosselin, D. Maresca, R.W. Bourdeau, M. Yin, J. Yan, C. Witte, D. Malounda, F.S. Foster, L. Schröder and M.G. Shapiro (2017). Preparation of biogenic gas vesicle nanostructures for use as contrast agents for ultrasound and MRI. *Nature Protocols*, 12, 2050-2080. ***Equal contribution**. doi: 10.1038/nprot.2017.081

A.L. participated in the conception of the manuscript layout and coordinated its writing, compiled and edited the manuscript text, as well as developed methods of GV production, functionalization, characterization and ultrasound imaging.

D. Maresca, **A. Lakshmanan**, A. L-Gosselin, J.M. Melis, Y-L. Ni, R.W. Bourdeau, D.M. Kochmann and M.G. Shapiro (2017). Nonlinear ultrasound imaging of nanoscale acoustic biomolecules. *Applied Physics Letters*, 110, 073704. doi: 10.1063/1.4976105

A.L. participated in the preparation of the samples and phantoms for the *in vitro* experiments.

A. Lakshmanan, A. Farhadi, S. P. Nety, A. Lee-Gosselin, R. W. Bourdeau, D. Maresca and M. G. Shapiro (2016). Molecular engineering of acoustic protein nanostructures. *ACS Nano*, 10[8], 7314-7322. doi: 10.1021/acsnano.6b03364

A.L. participated in the conception and design of the study, planned and conducted experiments, analyzed and processed the data and wrote the manuscript.

C. N. Bedbrook, M. Kato, S.R. Kumar, **A. Lakshmanan**, R.D. Nath, F. Sun, P.W. Sternberg, F.H. Arnold and V. Gradinaru (2016). Genetically encoded spy peptide fusion system to detect plasma membrane-localized proteins in vivo. *Chemistry & Biology*, 22, 1108-1121. doi: 10.1016/j.chembiol.2015.06.020

A.L. participated in constructing and testing some of the genetic constructs in the study.

TABLE OF CONTENTS

LIST OF ILLUSTRATIONS AND TABLES

Chapter 1

BACKGROUND AND MOTIVATION

Sections of this chapter have been adapted from:

D. Maresca*, **A. Lakshmanan***, M. Abedi, A. Bar-Zion, A. Farhadi, G.J. Lu, J.O. Szablowski, D. Wu, S. Yoo and M.G. Shapiro (2018). Biomolecular ultrasound and sonogenetics. *Annual Reviews in Chemical and Biomolecular Engineering*, 9, 229-252. *Equal contribution. doi: 10.1146/annurev-chembioeng-060817-084034

1.1 Molecular Imaging: current modalities and their performance

Studying biological function within the context of living systems and the development of biomolecular and cellular therapy requires methods to image the function of specific molecules and cells deep inside intact organisms. This challenge has led to the emergence and rapid growth of the interdisciplinary field of molecular imaging over the last two decades. Molecular imaging aims to combine *in vivo* imaging techniques with molecular biology tools to visualize, characterize and measure physiological processes occurring at the molecular and cellular scale (1-12). Currently, optical imaging (fluorescence or bioluminescence), positron emission tomography (PET), single-photon emission computed tomography (SPECT), magnetic resonance imaging (MRI), and ultrasound (US) constitute the most commonly adopted techniques for molecular imaging (1, 6-8, 12). However, each of these modalities comes with inherent strengths and limitations, such as trade-offs in spatial resolution, penetration depth and sensitivity, and thus complicate the possibility of continuous, precise and reliable monitoring at a disease site or tissue of interest *in vivo*. These trade-offs are further detailed below.

Optical imaging uses visible light excitation, has high spatiotemporal resolution, and enables excellent molecular precision and sensitivity (13). The development of a large range of synthetic fluorescent and bioluminescent probes, combined with the discovery and engineering of the green fluorescent protein (GFP) and its analogs into genetically encoded fluorescent reporters have enabled optical imaging of diverse cellular and molecular processes (9-11, 14-19). Some examples include monitoring of gene expression, RNA localization, protein-protein interactions, signal transduction, calcium flux exchange, as well as changes in intracellular pH, transmembrane voltage and enzymatic activity (9, 11, 14, 16, 17, 20-24). However, optical imaging has limited utility for real-time *in vivo* monitoring owing to the strong scattering and absorption of photons in biological tissue, that necessitates surgeries or invasive procedures for optical access to deeper organs.

Imaging technologies such as PET and SPECT have whole organism access and high sensitivity, and are routinely used along with radioactive tracers in clinical molecular imaging settings to track changes and levels of cellular-scale targets, such as metabolites, within a living subject. Numerous applications have been demonstrated in the fields of oncology, neurology and cardiology (7, 25-29). For example, one of the most commonly used PET tracers is [18F]-2-fluoro-2-deoxy-glucose ([18F]-FDG). It is used to detect and monitor tumors by imaging areas of increased metabolic activity based on glucose uptake (5, 30). However, these modalities have long acquisition times, are relatively expensive, subject the patient to irradiation exposure, are prone to motion artifacts and have low spatial resolution (~ 0.3 - 1mm for SPECT, < 1 mm for PET), and are thereby limited to clinical imaging applications where organ-scale resolution will suffice (7).

Magnetic resonance imaging (MRI) is another modality that provides virtually unlimited depth penetration into biological tissue at relatively high spatial and temporal resolution (~ 100 μm and ~1s respectively), with excellent soft-tissue contrast and no ionizing radiation (6, 31). Recent advances in engineering genetically encoded biomolecular reporters for MRI have improved its ability to visualize processes such as gene expression, neurotransmission and cell migration. However, MRI still remains an expensive technique with long acquisition times (mins-hours) and is susceptible to motion artifacts, requiring the subject to remain fixed to one position for an extended period of time (7) .

Ultrasound imaging (US) is a non-invasive imaging modality with exceptionally high temporal resolution (< 1 ms), soft tissue contrast, and scalable, frequency-dependent spatial resolution and penetration depth (~10-100 μm and 2-20 mm respectively for a 15-150 MHz range). The safety, portability, high sensitivity, ease-of-use, low cost and short acquisition times (in mins) for ultrasound have made it one of the world's leading modalities for medical imaging of anatomy, physiology, and noninvasive therapy (1, 32). In addition, it offers a relatively wide variety of physical interactions for potential biomolecular coupling. Many of these unique advantages stem from fortuitous physical parameters. The density and compressibility of tissue leads to ultrasound wavelengths in the mid-micrometer range, while the relative homogeneity of tissue on this size scale leads to low scattering, enabling sound waves to penetrate deeply and be treated as spatiotemporally coherent on their way in an out of the body. These characteristics also make it intrinsically straightforward to image biological targets with ultrasound that may be harder with other modalities, such as pulse and wave-front shaping and super-resolved signal reconstruction. In addition, the ability of ultrasound to deposit focused momentum and energy in media allows it to interact with appropriate molecules, cells and tissues through thermal and mechanical mechanisms. Ultrasound has no ionizing radiation and can be used easily on moving subjects, allowing for real-time imaging of physiological processes in a natural setting. These attributes highlight the vast potential of ultrasound for non-invasive molecular imaging in deep tissue. However, molecular imaging using ultrasound requires not just the imaging technology, but also contrast agents that can effectively couple sound waves to specific processes such as gene expression and cellular signaling. The next sections include a brief primer on biomedical ultrasound technology as it stands today, before moving on to synthetic contrast agents used for functional and molecular ultrasound imaging, and their limitations. A strategy to address these limitations is subsequently presented, based on hollow-protein nanostructures called gas vesicles (GVs) that have emerged as a new class of genetically encodable acoustic contrast agents. The opportunities and challenges to engineer these GVs as a next-generation biomolecular toolkit for ultrasound are then discussed, in order to define the scientific motivation and framework for my thesis. The organization of the thesis is covered in the concluding section of this chapter.

1.2 Biomedical ultrasound: a brief overview

1.2a Ultrasound- wave behavior and tissue interactions

Ultrasound is defined by sound wave frequencies above those audible to humans (> 20,000 Hz). Ultrasound waves are generated by transducers coupled to a transmission medium such as biological tissue. They travel through the medium and interact with its components or provide momentum and energy for perturbation. Compression waves are dominant in biological tissue and liquids, and are used for most modes of imaging and control. In tissue, sound waves travel at ~ 1540 m/s, are reflected and scattered wherever they experience a change in acoustic impedance – a physical parameter that varies with local density and compressibility (33) (**Fig. 1-1a**). The relative homogeneity of the speed of sound in soft tissues results in sound waves remaining coherent as they traverse the tissue, and thus enable simple image reconstruction without major aberrations (34). By comparison, visible light is strongly scattered in tissues, which makes it challenging to retain a ballistic path at depths greater than a few hundred microns (**Fig. 1-1b**).

Ultrasound reflection at tissue interfaces is highly directional and reveals anatomical contours. Soft tissues have similar acoustic impedance values, resulting in relatively low contrast between them; air and bones have much lower and higher acoustic impedances, respectively, resulting in strong reflections (34). When the ultrasound wave encounters a target smaller than approximately 1/10th the wavelength, it is scattered omnidirectionally (35). Biological tissues include a variety of such diffracting entities or ‘scatterers’, such as fibers, cells and organelles. The echo from a single scatterer is usually very weak. When a large number of very close scatterers are imaged, the result is a dominant spatially coherent interference pattern called speckle (34). The amplitude of the ultrasound wave decreases exponentially as a function of depth. Part of the energy of the ultrasonic wave is absorbed in the tissue and dissipated as heat. Attenuation refers to both absorption and any reduction in wave amplitude due to reflection or scattering. Each tissue is characterized by a different attenuation coefficient value, which increases nonlinearly with frequency (34). As they pass through a medium, ultrasound waves also deposit momentum into that medium, resulting in mechanical forces known as acoustic radiation forces (ARF). Appreciable at higher ultrasound intensities and pulse durations, these forces, as well as localized heating, can be used to perturb and manipulate tissues and other materials.

1.2b Ultrasound imaging modes

Ultrasound imaging is the most commonly prescribed diagnostic modality in clinical practice (36). Typical equipment involves an ultrasound scanner and an ultrasound probe made of a linear array of transducer elements (i.e. 128 to 256 ultrasound transmitting/receiving elements) (37). Numerous ultrasound imaging modes have been translated to clinical practice; several of these modes are relevant to biomolecular ultrasound.

B-mode imaging: Ultrasound scanners are primarily used to produce real-time 2-dimensional images of underlying tissue (**Fig. 1-1d**) These grayscale images are referred to as B-mode images (where B stands for brightness), and are acquired through transmission into a tissue of short ultrasound pulses and recording of backscattered echoes. The location of a scattering or reflecting source is reconstructed from the arrival time of its signal at each array element in a process known as beamforming. The position of a point in the reconstructed B-mode image depends on the time of flight of the echo and the position of the transmitting probe element. The axial resolution of B-mode images depends on the wavelength ($\lambda = c_{tissue}/f_{US}$) and the number of cycles of vibration of the transmitted pulse. The axial resolution typically ranges from 500 μm (medical imaging) down to 50 μm (ultrasound biomicroscopy) (38). Since both attenuation and resolution increase with frequency, there is an inherent tradeoff between resolution and imaging depth (**Fig. 1-1c**). The lateral resolution of B-mode images depends on the transmitted ultrasound beam width and is typically a few hundred microns. The transverse resolution or image thickness is usually on the order of a millimeter. B-mode imaging is used to image every organ of the body with the exception of bones or air-filled organs as the lungs.

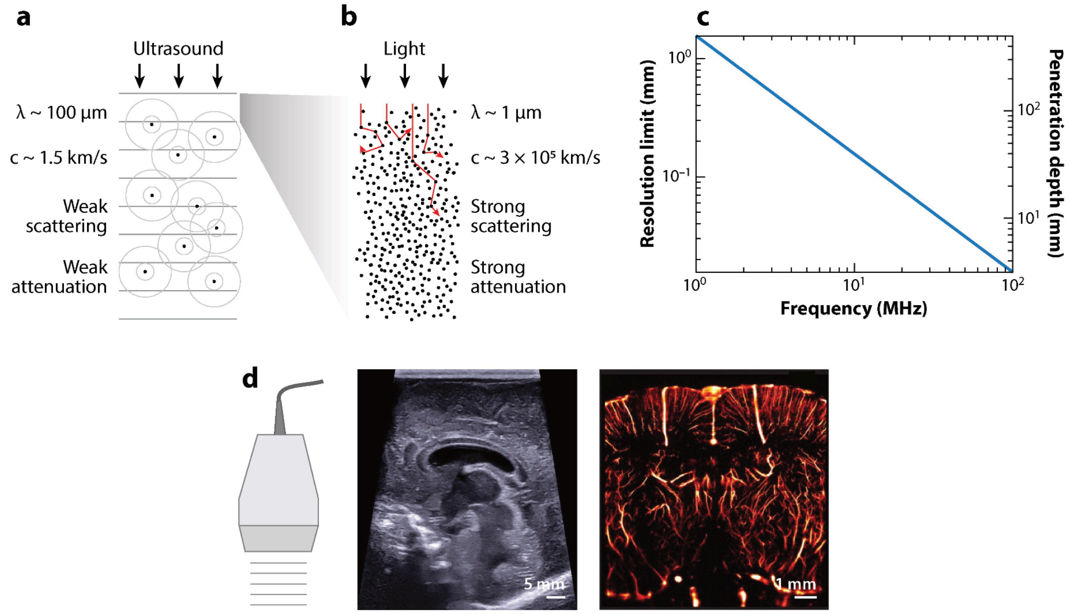

Figure 1-1: Properties and applications of ultrasound waves. (**a**) Physical properties of ultrasound waves in biological tissues. (**b**) Physical properties of light travelling in biological tissue. (**c**) Fundamental tradeoff between ultrasound resolution and penetration depth as a function of frequency in brain tissue (penetration depth was assessed based on a 60-decibel round-trip attenuation). At an ultrasound frequency of 15 MHz, one can expect to image the brain 2 cm deep at a 100 µm resolution. (**d**) Illustration of ultrasound imaging capabilities; conventional B-mode image of an infant brain with a submillimeter resolution of cerebral structures; 15 MHz super-resolution ultrasound image of the rat brain vasculature with an 8-µm resolution, breaking the classical tradeoff exposed in (c), adapted with permission from Errico et al. (39). Figure reprinted with permission from (32).

Doppler imaging: Ultrasound Doppler imaging consists in detecting the motion of red blood cells (RBCs) and, therefore, blood flow (40). RBCs scatter weak ultrasound echoes, which can be captured with modern ultrasound probes. At a given depth in tissue, the temporal shifts observed in consecutive RBC echoes allow detection of the displacement of RBCs and derivation of a Doppler signal proportional to RBC velocity. One can either generate vascular images displaying the velocity (color Doppler) or the energy of RBC echoes (Power Doppler) (41).

Ultrafast imaging: Conventional B-mode imaging utilizes a series of focused transmissions along an ultrasound array to form an image, such that the acquisition of a 10 cm-deep image with a 128-element probe takes at least 128 * 10 cm * 2 / 1540 m/s ~ 17 ms, resulting in a framerate of 59 Hz. A major recent advance, known as ultrafast ultrasound, uses single plane wave transmissions, rather than focused line transmissions, to form images, resulting in a two-orders-of-magnitude acceleration in framerate (42). The equivalent temporal resolution for a 10 cm image is 10 cm * 2 / 1540 m/s ~ 130 μs, or 7,700 frames per second. This advance was made possible by improvements in computer hardware allowing flexible software beamforming. This technology was initially developed for shear wave elastography and later applied to Doppler imaging.

Functional ultrasound imaging: Ultrafast Doppler imaging has raised the sensitivity of conventional Doppler imaging by a factor 30, leading to high-resolution, high signal-to-noise ratio (SNR) maps of the brain vasculature in rodents (43). The sequential acquisition of vascular maps of the brain with ultrafast Doppler has enabled the detection of neural activity through neurovascular coupling (44). Research efforts are ongoing to turn functional ultrasound imaging of the brain into a full-fledged neuroscience modality which complements fMRI, but additionally offers improved spatiotemporal resolution, portability, and cost.

Ultrasound localization microscopy: Super-resolution ultrasound imaging, also based on ultrafast ultrasound, was recently introduced using microbubbles as blinking sources. It was used to generate sub-10 μm resolution images of the brain or tumors at the organ scale (**Fig. 1-1d**) (39, 45). To obtain 3D information, linear array transducers are typically translated in the transverse direction, acquiring multiple 2D planes. In the future, all the imaging modes described above could be translated into 3D with the use of dedicated ultrasound probes made of 2D arrays of transducers.

Contrast imaging: Contrast-enhanced ultrasound relies on the administration of contrast agents to label specific aspects of anatomy or physiology. The conventional contrast agents used for this purpose are microbubbles (detailed in the next section) (46-49). When injected into the blood stream, microbubbles produce strong scattering as they resonate at ultrasound imaging frequencies (1 - 20 MHz), producing harmonic signals. Dedicated ultrasound contrast modes have been developed to benefit from that resonant behavior, such as amplitude modulation (50) or phase inversion (51), allowing the detection of microbubbles *in vivo* with higher specificity. Microbubbles can also be used to enhance Doppler imaging. Synthetic contrast agents used for ultrasound imaging and their limitations are detailed in the next section.

1.3 Synthetic ultrasound contrast agents and their limitations

Small gas bubbles to enhance ultrasound contrast were first reported by Gramiak and Shah in 1969 (52). Air bubbles without a stabilizing shell had a very short *in vivo* half-life, prompting development of methods to stabilize their gas-liquid interface. Over the last few decades, synthetic micron-sized bubbles or microbubbles have become the gold standard for contrast agents used in clinical ultrasound imaging (47, 48, 53-57). Microbubbles consist of a gas core typically composed of air, nitrogen or perfluorocarbons, surrounded by a shell made of lipids, proteins, polymers or surfactants (58). Low diffusivity gases have been used to increase microbubble circulation time and the shell composition and properties have been extensively optimized to improve the stability and functionality of these contrast agents. Microbubbles enhance ultrasound contrast by strongly scattering sound waves owing to the acoustic impedance mismatch between the gas core and the surrounding liquid medium. A key feature of microbubble behavior is that at certain ultrasound frequencies used in clinical imaging, they oscillate nonlinearly, causing the backscattered signal to contain a range of nonlinear or harmonic frequencies in addition to the transmitted frequency. The transmitted frequency is called the resonant frequency, and is inversely proportional to the size of the microbubble. Technological improvements have enabled the creation of small microbubbles that are more uniform in size (59). In addition, numerous ultrasound imaging and signal processing techniques have been implemented to harness this resonant behavior of microbubbles and separate harmonic signals generated by them from the signals originating from the tissue or noise background, enabling highly selective and sensitive imaging of these imaging agents *in vivo* (60). Microbubbles have also been functionalized to recognize and bind to specific targets in the bloodstream (60-64). These advancements have enabled many functional ultrasound imaging applications using microbubbles, including perfusion imaging of internal organs such as the heart and liver, super-resolution imaging of blood vessels, quantitative velocimetric imaging of blood flow in microvasculature and diagnostic imaging of tumors and their metastases (39, 61, 65-70). More recently, several groups have tried developing synthetic perfluorocarbon nanodroplets and nanovesicles to reduce the limitations that come with the large size of microbubbles (71-78).

Despite all these developments, bubbles have certain inherent limitations for *in vivo* molecular imaging. Firstly, the pressure drop across a bubble interface (ΔP) is given by the Laplace equation: $\Delta P = \frac{2\sigma}{r}$, where σ is the surface tension and r is the radius of the bubble (46). Hence, smaller bubbles will experience a higher pressure gradient across their interface, which would increase their likelihood of collapse, thereby rendering them physically unstable *in vivo*. Ultrasound insonated bubbles undergo rapid and extreme oscillations, causing leaking of gas from their interior during expansion and detachment of synthetic shell components during compression that compromises their stability (46). They also experience a large shear force and turbulence as they circulate in the vasculature (79, 80). Furthermore, the larger bubbles are also unable to escape the vasculature and extravasate to reach specific cells or tissues of interest, thereby limiting most of their applications to vascular imaging.

1.4 Gas vesicles as acoustic biomolecules

Due to the limitations of synthetic ultrasound contrast agents, it is imperative to develop ultrasound reporters that are nanoscale as well as genetically encodable, so that they can be synthesized by and within cells in response to intracellular processes that drive physiological function. In 2014, a unique class of gas-filled proteins called gas vesicles (GVs) were introduced as the first biomolecular contrast agents for ultrasound, paving the way for a more direct visualization of cellular and molecular function using sound waves (81). GVs were initially identified in 1965 as components of gas vacuoles found in cyanobacteria (82), themselves first observed in 1895 as intracellular bodies whose native function is to regulate cellular buoyancy for optimal access to light and nutrients (83). GVs of different shapes and sizes have been identified in a variety of bacteria and archaea, and studied by pioneering biology groups to determine their basic genetic, structural, physical and biochemical properties (84, 85). GVs have been characterized as cylindrical or spindle-shaped protein nanostructures, with lengths ranging from 100 nm to 2 µm, and widths of 45 - 200 nm (**Fig. 1-2, a-b**). GVs comprise a 2 nm thick amphiphilic shell that allows gas from the surrounding media to freely permeate in and out of their hollow interior, while excluding the aqueous phase. This amphiphilicity is accomplished by the primary structural constituent of GVs, a ~7.5 kDa protein called GvpA, which is predicted to fold into a beta sheet structure with hydrophobic and hydrophilic faces (86) (**Fig. 1-2c**). In addition to GvpA, a cluster of 7-13 other genes is needed to enable GV production (**Fig. 1-2d**), encoding minor structural proteins and assembly factors such as chaperones and nucleators (84, 85).

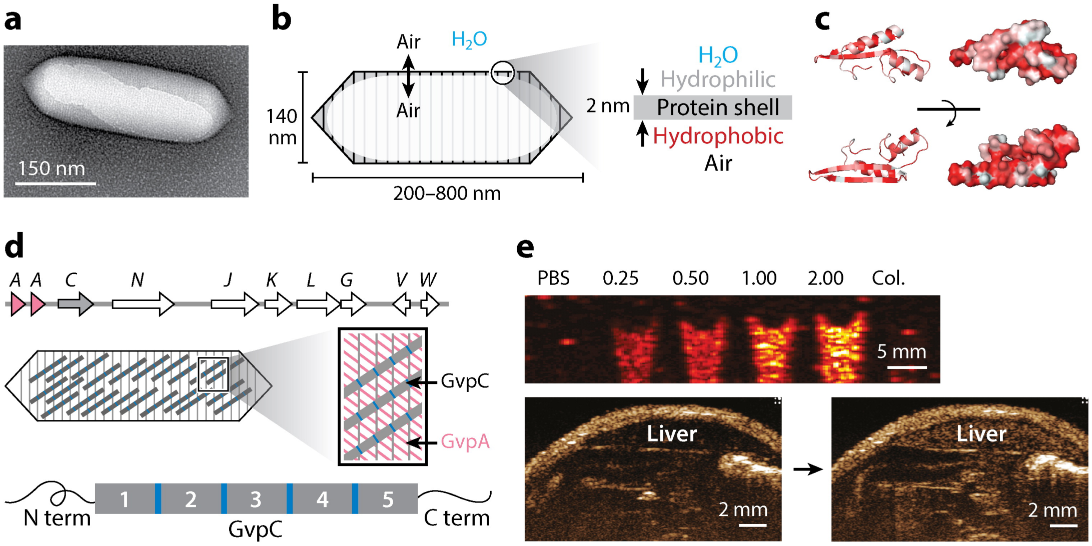

Figure 1-2: Gas vesicles as acoustic biomolecules. (**a**) Transmission electron micrograph of individual gas vesicle (GV) from *Anabaena flos-aquae*. (**b**) Illustration of GV structure. (**c**) Protein folding model for *A. flos aquae* gas vesicle protein A (GvpA), colored to indicate hydrophobilicy (red). Structure from Ezzeldin et al. (86), rendered in PyMOL. (**d**) Gene cluster encoding *A. flos aquae* GVs (top), illustration of GvpA and GvpC spatial arrangement (middle), and repeat structure of GvpC protein (bottom). (**e**) Ultrasound image of GVs at various optical densities and after hydrostatic collapse *in vitro*. Image of mouse

during and after GV administration *in vivo*, showing contrast in the liver owing to GV accumulation. Figure reprinted with permission from (32).

GVs are a remarkable product of evolution. First, whereas nanoscale bubbles are highly unstable due to their high Laplace pressure, GVs are fundamentally physically stable in equilibrium with their surroundings; gas dissolved in surrounding media equilibrates with the contents of GVs on a microsecond timescale (87). Second, despite having a ratio of ~75:1 between their diameter and shell thickness, GVs are able to withstand pressures of up to 1.3 MPa before collapsing (84). Third, the entire GV structure, with a molecular weight in the range of ~ 50-350 MDa, is self-assembled mostly from a single 7 kDa protein repeated in its shell in a highly-ordered arrangement (84, 85, 88).

The first demonstration of GVs as acoustic biomolecules, published in 2014, showed that GVs from *Anabaena flos-aquae* (Ana) and *Halobacterium salinarum NRC-1* (Halo) could produce ultrasound contrast in their purified form, inside cells and after injection *in vivo* (**Fig. 1-2e**), opening the door to their development as biomolecular reporters for ultrasound and as targeted nanoscale agents for molecular imaging (81). The GVs were detectable at concentrations below 12 pM (corresponding to ~ 3.5 µg/ml or 0.005 % volume fraction) (81). The next section discusses opportunities and challenges for engineering GVs as the next-generation of molecular imaging agents for ultrasound.

1.5 Opportunities and challenges for engineering GVs as next-generation molecular imaging agents for ultrasound

From a biomolecular engineering perspective, the genetic encodability of GVs raises a plethora of possibilities to fine-tune the properties of these acoustic contrast agents at the level of their DNA sequence and constituent proteins. Using established genetic and protein engineering methods such as recombinant protein expression, directed evolution and rational mutagenesis, specific GV genes or proteins could be modified to evaluate their effect on the mechanical, surface and acoustic properties of these nanostructures. Initial molecular engineering efforts could focus on substituting individual protein components of self-assembled GV nanostructures purified from native hosts, with modified versions.

These purified native or engineered GVs could then be intravenously or locally administered and evaluated *in vivo*. Chemical or genetic functionalization of the GV surface along with their nanoscale dimensions would enable these acoustic nanostructures to be targeted to specific cells and tissues of interest outside the vasculature. In addition, the ability to erase acoustic contrast from GVs by collapsing them is another property that could be utilized to specifically and sensitively detect them from tissue background *in vivo*.

Alternatively, GVs could be engineered entirely at the level of their DNA sequence and expressed in native or heterologous hosts. Natural GVs come in a variety of shapes, sizes and collapse pressures depending on their microbial origin (84, 85). A rational genetic engineering approach combining elements from different native GV gene clusters, or making functionally conservative mutations in GV genes could be used to engineer hybrid or mutant GVs that display unique mechanical and acoustic phenotypes. Such mutations have been shown in basic studies to produce a variety of GV shape phenotypes (89-91).

The ability of GVs to be endogenously synthesized by cells provides immense opportunity for developing them as biomolecular reporters for ultrasound imaging *in vivo*. Firstly, unlike synthetic contrast agents, genes encoding GVs can be delivered to target cells and tissues by leveraging recent advances in gene delivery (92, 93). Secondly, functional expression of naturally-occurring or modified GV gene clusters in new microbial and mammalian hosts would enable their development as acoustic reporter genes. Thirdly, directly coupling GV expression and acoustic behavior to molecular and cellular events would enable them to serve as genetically encodable acoustic biosensors for non-invasively tracking the activity and concentration of physiologically relevant ions and molecules.

While the discovery that gas vesicles produce acoustic contrast raises exciting avenues for their engineering and development, several challenges exist along the way to realizing their full potential as next-generation molecular imaging agents for ultrasound. First, there is no precedent for modifying GVs to tune their acoustic properties, requiring the establishment of engineering strategies and standardized experimental workflows for this purpose. Second, unlike the genetic engineering of well-characterized optical reporters such as GFP, gas vesicles are encoded by a cluster of 8-14 genes, with the precise function of some genes in the cluster not fully characterized or understood (84, 85, 89, 91, 94). This makes it less straightforward to engineer and express them in non-native hosts. Furthermore, the metabolic burden of expressing large GV gene clusters and assembling these protein nanostructures in non-native hosts is unknown. Other technical challenges include the lack of standardized workflows to scale up the production and purification of GVs from their native microbes in sufficiently large quantities for molecular engineering and characterization, and also to modify and test different variants in reasonably high-throughput. Finally, this new class of imaging agents would benefit from the concordant development of ultrasound imaging techniques and approaches that help decipher and characterize the physical basis of their acoustic properties in greater detail, as well as provide the ability to harness these unique properties for more specific and sensitive acoustic imaging *in vivo*.

1.6 Thesis organization

This thesis is presented as six chapters, beginning with this introductory chapter. Chapter 2 – titled as 'Production and characterization of gas vesicles for ultrasound imaging'– details the theoretical considerations and experimental methodology that we developed and optimized to prepare these protein nanostructures for acoustic imaging. Chapter 3 on 'Molecular engineering of acoustic protein nanostructures' elaborates our efforts in establishing a facile and modular engineering platform for tuning the mechanical, acoustic, surface and targeting properties of gas vesicles. Chapter 4 introduces the first 'Acoustic reporter genes for noninvasive imaging of microbes in mammalian hosts' by successful heterologous expression of engineered GV gene clusters in non-native microbial hosts. Chapter 5 describes how we extend the GV engineering platform introduced in Chapter 3 to build 'Acoustic biosensors for ultrasonic imaging of enzymatic activity' and expand the biomolecular toolkit for functional ultrasound imaging. Chapter 6 is the final chapter of the thesis, which demonstrates the feasibility of 'Engineering acoustic biosensors with reversible dynamics for molecular ultrasound imaging of calcium.'

Chapter 2

PRODUCTION AND CHARACTERIZATION OF GAS VESICLES FOR ULTRASOUND IMAGING

This chapter is adapted from:

A. Lakshmanan*, G. J. Lu*, A. Farhadi*, S. P. Nety*, M. Kunth, A. L-Gosselin, D. Maresca, R.W. Bourdeau, M. Yin, J. Yan, C. Witte, D. Malounda, F.S. Foster, L. Schröder and M.G. Shapiro (2017). Preparation of biogenic gas vesicle nanostructures for use as contrast agents for ultrasound and MRI. *Nature Protocols*, 12, 2050-2080. ***Equal contribution**. doi: 10.1038/nprot.2017.081

2.1 Introduction

Gas vesicles (GVs) – genetically encoded gas-filled protein nanostructures from buoyant photosynthetic microorganisms recently introduced a new class of molecular imaging agents for ultrasound (81). In order to engineer GVs and use them for acoustic imaging applications, we had to first produce and isolate them in sufficient yields from their microbial hosts, as well as establish standardized methods to quantify and characterize them. This chapter briefly outlines the theoretical and experimental considerations for the production, purification, characterization and utilization of gas vesicles from native GV gene clusters for ultrasound imaging. Detailed step-by-step protocols are provided in Appendix A.

2.2 Theoretical and experimental considerations

2.2a Production and purification of gas vesicles (GVs)

For GV production, an important initial consideration is the choice of GV-producing species. GVs differ in their size, shape, mechanical and acoustic properties depending on their genetic origins, with particular types of GVs being most suited for a given imaging application. GVs can be produced and isolated from microbes such as *Anabaena flos-aquae* (Ana), *Halobacterium salinarum* (Halo) or heterologously-expressing *E. coli* (84, 85, 95). Ana is a green, filamentous cyanobacterium that naturally inhabits fresh water lakes (84). Halo is a pink halophilic and thermophilic archaea that grows in salt-water ponds (85). Ana is cultured in low-salinity medium, supplemented with trace metals and buffering agents, while Halo is cultured in high salinity medium for GV production. The characteristics of different types of GVs are summarized in **Table 2-T1**.

Parameters	**Ana GV**	**Halo GV**	**Mega GV**
Host/origin	*Anabaena flos-aquae*	*Halobacteria salinarum*	Heterologous expression of a gene cluster from *Bacillus megaterium* in *E. coli*
Shape	Cylindrical	Spindle	Cylindrical
Resistance to pressure-induced collapse	Medium (can be tuned)	Low	High
Ultrasound contrast	High Linear in their native form	High Nonlinear	Low
Stability in phantoms	High	Low	High
Ease of genetic modification	High	Low	Not established

Table 2-T1: Characteristics of different types of GVs.

Unmodified Halo GVs can be used directly after purification, in ultrasound imaging, to obtain non-linear signals (81, 96). Ana GVs are the system of choice, if one wishes to genetically tune the properties of GVs for multiplexing, multimodal imaging and targeting applications (described in Chapter 3). Mega GVs produce lower echogenicity under ultrasound compared to Ana and Halo GVs (**Fig. 2-S1, a-d**), but have a higher critical collapse pressure that may make them useful for multiplexing. Halo GVs produce non-linear ultrasound contrast immediately after purification (81), while Ana GVs require genetic engineering or chemical treatment (Chapter 3).

Ana and Halo cultures natively produce ample GVs after a few weeks of growth (81, 97, 98). Ana cultures additionally require a controlled gaseous environment and illumination for optimal growth **(Fig. 2-1, a-b)**. A freshly inoculated culture of Ana or Halo cells may require several rounds (typically 2-3) of subculturing to become strongly proliferative **(Fig. 2-1, c-d)**. Healthy, viable Ana and Halo cultures look dark green **(Fig. 2-1c)** and light pink **(Fig. 2-1d)** respectively, upon reaching confluency. The confluent culture of microbes is then transferred to a separatory funnel that is left undisturbed for up to a week, to allow the buoyant cells producing GVs, to float to the top and separate from spent media **(Fig. 2-1, e-f)**. Buoyant cells are then lysed using hyper-osmotic shock for Ana and hypo-osmotic shock for Halo. Subsequently, centrifugally assisted floatation is used to isolate GVs from the cell lysate to yield a concentrated, milky-white solution of GVs in the buffer of choice **(Fig. 2-1, g-j)**. Heterologous production of Mega GVs in *E. coli* is accomplished by expression from a plasmid, encoding a Mega GV gene, followed by detergent-mediated lysis (95, 99). The typical yield is ~ 3 mL of a GV suspension, with a pressure-sensitive optical density ($OD_{500,ps}$) of 10 for Ana and Halo per flask of culture, and approximately 1.5 mg/L cells per unit of OD_{600} for Mega GVs .

The procedures leading from inoculation of GV-producing microbes to harvesting and purification are summarized in **Table 2-T2**, along with important parameters that affect processing time, yield and quality.

Procedure	Design Parameters
Inoculation of starter culture	Type of culture (suspension vs. solid), amount of inoculum, total volume of culture
Growth of starter culture	Temperature, rotation speed, duration, illumination
Sub-culturing	Number of flasks, volume of culture and media
Harvesting of GVs	Composition of lysis buffer and duration of lysis, concentration of cells
Purification	Selection of centrifugation speed, type of rotor, tube and syringe needle
Storage	Storage temperature, buffer and type of vial/tube

Table 2-T2: Experimental parameters for GV production, purification and storage.

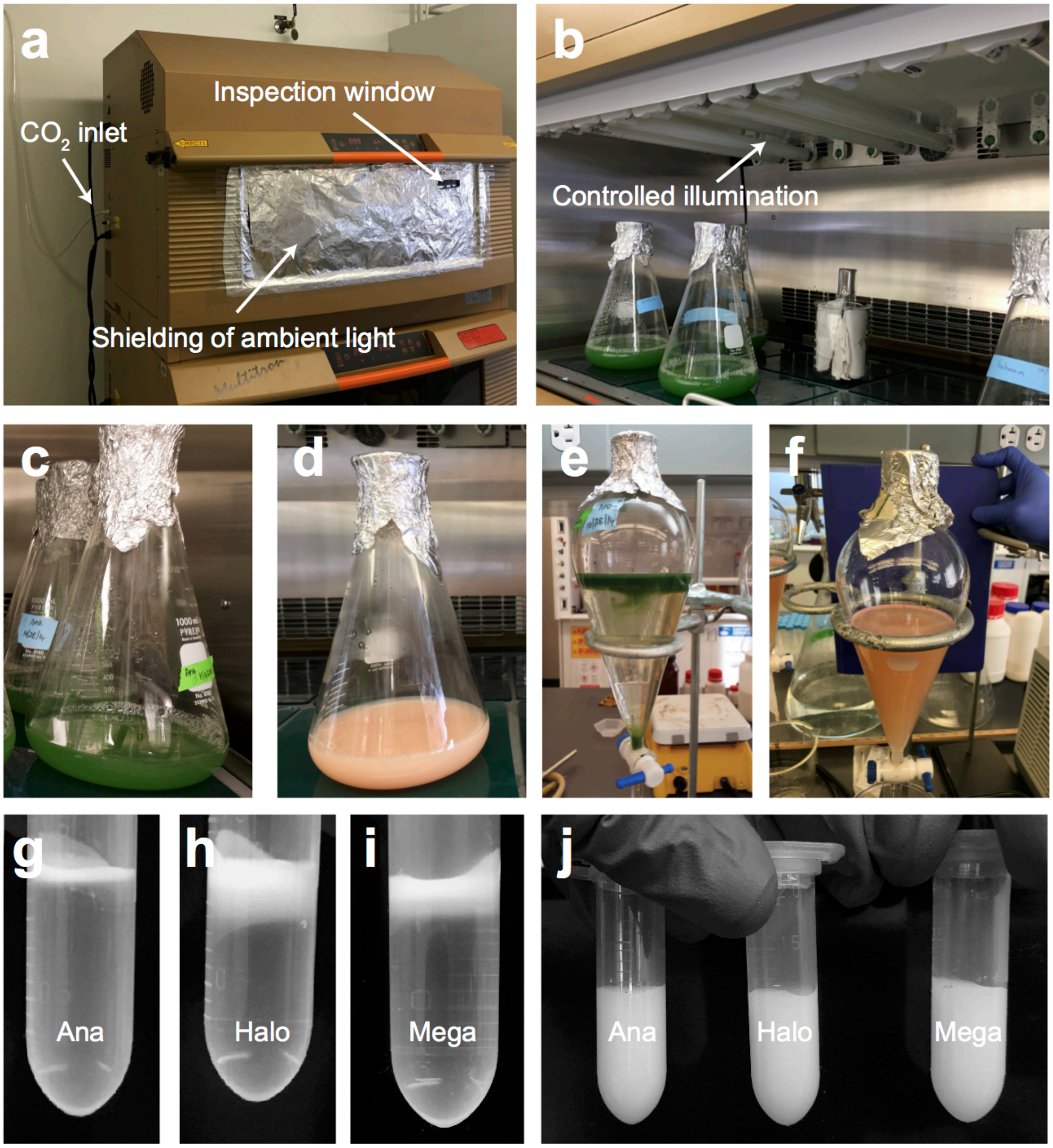

Figure 2-1: Equipment setup and expected results for native production and purification of GVs. (**a, b**) Shaker-incubators adapted for the growth of cyanobacteria *Anabaena flos-aquae* providing controlled illumination, temperature, aeration and CO_2. (**c, d**) Confluent green and pink cultures of *Anabaena flos-aquae* and *Halobacteria salinarum* respectively, just before harvesting. (**e, f**) Effective separation of buoyant cells from spent media in separatory funnel for isolation and harvesting of Ana and Halo cells producing GVs. Purified Ana (**g**) Halo (**h**) and Mega (**i**) GVs as a dense milky-white layer post centrifugally assisted floatation. (**j**) Resuspended milky-white solutions of purified Ana (left), Halo (middle) and Mega (right) GVs in PBS at $OD_{500,ps}$ ~6 prior to use in ultrasound imaging experiments.

Growth conditions are chosen to facilitate optimal proliferation of each host strain and GV expression. One unusual variable to keep track of is pressure, since GVs collapse irreversibly at hydrostatic pressures of 50 to 800 kPa, depending on species (84). For example, the cultures should be grown under mild agitation, as excessive shaking may lead to GV collapse. During centrifugation, it is necessary to calculate the hydrostatic pressure generated for a particular g-force on the liquid column of GVs and ensure that it is well below the GV critical collapse pressure. Long-term storage of purified GV stocks should preferably be done in screw-top vials, as micro-centrifuge tubes with snap-lock caps may cause GV collapse due to pressurization of the sample while opening or closing the tube.

2.2b Quantification and characterization of GVs

Purified GVs resuspended in the buffer of choice (e.g. phosphate buffered saline or Tris) can be quantified by measuring the optical density at 500 nm, or OD_{500}, since GVs scatter visible light. Collapsed GVs (in the same buffer), which do not scatter light, are typically used as the blank control for measurements, yielding a pressure-sensitive OD reading ($OD_{500,\ ps}$). It is important to note that clustering of GVs, whether by design or due to functionalization with aggregation-prone moieties can confound OD_{500} measurements and contribute to errors in calculating concentration from OD_{500}. Pressurized absorbance spectroscopy assays GV mechanical strength by measuring change in OD_{500nm} of GV samples under increasing hydrostatic pressure using the device described in **Fig. 2-2**. The mean collapse pressures are 59 kPa (Halo), 587 kPa (Ana $GvpC_{WT}$) and 750 kPa (Mega).

Dynamic light scattering (DLS) is used to estimate the hydrodynamic size of GVs for routine non-destructive characterization and quality control. DLS can be used to assess GV clustering. Care should be taken in the interpretation of DLS readings of GVs due to the spherical assumption of the Einstein–Smoluchowski relation and the non-spherical shape of GVs. DLS values for hydrodynamic diameters exhibit variability due to the biogenic nature of GVs. Hydrodynamic diameters of Halo GVs range from 260 nm – 320 nm (polydispersity 0.15 – 0.21), Ana GVs range from 240 nm – 340 nm (polydispersity 0.17 – 0.26) and Mega GVs from 200-380 nm (polydispersity 0.23 – 0.34).

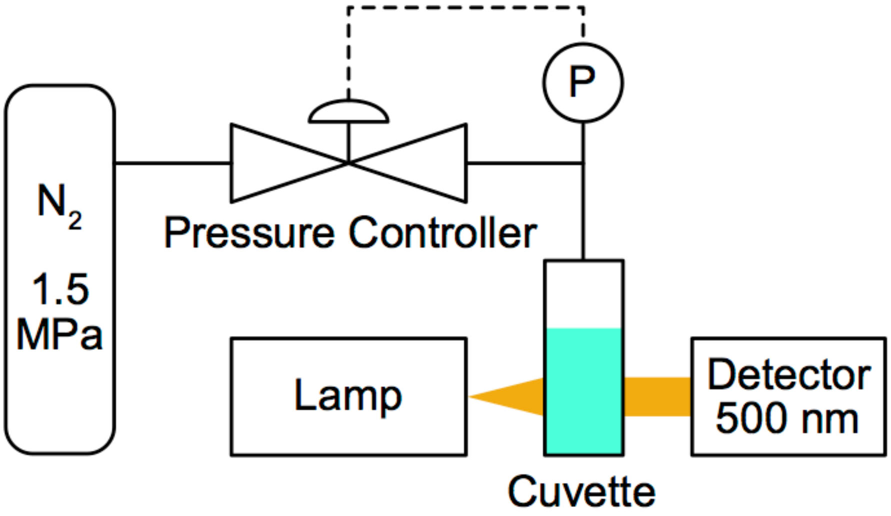

Figure 2-2: Collapsometry setup. Illustration of the collapsometry setup used for determining the critical collapse pressure of GVs.

Negative contrast TEM is used for imaging GV size, shape, texture and integrity following production and physical or biochemical treatments. Negative staining with uranyl acetate is used to produce contrast, and use of a buffer such as HEPES is preferred over phosphate buffers that may precipitate with the uranyl acetate. The concentration of the GV solution spotted on the grid directly correlates with the density of GV particles on the grid. While Halo GVs appear spindle-shaped, Ana and Mega GVs are more cylindrical with conical tips in the longitudinal dimension. Although the size and shape of GVs are determined primarily by the genotype, each type possesses a certain degree of heterogeneity. For example, Ana GVs have length distribution with a standard deviation of 35% of the mean (84). It is also important to note that not all Halo GVs have a spindle morphology, and a small subpopulation may appear more cylindrical with biconical ends (100). Ana GVs that are produced in their native host are usually longer and wider than heterologously-expressed Mega GVs. The high resolution provided by TEM allows the visualization of ribs on the surface of the gas vesicles at higher magnifications. GV collapse causes complete rupture and opening of the protein shell, leading to a flattened pancake-like structure (81). Typical GV dimensions obtained from TEM images are summarized in **Table 2-T3**.

Spatial Dimension	Ana GV	Halo GV	Mega GV
Length (nm)	519 ± 160	400 ± 113	249 ± 99
Width (nm)	136.3 ± 21.0	250.8 ± 51.4	72.5 ± 13.6

Table 2-T3: GV Dimensions. N=107, 125 and 61 for Ana, Halo and Mega respectively, errors indicate standard deviation.

We have also established the protein concentrations to OD relationships for the three types of GVs mentioned in this chapter, and the results are as shown in **Table 2-T4** below (N = 4, 5, 3 for Mega, Ana and Halo GVs respectively and the errors are in SEM). The molecular weight is derived from the TEM data summarized in **Table 2-T3**, assuming a spindle shape for Halo GVs, a cylindrical shape for Mega and Ana GVs, a wall thickness of 18 Å and a protein density of 1.4 g/mL.

GV quantification parameters	Ana	Halo	Mega
Protein concentration to OD_{500} ratio ([μg/mL] / OD)	36.6 ± 2.6	13.4 ± 2.2	145.5 ± 6.4
Estimated molecular weight (MDa)	320	282	71.7
Estimated molar protein concentration to OD_{500} ratio (pM / OD)	114	47.3	2,030
Estimated gas fraction to OD_{500} ratio (v/v/OD)	0.000417	0.000178	0.000794

Table 2-T4: Quantification and calculation of GV molecular weight and molar concentration.

2.2c Chemical functionalization of GVs

Chemical conjugation to GVs makes use of lysine residues on their protein shells and amine-reactive crosslinkers such as sulfo-N-hydroxysuccinimide esters (Sulfo-NHS). Chemical moieties including polymers (e.g. polyethylene glycol), fluorophores and small molecules (e.g. biotin) can be conjugated using this method. Biotinylated GVs can subsequently react with streptavidin or avidinated antibodies (81). The Sulfo-NHS coupling reaction can be conducted in PBS (pH 7.4) as a one-pot reaction. Depending on the application, the desired extent of labeling can be tuned by varying the molar ratio of Sulfo-NHS to GVs and by changing the incubation time. Either dialysis or buoyancy purification can be used to separate the labeled GVs from excess reactants.

2.2d Ultrasound imaging of GVs

For *in vitro* imaging, GVs can be embedded and imaged in multi-well agarose phantoms (**Fig. 2-3a**). A typical experimental setup for *in vitro* and *in vivo* ultrasound imaging is shown in **Figure 2-3, a-d**. Experimental design parameters include phantom composition, (i.e. percentage of agarose, buffer, background scattering particles), concentration and amount of GV sample loaded. Phantom molds can be made using 3-D printing to obtain defined well size, shape and spacing. Imaging parameters include plane of imaging (longitudinal versus transverse cross-section of the phantom wells), mode of ultrasound imaging (conventional or nonlinear imaging), transducer frequency range, transmit waveform characteristics such as pulse envelope shape, number of cycles, amplitude and frequency. Importantly, the amplitude used for imaging must be below the GVs' acoustic critical collapse pressure. PBS is typically used as a negative control for ultrasound contrast and 5 μm polystyrene beads that scatter linearly at medical ultrasound frequencies, are used as a reference sample. All GV samples and controls are mixed with melted agarose solution prior to loading. Solidification of the agarose after loading into the phantom wells, ensures that samples are uniformly distributed throughout the well and that GVs remain suspended in the agarose matrix without floating during imaging. Typically, a final OD_{500} of 2.25 for Ana GVs and 0.4% (wt/vol) for polystyrene beads is used to match echogenicity. For Halo GVs, a final OD of 0.5 gives good signal without attenuation, with 0.83% (wt/vol) polystyrene beads to match echogenicity. In-situ collapse of GVs using pulses with amplitudes above the GVs' acoustic critical collapse pressures cause GV ultrasound signals to disappear, allowing confirmation of GV-based signals and background subtraction. The acoustic behavior of Halo GVs at ultrasound frequencies of 12.5-27.5 MHz has also been investigated through modeling and experiments, suggesting acoustic buckling as the mechanism underlying generation of non-linear signals (96). In parallel, custom amplitude modulation schemes have been developed to take advantage of the nonlinear pressure dependence of backscattered signals in engineered Ana GVs, allowing selective imaging of these nanostructures (98, 101). Quantification of signals in ultrasound images is typically performed using MATLAB or ImageJ software.

The *in vivo* ultrasound imaging procedures can be used to look at GV passage through the inferior vena cava (IVC) and subsequent induced contrast enhancement in the liver after intravenous injection (81) or adapted to visualize GVs in other organs and tissues. Depending on the tissue region of interest, some ultrasound imaging parameters, such as image gain and field of view may need to be adjusted accordingly. As in *in vitro* imaging, it is critical that the transmit power is kept at a value that provides sufficient signal without collapsing the GVs. Further adjustments can be made to GV solution concentration and volume, according to experimental needs. Functionalized GVs can also be imaged using this protocol, as long as appropriate controls are used. When planning an imaging experiment using functionalized GVs, we suggest using native GVs from the same batch as a control. It is possible to administer multiple injections of GVs in the same mouse, as long as the total injection volume does not exceed the limit stated in institutional guidelines. If required, GV solutions can be tested for bacterial endotoxins, using quantitative, chromogenic endpoint LAL assays, such as the QCL-1000™ Assay (Lonza). Endotoxins can potentially be removed using commercially available affinity resins such as the ToxinEraser™ Endotoxin Removal Resin (GenScript). Once injected, ensure GVs have cleared completely and tissue contrast signal is back to baseline before a second bolus injection.

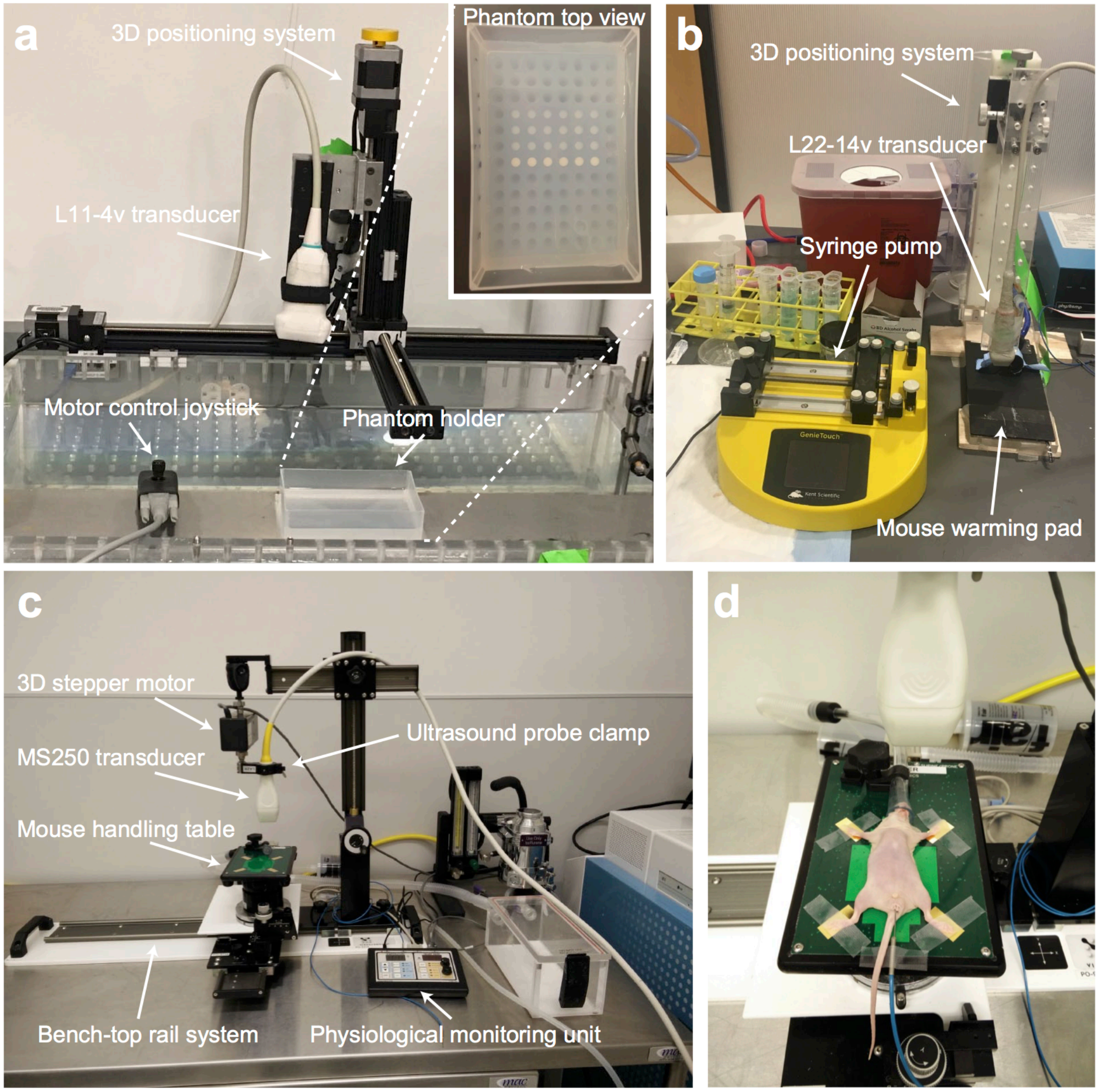

Figure 2-3: Ultrasound setup for *in vitro* and *in vivo* imaging. (**a**) Setup of the *in vitro* imaging system with the Verasonics L11-4v transducer mounted on a 3-D translatable clamp (computer-controlled) and a fixed imaging phantom holder. Inset shows an agarose phantom loaded with GV and polystyrene samples prior to imaging. (**b**) *In vivo* imaging setup with the Verasonics L22-14v transducer, mounted on a 3-D positioning system (manual), an animal mounting platform with a heating pad and a syringe pump for controlled sample injections. (**c**) Setup of a second *in vivo* imaging station that includes the ultrasound probe clamp attached to the 3D stepper, the mouse handling table and the physiological monitoring unit. All components except the physiological monitoring unit are attached to the bench-top rail system. (**d**) Animal positioning with the mouse being laid down in a supine position with the nose and mouth in the nose cone and each paw extending outwards onto the electrodes and secured with surgical tape. A rectal probe is used to monitor the core temperature of the animal. All procedures involving animal use must be

performed in accordance to institutional guidelines and regulations and approved by relevant Animal Care and Use Committees.

2.3 Supplementary figures

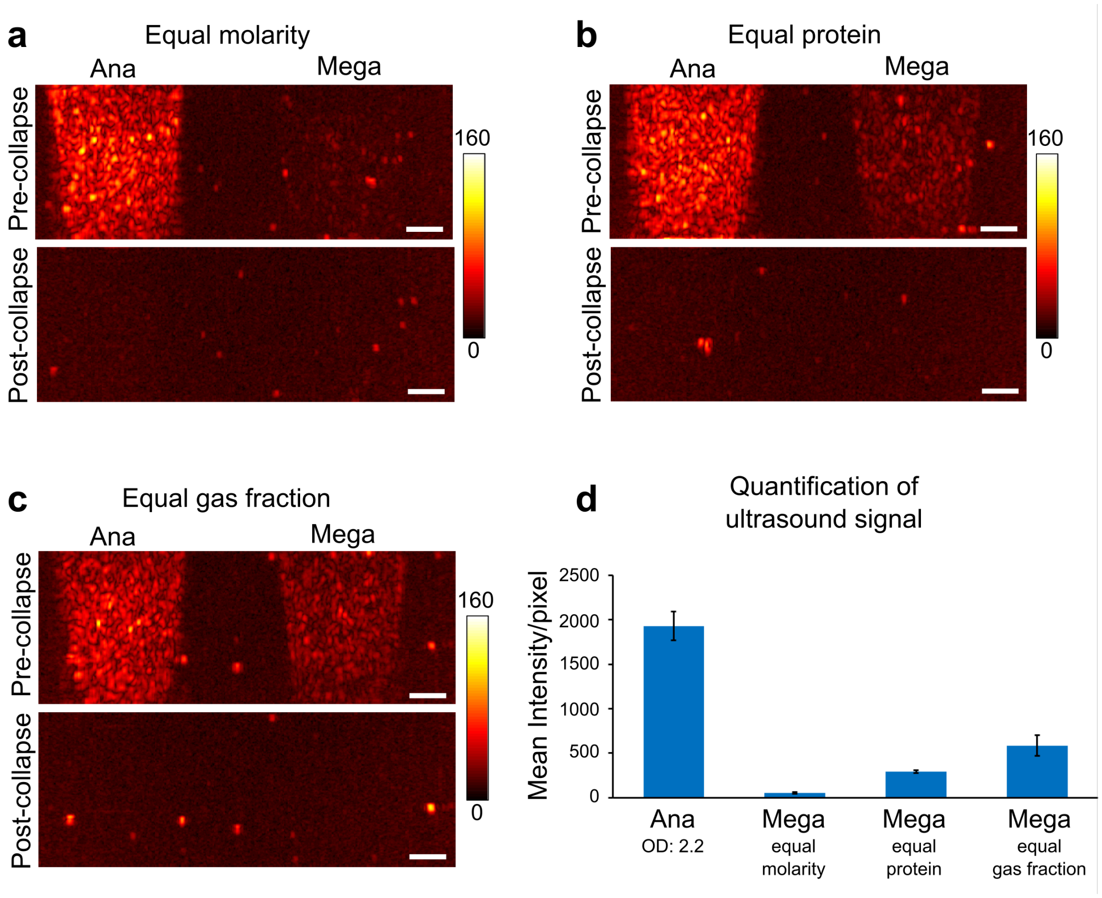

Figure 2-S1: Ultrasound imaging of Mega GVs. B-mode ultrasound images of purified, wild-type Ana GVs ($OD_{500,ps}$ 2.2) versus a purified and unclustered batch of Mega GVs at (**a**) equal molarity, (**b**) equal protein concentration and (**c**) equal gas fraction. Scale bars are 1 mm. Images were acquired using the Verasonics L22-14v transducer and the ray-lines script with the following parameters: transmit frequency: 18MHz, number of cycles of the transmitted pulse: 6, F number: 2, imaging voltage: 3V, with the transducer focus (8 mm depth) aligned close to the center of the sample well. Images were processed and analyzed using MATLAB. Images are shown before (top panel) and after collapse (bottom panel) using a highpower burst from the transducer at 25V for 10 s. (**d**) Quantification of ultrasound signal was performed by selecting a region of interest (ROI) of defined size within the sample well and calculating the mean intensity per pixel for the selected ROI, after post-collapse background subtraction (n=12 for Ana GVs, n=4 for Mega GVs at each condition shown in (a), (b) and (c); error bars are SEM).

C h a p t e r 3

MOLECULAR ENGINEERING OF ACOUSTIC PROTEIN NANOSTRUCTURES

A. Lakshmanan, A. Farhadi, S. P. Nety, A. Lee-Gosselin, R. W. Bourdeau, D. Maresca and M. G. Shapiro (2016). Molecular engineering of acoustic protein nanostructures. *ACS Nano*, 10[8], 7314-7322. doi: 10.1021/acsnano.6b03364

3.1 Introduction

Ultrasound is among the most widely used biomedical imaging modalities due to its superior spatiotemporal resolution, safety, cost and ease of use compared to other techniques such as magnetic resonance and nuclear imaging. In addition to visualizing anatomy and physiology, ultrasound can take advantage of contrast agents to more specifically image blood flow, discern the location of certain molecular targets, and resolve structures beyond its normal wavelength limit *via* super-localization (39, 53). However, existing "microbubble" contrast agents - micron-sized bubbles of gas stabilized by a biocompatible shell - face limitations as molecular reporters, due to their size and inherent physical instability, restricting their use to primarily within the vasculature (46, 62). Recently, we introduced gas vesicles (GVs) as a new class of nanoscale imaging agents for ultrasound (81). GVs are gas-filled protein-shelled nanostructures (**Fig. 3-1a**) expressed intracellularly in certain bacteria and archaea as a mechanism to regulate cellular buoyancy in aqueous environments (84, 85). GVs have widths of 45 - 250 nm and lengths of 100 - 800 nm depending on their genetic origins (84, 85). Unlike microbubbles, which trap pre-loaded gas in an unstable configuration, GVs' 2-nm-thick protein shells exclude water but permit gas to freely diffuse in and out from the surrounding media (84) (**Fig. 3-1b**), making them physically stable despite their nanometer size. GVs produce robust ultrasound contrast across a range of frequencies at picomolar concentrations, exhibit harmonic scattering to enable enhanced detection *versus* background *in vivo*, and have species-dependent thresholds for pressure-induced collapse to enable multiplexed imaging (81). Furthermore, the genetic encodability of GVs raises the possibility of engineering the properties of these nanoscale imaging agents at the level of their protein composition and DNA sequence. Here, we establish this capability by biochemically and genetically engineering the mechanical, acoustic, surface and targeting properties of GVs from the cyanobacterium *Anabaena flos-aquae* (Ana GVs).

Ana GVs are cone-tipped cylindrical structures with a diameter of approximately 140 nm and length of 200-800 nm **(Fig. 3-1, a-b)**. These structures are encoded by a cluster of 9 different genes, including the two primary structural proteins, GvpA and GvpC, and several putative minor components and chaperones (85, 102, 103) (**Fig. 3-1, b-c**). GvpA is a 7.4 kDa amphiphilic protein that assembles into the main structural backbone of the GV shell by forming 4.6-nm-wide ribs that run perpendicular to the long axis of the nanostructure (63, 88) (**Fig. 3-1c**). GvpC is the second most abundant protein, and strengthens the GV shell by binding to its exterior surface (63, 87). This protein comprises five highly-conserved 33-amino acid repeats with predicted alpha-helical structure, and is believed to bind across GvpA ribs to provide structural reinforcement (63) (**Fig. 3-1c**). In biochemical studies, removal of GvpC and truncations to its sequence were shown to result in a reduced threshold for Ana GV collapse under hydrostatic pressure (87, 104). In addition, previous studies using other species have demonstrated that GvpC can tolerate fusions of bacterial and viral polypeptides (105, 106). Given these properties, we hypothesized that GvpC could serve as a versatile platform for molecular engineering of GV-based ultrasound contrast agents. Specifically, we predicted that changes in GV mechanical properties resulting from the removal, addition or modification of GvpC would alter the acoustic properties of Ana GVs, thereby allowing us to tune their ultrasound response and enable harmonic and multiplexed imaging (**Fig. 3-1 d, e**). Furthermore, we hypothesized that GvpC could serve as a modular genetic hook enabling the tuning of GV surface properties such as zeta potential, the display of ligands for reduced or enhanced cellular targeting and uptake, and the attachment of fluorescent proteins to enable multimodal imaging (**Fig. 3-1e**).

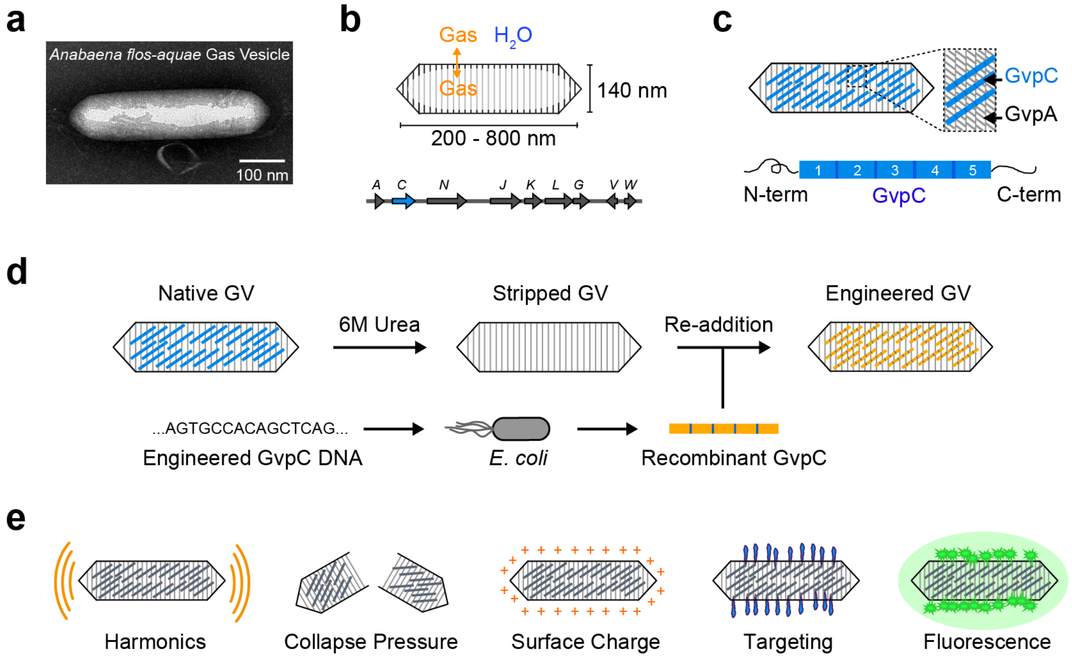

Figure 3-1: Molecular engineering platform for acoustic protein nanostructures. (a) Transmission Electron Microscopy (TEM) image of a single Ana GV. (**b**) Schematic illustration of Ana GV, and the gene cluster encoding GvpA, GvpC and several other essential proteins. (**c**) GvpA and GvpC are the two major structural constituents of GVs, with GvpA ribs (gray) forming the primary GV shell and the outer scaffold protein GvpC (blue) conferring structural integrity. Each GvpC molecule has five 33-amino acid repeats flanked by N- and C- terminal regions (**d**) Paradigm for modular genetic engineering of Ana GVs. Native gas vesicles are treated with 6M urea to produce stripped Ana GVs without native GvpC (blue). Genetically engineered GvpC is recombinantly expressed in *Escherichia coli* (orange) and added to the stripped Ana GVs during dialysis to create engineered GVs with a modified GvpC layer. (**e**) GvpC engineering can be used to modulate the properties of acoustic GV nanostructures including their harmonic response, collapse pressure, surface charge, targeting specificity and fluorescence.

3.2 Results and Discussion

3.2a Modular genetic engineering platform for acoustic protein nanostructures

To enable modular molecular engineering of Ana GVs, we established a platform in which genetically engineered GvpC variants are recombinantly expressed in *Escherichia coli* and subsequently added to Ana GVs that have been purified from *Anabaena flos-aquae* and stripped of their native GvpC proteins (**Fig. 3-1d**). The GVs were isolated by hypertonic and detergent-mediated lysis, followed by purification with centrifugally assisted floatation. Native GvpC was removed by treating the GVs with 6M urea, which leaves the GvpA-based shell intact (87, 104). We produced genetically engineered variants of Ana GvpC containing N- or C-terminal hexahistidine sequences in *Escherichia coli* and purified the resulting inclusion bodies by nickel chromatography in 6M urea. Dialysis of recombinant GvpC in the presence of stripped Ana GVs into physiological buffer resulted in Ana GVs with a new, engineered GvpC layer (**Fig. 3-1d**). SDS-PAGE analysis confirmed the complete removal of GvpC from native Ana GVs and the re-addition of engineered proteins (**Fig. 3-S1**).

3.2b Genetic engineering enables tuning of collapse pressure for acoustic multiplexing

The gaseous interior of GVs can be collapsed with hydrostatic and acoustic pressure, erasing their ultrasound scattering signal and enabling multiplexed imaging of GVs with distinct collapse pressure thresholds (81). To determine whether genetic tuning could enable enhanced multiplexing, we engineered three Ana GV variants with distinct mechanical properties. ΔGvpC comprises GVs completely lacking the outer GvpC layer; ΔN&C contains a truncated form of GvpC without its N- and C- terminal regions; GvpC_{WT} has an engineered GvpC protein that closely resembles the wild-type sequence (**Fig. 3-2a, Fig. 3-S5**). We assessed the hydrostatic collapse behavior of these nanostructures using pressurized absorbance spectroscopy, in which the optical density of GVs (which scatter 500 nm light when intact) is measured under increasing hydrostatic pressure. This provides a rapid assessment of GV mechanics and allows comparisons to literature (84).

Our three variants spanned a dynamic range of 380 kPa (**Fig. 3-2b, Supplementary table 3-T1**). ΔGvpC had the lowest collapse pressure midpoint at 195.3 ± 0.3 kPa, the ΔN&C variant showed an intermediate value of 374.3 ± 1 kPa and GvpC_{WT} had the highest value of 569.9 ± 4 kPa (**Supplementary table 3-T1**, N=7, ± SEM). To ensure that the decrease in collapse pressure for the ΔN&C variant was not due to unsaturated binding caused by reduced affinity of this GvpC variant for GvpA, we measured collapse midpoints as a function of re-added GvpC concentration and confirmed that binding was near saturation (**Fig. 3-S2, 3-S3**).

Next, we evaluated collapse profiles under ultrasound. GVs were imaged in multi-well agarose phantoms at 6.25 MHz while being subjected to ultrasound pulses with increasing peak positive pressure amplitudes ranging from 290 kPa to 1.23 MPa. Similar to trends observed for hydrostatic collapse, the ΔGvpC variant collapses under the lowest acoustic pressure, followed by ΔN&C and GvpC_{WT} (**Fig. 3-2c, Supplementary table 3-T2**). Notably, the collapse midpoints in the acoustic regime were substantially higher than in the hydrostatic regime. This is explained by GVs having a gas efflux time of approximately 1.5 µs (107), which is too slow for gas molecules contained in the GV to exit the nanostructure during the 80 ns positive half-cycle of 6.25 MHz ultrasound, allowing the gas to compressively reinforce the GV shell. On the other hand, under hydrostatic conditions, pressure changes occur on the time scale of seconds, allowing gas molecules to exit the GV during pressurization and resulting in the shell carrying the full compressive load by itself (96). We also note that the acoustic collapse curves appear somewhat more closely spaced than hydrostatic collapse curves, which can be explained by the applied acoustic pressure field having a non-uniform profile over the imaged GV sample. Fitting a Boltzmann sigmoidal function to these collapse curves reveals a unique acoustic collapse spectrum for each engineered GV (**Fig. 3-2d**).

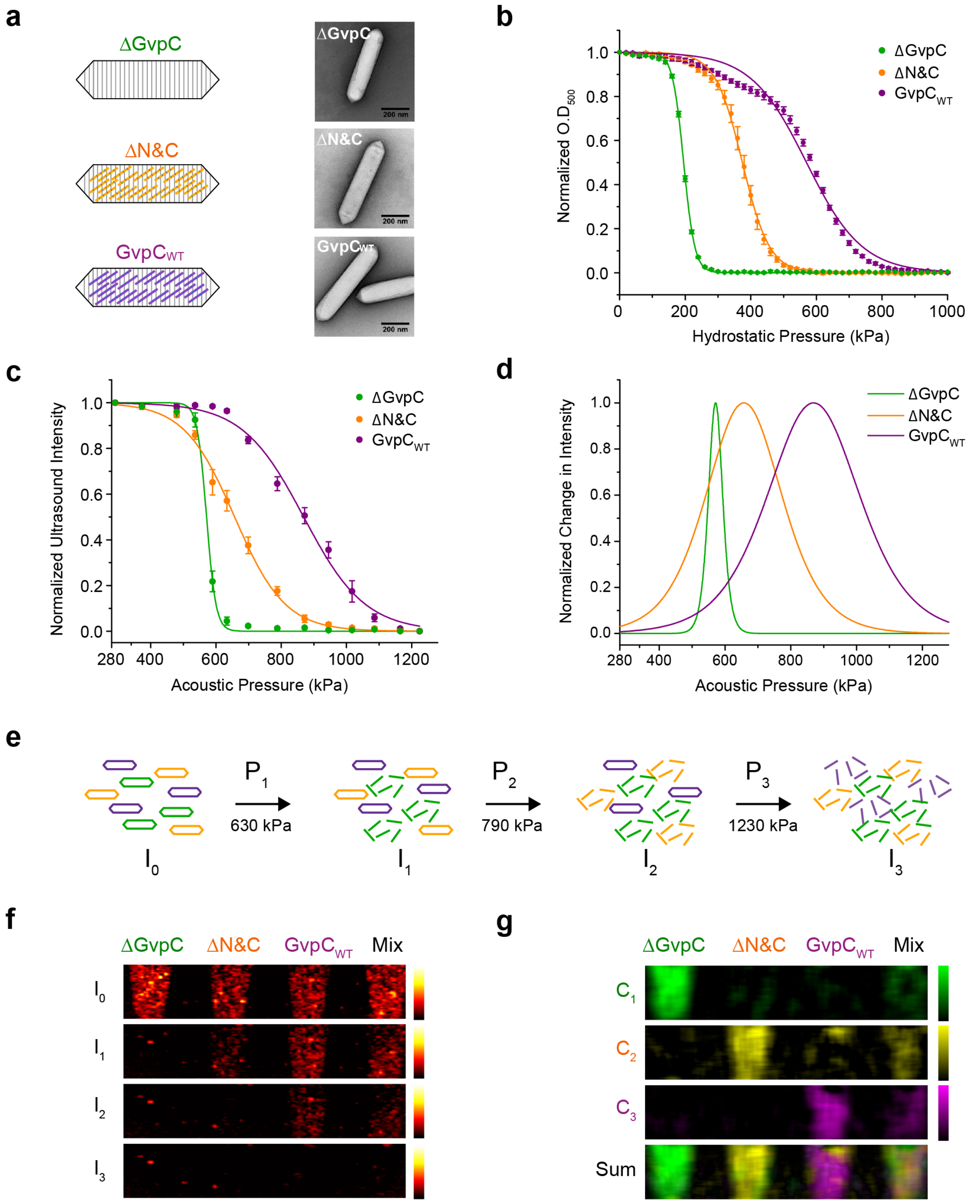

Figure 3-2: GvpC engineering enables tuning of GV collapse pressure for acoustic multiplexing. (**a**) Schematic illustration of the three engineered GV variants used for acoustic multiplexing. ΔGvpC, ΔN&C and GvpC$_{\mathrm{WT}}$ variants are represented by green, orange and purple colors respectively. Accompanying TEM images show the conservation of GV shape among the three variants (scale bars are 200 nm). (**b**) Optical density

measurements of engineered Ana GVs as a function of hydrostatic pressure (N=7 independent preparations, error bars are SEM). The data was fitted with a Boltzmann sigmoid function. Fit parameters and R^2 values are provided in Supplementary table **3-T1**. (**c**) Acoustic collapse curves for the GV variants showing normalized ultrasound signal intensity as a function of increasing peak positive pressure from 290 kPa to 1.23 MPa (N= 3 independent trials, error bars are SEM). The data was fitted with a Boltzmann sigmoid function (parameters provided in Supplementary table **3-T2**), the derivatives of which with respect to pressure are plotted in (**d**). (**e**) Schematic illustration of acoustic spectral unmixing, showing serial collapse of the GV variants based on their critical collapse pressure and indicating the pressures used in panels (f) and (g). (**f**) Ultrasound images of an agarose phantom containing wells with ΔGvpC, ΔN&C, GvpC_{WT} and a mixture of the three variants (all GVs at final OD 1.0 in PBS), acquired at 6.25 MHz. I_0; before collapse I_1: after collapse at 630 kPa I2: after collapse at 790 kPa I3: after collapse at 1230 kPa. (**g**) Spectrally unmixed images processed from the raw ultrasound data in (f). The bottom panel shows an overlay of the three unmixed channels C_1, C_2, and C_3.

To take advantage of the distinct acoustic collapse spectra of GV variants for multiplexed imaging, we developed a pressure spectral unmixing paradigm. This paradigm posits that the total signal for a mixed population of GVs in any given pixel is the sum of signals contributed by each sub-population present in that pixel. Images acquired after sequentially applying collapse pulses of increasing pressure (P_i) reveal changes in pixel-wise signal intensity (I) that provide information about the abundance of each GV type in the pixel (**Fig. 3-2e**). This information is extracted by multiplying the measured differential signals

$$\Delta_i = I(P_{i-1}) - I(P_i)$$

by the inverse of a matrix containing the collapse spectrum of each type of GV, denoted by $\alpha_{i,j}$. The contribution of each GV type to the observed signal represented as C_j is given by the matrix operation:

$$C = \alpha^{-1} \Delta.$$

We used pressure spectral unmixing to obtain multiplexed images of our three GV variants. **Figure 3-2f** shows ultrasound images taken at a non-destructive baseline pressure before and after exposing the GV samples to three sequentially increasing collapse pulses. The spectrally unmixed images (**Fig. 3-2g**) uniquely identify acoustic signals from each GV variant. **Figure 3-S4** shows the matrix of coefficients used to generate these images. We anticipate that this combination of engineered GVs and pressure spectral unmixing will be useful in many scenarios requiring ultrasound imaging of multiple molecular targets in the same sample.

3.2c Molecular engineering enables modulation of harmonic ultrasound signals

Nonlinear signals from ultrasound contrast agents can dramatically enhance their ability to be distinguished from background tissues, which mainly scatter linearly (108, 109). In our initial description of gas vesicles as ultrasound reporters, we found that GVs from *Halobacterium salinarum* (Halo GVs) produce strong nonlinear signals in the form of harmonics of the insonation frequency, while Ana GVs show no harmonic response (81). Since Halo GVs also have a significantly lower critical collapse pressure than Ana GVs (84), we hypothesized that altering Ana GV shell mechanics by engineering GvpC could yield Ana GVs that produce harmonic signals. Accordingly, we characterized the frequency response of engineered Ana GVs to 4.46 MHz pulses over a receive bandwidth of 2-10 MHz. Consistent with our hypothesis, ΔGvpC showed a sharp peak at the second harmonic frequency of 8.9 MHz in addition to the fundamental peak at the transmitted frequency, while $\mathrm{GvpC_{WT}}$ showed only a linear signal (**Fig. 3-3a**). Ultrasound images formed by bandpass filtering around the fundamental and second harmonic frequencies showed a substantial difference in the harmonic acoustic response of GV variants ($p<0.01$, $N = 7$, paired t-test), for the same level of fundamental signal (**Fig. 3-3, b-e**). The harmonic signals from ΔGvpC were 3.71fold higher than $\mathrm{GvpC_{WT}}$ (**Fig. 3-3e**). These results demonstrate that protein engineering can be used to modulate the acoustic properties of a nanostructure.

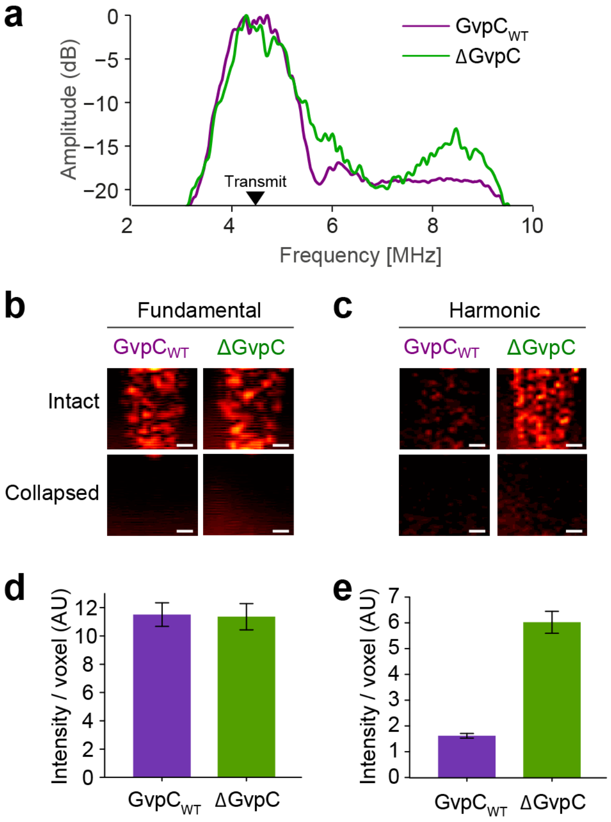

Figure 3-3: GV engineering enables modulation of harmonic signals *in vitro*. (**a**) Power spectrum of signal backscattered from ΔGvpC (green) and GvpC$_{WT}$ (purple) variants in an agarose phantom in response to 4.46 MHz pulses. (**b**) Fundamental and (**c**) second harmonic ultrasound images of ΔGvpC and GvpC$_{WT}$ GVs acquired with 4.46 MHz transmission and band-pass filtered around 4.46 and 8.92 MHz respectively. Images are shown before and after collapse using a high-power burst from the transducer to collapse the GVs. Scale bars are 1 mm. (**d**) Mean fundamental and (**e**) harmonic signals from ΔGvpC and GvpC$_{WT}$ variants after filtering at the indicated frequencies (N = 7 independent measurements, error bars are SEM). Data in all panels comes from GVs prepared at OD 2.5 in PBS and loaded into 1% agarose phantoms.

To show that engineered Ana GV variants are capable of producing harmonic signals *in vivo*, we performed intravenous injections of the ΔGvpC and GvpC$_{WT}$ variants into live, anaesthetized mice. Ultrasound imaging of the inferior vena cava (IVC) was performed in fundamental and second-harmonic modes (transmission at 4.46 MHz and reception filtered around 4.46 MHz and 8.9 MHz center frequencies, respectively). **Figure 3-4a** provides a schematic illustration of the *in vivo* experiment. Five seconds after the start of the injection, enhanced nonlinear signals were observed for the ΔGvpC variant compared to GvpC$_{WT}$, while their fundamental signals were comparable (**Fig. 3-4, b-d**). Repeated trials showed a statistically significant difference ($p<0.01$, N = 6, paired t-test) in the harmonic response of the two variants for the same level of fundamental signal (**Fig. 3-4e**), consistent with *in vitro* results. The ability to genetically tune the harmonic properties of GV contrast agents will enhance their utility for *in vitro* and *in vivo* imaging.

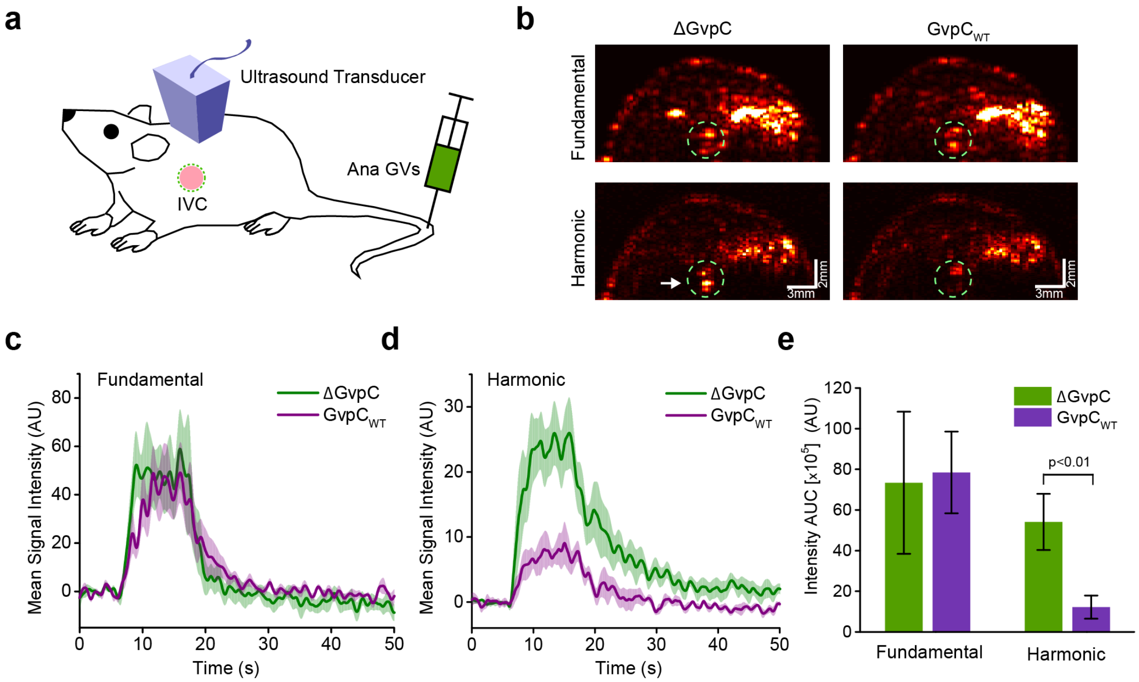

Figure 3-4: GV engineering enables modulation of harmonic signals *in vivo*. (**a**) Schematic depiction of intravenous GV injection and *in vivo* ultrasound imaging during passage through the inferior vena cava (IVC). (**b**) Fundamental and second harmonic ultrasound images taken at 4.46 MHz transmission frequency and band-pass filtered receive around 4.46 and 8.92 MHz respectively. Engineered Ana GVs at OD 23.5 in PBS were used for injections. The IVC ROI used for subsequent analysis is circled in green. The white arrow points to the increased harmonic signal observed in the IVC for the ΔGvpC variant. Time course of the mean **(c)** fundamental and (**d**) harmonic acoustic signal in the IVC before, during and after steady infusion, with shaded regions representing SEM (N = 6 mice). (**e**) Histogram showing the area under the curve (AUC) of average fundamental and harmonic contrast in the IVC after ΔGvpC and GvpC$_{WT}$ GV injections (N=6, error bars are SEM).

3.2d Genetic engineering enables tuning of surface charge, targeting specificity and multimodal imaging

After demonstrating the ability of GvpC to serve as a genetic platform for tuning the mechanical and acoustic properties of GVs, we examined its capacity to enable the engineering of GV surface and targeting properties. To do so, we used the C-terminus of GvpC as a modular site for protein fusion (**Fig. 3-5a, Fig. 3-S5**). As a first proof of concept, we tested the ability of GvpC fusions to modulate GV surface charge, an important property that influences the behavior of nanostructures in solution and *in vivo* (110). We fused GvpC with the lysine rich protein (LRP), which contains 100 positive charges at physiological pH. Re-addition of this protein to GVs resulted in nanostructures with 28 ± 4 mV higher zeta potential compared to GvpC_{WT} (**Fig. 3-5b**).

Next, we tested the ability of GvpC fusions to endow GVs with functionality for specific cellular targeting. A well-studied receptor-targeting peptide is RGD, which binds effectively to a wide range of integrins (111). GVs engineered to express GvpC_{RGD} on their surface were compared with wild-type GvpC and scrambled GvpC_{RDG} controls in terms of their ability to target the integrin-overexpressing U87 glioblastoma cell line *in vitro*. The GVs were chemically conjugated with the Alexa Fluor-488 fluorophore for visualization using confocal microscopy. GVs functionalized with RGD exhibited a marked increase in cell binding, compared to controls (**Fig. 3-5, c-d**). This technique presents a generalizable approach for future studies targeting GVs to molecular markers *in vivo*.

Using a similar engineering strategy, we created GvpC fusions to modulate the interaction of GVs with macrophages, which are both imaging targets and important actors in nanoparticle clearance from circulation. CD47, present on endogenous cell membranes in humans, mice, and other mammals, is a well-studied putative marker of self. Discher and colleagues recently described a minimized peptide from the human CD47 protein, dubbed the ‘self’ peptide, which led to reduced uptake of cells and nanoparticles by the mononuclear phagocytic system (112). On the other hand, polycationic peptides such as polyarginine (R8) promote particle uptake by phagocytic cells (113). By fusing each of these molecules to GvpC, we tested whether genetic engineering could modulate GV uptake in RAW 264.7 murine macrophages. As visualized by confocal microscopy, GVs genetically functionalized with $GvpC_{mCD47}$ showed reduced macrophage uptake compared to GVs with $GvpC_{WT}$. On the other hand, GVs functionalized with $GvpC_{R8}$ were taken up much more efficiently (**Fig. 3-5 e, f**). These molecular strategies can be used in future studies to enable cellular labeling for *in vivo* tracking applications or to enhance the circulation lifetime of targeted GVs.

Finally, to further simplify GV functionalization, we developed a highly modular approach through which the GV surface can be covalently conjugated to other recombinant proteins through a facile process that does not involve urea treatment and dialysis. To achieve this goal, we fused GvpC with SpyTag (ST), a 13-residue peptide that forms a covalent amide bond with a partner SpyCatcher protein under physiological conditions (114). This system allows SpyTagged GVs to be functionalized with SpyCatcher fusions in a rapid, biocompatible reaction. We found that $GvpC_{ST}$ binds to GVs with similar stoichiometry to $GvpC_{WT}$ and provides reinforcement against pressure-induced collapse (**Fig. 3-S6**). Each modified GV had an average of 1,000 SpyTag functionalities (**Fig. 3-S7**). To demonstrate the utility of this modular functionalization approach, we reacted these GVs with the recombinantly expressed fluorescent protein SpyCatcher-mNeonGreen (SC-mNG) to enable multimodal acoustic and fluorescent imaging. The resulting fluorescent GVs were purified by buoyancy enrichment. SDS-PAGE analysis confirmed SpyTag-SpyCatcher covalent bond formation (**Fig. 3-S8**), and **Figure 3-5g** shows multimodal imaging of mNG-labeled GVs with ultrasound and fluorescence. The ultrasound images show similar echogenicity between fluorescently-labeled GVs, wild-type and unreacted controls. $GvpC_{WT}$ Ana GVs do not show any fluorescence after reaction with SC-mNG **(Fig. 3-5g)**, highlighting the specificity of the SpyTag-SpyCatcher reaction and confirming that buoyancy enrichment eliminates unreacted fluorescent proteins (**Fig. 3-S8**). Notably, labeled ST-GVs remain fluorescent after acoustic pressure-induced collapse, which may be useful for follow-up histological examinations after ultrasound imaging. These results establish the GvpC_{ST}-SpyCatcher system as a highly modular and convenient approach to generate functionalized GVs, thereby enabling dual-mode imaging of these nanostructures.

3.3 Conclusion

In summary, our results demonstrate the genetic engineering of a biologically-derived acoustic nanomaterial, which we use as an imaging agent for ultrasound. Remarkably, a single constituent protein on the surface of GVs can serve as a genetic platform to modulate the mechanical, acoustic, surface and targeting properties of these nanostructures. This molecular engineering capability will enable the design of GV-based contrast agents with enhanced harmonic responses, biodistribution, multiplexing, multimodal detection and molecular targeting to help ultrasound fulfill its potential as a high-performance modality for molecular imaging. In addition, as a nanomaterial with genetically tunable mechanical properties, GVs may create opportunities for applications outside biology and medicine.

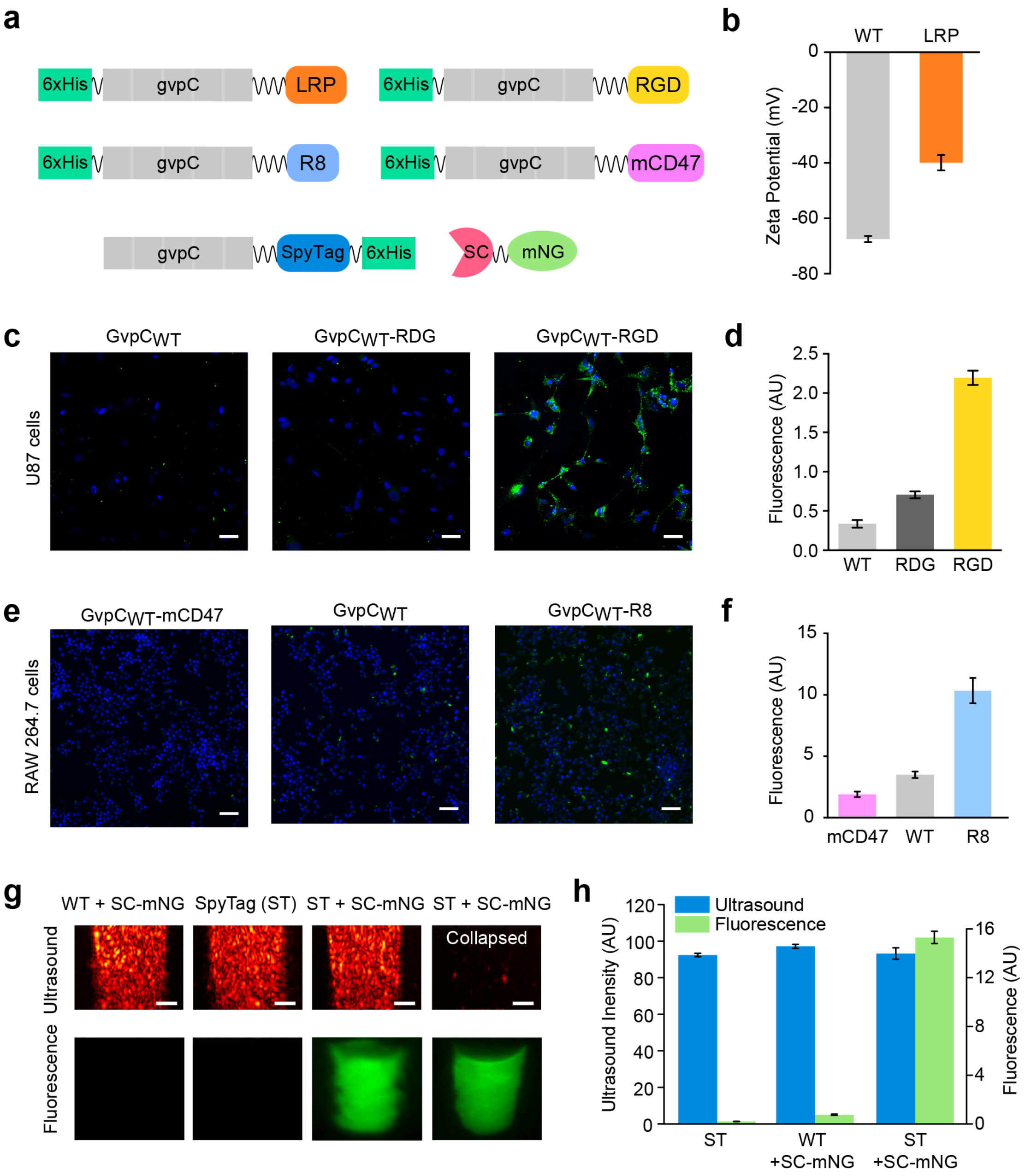

Figure 3-5: Genetic engineering of GV surface properties, cellular targeting and multimodal imaging. (**a**) Diagram of GvpC genetic fusions used to engineer novel GV properties and functions. (**b**) Zeta potential measurements of engineered GVs having GvpC fused to LRP and wild-type GvpC (N = 4, error bars are SEM) (**c**) Confocal fluorescence images showing RGD-functionalized, RDG-functionalized and wild-type Alexa Fluor-488 fluorescently labeled (green) GVs after 24 hr incubation with U87 glioblastoma cells (DAPI-stained nuclei, blue). Scale bars are 50 μm (**d**) Mean GV fluorescence measured for

each condition in (c) (N = 3, error bars are SEM). (**e**) Confocal fluorescence images of RAW 264.7 macrophages (DAPI-stained nuclei, blue) incubated for 30 min with fluorescently labeled GVs (green) displaying GvpC fused to mCD47, R8 or wild-type GvpC. Scale bars are 50 µm. (**f**) Mean GV fluorescence measured for each condition in (e) (N = 3, error bars are SEM). (**g**) Top panel: Ultrasound images of engineered and SpyCatcher-mNeonGreen (SC-mNG) reacted GVs at OD 2.5 in PBS, acquired using a 19 MHz transmission pulse in fundamental mode. Scale bars are 1 mm. Bottom panel: Fluorescence images of the agarose phantoms before and after acoustic collapse. (**h**) Mean ultrasound and fluorescence signals from the GV samples tested in (g). (N ≥ 4, error bars are SEM).

3.4 Methods

Gas Vesicle Preparation

Anabaena flos-aquae (Ana) was cultured in Gorham's media supplemented with BG-11 solution (Sigma, St. Louis, MO) and 10 mM $NaHCO_3$ at 25°C, 100 rpm shaking and 1% CO_2 under a 14h light cycle and 10h dark cycle. Once confluency was reached, the cultures were transferred to sterile separating funnels and the buoyant cells were allowed to float to the top and separate from the spent media over a 48h period. Ana GVs were harvested by hypertonic lysis of the buoyant cells with 500 mM sorbitol and 10% Solulyse (Genlantis, San Diego, CA). Purification was done by repeated centrifugally assisted floatation followed by resuspension in 1x PBS (Corning, Union City, CA). GV concentration was determined by pressure-sensitive OD measurements at 500 nm ($OD_{PS,500}$). Pre-collapsed GVs prepared by application of hydrostatic pressure in a capped syringe were used as the blank.

Expression and Purification of Ana GvpC variants

The Ana GvpC gene sequence codon-optimized for *Escherichia coli* expression was synthesized by Life Technologies, Santa Clara, CA. Ana GvpC was cloned into a pET28a(+) plasmid (Novagen, Temecula, CA) downstream of a T7 promoter with an N or C-terminal His-tag. All constructs were made *via* restriction cloning, KLD mutagenesis, or Gibson assembly using enzymes from New England Biolabs, Ipswich, Massachusetts. Purified plasmids with the genetically engineered GvpC constructs were transformed into

BL21(DE3) cells (Invitrogen, Carlsbad, CA). Starter cultures were diluted 1:250 in Terrific Broth (Sigma, St. Louis, MO) and allowed to reach OD_{600}~ 0.4 - 0.7. Protein expression was induced by addition of IPTG (to a final concentration of 1mM), and cells were harvested by centrifugation after overnight expression at 30 ºC.

GvpC in the form of inclusion bodies were purified by lysing the cells using Solulyse supplemented with DNAseI (10 µg/mL) and lysozyme (400 µg/mL) at room temperature. Inclusion bodies were recovered by centrifugation at 27,000g for 15 min in an ultracentrifuge. The inclusion body pellets were resuspended in 20 mM Tris-HCl buffer with 500 mM NaCl and 6 M urea (pH: 8.0) and incubated with Ni-NTA resin (Qiagen, Valencia, CA) for 2 h at 4°C. After washing, proteins were eluted using 250 mM imidazole. Bradford assay was used to measure the concentration of the purified protein. Recombinant GvpC variants were verified to be >95% pure by SDS-PAGE analysis.

Ana GV stripping and re-addition of engineered GvpC variants

Native Ana GVs were stripped of their outer GvpC layer by treatment with 6 M urea solution buffered with 100 mM Tris-HCl (pH 8.5). Two rounds of centrifugally assisted floatation followed by removal of the subnatant layer were done to ensure complete removal of native GvpC, as confirmed by SDS-PAGE. Stripped Ana GVs were then combined with 2x molar excess of the engineered GvpC variant in 6M urea buffer after accounting for a 1:25 binding ratio of GvpC : GvpA. Estimating 12,768 GvpA molecules per Ana GV and 564.2 pM of GVs per $O.D_{PS,500}$ (1 cm pathlength), the molar concentration of GvpA per $O.D_{PS,500}$ of Ana GVs was determined to be 7.2 µM and used for calculating the amount of engineered GvpC to be added. The engineered GvpC was then allowed to slowly refold onto the surface of the stripped Ana GVs by dialysis against 1x PBS for >12 h at 4°C using a regenerated cellulose membrane with a 6-8 kDa M.W. cutoff (Spectrum Labs, Rancho Dominguez, CA). Dialyzed samples were subjected to at least 2 rounds of centrifugally assisted floatation to remove any excess unbound GvpC.

Transmission electron microscopy

GV samples were diluted to $O.D_{PS,500}$ ~ 0.2 in 10 mM HEPES buffer containing 150 mM NaCl (pH 8) and spotted on Formvar/Carbon 200 mesh grids (Ted Pella, Redding, CA) that were rendered hydrophilic by glow discharging (Emitek K100X). GV samples were negatively stained using 2% Uranyl Acetate. Images were acquired using the Tecnai T12 LaB6 120kV TEM equipped with a Gatan Ultrascan 2k X 2k CCD and 'Leginon' automated data collection software suite.

Pressurized absorbance spectroscopy

GV samples were diluted to $O.D_{PS,500}$ ~ 0.2 and loaded onto a flow-through, 1 cm path-length quartz cuvette (Hellma Analytics, Plainview, NY) that was connected to a N_2 cylinder through a pressure controller (Alicat Scientific, Tucson, AZ). The pressure was increased stepwise in 20 kPa increments up to 1 MPa and the $O.D_{PS,500}$ at each step was measured using a spectrophotometer (EcoVis, OceanOptics, Winter Park, FL). Fully collapsed GV sample was used as the blank.

In vitro ultrasound imaging

Imaging phantoms were prepared from 1% agarose in PBS. Two times concentrated GV samples were mixed 1:1 with melted 1% agarose at 50°C, and 100 μL of the mixture was quickly loaded into the phantom wells. Imaging was performed using a Verasonics Vantage programmable ultrasound scanning system. The L11-4v or L22-14v 128-element linear array transducers (Verasonics, Kirkland, WA) were used for image acquisition, with a pitch of 0.3 mm or 0.1 mm and elevation focus of 15-20 mm or 6 mm respectively. The phantom was placed on a custom 3-D printed holder and the transducer was mounted on a computer-controlled 3-dimensional translating stage (Velmex, Inc., Bloomfield, NY). During imaging, the transducer was immersed in PBS at an elevation that positioned the focal zone of the ultrasound beam at the center of the sample well. All images were acquired using a conventional B-mode sequence with 128 ray lines.

The acoustic multiplexing and collapse spectrum measurements were obtained by using GV samples at a final OD of 1 and a transmit frequency of 6.25 MHz on the L11-4v, with a 4-cycle pulse and transmit focus of 20 mm, F-number 2 and persistence 90. The images were acquired at a transmit voltage of 1.6 V. To collapse GVs, acoustic pressure was delivered to the specimen by lowering the F-number to 0.1 and ramping up the voltage gradually. At each collapse step, the transducer was translated in the y and z planes to ensure homogenous GV collapse over the entire well.

Nonlinear imaging experiments were performed using the L11-4v transducer with a transmit frequency of 4.46 MHz and receive filtering using a 2 MHz band pass around 4.46 MHz and 8.92 MHz for the fundamental and second harmonic signals, respectively. GV samples at OD 2.5 were imaged at 2.5 V and F-number 3 using a 3-cycle pulse and a persistence of 90.

In vivo **ultrasound imaging**

Intravenously injected gas vesicles were imaged in 5-7 weeks old female SCID mice using the L11-4v transducer. To be consistent with *in vitro* experiments, a transmit frequency of 4.46 MHz and reception frequencies of 4.46 MHz and 8.92 MHz were used for the fundamental and nonlinear imaging respectively. Imaging was done at 2.5 V using a 3-cycle pulse at an F-number 3 and persistence of 20. The mice were maintained under isofluorane anesthesia on a heated imaging platform. Images were acquired at a rate of 16 frames/sec for ~ 50 s. A 50 µL volume of gas vesicles at OD 23.5 in PBS was infused ~ 5 s after the start of the experiment at a flow rate of 0.3 ml min^{-1}. Between sample injections, a 10s high-power burst from the transducer was used to completely collapse any residual GVs in circulation.

Image analysis

MATLAB and ImageJ (NIH, Bethesda, MD) were used to process *in vitro* and *in vivo* ultrasound data. Regions of interest (ROIs) were manually defined so as to capture signals from the entire sample well or the IVC. ROI dimensions were preserved between different GV samples and the mean intensity per pixel calculated using all pixels within the ROI.

Quantification of *in vitro* harmonic and fundamental GV signals was performed by subtraction of the post-collapse images from the pre-collapse images. *In vivo* IVC signals were analyzed for all acquired frames over the 50 s imaging window and smoothed infusion time-course curves were generated using locally weighted scatterplot smoothing. Area under the curve (AUC) values were obtained from the raw data normalized to the pre-infusion baseline. Acoustic spectral unmixing was performed using MATLAB after applying a spectral averaging filter with a kernel size of [20 20] pixels to reduce out-of-well noise. Pseudocolor assignments and merging of spectrally unmixed images were performed using ImageJ (color maps are shown next to the images in Figure 2g).

Zeta potential measurements

Zeta potential of GVs with GvpC-WT and GvpC-LRP were measured using Brookhaven Instruments Corporation Zeta-PALS instrument (Hotsville, NY). 40 µL of GVs (in PBS) were added to 1.5 mL of double distilled water at a final concentration of 35 pM and conductance of 1 mS. Electrodes were placed in the cuvette with the samples and average zeta potential for each run was determined from 10 measurements.

In vitro characterization of functionalized GVs

Alexa-488 succinimidyl ester fluorescent dye (Invitrogen, Carlsbad, CA) was reacted with GVs in PBS for 2 hours at 10,000:1 molar excess of dye to GVs. Excess succimidyl ester was quenched with 10 mM Tris. Fluorescently-labeled GVs were purified using dialysis against PBS. Cells were seeded on 22x22 mm coverglass and cultured for 24 hours prior to the start of the experiments. Due to the buoyant nature of GVs, *in vitro* characterization was carried out using modified 6-well plates that contain 3 pegs to enable inverted cell growth (facing down). For receptor ($\alpha_v\beta_3$) targeting experiments, 16 µL of fluorescently-labeled GVs (GvpC$_{WT}$, GvpC$_{WT}$-RGD, and GvpC$_{WT}$-RDG) at 1.2 nM were added to U87 cells (ATCC, Manassas, VA) and incubated for 24 hrs. To test phagocytic uptake using GvpC$_{WT}$, GvpC$_{WT}$-mCD47, and GvpC$_{WT}$-R8, 8 µL of fluorescently labeled GVs at 1.2 nM were added to RAW 264.7 cells (ATCC). After the allotted GV incubation, cells were washed 3x with PBS, fixed with 4% paraformaldehyde, and mounted with DAPIcontaining mounting media. Confocal fluorescence images were acquired using inverted Zeiss LSM 710 NLO (Thornwood, NY) using a 20x objective.

SpyTag – SpyCatcher functionalization of Ana GVs

SpyTag-Ana GVs were prepared using the re-addition protocol described above. SpyCatcher-mNeonGreen (SC-mNG) was expressed and purified from BL21 *E. coli* using non-denaturing Ni-NTA purification. ST-GVs (OD 5-10) were incubated with SC-mNG at a 2x molar excess of SpyCatcher:SpyTag in PBS for 1 hr at room temperature. GVs were spun at 300g for 4 hrs twice in order to remove excess unbound protein; the supernatant containing GVs was resuspended in fresh PBS.

ST-GV (± SC-mNG) and WT-GV (+ SC-mNG) samples were prepared in a 1% agarose phantom at a final OD of 2.5 and imaged with the Verasonics L22-14V transducer at 19 MHz, 5.0V and F-Number 3 with a persistence of 90. The agarose phantom was also imaged through the green channel of a BioRad Chemidoc MP system (Hercules, CA). The fluorescence intensity of the ST-GV (± SC-mNG) and WT-GV (+ SC-mNG) samples was determined by first collapsing the samples and then measuring fluorescence intensity (ex 506nm, em 550nm) in a Molecular Devices SpectraMax M5 plate reader (Sunnyvale, CA).

3.5 Supplementary figures and tables

GV Variants	Midpoint of Collapse (P_c) (kPa)	P_c (SEM) (kPa)	ΔP (kPa)	ΔP (SEM) (kPa)	Adj. R-Square
ΔGvpC	195.30	0.27	17.01	0.24	0.999
ΔN&C	374.30	1.01	41.46	0.89	0.999
$GvpC_{WT}$	569.85	3.64	84.87	3.21	0.992

Supplementary table 3-T1: Hydrostatic midpoint of collapse for engineered Ana GVs used in acoustic multiplexing experiments (shown in Figure 3-2b). The data was fitted with a Boltzmann sigmoid function of the form $f(p) = \left(1 + e^{(p-p_c)/\Delta p}\right)^{-1}$ with p_c representing the average midpoint of collapse. Fit parameters and R^2 values for each of the GV variants are provided in the table.

GV Variants	Midpoint of Collapse (Pc) (kPa)	P_c (SEM) (kPa)	ΔP (kPa)	ΔP (SEM) (kPa)	Adj. R-Square
ΔGvpC	571.00	1.51	14.48	1.03	0.998
ΔN&C	657.04	3.94	77.47	3.70	0.997
$GvpC_{WT}$	868.81	6.56	94.00	5.57	0.994

Supplementary table 3-T2: Acoustic midpoint of collapse for engineered Ana GVs used in multiplexing experiments (shown in Figure 3-2c). The data was fitted with a Boltzmann sigmoid function of the form $f(p) = \left(1 + e^{(p - p_c)/\Delta p}\right)^{-1}$ with p_c representing the average midpoint of collapse. Fit parameters and R^2 values for each of the GV variants are provided in the table.

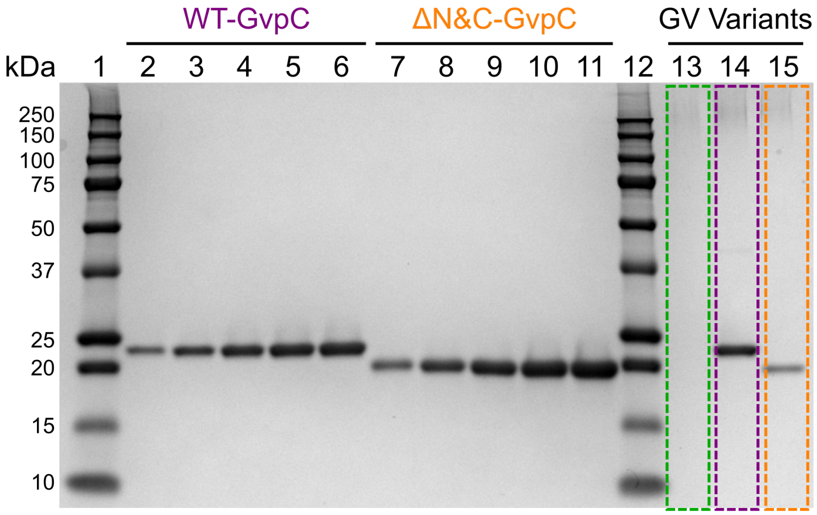

Lane	Sample
1	Ladder
2	WT-GvpC (200ng)
3	WT-GvpC (400ng)
4	WT-GvpC (600ng)
5	WT-GvpC (800ng)
6	WT-GvpC (1000ng)
7	ΔN&C-GvpC (200ng)
8	ΔN&C-GvpC (400ng)
9	ΔN&C-GvpC (600ng)
10	ΔN&C-GvpC (800ng)
11	ΔN&C-GvpC (1000ng)
12	Ladder
13	ΔGvpC Ana GVs (OD: 5)
14	GvpC_{WT} Ana GVs (OD: 5)
15	ΔN&C Ana GVs (OD: 5)

Figure 3-S1: SDS-PAGE analysis of GvpC re-addition. Gel confirming the complete removal of GvpC from native Ana GVs (lane 13) and the re-addition of engineered proteins (lane 14-15). Quantification of re-added GvpC on urea-stripped Ana GVs was done by comparison against a standard curve (200 – 1000 ng) of the pure proteins (lanes 2-6 for WT-GvpC and lanes 7-11 for ΔN&C-GvpC). The number of re-added GvpC molecules was determined to be ~ 1980 per GV for GvpC_{WT} and ~ 877 per GV for ΔN&C respectively.

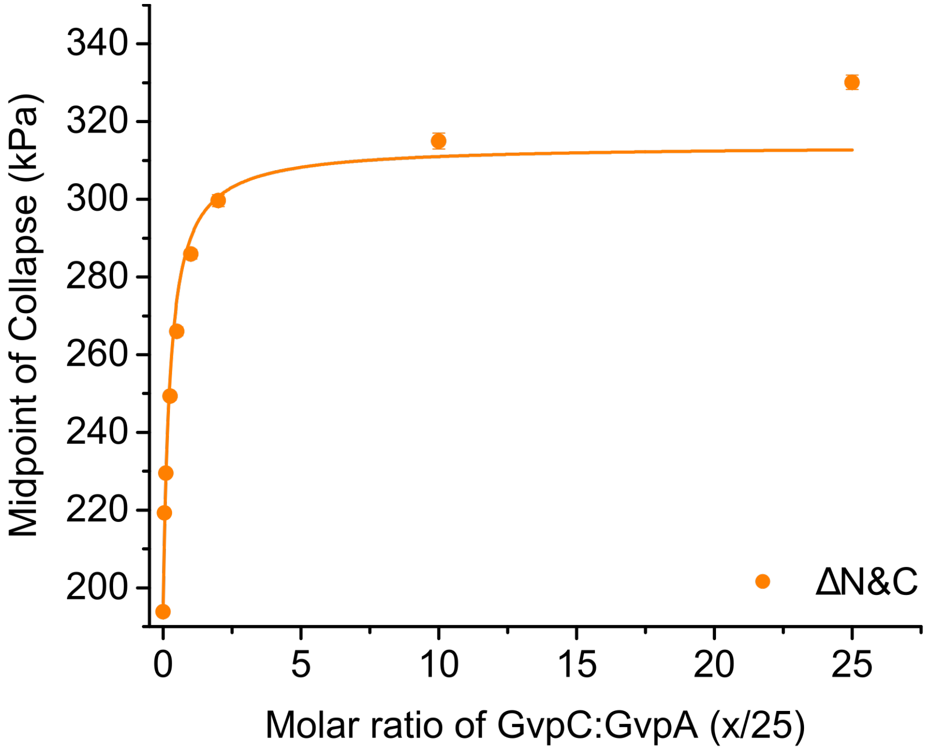

Molar ratio of GvpC : GvpA (x/25)	Midpoint of Collapse (Pc) (kPa)	P_c (SEM) (kPa)	ΔP (kPa)	ΔP (SEM) (kPa)	Adj. R-Square
0	193.77	0.31	16.72	0.27	0.999
0.05	219.29	0.46	20.44	0.40	0.999
0.1	229.47	0.62	21.9	0.55	0.999
0.25	249.28	0.99	28.07	0.88	0.998
0.5	266.01	1.13	30.94	0.99	0.998
1	285.85	1.19	33.95	1.05	0.998
2	299.66	1.53	40.31	1.35	0.997
10	314.99	2.01	50.84	1.77	0.996
25	330.11	1.88	50.75	1.65	0.997

Figure 3-S2: Effect of re-added ΔN&C GvpC concentration on hydrostatic collapse of engineered GVs. Midpoint of collapse (hydrostatic) plotted as a function of re-added GvpC concentration for the ΔN&C variant. The midpoint of collapse was determined by fitting the raw data with a Boltzmann sigmoid function of the form $f(p)=\left(1+e^{(p-p_c)/\Delta p}\right)^{-1}$ with p_c representing the average midpoint of collapse. Fit parameters and R^2 values for each of the GV variants are provided. The saturation curve was plotted by fitting the data to a bimolecular binding function of the form $f(x) = C_1 * x / (K_d + x) + C_2$.

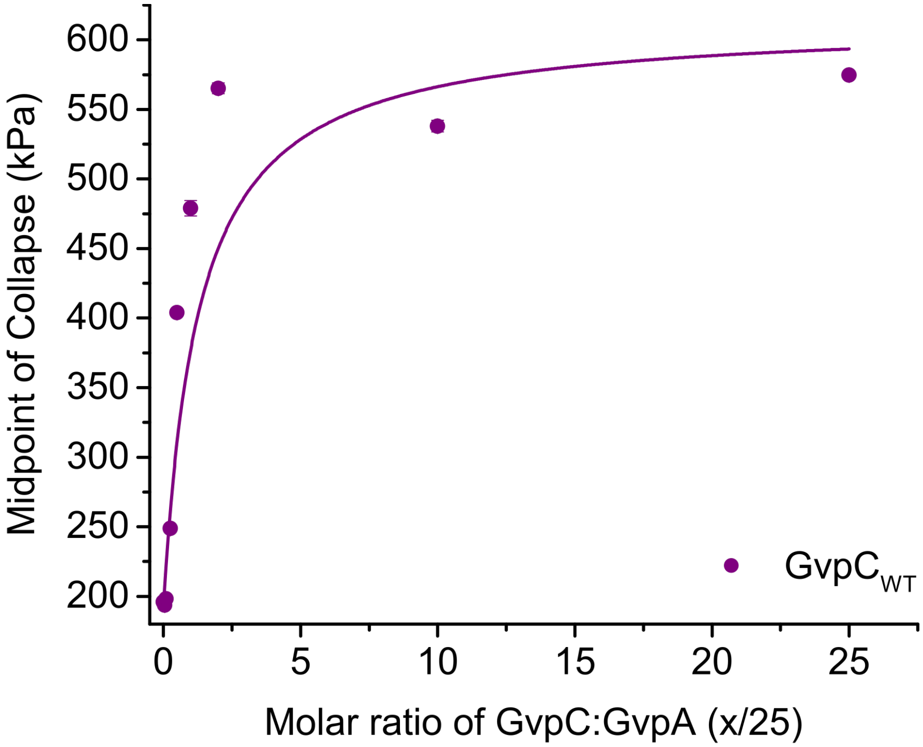

Molar ratio of GvpC : GvpA (x/25)	Midpoint of Collapse (Pc) (kPa)	P_c (SEM) (kPa)	ΔP (kPa)	ΔP (SEM) (kPa)	Adj. R-Square
0	195.95	0.21	16.23	0.18	0.999
0.05	193.48	0.43	17.54	0.38	0.999
0.1	198.12	0.91	19.90	0.80	0.998
0.25	248.68	1.24	33.60	1.09	0.998
0.5	403.93	2.24	61.03	1.98	0.996
1	479.01	5.50	108.11	4.88	0.985
2	565.15	3.92	79.10	3.46	0.990
10	537.95	4.24	86.97	3.74	0.989
25	574.72	2.29	62.93	2.03	0.996

Figure 3-S3: Effect of re-added GvpC$_{WT}$ concentration on hydrostatic collapse of engineered GVs. Midpoint of collapse (hydrostatic) plotted as a function of re-added GvpC concentration for the GvpC$_{WT}$ variant. The midpoint of collapse was determined by fitting the raw data with a Boltzmann sigmoid function of the form $f(p) = \left(1 + e^{(p-p_c)/\Delta p}\right)^{-1}$ with p_c representing the average midpoint of collapse. Fit parameters and R^2 values for each of the GV variants are provided. The saturation curve was plotted by fitting the data to a bimolecular binding function of the form $f(x) = C_1 * x / (K_d + x) + C_2$.

$$\underset{\Delta}{\begin{bmatrix} 6.26 \\ 3.98 \\ 4.82 \end{bmatrix}} = \underset{\alpha}{\begin{bmatrix} 0.955 & 0.429 & 0.036 \\ 0.033 & 0.395 & 0.318 \\ 0.012 & 0.176 & 0.646 \end{bmatrix}} \underset{C}{\begin{bmatrix} 4.15 \\ 4.83 \\ 6.07 \end{bmatrix}} \qquad C = \alpha^{-1}\,\Delta$$

Figure 3-S4: **Matrix of coefficients used for spectral unmixing.** The matrix of coefficients used for generating spectrally unmixed images shown in Figure 2g from the pixel-wise ultrasound signal intensities in Figure 3-2f (I), before and after exposing the GV samples to three sequentially increasing acoustic pressures (P_i). Δ represents the measured differential signals with $\Delta_i = I(P_{i-1}) - I(P_i)$, while α is the matrix containing the acoustic collapse spectrum for each GV variant ($\alpha_{i,j}$). C represents the contribution of each GV variant to the observed signal, with C_j calculated by the matrix operation: $C = \alpha^{-1} \Delta$.

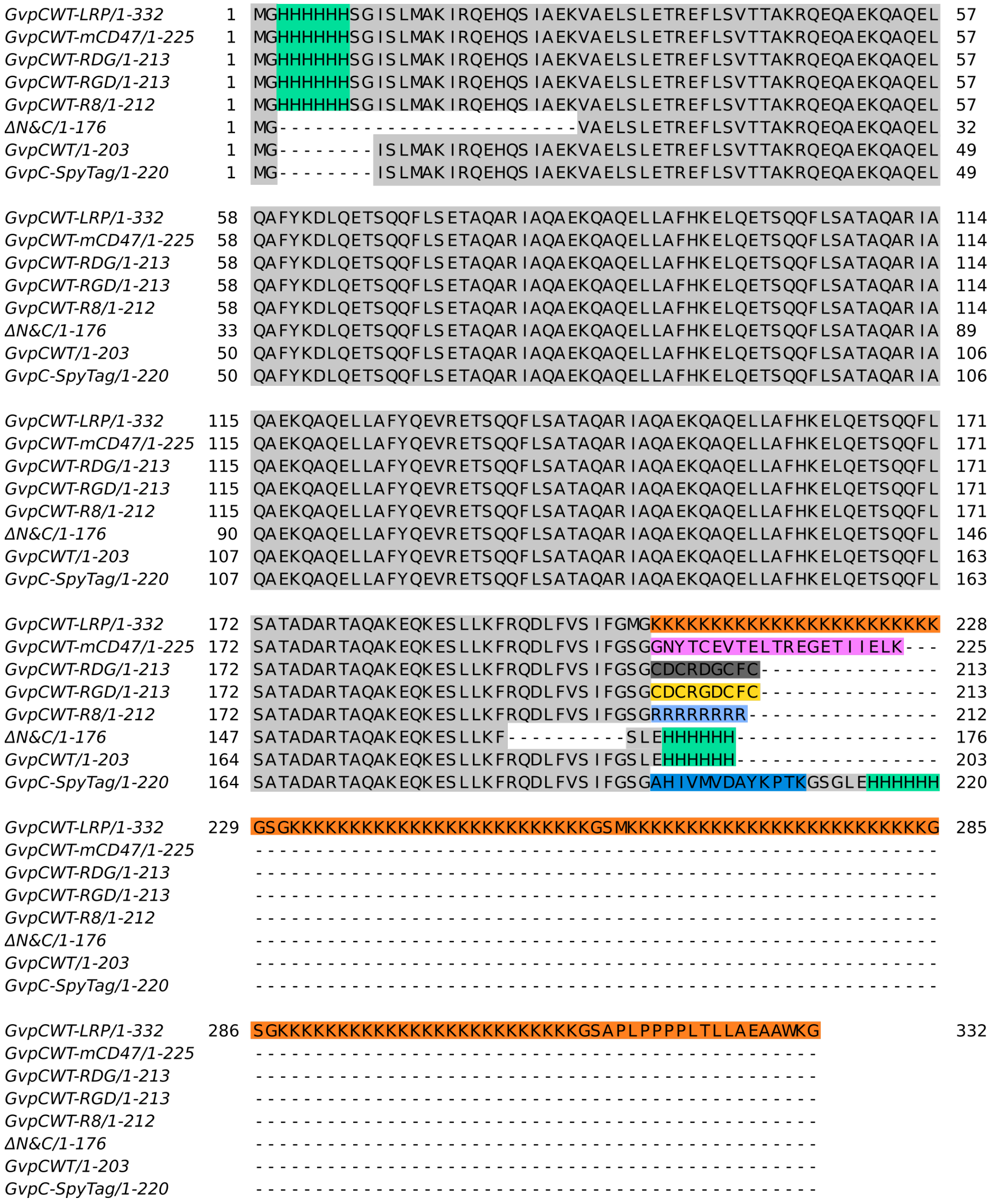

```
GvpCWT-LRP/1-332       1  MGHHHHHHSGISLMAKIRQEHQSIAEKVAELSLETREFLSVTTAKRQEQAEKQAQEL  57
GvpCWT-mCD47/1-225     1  MGHHHHHHSGISLMAKIRQEHQSIAEKVAELSLETREFLSVTTAKRQEQAEKQAQEL  57
GvpCWT-RDG/1-213       1  MGHHHHHHSGISLMAKIRQEHQSIAEKVAELSLETREFLSVTTAKRQEQAEKQAQEL  57
GvpCWT-RGD/1-213       1  MGHHHHHHSGISLMAKIRQEHQSIAEKVAELSLETREFLSVTTAKRQEQAEKQAQEL  57
GvpCWT-R8/1-212        1  MGHHHHHHSGISLMAKIRQEHQSIAEKVAELSLETREFLSVTTAKRQEQAEKQAQEL  57
ΔN&C/1-176             1  MG-------------------------VAELSLETREFLSVTTAKRQEQAEKQAQEL  32
GvpCWT/1-203           1  MG--------ISLMAKIRQEHQSIAEKVAELSLETREFLSVTTAKRQEQAEKQAQEL  49
GvpC-SpyTag/1-220      1  MG--------ISLMAKIRQEHQSIAEKVAELSLETREFLSVTTAKRQEQAEKQAQEL  49

GvpCWT-LRP/1-332      58  QAFYKDLQETSQQFLSETAQARIAQAEKQAQELLAFHKELQETSQQFLSATAQARIA  114
GvpCWT-mCD47/1-225    58  QAFYKDLQETSQQFLSETAQARIAQAEKQAQELLAFHKELQETSQQFLSATAQARIA  114
GvpCWT-RDG/1-213      58  QAFYKDLQETSQQFLSETAQARIAQAEKQAQELLAFHKELQETSQQFLSATAQARIA  114
GvpCWT-RGD/1-213      58  QAFYKDLQETSQQFLSETAQARIAQAEKQAQELLAFHKELQETSQQFLSATAQARIA  114
GvpCWT-R8/1-212       58  QAFYKDLQETSQQFLSETAQARIAQAEKQAQELLAFHKELQETSQQFLSATAQARIA  114
ΔN&C/1-176            33  QAFYKDLQETSQQFLSETAQARIAQAEKQAQELLAFHKELQETSQQFLSATAQARIA  89
GvpCWT/1-203          50  QAFYKDLQETSQQFLSETAQARIAQAEKQAQELLAFHKELQETSQQFLSATAQARIA  106
GvpC-SpyTag/1-220     50  QAFYKDLQETSQQFLSETAQARIAQAEKQAQELLAFHKELQETSQQFLSATAQARIA  106

GvpCWT-LRP/1-332     115  QAEKQAQELLAFYQEVRETSQQFLSATAQARIAQAEKQAQELLAFHKELQETSQQFL  171
GvpCWT-mCD47/1-225   115  QAEKQAQELLAFYQEVRETSQQFLSATAQARIAQAEKQAQELLAFHKELQETSQQFL  171
GvpCWT-RDG/1-213     115  QAEKQAQELLAFYQEVRETSQQFLSATAQARIAQAEKQAQELLAFHKELQETSQQFL  171
GvpCWT-RGD/1-213     115  QAEKQAQELLAFYQEVRETSQQFLSATAQARIAQAEKQAQELLAFHKELQETSQQFL  171
GvpCWT-R8/1-212      115  QAEKQAQELLAFYQEVRETSQQFLSATAQARIAQAEKQAQELLAFHKELQETSQQFL  171
ΔN&C/1-176            90  QAEKQAQELLAFYQEVRETSQQFLSATAQARIAQAEKQAQELLAFHKELQETSQQFL  146
GvpCWT/1-203         107  QAEKQAQELLAFYQEVRETSQQFLSATAQARIAQAEKQAQELLAFHKELQETSQQFL  163
GvpC-SpyTag/1-220    107  QAEKQAQELLAFYQEVRETSQQFLSATAQARIAQAEKQAQELLAFHKELQETSQQFL  163

GvpCWT-LRP/1-332     172  SATADARTAQAKEQKESLLKFRQDLFVSIFGMGKKKKKKKKKKKKKKKKKKKKKKKK  228
GvpCWT-mCD47/1-225   172  SATADARTAQAKEQKESLLKFRQDLFVSIFGSGGNYTCEVTELTREGETIIELK---  225
GvpCWT-RDG/1-213     172  SATADARTAQAKEQKESLLKFRQDLFVSIFGSGCDCRDGCFC---------------  213
GvpCWT-RGD/1-213     172  SATADARTAQAKEQKESLLKFRQDLFVSIFGSGCDCRGDCFC---------------  213
GvpCWT-R8/1-212      172  SATADARTAQAKEQKESLLKFRQDLFVSIFGSGRRRRRRRR----------------  212
ΔN&C/1-176           147  SATADARTAQAKEQKESLLKF----------SLEHHHHHH-----------------  176
GvpCWT/1-203         164  SATADARTAQAKEQKESLLKFRQDLFVSIFGSLEHHHHHH-----------------  203
GvpC-SpyTag/1-220    164  SATADARTAQAKEQKESLLKFRQDLFVSIFGSGAHIVMVDAYKPTKGSGLEHHHHHH  220

GvpCWT-LRP/1-332     229  GSGKKKKKKKKKKKKKKKKKKKKKKKKKGSMKKKKKKKKKKKKKKKKKKKKKKKKKG  285
GvpCWT-mCD47/1-225        ---------------------------------------------------------
GvpCWT-RDG/1-213          ---------------------------------------------------------
GvpCWT-RGD/1-213          ---------------------------------------------------------
GvpCWT-R8/1-212           ---------------------------------------------------------
ΔN&C/1-176                ---------------------------------------------------------
GvpCWT/1-203              ---------------------------------------------------------
GvpC-SpyTag/1-220         ---------------------------------------------------------

GvpCWT-LRP/1-332     286  SGKKKKKKKKKKKKKKKKKKKKKKKKKGSAPLPPPPLTLLAEAAWKG            332
GvpCWT-mCD47/1-225        -----------------------------------------------
GvpCWT-RDG/1-213          -----------------------------------------------
GvpCWT-RGD/1-213          -----------------------------------------------
GvpCWT-R8/1-212           -----------------------------------------------
ΔN&C/1-176                -----------------------------------------------
GvpCWT/1-203              -----------------------------------------------
GvpC-SpyTag/1-220         -----------------------------------------------
```

Figure 3-S5: Sequence information for GvpC variants. Clustal Omega sequence alignment of all the genetically engineered GvpC proteins used in our study. Colors highlight important features and are set to match the schematic illustration in Figure 3-5a.

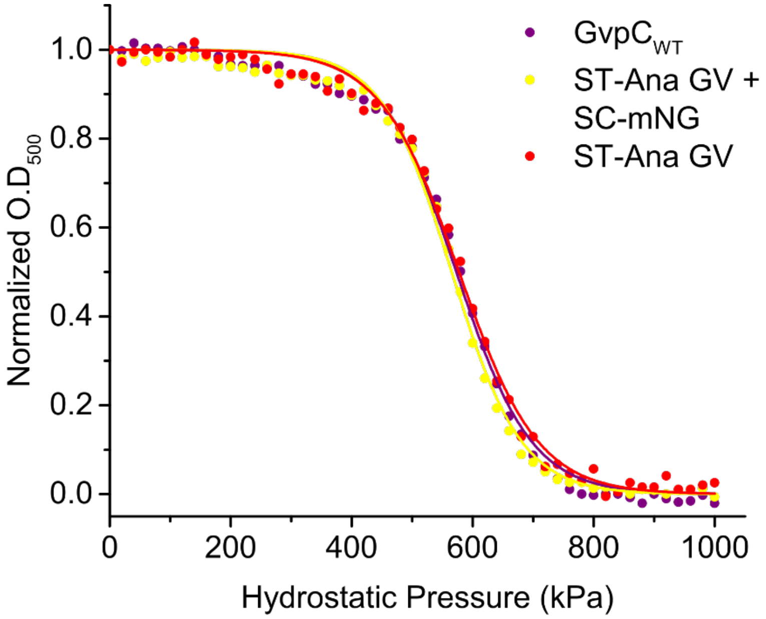

GV Variants	Midpoint of Collapse (P_c) (kPa)	P_c (SEM) (kPa)	ΔP (kPa)	ΔP (SEM) (kPa)	Adj. R-Square
GvpC$_{WT}$	572.84	2.33	62.00	2.05	0.996
ST-Ana GV + SC-mNG	565.13	2.18	57.70	1.92	0.996
ST-Ana GV	577.31	2.29	65.09	2.01	0.996

Figure 3-S6: Hydrostatic collapse profiles of Spytag-SpyCatcher functionalized GV variants. Optical density measurements of engineered Ana GVs as a function of hydrostatic pressure. The data was fitted with the Boltzmann sigmoid function $f(p) = \left(1 + e^{(p-p_c)/\Delta p}\right)^{-1}$ and the table provides the midpoint of collapse as well as other fit parameters and R^2 values. The data show that the collapse profile is unaltered even after reacting the ST-GVs with SC-mNG fluorescent protein.

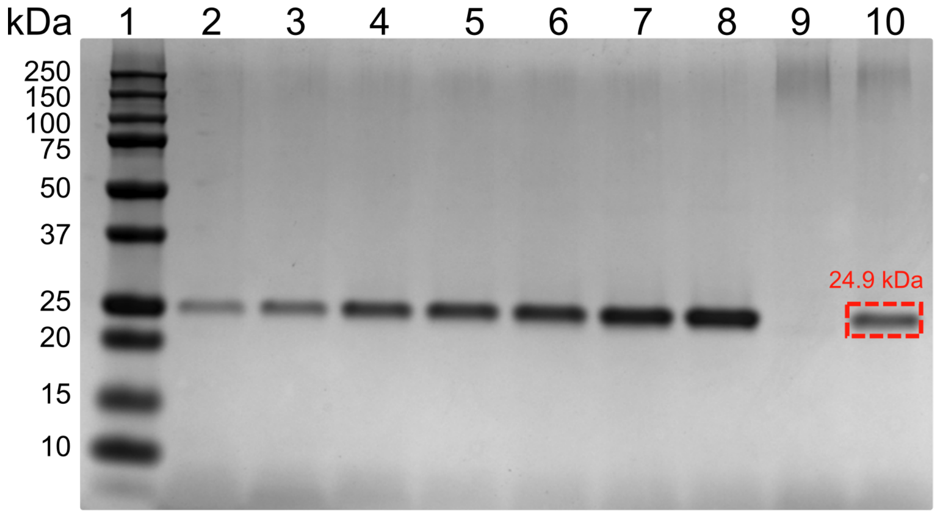

Lane	Sample
1	Ladder
2	GvpC-ST (100ng)
3	GvpC-ST (200ng)
4	GvpC-ST (400ng)
5	GvpC-ST (500ng)
6	GvpC-ST (600ng)
7	GvpC-ST (800ng)
8	GvpC-ST (1000ng)
9	ΔGvpC Ana GVs (OD: 7.8)
10	ST-Ana GVs (OD: 3.0)

Figure 3-S7: SDS-PAGE quantification of SpyTag functionalities on the surface of engineered Ana GVs. Comparison of ST-Ana GVs (lane 10) against a standard curve comprising GvpC-ST concentrations ranging from 100-1000 ng (lanes 2-8) shows that each modified GV has ~ 1000 SpyTag functionalities. Stripped Ana GVs used for GvpC-ST re-addition (lane 9) have negligible amount of native GvpC.

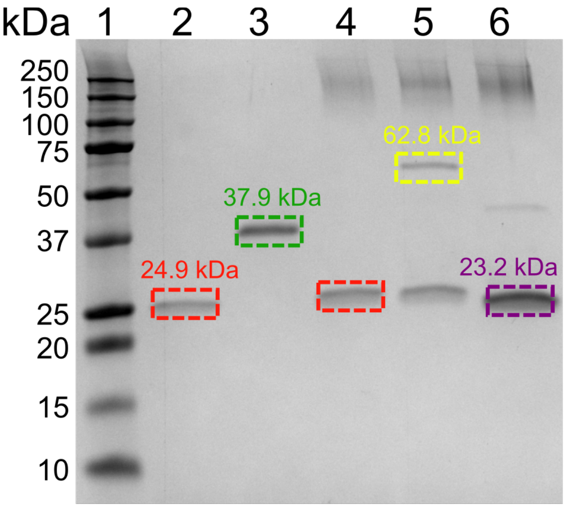

Lane	Sample
1	Ladder
2	GvpC-ST (24.9 kDa)
3	SC-mNG (37.9 kDa)
4	ST-Ana GVs (OD:3)
5	ST-Ana GVs (OD: 3) + SC-mNG (62.8 kDa)
6	GvpC$_{WT}$ Ana GVs (OD: 6) + SC-mNG

Figure 3-S8: SDS-PAGE analysis of SpyTag-SpyCatcher reaction. Gel confirming SpyTag-SpyCatcher bond formation (yellow) upon a one-hour incubation of ST-GVs having an outer layer of GvpC-SpyTag (red) with SpyCatcher-mNeonGreen (green). Incubation of Ana GVs containing an outer layer of WT-GvpC (purple) with SC-mNG, followed by buoyancy purification to remove unreacted fluorescent molecules results in GVs that are not fluorescent as shown in Figure 3-5g (left bottom panel). This also highlights the specificity of the SpyTag-SpyCatcher reaction and confirms that all the unreacted fluorescent molecules are completely removed during buoyancy purification.

Chapter 4

DEVELOPMENT OF ACOUSTIC REPORTER GENES FOR NON-INVASIVE IMAGING OF MICROBES IN MAMMALIAN HOSTS

R. W. Bourdeau, A. L-Gosselin, **A. Lakshmanan**, A. Farhadi, S.R. Kumar, S. P. Nety and M.G. Shapiro (2018). Acoustic reporter genes for non-invasive imaging of microbes in mammalian hosts. *Nature*, 553, 86-90. doi: 10.1038/nature25021

4.1 Foreword

The research work detailed in this chapter started around the same time as my efforts on molecular engineering of GVs to tune their properties, covered in Chapter 3. These projects represented complementary approaches towards addressing the same overarching goal – to create a biomolecular toolkit that would provide ultrasound with new capabilities for cellular and molecular imaging. The development of acoustic reporter genes required extensive tinkering and characterization of native and engineered GV gene clusters for heterologous expression in microbial hosts. Meanwhile, the molecular engineering platform based on protein-level modifications to *Anabaena flos-aquae* GVs was already providing us important information about how the outer GV shell protein 'GvpC' influenced the mechanical and acoustic properties of these protein nanostructures. As I gathered data about different GvpC variants and their influence on GV acoustic phenotypes, Ray Bourdeau – a postdoctoral fellow in my lab – incorporated the more interesting variants in his engineered GV gene clusters for specific purposes, such as acoustic multiplexing. Very soon, there was a lot of cross-talk between the two projects, with both of us learning from one another in terms of optimal ways to purify, characterize and image GVs. I also contributed to testing and characterizing initial ARG constructs by evaluating the effect of different plasmid architectures, *E.Coli* strains, expression times and temperatures on the size, shape, yield and properties of the resultant GVs by transmission electron microscopy (TEM) and pressurized absorbance spectroscopy. In the later stages of the project, I conducted experiments to characterize the metabolic burden of ARG expression in *E. Coli* Nissle by quantifying growth and viability of host cells after GV production, as well as the ability of individual bacteria to retain and express ARG constructs through multiple rounds of cell division by plating them on solid induction media after overnight induction in liquid cultures.

4.2 Introduction

Studies of the mammalian microbiome are uncovering an increasing number of critical roles for bacteria in health and disease, ranging from infection and immunity to nervous system function (115-119). Additionally, advances in synthetic biology and genome engineering are enabling the development of microbial therapeutics and diagnostics for diseases such as gastrointestinal inflammation and cancer (120-129). The function of both natural and engineered microbes depends strongly on their anatomical location within the host organism, making it important to monitor their spatial distribution, viability, proliferation and function inside the body (130-132). Such monitoring requires reporter genes that can be produced by proliferating cells and connected to specific genetic circuits. However, conventional reporters based on fluorescent and luminescent proteins or radionuclide capture suffer from the poor penetration of light into tissue or the need to administer radioactive tracers (133-135). In contrast to these techniques, ultrasound is a widely available, inexpensive, radiation-free technology capable of noninvasively imaging deep tissues (136). Its spatial resolution is routinely on the order of 100 µm (38, 137) and can approach the single-micron level with recently developed super-resolution techniques (39). With these performance characteristics and the ability to place signals within an anatomical context, ultrasound is an ideal technique for imaging genetically labeled microbes *in vivo*. However, no reporter genes for ultrasound are currently available.

Here, we introduce the first acoustic reporter genes (ARGs) to enable ultrasound imaging of microbes inside mammalian hosts. These reporter genes are based on gas vesicles, a unique class of gas-filled protein nanostructures expressed primarily in water-dwelling photosynthetic organisms as a means to regulate buoyancy (84, 85). Gas vesicles comprise all-protein shells with sizes on the order of 200 nm that enclose hollow interiors, allowing dissolved gases to freely permeate in and out while excluding water (84). We recently discovered the ability of these proteins to scatter sound waves and thereby produce ultrasound contrast (81). However, the ability of the multi-gene clusters encoding gas vesicles to serve as reporter genes in heterologous species has not been demonstrated, and is expected to be challenging due to their polycistronic composition. Here, we set out to address this challenge by engineering gas vesicle operons for efficient expression in *Escherichia coli* and *Salmonella typhimurium* – two important commensal and pathogenic species that are also chasses for the development of microbial therapeutics – and showing that ARG-expressing cells can be visualized *in vivo* in settings relevant to gastrointestinal (GI) colonization and antitumor therapy. We demonstrate that the expression of engineered ARGs makes cells visible to ultrasound at volumetric concentrations below 0.01%, enables dynamic imaging of gene expression, and allows the visualization of bacteria injected into mouse colons and tumor xenografts. In addition, we establish the potential of ARGs for further genetic engineering by rationally designing variants with distinct acoustic properties for multiplexed imaging and demonstrating the compatibility of these genetic constructs with high-throughput screening for directed evolution.

4.3 Results

4.3a Genetic engineering of acoustic reporter genes

Gas vesicles are encoded in their native bacterial or archaeal hosts by operons of 8-14 genes, which include the primary structural protein GvpA, the optional external scaffolding protein GvpC, and several secondary proteins that function as essential minor constituents or chaperones (85). As a starting point for developing ARGs, we chose a compact *E. coli*-compatible gas vesicle gene cluster from *Bacillus megaterium* (138) (**Fig. 4-1a, top, left**). While cells containing this construct were able to produce small, bicone-shaped gas vesicles (**Fig. 4-1, b-c, left**), its expression did not result in bacteria detectable by ultrasound (**Fig. 4-1d, left**), most likely because the small gas vesicles produced from this construct have weak acoustic scattering. At the same time, transforming *E. coli* with a gas vesicle gene cluster derived from the cyanobacterium *Anabaena flos-aquae*, whose gas vesicles are highly echogenic (81, 97), did not result in gas vesicle expression. Given the high sequence homology of GvpA between organisms (**Fig. 4-S1**), we hypothesized that a combination of the structural GvpA genes from *A. flos-aquae* with the accessory genes GvpR-U from *B. megaterium* (**Fig. 4-1a, middle**) would result in the formation of gas vesicles with characteristics favorable for ultrasound imaging. Indeed, expression of this engineered gene cluster resulted in *E. coli* containing gas vesicles with significantly larger dimensions compared to the *B. megaterium* operon, and these nanostructures appeared to occupy a greater fraction of intracellular volume (**Fig. 4-1, b-c, middle**). Strikingly, these cells produced robust ultrasound contrast compared to green fluorescent protein (GFP) controls (**Fig. 4-1d, middle**). Additional engineering comprising the addition of a gene encoding the *A. flos-aquae* scaffolding protein GvpC (**Fig. 4-1a, right**) resulted in wider and more elongated gas vesicles more closely resembling those native to *A. flos-aquae* (81) (**Fig. 4-1, b-c, right**), and generated stronger ultrasound contrast (**Fig. 4-1d, right**). We refer to this optimized genetically engineered construct as ARG1 or acoustic reporter gene 1.

To confirm that the ultrasound signal from ARG1-expressing cells is due to the presence of gas vesicles, we applied acoustic pulses with amplitudes above the gas vesicles' critical collapse pressure. In purified form, this results in the immediate collapse of these protein nanostructures and dissolution of their gas contents, eliminating ultrasound contrast (81, 97). As expected, the application of high-pressure pulses made cells expressing ARG1 invisible to ultrasound (**Fig. 4-1d**). The ability of ARG-based contrast to be erased *in situ* is used throughout this study to confirm the source of acoustic signals and subtract background.

ARG1 expression resulted in average gas vesicle contents of 9.4 ± 0.4 mg/g *E. coli* (N=3, ±SEM), corresponding to approximately 100 gas vesicles per cell. These nanostructures occupy roughly 10 percent of the intracellular space. Acoustically silent cells expressing the *B. megaterium* gene cluster produced a similar quantity of gas vesicle proteins (9.7 ± 1.5 mg/g, N=3, ±SEM), underlining the importance of genetic engineering in producing intracellular nanostructures with the appropriate size and shape to be detected with ultrasound. A fraction of ARG1-expressing cells was buoyant in aqueous media (**Fig. 4-S2, a-b**), suggesting that gas vesicles occupy more than 10% of their volume. However, the expected buoyant force on these cells, even at much higher expression levels, is weak compared to other forces such as flagellar thrust (**Supplementary table 4-T1**).

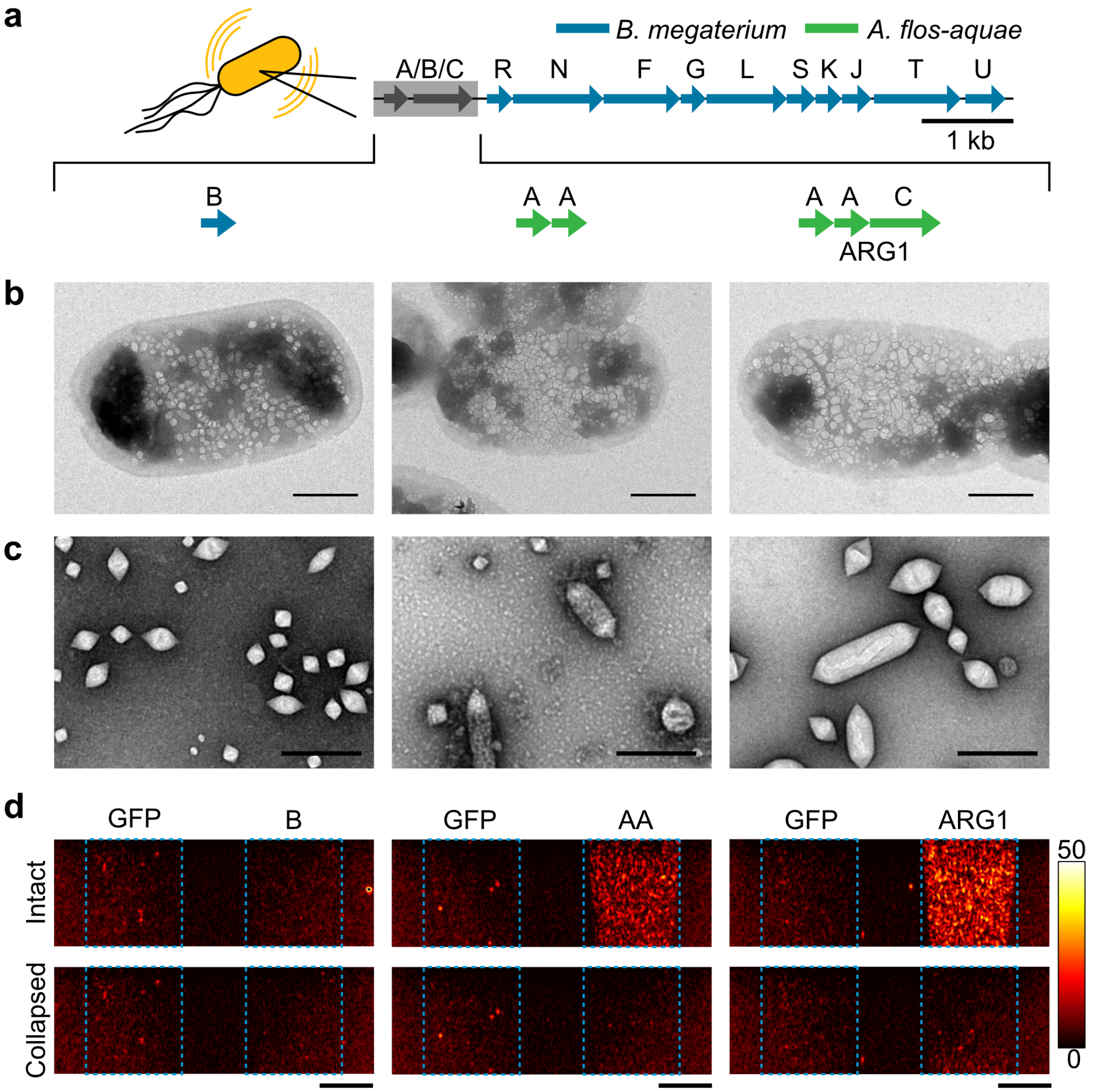

Figure 4-1: Genetic engineering of acoustic reporter genes. (**a**) Architecture of acoustic reporter gene clusters. Panels (b)–(f) are organized in columns corresponding to each of these constructs. (**b**) TEM images of representative *E. coli* cells expressing each construct. (**c**) TEM images of gas vesicles isolated from *E. coli* expressing each construct. (**d**)

Ultrasound images of agarose phantoms containing *E. coli* expressing each construct or GFP. The cell concentration is 10^9 cells/ml. Images in bottom panels were acquired after acoustic collapse. Blue outlines indicate the location of each specimen. Color bar represents linear signal intensity. Scale bars represent 500 nm in (b), 250 nm in (c) and 2 mm in (d). All imaging experiments were repeated 3 times with similar results.

4.3b ARGs enable the imaging of dilute cell populations and conditional gene expression

To enable a broad range of *in vivo* applications, noninvasive imaging must be able to detect relatively dilute cellular populations. For example, the large intestine, a key target of microbiome research and engineered microbial therapeutics (123, 124, 126, 139, 140), hosts a bacterial population of approximately 10^{10} cells/ml (141), representing a volume fraction of about 1%. To determine the detection limit of ARG-expressing cells, we imaged a concentration series of *E. coli* transformed with ARG1 (**Fig. 4-2a**). Cells at concentrations as low as 5 x 10^7 cells/ml produced detectable signal (**Fig. 4-2, a-b**). This equates to a roughly 0.005% volume fraction, or approximately 100 cells per voxel based on cubic voxel dimensions of 100 μm. This sensitivity should be sufficient for many *in vivo* scenarios. Furthermore, bacteria enriched for buoyancy prior to imaging provide 2.4-fold higher signal (**Fig. 4-S2**), suggesting that sensitivity could be improved further by optimizing ARG expression.

In addition to observing the spatial distribution of cells, it is desirable to monitor dynamic cellular signals. Many biological states, signaling pathways and environmental stimuli can be connected to gene expression, as often done with gene circuits wired to fluorescent indicators (142). To test whether ARGs could provide a similar readout of state-dependent genetic pathways, we placed ARGs under the control of a promoter regulated by the chemical inducer isopropyl β-D-1-thiogalactopyranoside (IPTG). Ultrasound signals from *E. coli* expressing ARG1 in this configuration followed the expected dose-response curve of IPTG-controlled expression (**Fig. 4-2, c-d**), confirming their ability to serve as the output signal for engineered genetic circuits. Significant ultrasound contrast could be observed 4 hours after IPTG induction (p-value = 0.01, N=4), and continued to increase during the 22-hour culturing period (**Fig. 4-S3**).

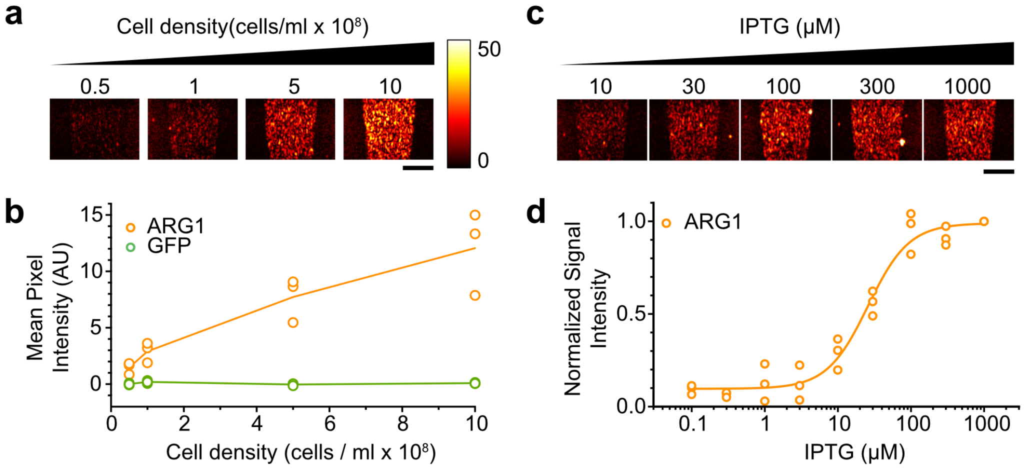

Figure 4-2: Imaging dilute bacterial populations and dynamically regulated gene expression. (**a**) Ultrasound images of ARG1-expressing *E. coli* at various cellular concentrations, before and after acoustic collapse. (**b**) Mean ultrasound contrast from *E. coli* expressing ARG1 and GFP at various cell densities. N=3 biological replicates per sample; lines show the mean. (**c**) Ultrasound images of *E. coli* expressing ARG1 after induction with various IPTG concentrations. Cell concentration was 5 x 10^8 cells/ml. (**d**) Normalized ultrasound contrast as a function of IPTG concentration. N=3 biological replicates per sample. Line shows a fit of the data with the Hill equation to facilitate visualization. Scale bars represent 2 mm. Each imaging experiment was repeated 3 times with similar results.

4.3c ARG expression and ultrasound imaging do not affect cell viability

To determine whether the expression of ARGs has any deleterious effect on host cells, we measured the growth curves of *E. coli* expressing ARG1 or GFP. After induction, cells expressing both constructs continued to divide and reached similar saturation densities (**Fig. 4-3a**). For both ARG1 and GFP the final density was somewhat lower than in uninduced controls, as expected from the metabolic demand of protein expression (143). This has not been a major limitation for the use of GFP-based reporters.

Next, we assessed the viability of ARG-expressing cells after ultrasound imaging and acoustic collapse. TEM images of cells acquired before and after exposure to collapsing acoustic pulses show that gas vesicles can be eliminated without obvious cellular damage

(**Fig. 4-3b**). To examine the impact of ultrasound exposure on cell growth, we cultured *E. coli* expressing ARG1 as colonies on solid media and applied acoustic collapse pulses to half the plate. Gas vesicle collapse in insonated cells was confirmed by a decrease in optical scattering, as seen on dark-field images of the plates (**Fig. 4-3, c-d**). After incubation for an additional 20 h, no significant difference was observed in the diameter of the insonated colonies compared to un-insonated controls, indicating that ultrasound exposure does not affect cell viability (**Fig. 4-3e**). Strikingly, insonated colonies re-expressed gas vesicles during this period, as indicated by the restoration of pressure-sensitive light scattering (**Fig. 4-3, e-f**). This result suggests that ultrasound could be used for pulse-chase studies analogous to fluorescence photobleaching recovery assays (144).

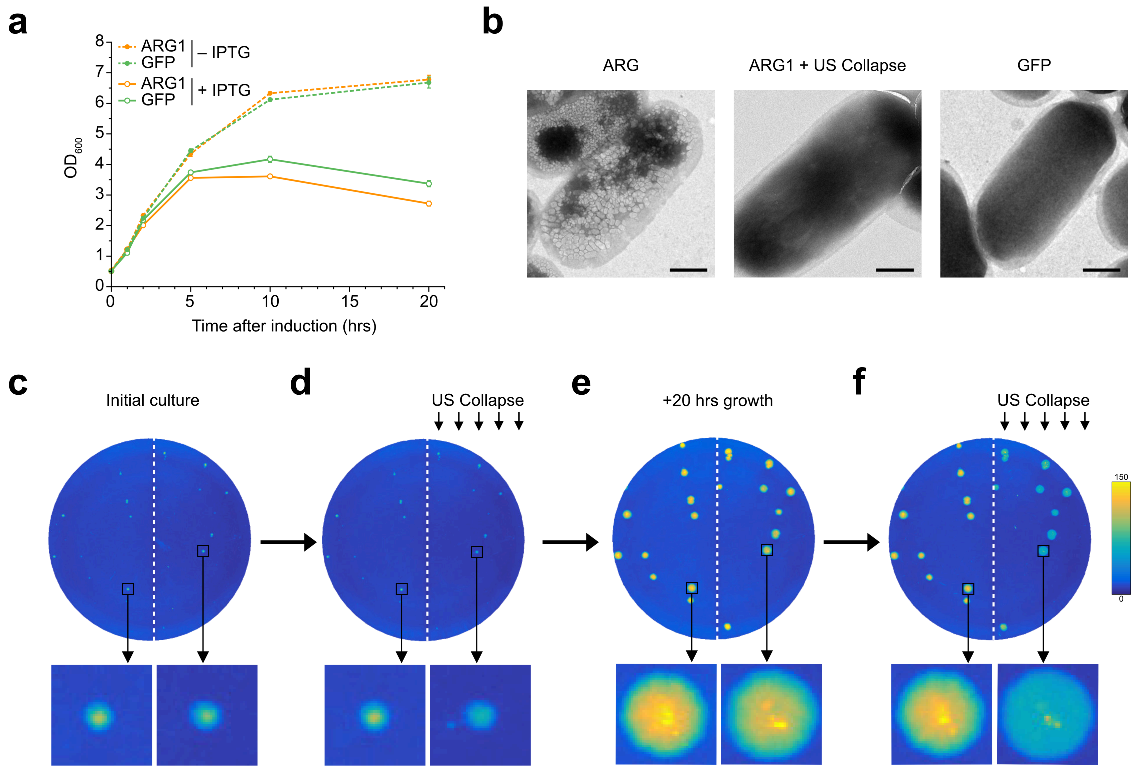

Figure 4-3: Acoustic reporter gene expression and ultrasound imaging does not affect cell viability. (**a**) Growth curves of *E. coli* containing the ARG1 or GFP expression plasmid, with or without induction using 0.4 mM IPTG (N=3 per sample). (**b**) Representative TEM images of whole *E. coli* cells expressing ARG1 with and without exposure to acoustic collapse pulses, and *E. coli* cells expressing GFP. (**c**) Dark field optical image of agar plate containing colonies of *E. coli* expressing ARG1 14 hours after seeding.

(**d**) Image of the same plate after the right half of the plate was insonated with high-pressure ultrasound. (**e**) Image of the same plate 20 h after insonation. (**f**) Image after the right half of the plate in (e) was insonated with high-pressure ultrasound. Zoomed in images of representative colonies shown below each plate image. Scale bars represent 500 nm. Error bars represent ± S.E.M; where not seen, they are smaller than the symbols.

4.3d Engineered variants of ARGs enable multiplexed cellular imaging

It is often informative to simultaneously image more than one population of cells, for example to monitor the dynamics of competing microbial species or the interaction of multiple therapeutic or diagnostic constructs. Optical multiplexing typically makes use of spectrally distinct fluorescent proteins, and analogous acoustic multiplexing can be performed using genetic variants of gas vesicles that collapse at different pressures (97). Such gas vesicles can be distinguished from each other by applying acoustic pulses of gradually increasing amplitude and monitoring the disappearance of backscattered signal: one subset of gas vesicles collapses first, followed by another, and so on. A signal processing paradigm similar to spectral unmixing then determines the contribution of each population to the total signal (97). We hypothesized that if ARGs could be engineered to produce intracellular gas vesicles collapsing at different pressures, this would enable multiplexed imaging of distinct cellular populations.

To explore this possibility, we constructed a new version of the ARG gene cluster containing a modified version of *A. flos-aquae* GvpC. Deletion or truncation of this outer scaffolding protein results in gas vesicles with lower collapse pressures (87, 104), allowing the production of nanostructures distinguishable from each other under ultrasound (97). Following this approach, we modified our gene cluster by truncating GvpC to retain only one of its five repeating alpha-helical domains (**Fig. 4-4a**). *E. coli* expressing the resulting gene cluster, which we refer to as ARG2, showed robust gas vesicle production and ultrasound contrast, similar to ARG1 (**Fig. 4-4, b-d, Fig. 4-S4**). Consistent with our design, gas vesicles purified from ARG2-expressing *E. coli* had a lower critical hydrostatic collapse pressure than nanostructures formed by cells expressing ARG1 (**Fig. 4-4e**), and cellular ARG2 contrast was erasable at lower acoustic pressures (**Fig. 4-4f**). The two variants’ distinct collapse spectra (**Fig. 4-4g**) allowed *E. coli* expressing ARG1 and ARG2 to be imaged in multiplex using pressure spectrum unmixing (**Fig. 4-4, h-j**).

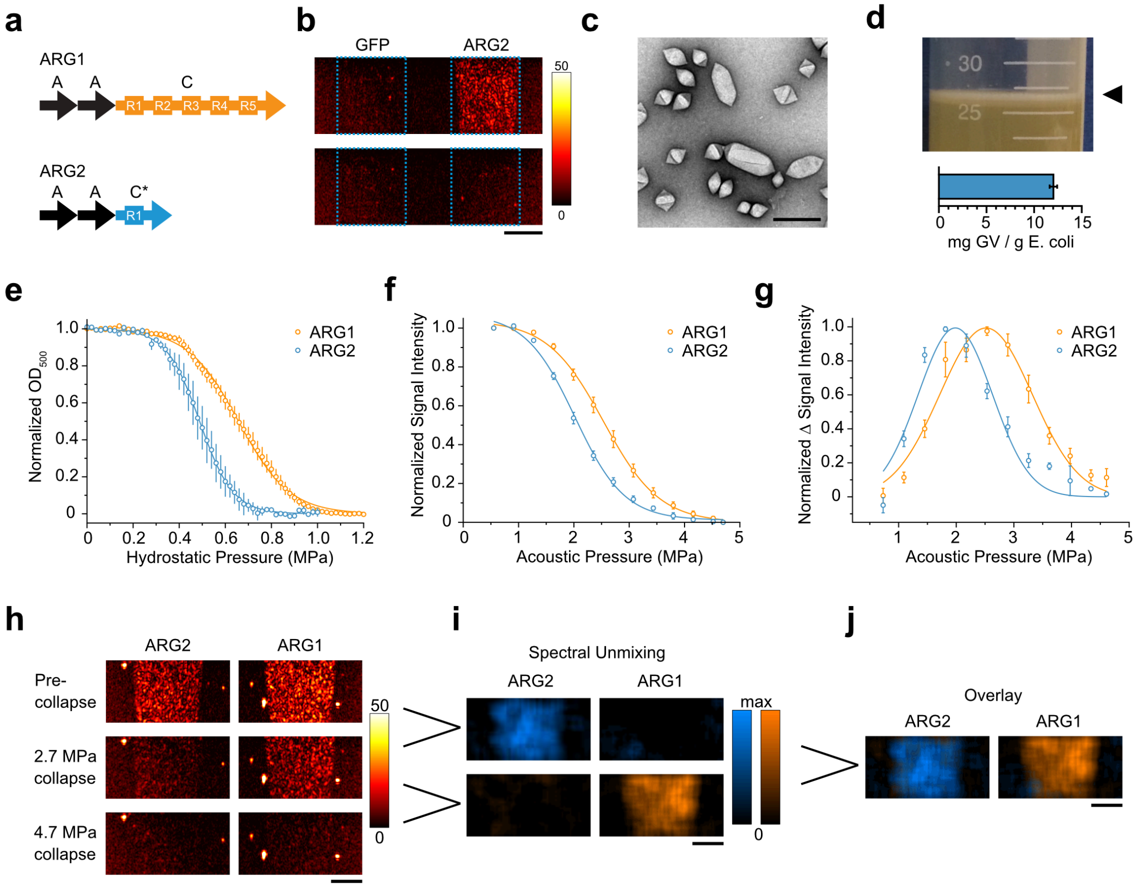

Figure 4-4: Multiplexed imaging of genetically engineered reporter variants. (**a**) Diagram of the GvpA and GvpC sequences included in the ARG1 and ARG2 gene clusters. ARG2 was created by deleting 4 of the 5 repeat domains in wild-type GvpC. (**b**) Ultrasound images of a gel phantom containing *E. coli* expressing ARG2 or GFP (10^9 cells/ml). Blue outlines indicate the location of each specimen. (**c**) Transmission electron micrographs of isolated ARG2 gas vesicles. (**d**) Top: image of ARG2 *E. coli* culture 22 hours after induction showing the presence of buoyant cells. Bottom: mass fraction of gas vesicles produced 22 hours after induction. Line represents mean. (**e**) Normalized optical density (representing the intact fraction) of gas vesicles isolated from ARG1- or ARG2-expressing *E. coli* as a function of applied hydrostatic pressure (N=3 per sample). (**f**) Normalized ultrasound intensity as a function of peak positive pressure from 0.6 to 4.7 MPa for *E. coli* expressing ARG1 or ARG2 (N=3 per sample). (**g**) Acoustic collapse spectra derived by differentiating the data and curves in (F) with respect to applied pressure (N=3 per sample). (**h**) Ultrasound images of gel phantoms containing ARG1 or ARG2 before collapse, after collapse at 2.7 MPa and after collapse at 4.7 MPa (10^9 cells / mL). (**i**) Spectrally unmixed

maps of ARG2 and ARG1 obtained from the set of images in (h). (**j**) Overlay of the blue and orange-colored maps from (i). Scale bars represent 2 mm in (b) and (h-j) and 250 nm in (c). Error bars represent +/- S.E.M.

4.3e In vivo gastrointestinal imaging of engineered microbes

After establishing the core capabilities of ARGs *in vitro*, we set out to demonstrate their detectability *in vivo* by imaging ARG-expressing cells in biologically relevant anatomical contexts. One particularly important target for *in vivo* microbial imaging is the mammalian GI tract, given recent findings concerning the impact of the gut microbiome on human health (115, 130-132) and the development of GI-targeted microbial therapeutics (123, 124, 126, 139, 140). Due to its location deep inside the body, the GI tract is difficult to image using optical techniques, and therefore represents a major opportunity for ultrasound. To establish a proof of concept for ultrasonic imaging of microbes in the GI tract, we expressed ARGs in a probiotic bacterial strain and assessed the ability of ultrasound to localize this bacterium inside the colon (**Fig. 4-5a**) in comparison with bioluminescent imaging.

The *E. coli* strain Nissle 1917 (EcN) is a probiotic microbe capable of colonizing the mammalian GI tract (145). EcN has been used clinically in humans for 100 years to treat enteric infection and inflammatory bowel conditions (145), and is a common chassis for therapeutic synthetic biology (121, 125, 127, 146). EcN cells transformed with a plasmid expressing ARG1 produced abundant gas vesicles (**Fig. 4-5b**) and ultrasound contrast (**Fig. 4-5, c-d**). Control EcN cells transformed with the luminescence operon LuxABCDE (LUX) produced no ultrasound contrast. For comparison, we transformed EcN cells with the luminescence operon LuxABCDE (LUX), which has previously been used to visualize gene expression in microbial populations *in vivo* using bioluminescent imaging (121, 127, 147). LUX-expressing EcN cells produced no ultrasound contrast (**Fig. 4-5, c-d**).

To establish a proof of concept for ultrasound imaging of ARG-expressing bacteria within the GI tract, and to compare the result to bioluminescent imaging, we introduced EcN cells expressing ARG1 or LUX into the colons of anesthetized mice. To assess the ability of each modality to resolve the spatial distribution of bacteria within the colon, we injected the ARG1 and LUX cells in the center or periphery of the colonic lumen (**Fig. 4-5, e-h**). Ultrasound images clearly revealed the localization of ARG-expressing EcN cells in the appropriate region of the colon (**Fig. 4-5, e and g**) at concentrations of 10^9 cells/ml – within the range of certain commensal and therapeutic scenarios, and below the density reached by EcN in some gnotobiotic models(141, 145). In contrast, bioluminescent images showed only that the bacteria are present somewhere in the mouse abdomen (**Fig. 4-5, f and h**). To facilitate visualization of ARG-specific signals, our ultrasound image analysis used background subtraction following gas vesicle collapse, with the resulting contrast overlaid on grayscale anatomical images to show the location of the bacteria within the context of other internal organs. Alternatively, ARG-expressing cells can also be seen in the colon in raw ultrasound images (**Fig. 4-S5**). Contrast from colon-localized *E. coli* was consistent across mice (**Fig. 4-5d**, **Fig. 4-S6**). These results establish the ability of ARGs to make genetically labeled microbes visible noninvasively in deep tissue, and demonstrate the advantage of ultrasound relative to optical imaging in terms of spatial localization within deep organs.

Some degree of burden is expected to accompany heterologous protein expression(148, 149). To assess the burden on EcN cells presented by ARG1, we characterized their growth, viability, reporter expression maintenance, and release of microcins. The growth of cultures expressing ARG1 and LUX followed a similar time course after IPTG induction (**Fig. 4-S7a**), reaching final OD_{600} values of 5.66 ± 0.76 and 8.16 ± 1.12, respectively – a trend toward somewhat higher density for LUX. The quantity of viable colony forming units per OD was also similar between these samples (**Fig. 4-S7b**). Most EcN cells transformed with the ARG1 plasmid retained their ability to express gas vesicles after overnight induction (**Fig. 4-S7c**); a fraction of the colonies was non-gas vesicle-producing, suggesting that some shutdown of transgene expression occurs in EcN cells during transformation, recovery or growth. EcN cultures expressing ARG1 and LUX both retained their ability to inhibit the growth of the microcin-sensitive bacterial strain *E. coli* K-12 H5316(150) (**Fig. 4-S7d**). Overall, these results suggest that ARG1 expression at levels that make EcN cells brightly visible to ultrasound is reasonably well tolerated, with scope for further optimization to reduce burden and ensure reporter gene retention.

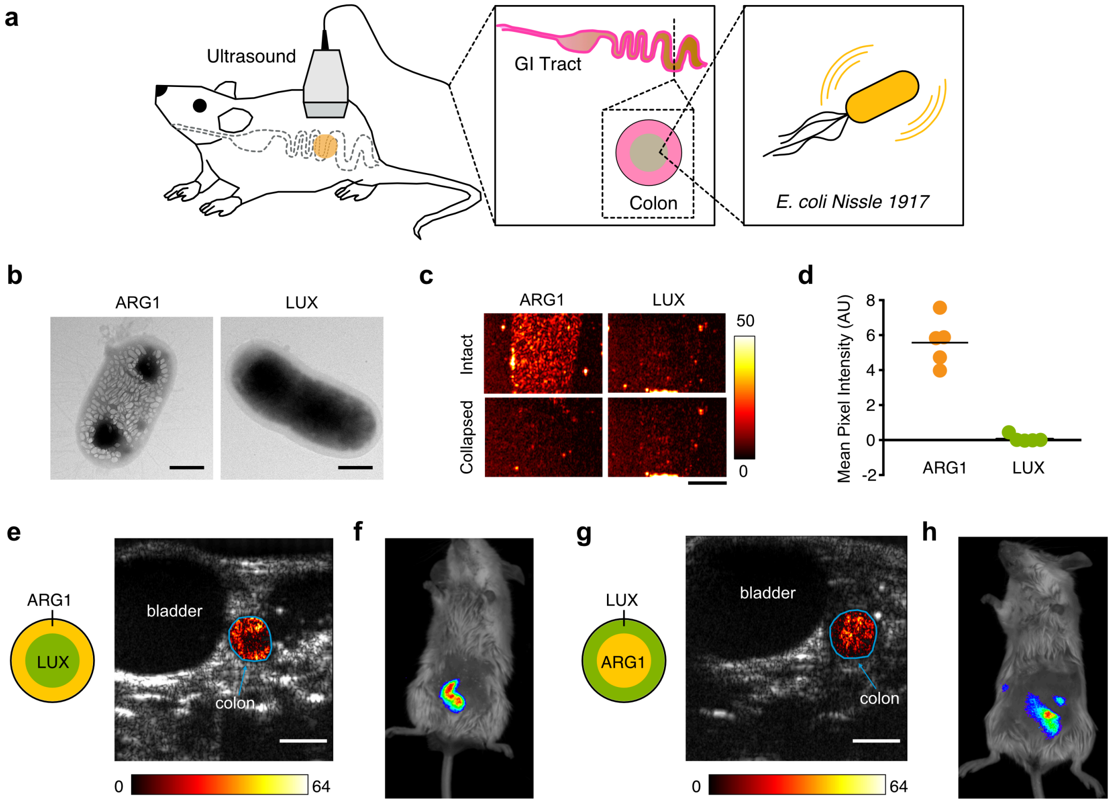

Figure 4-5: Ultrasound imaging of bacteria in the gastrointestinal tract. (**a**) Diagram of GI imaging experiment. EcN cells expressing ARG1 or the LUX operon were introduced into the colon of mice and imaged with ultrasound or luminescence imaging. (**b**) Representative TEM images of whole EcN cells expressing ARG1 or the LUX operon. (**c**) Ultrasound images of a gel phantom containing EcN expressing ARG1 or the LUX operon. (**d**) Mean collapse-sensitive ultrasound signal in phantoms containing EcN cells expressing ARG1 or LUX. Line represents mean. (P-value = 0.0007, N=5). Cell concentration in (c-d) was 10^9 cells/ml. (**e**) Transverse ultrasound image of a mouse whose colon contains EcN expressing ARG1 proximal to the colon wall, and EcN expressing LUX at the center of the lumen. (**f**) Luminescence image of mouse with the same arrangement of colonic bacteria. (**g** and **h**) Same as (e) and (f), but with EcN expressing ARG1 at the center of the lumen and EcN expressing LUX at the periphery. Cells are loaded at a final concentration of 10^9 cells/ml. In (e) and (g), a difference heat map of ultrasound contrast within the colon ROI before and after acoustic collapse is overlaid on a grayscale anatomical image. In (f) and (h), a thresholded luminescence map is overlaid on a bright field image of the mouse. Scale bars represent 500 nm in (b), 2 mm in (c), and 2.5 mm in (e and g).

4.3f ARG expression in Salmonella typhimurium and imaging inside tumors

Another emerging application of engineered microbes is as antitumor therapies and diagnostics (121, 127, 151). For example, *Salmonella typhimurium* has been engineered to colonize tumors after intratumoral or systemic injection and secrete proteins causing cancer cell lysis and immune system stimulation (127, 151). Being able to image such therapies in the body (**Fig. 4-6a**) could facilitate their development and clinical translation. To enable this possibility, we adapted the genetic construct encoding ARG1 for expression in attenuated *S. typhimurium* strain ELH1301, which has been used in tumor-homing studies (127, 151). Upon induction with N-(β-ketocaproyl)-L-homoserine lactone (AHL), ARG-expressing *S. typhimurium* cells produced abundant intracellular gas vesicles and were readily observable using ultrasound compared to controls expressing the LUX operon (**Fig. 4-6, b-c**). The level of ultrasound contrast was similar to ARG-expressing *E. coli*, with mean intensities per pixel of 9.5 ± 0.7 and 12.1 ± 2.1, respectively, at a density of 10^9 cells/ml. Following pressure-induced collapse, these cells are indistinguishable from luciferase-expressing controls (**Fig. 4-6b**).

As a proof of concept, we tested whether ARG-expressing *S. typhimurium* could be imaged *in vivo* in a murine tumor, where these bacteria can proliferate to densities of 10^{10} cells per gram tissue (151). Live ARG-expressing cells were injected into OVCAR8 ovarian adenocarcinoma xenografts in nude mice at one third of this concentration and imaged with ultrasound. Contrast was readily apparent in tumors containing the engineered *S. typhimurium*, and disappeared after acoustic collapse (**Fig. 4-6, d-e**). Cells expressing the luciferase operon had no discernable ultrasound contrast (**Fig. 4-6e**). These results demonstrate that ARGs can be employed in more than one bacterial species and that bacteria are detectable inside tumors at concentrations relevant to therapeutic and diagnostic applications.

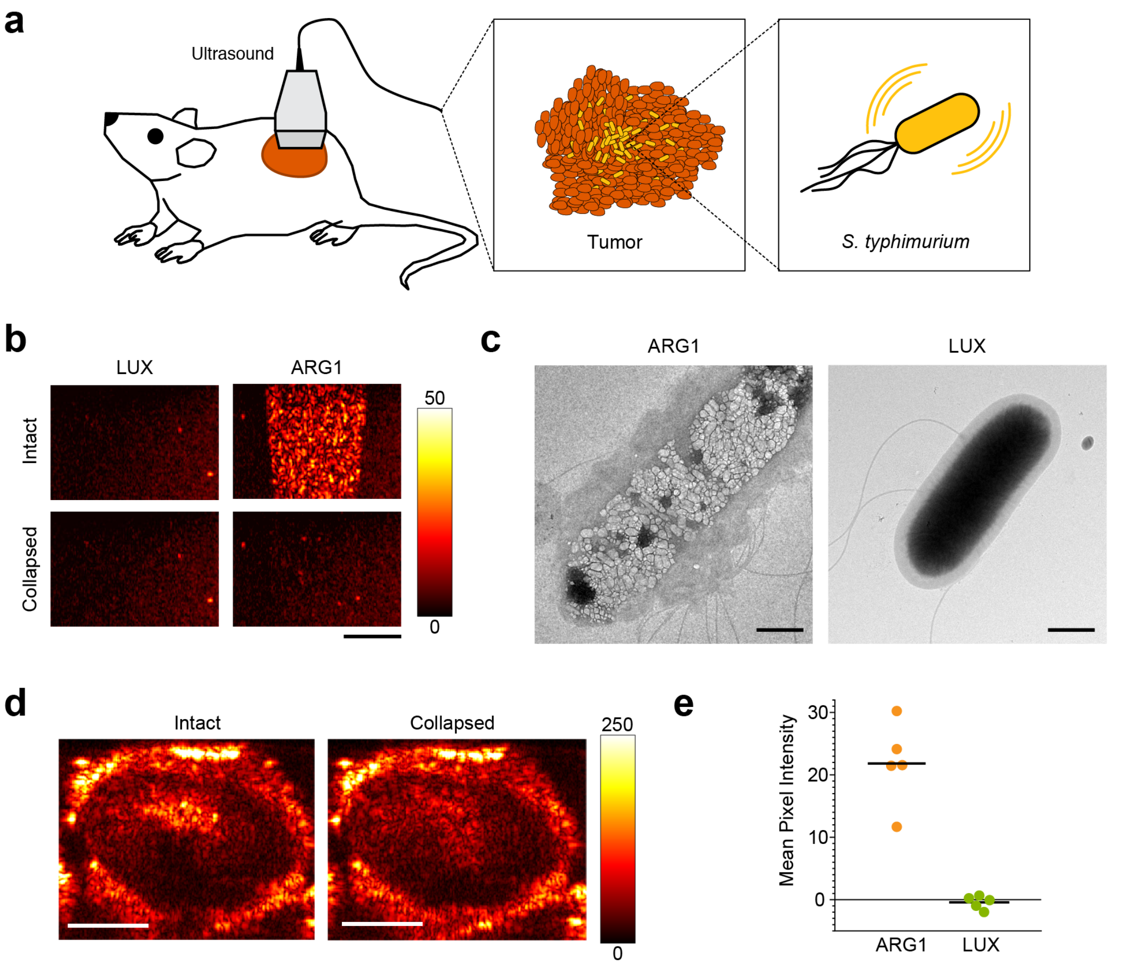

Figure 4-6: Ultrasound imaging of *S. typhimurium* in tumor xenografts. (**a**) Diagram of tumor imaging experiment. *S. typhimurium* expressing ARG1 were introduced into the tumor of mice and imaged with ultrasound. (**b**) Ultrasound images of a gel phantom containing *S. typhimurium* expressing ARG1 or the LUX operon. Cell concentration is 10^9 cells/ml. Experiment repeated 3 times with similar results. (**c**) TEM images of whole *S. typhimurium* cells expressing ARG1 with and without exposure to acoustic collapse pulses. At least 20 cellular images were acquired for each sample type (from one biological preparation each) with similar results. (**d**) Ultrasound images of mouse OVCAR8 tumors injected with 50 μL of 3.2 x 10^9 cells/ml ARG1-expressing *S. typhimurium*, before and after acoustic collapse. Experiment repeated 5 times with similar results. (**e**) Collapse-sensitive ultrasound contrast in tumors injected with ARG1-expressing or LUX-expressing cells. N=5 animals. Line represens the mean. P-value = 0.002 using a two-sided heteroscedastic t-test. Scale bars 2 mm (b), 500 nm (c) and 2.5 mm (d).

4.3g High-throughput screening of acoustic reporter genes

Finally, to enable future genetic engineering of ARGs, we assessed the amenability of these constructs to high throughput screening. In fluorescent protein engineering, directed evolution has served as an effective approach to identify variants with new spectral and biochemical properties (152-154). This approach typically requires a high-throughput screen, which is commonly implemented by plating a bacterial library of genetic variants on agar and imaging the resulting colonies to identify mutants with desired optical properties (153, 154). To determine whether a similar approach could be used with ARGs, we developed a method to scan bacterial colonies with ultrasound (**Fig. 4-7, a-c**). In this method, colonies are immobilized on agar plates with an over-layer of agarose, then scanned with an ultrasound transducer translated by a computer-controlled robot. This results in a series of transverse images that can be reconstructed to from an in-plane image of the plate. To assess the ability of this screening platform to discriminate acoustic phenotypes, we imaged a mixed plate of *E. coli* transformed with ARG1, ARG2 or GFP. Serial acoustic collapse imaging (**Fig. 4-7b**) revealed three distinct colony populations: one lacking ultrasound signal (**Fig. 4-7d**), one collapsing at a lower pressure, and one collapsing at a higher pressure (**Fig. 4-7e**). Based on these acoustic properties, the ARG1, ARG2 and GFP genotypes could be distinguished from each other with 100% accuracy, as determined by DNA sequencing (**Fig. 4-7f**). This result suggests that colony screening can discriminate acoustic phenotypes with sufficient accuracy to serve as a high-throughput assay for acoustic protein engineering.

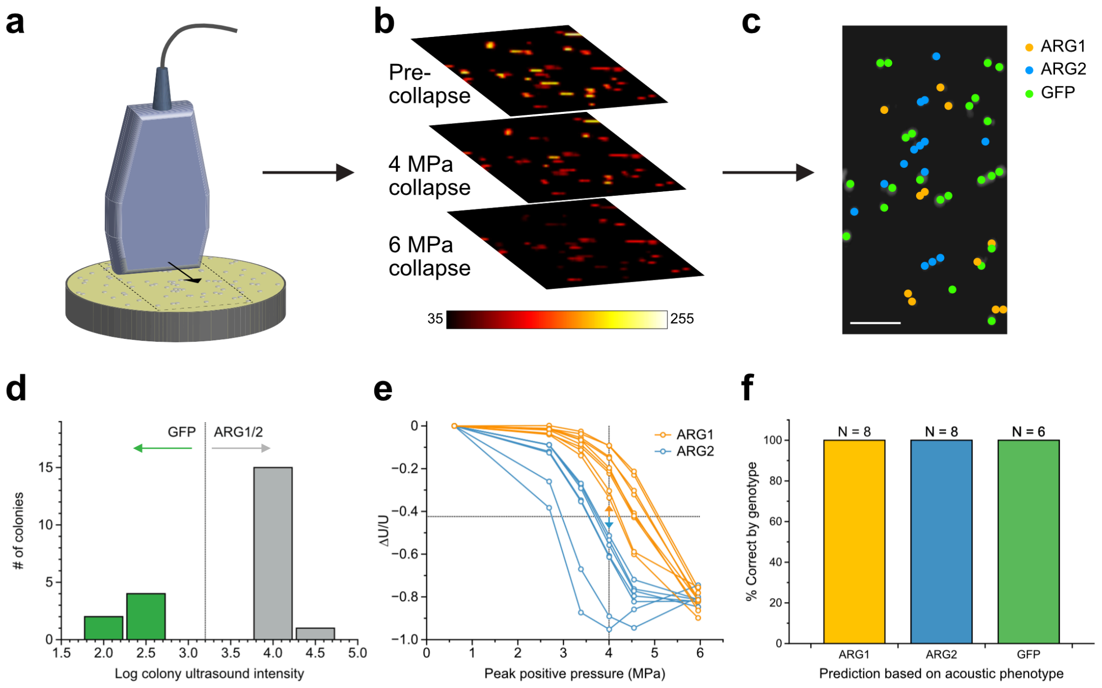

Figure 4-7: High throughput screening of acoustic phenotypes. (**a**) Illustration of acoustic colony screening. Bacteria plated on agar are scanned with an ultrasound transducer that collects images and applies various peak pressures for acoustic collapse. An image of the 2D colony surface perpendicular to the transducer is computed from a series of contiguous images acquired in the transducer's imaging plane. (**b**) Colony ultrasound images of a mixed population of ARG1, ARG2, and GFP expressing *E. coli* colonies. Images were acquired before collapse and after collapse at 4.0 and 6.0 MPa peak acoustic pressures. (**c**) Predicted genotypes of each colony based on the acoustic phenotype seen in the images in (b). (**d**) Ultrasound intensity histogram of 22 randomly picked colonies. Colonies with low contrast were predicted to be GFP and those with high contrast to be ARG1 or ARG2. (**e**) Normalized change in ultrasound intensity for each of the randomly picked colonies after insonation at increasing pressures. At 4 MPa, colonies with signal above the indicated threshold were predicted to be ARG1 and below to be ARG2. (**f**) Confirmation of predicted genotypes by sequencing. Scale bar in (c) represents 10 mm.

4.4 Conclusion and Outlook

Our study establishes engineered gas vesicle gene clusters as the first reporter genes for ultrasound, giving this widely used noninvasive imaging modality the ability to visualize genetically modified bacteria inside living animals with sub-100 μm resolution. ARGs allow cells to be detected at concentrations below 0.005% v/v or 100 cells per ultrasound voxel, making this technology relevant to a broad range of studies involving commensal, disease-causing and engineered microbes. In addition to visualizing cellular location, ARGs allow ultrasound to follow regulated gene expression. With appropriate genetic engineering, this should make it possible to monitor the activity of various natural and engineered signaling circuits, for example the dynamic responses of cells to environmental metabolites or host pathology (121-123, 129). Furthermore, the ability to distinguish bacterial species through acoustic multiplexing of distinct ARGs may enable the study of more complex population dynamics or the monitoring of multiple engineered therapeutic or diagnostic agents. Importantly, ARG expression and imaging was not toxic to bacterial cells, and any changes in buoyancy resulting from a reduction in cellular density would generate forces in the fN range – orders of magnitude smaller than flagellar swimming or molecular attachment, thereby minimally perturbing cellular biodistribution.

In this study, we imaged bacteria injected into the murine GI tract and tumor xenografts to demonstrate the ability of ARG-expressing cells to be detected within living animals at relevant concentrations. Future work must build on these proofs of concept to answer scientific and translational questions. This research will benefit from the development of ultrasound techniques to optimally detect ARG signals and distinguish them from background by leveraging the unique acoustic properties of gas vesicles, including their nonlinear responses to ultrasound (81, 96-98). Additional insights may arise from studying the frequency dependence of gas vesicle backscattering and collapse, especially at frequencies approaching their gas exchange rate of around 670 kHz (96, 107) – well below the 19 MHz and 6.25 MHz pulses used here. Simultaneous improvements in ultrasound technology, such as ultrafast contrast imaging (155, 156), may also improve detection sensitivity, and ARG-expressing cells moving through blood could potentially be localized with super-resolution techniques (39).

In addition, although *E. coli* Nissle 1917 and *S. typhimurium* are both widely studied human-colonizing microbes and popular chasses for microbial engineering, it will be useful to adapt ARGs to a broader range of bacterial hosts such as the commensal genera

Bacteroides and *Lactobaccili* or the pathogens *Clostridium* and *Pseudomonas*, as well as recently developed strains of *E. coli* optimized for stable colonization of the gastrointestinal tract(122, 129). Since both of the cell types used in this study are Gram-negative, expressing ARGs in Gram-positive species may require modifying the ARG cassette; the feasibility of such expression is supported by the natural formation of gas vesicles in certain Gram-positive bacteria, such as *Desulfotomaculum* (84, 157).

Furthermore, for studies involving *in vivo* colonization, it will be important to maintain ARG construct stability, and ensure that ARG expression does not disadvantage cells in their ability to grow and compete within their niche. Although ARG-expressing EcN cells were able to grow, remain viable and release microcins (**Fig. 4-S7**), trends in our experimental data suggest some degree of burden due to ARG expression, as expected in heterologous expression systems(148, 149). In future studies, this burden could be mitigated by regulating the overexpression of gas vesicles with negative feedback, triggering ARG expression transiently before imaging using two-step circuits (in which the ARG operon is controlled by a chemically inducible transcription factor whose own expression is connected to the circuit of interest), or stochastically expressing ARGs in a subset of the overall cell population to enable unburdened growth by the remaining cells. Additionally, to enhance the long-term stability of ARG constructs, it may be useful to incorporate them into the bacterial genome, or into plasmids containing engineered stability elements(158-161). Similar approaches were needed to stabilize the *in vivo* expression of LUX, whose burden resulted in the loss of the unstable plasmid shortly after *in vivo* administration (121, 151). The fact that gas vesicles are expressed naturally in a wide range of bacterial and archaeal species as part of their normal life cycle (84, 85) suggests that regulated expression of these proteins is compatible with healthy cellular function.

To use ARGs in imaging a broader range of cell types, the sensitivity of ARG detection must be improved beyond the level demonstrated in this initial study, since many microbes of interest exist in tissues at densities below this level. Sensitivity improvements may be obtained in future studies through rational engineering or directed evolution of gas vesicle gene clusters. The enhanced ultrasound contrast produced by buoyancy-enriched cells (**Fig. 4-S2**) suggests that more efficient ARG expression could, on its own, more than double detection sensitivity. Combined with advanced nonlinear and ultrafast detection schemes(98, 155, 156), such improvements could also facilitate imaging in larger organisms. While optical techniques, such as fluorescent, luminescent and photoacoustic imaging, are also becoming more capable of visualizing cells in mice with improved resolution using advanced contrast agents (162-165), photon scattering and absorption make it challenging to scale them up to larger animals or patients. By contrast, ultrasound is intrinsically scalable to human subjects, making it possible to conceive of future clinical applications for ARGs. In addition, it is ultimately desirable to express ARGs in mammalian cells, which will require a significant dedicated effort.

We anticipate that the ARGs presented in this work are only a starting point for future engineering of ultrasound reporter genes with new capabilities for noninvasive imaging and sensing. Since their initial discovery as optical reporters, fluorescent proteins have been engineered, evolved and used in thousands of unforeseen optical imaging applications. Our findings that genetic engineering can be used to generate ARGs with distinct acoustic properties and that ARGs are amenable to colony-based high-throughput screening suggest that a similar trajectory may be available for this new technology.

4.5 Methods

Molecular cloning

To construct the plasmid for E. coli BL21(A1) expression of ARGs, the gene cluster encoding *B. megaterium* gas vesicle (GV) proteins BRNFGLSKJTU was amplified from pNL29 (138) (gift of Maura Cannon) and cloned into pET28a using Gibson assembly. The amplicon included an additional 46 bp upstream of the GvpB start codon and 180 bp downstream of the GvpU stop codon. To generate hybrid gene clusters, the genes encoding GvpA and GvpC were amplified from *A.flos-aquae* and cloned into pET28-RNFGLSKJTU using Gibson assembly. A control gene encoding the green fluorescent protein (GFP) mNeonGreen (166) was similarly constructed in the pET28 vector. For expression of ARGs in *E. coli* Nissle 1917, the pET28 T7 promoter was replaced by the T5 promoter. For *S. typhimurium* expression, the ARG gene cluster was cloned into pTD103 (gift of Jeff Hasty). A plasmid encoding the luxCDABE gene cluster from *Photorhabdus luminescens* on the pTD103 backbone was also a gift of Jeff Hasty.

Bacterial expression

Plasmids expressing ARGs or GFP were transformed into chemically competent *E. coli* BL21(A1) cells (Thermo Fisher Scientific, Carlsbad, CA) and grown in 5 ml starter cultures in LB media with 50 µg/ml kanamycin, 1% glucose for 16 h at 37 ºC. Large-scale cultures in LB media containing 50 µg/ml kanamycin and 0.2% glucose were inoculated 1:100 with the starter culture. Cells were grown at 37ºC to OD600 = 0.5, then induced with 0.5% L-arabinose and 0.4 mM IPTG for 22h at 30 ºC. For *E. coli* Nissle 1917 (Ardeypharm GmbH, Herdecke, Germany) the same protocol was followed except constructs were electroporated into the cells and induction was performed at OD600 = 0.3 with 3 µM IPTG (ARG1) and 3 nM N-(β-ketocaproyl)-L-homoserine lactone (AHL) (LUX). Strain identity of *E. coli* Nissle 1917 cells was confirmed by PCR(167). For *Salmonella typhimurium* expression, the same protocol was followed except constructs were electroporated into *S. typhimurium* ELH1301 (gift of Jeff Hasty) and induction was with 3 nM AHL.

Gas vesicle purification and quantification

Harvested cells were centrifugated at 350 g in 50 ml conical tubes for 4 h with a liquid height < 10 cm to prevent collapse of GVs by hydrostatic pressure. For ARG variants that produce a buoyant band of cells, the midnatant was removed and discarded. For ARG variants that do not produce a buoyant band, the supernatant was discarded. The remaining cells were resuspended in 8 ml Solulyse-Tris #L200500 (Genlantis, San Diego, CA) per 100 ml culture and 250 µl/ml lysozyme, and incubated for 1 h at 4 ºC with rotation. Subsequently, 10 µl/ml DNAseI was added to the lysate and incubated for 10 min at 25 ºC.

The lysate was transferred to 2 ml tubes and centrifugated for 2 h at 400 g at 8 ºC. The subnatant was removed with a 21.5 G needle, and the supernatant containing the GVs was transferred to a clean tube. PBS was added to the GVs in a 3-fold volume excess and centrifugation, removal of subnatant and PBS dilution was repeated 3 times. Purified GVs were quantified using the Micro BCA Protein Assay Kit (Thermo Fisher Scientific, Carlsbad, CA). GVs were collapsed with hydrostatic pressure prior to quantification. Bovine serum albumin was used to generate the standard curve. Absorbance measurements were taken on a Spectramax M5 spectrophotometer (Molecular Devices, Sunnyvale, CA).

TEM sample preparation and imaging

Cells expressing ARGs, or purified GVs, were exchanged into water or 10 mM HEPES pH8.0 with 150 mM NaCl, respectively, via 3 rounds of buoyancy purification and buffer exchange as described above. Samples were deposited on Formvar/carbon 200 mesh grids (Ted Pella) that were rendered hydrophilic by glow discharging (Emitek K100X). For purified GVs, 2% uranyl acetate was added for staining. The samples were then imaged on a FEI Tecnai T12 transmission electron microscope equipped with a Gatan Ultrascan CCD. Images were processed with FIJI (168).

Hydrostatic collapse pressure measurements

Cells expressing ARGs, or purified GVs, were diluted to OD600 = 1.0 in PBS and 0.4 ml was loaded into an absorption cell (176.700-QS, Hellma GmbH & Co. KG, Müllheim, Germany). A single valve pressure controller (PC series, Alicat Scientific, Tuscon, AZ, USA) supplied by a 1.5 MPa nitrogen gas source applied hydrostatic pressure in the cell, while a microspectrometer (STS-VIS, Ocean Optics, Dunedin FL, USA) measured the optical density of the sample at 500 nm. OD500 was measured from 0 to 1.2 MPa gauge pressure with a 10 kPa step size and a 7-second equilibration period at each pressure.

In vitro ultrasound imaging

Phantoms for imaging were prepared by melting 1% w/v agarose in PBS and casting wells using a custom 3D-printed template. Cells at 2X the final concentration were mixed 1:1 with molten agarose (at 50 ºC) and immediately loaded into the phantom. The concentration of cells was determined prior to loading by measuring their OD600 after exposure to 1.2 MPa hydrostatic pressure to eliminate any contribution to light scattering from GVs. The optical density was then converted into cells/ml using the relationship 1 OD=8x10^8cells/ml(http://www.genomics.agilent.com/biocalculators/calcODBacterial.jsp. Cell samples collected at early time points following induction, which had an OD insufficient for loading, were first concentrated using centrifugation at 350 g. Ultrasound imaging was performed using a Verasonics Vantage programmable ultrasound scanning system and L22-14v 128-element linear array transducer (Verasonics, Kirkland, WA). The transducer was mounted a computer-controlled 3D translatable stage (Velmex, Inc., Bloomfield, NY). Image acquisition was performed using conventional B-mode imaging using a 128 ray lines protocol with a synthetic aperture to form a focused excitation beam. The transmit waveform was set to a frequency of 19 MHz, 67% intra-pulse duty cycle, and a one cycle pulse. Samples were positioned 6 mm from the transducer face, which is the elevation focus of the L22-14v transducer, coupled through a layer of PBS. The transmit beam was also digitally focused at 6 mm. For imaging, the transmit voltage was 2 V and the f-number was 3, resulting in a peak positive pressure of 0.4 MPa. Backscattered ultrasound signals were filtered with a 7 MHz bandpass filter centered at 19 MHz. Signals backscattered from four transmit events were summed prior to image processing. Pixel gain was set to 3 and persistence to 90.

For GV collapse using the L22-14 array, we set the f-number to 0.2 (thereby ensuring that all transducer elements were active) and scanned the transmit focus from 3 mm to 9 mm. During the 10-second collapse scan, single-cycle pulses were applied using a ray-lines protocol at 19 MHz with a frame rate of 12 frames per second. To measure GV collapse in ARG-expressing cells as a function of acoustic pressure, images were acquired as described above at a peak positive pressure of 0.4 MPa after sequentially exposing the samples to collapse pulses of increasing amplitude, with pressures varied from 0.55 MPa to 4.7 MPa. To achieve complete collapse, we applied the maximal pressure of 4.7 MPa. Collapse data was fitted with a Boltzmann sigmoid function to facilitate visualization of collapse curves. This function of the form $f(p) = (1 + e^{\frac{p-p_c}{s}})^{-1}$ where p is the pressure, and p_c and s are fitted parameters representing the collapse midpoint and slope, respectively. For spectral unmixing, the two collapse pressures applied were 2.7 MPa and 4.7 MPa. Transducer output pressures were measured in a degassed water tank using a fiber-optic hydrophone (Precision Acoustics, Dorset, UK).

Plate-based induction and optical imaging

ARG and GFP constructs were transformed as described above, and the transformation mix after recovery was plated on two-layer LB-Agar plates. The underlayer contained 50 µg/ml kanamycin, 1.0% L-arabinose, and 0.8 mM IPTG. The overlayer contained 50 µg/ml kanamycin and 0.4% glucose. The overlayer was poured 30 min prior to plating, and each layer was 4 mm thick. Plates with transformants were incubated at 30 ºC for 20 h and then imaged for white light scattering and green fluorescence using a Chemidoc MP instrument (Bio-Rad, Hercules, CA).

Cell growth, viability and microcin production assays

E. coli Nissle 1917 cells were transformed by electroporation with pET28 plasmids containing either the ARG1 or LUX gene cluster under the T5 promoter. Transformed cells were grown in 5 mL starter cultures in LB media containing 50 µg/ml kanamycin, 1% glucose for 16 h at 37 °C. The overnight cultures were diluted 1:100 in 50 mL of LB media containing 50 µg/ml kanamycin and 0.2% glucose. Cultures were grown at 30 °C to OD600 ~0.2–0.3 and induced with 3 µM IPTG (+IPTG), or left uninduced (-IPTG). Both induced and uninduced cultures were allowed to grow for 22 h at 30 °C. For time point OD measurements, 1 mL of the culture was taken out and measured. For plating after 22 h of growth, the cultures were diluted to a uniform OD600 of 0.2, before further serial dilution by a factor of 2 x 10^4 in LB supplemented with 50 µg/ml kanamycin and 0.2% glucose. 100 uL of the final dilutions were plated on two-layer LB-Agar plates using a cell spreader. The underlayer of the plates contained 50 µg/ml kanamycin and 9 µM IPTG. The overlayer contained 50 µg/ml kanamycin and 0.4% glucose. The overlayer was poured 30 min prior to plating, and each layer was 3 mm thick. Cells uniformly spread on the two-layer plates were allowed to grow at 30°C for 21 h. Colonies were then imaged for light scattering using the Chemidoc MP instrument under white light transillumination and 605 ± 50 nm receive filter, and both opaque (gas vesicle-producing) and clear colonies were counted to determine total cfu/mL and gas vesicle-expressing fraction. Plates had a minimum of 82 and a maximum of 475 total colonies, enabling manual counting.

To assay microcin production, *E. coli* Nissle 1917 cells containing ARG1 or LUX were cultured as described above and spotted on microcin assay plates containing *E. coli* K-12 H5316 cells (gift from Klaus Hantke). Wild-type H5316 were grown in 5 mL LB media, and H5316 cells transformed with pET plasmid containing mWasabi and KanR under a T5 promoter (H5316* cells) were grown in 5 mL LB media containing 50 µg/ml kanamycin and 1% glucose for 16 h at 37 °C. Two-layer LB plates were used to assay the growth inhibition of H5316 cells by microcin peptides produced by Nissle 1917 cells. Plates used to assay with wild-type H5316 cells contained 20 mL of 1% LB agar at the bottom, and the top layer contained 2 x 10^7 H5316 cells in 20 mL of 0.3% LB agar. Plates using H5316* cells contained 20 mL of 1% LB agar with 50 µg/ml kanamycin, 50 µM desferal, and 3 µM IPTG, and the top layer contained 2x10^7 H5316* cells in 20 mL of 0.3% LB agar with 50 µg/ml kanamycin, 50 µM desferal, and 3 µM IPTG. Nissle cells containing ARG1 or LUX genes were cultured at 30˚C for 22 h with or without 3 µM IPTG. Nissle cells with ARG1 were exposed to 1 MPa of hydrostatic pressure to facilitate the removal of kanamycin by centrifugation before spotting on H5316 plates. Nissle cells containing ARG1 and LUX induced and uninduced with IPTG, as well as H5316* cells, were washed 3x in PBS by pelleting and adjusted to OD 1 in LB. All cells were spotted in 2 µL volume on 5 mm sterile filter paper (Bel-Art Products), placed on the microcin assay plates. Unsupplemented LB and 100 mg/mL ampicillin (2 µL each) were similarly spotted as controls. After 17 h at 37 ºC, the plates were imaged with the Chemidoc MP instrument with blue transillumination, and unfiltered light was collected to form an image. Images shown are representative of four experiments each.

Colony Ultrasound

ARG and GFP constructs were transformed into BL21(A1) one-shot competent cells (Thermo Fisher Scientific, Carlsbad, CA) and plated onto LB-Agar two-layer inducer plates as described above. Plates were grown at 37 ºC for 14h. The colonies were immobilized by depositing a 4 mm layer of 0.5% Agarose-PBS gently onto the plate surface. Ultrasound imaging was performed using a L11-4v128-element linear array transducer (Verasonics, Kirkland, WA) to obtain a larger field of view. The transducer was mounted a computer-controlled 3D translatable stage (Velmex, Inc., Bloomfield, NY). Image acquisition was performed using conventional B-mode imaging using a 128 ray lines protocol with a synthetic aperture to form a focused excitation beam. The transmit waveform was set to a frequency of 6.25 MHz, 67% intra-pulse duty cycle, and a four-cycle pulse. Colonies were positioned 20 mm from the transducer face, which is the elevation focus of the L11-4v transducer, coupled through a layer of PBS. The transmit beam was also digitally focused at 20 mm. For imaging, the transmit power was 2 V and the f-number was 3, resulting in a peak positive pressure of 0.61 MPa. To measure GV collapse in bacterial colonies as a function of acoustic pressure, images were acquired as described above at a peak positive pressure of 0.61 MPa after sequentially exposing the samples to collapse pulses at 6.25 MHz, with increasing amplitude from 0.61 MPa to 5.95 MPa. Pixel gain in the images was set to 0.1 and persistence to 20. Cross-sectional images of the plate (perpendicular to the plate surface) were acquired at spatial intervals of 250 µm using computer-controlled steps. The cross-sectional images were processed in MATLAB to form 2D images of the plate surface. First, the cross-sectional images were stacked to produce a 3D-volumetric reconstruction of the plate. We then summed the signals in a 2mm slice of the volume parallel to and centered on the bacterial growth surface after thresholding to eliminate background, forming a 2D projection image of the plate.

After ultrasound imaging, image processing, and acoustic phenotype prediction, the colonies were picked using 10 µl sterile pipet tips. Each colony was used to inoculate a 5 ml LB + 50 µg/ml kanamycin culture. The cultures were mini-prepped and sequenced to determine whether the plasmid contained GFP, ARG1, or ARG2.

In vivo ultrasound and bioluminescence imaging

All *in vivo* experiments were performed on BALB/c or SCID nude female mice, aged 14-15 weeks, under a protocol approved by the Institutional Animal Care and Use Committee of the California Institute of Technology. No randomization or blinding were necessary in this study. Ultrasound imaging was performed as follows. Mice were anesthetized with 1-2% isoflurane, maintained at 37ºC on a heating pad, depilated over the imaged region, and imaged using an L22-14v transducer with the pulse sequence described above. For imaging of *E. coli* in the gastrointestinal tract (GI), BALB/c mice were placed in a supine position, with the ultrasound transducer positioned on the lower abdomen, transverse to the colon. Anatomical landmarks including the bladder were used to identify the colon’s position. Prior to imaging, buoyancy-enriched *E. coli* Nissle 1917 expressing ARG1 or LUX were mixed 1:1 with 42ºC 4% agarose-PBS for a final bacterial concentration of 10^9 cells/ml. An 8-gauge needle was filled with the mixture of agarose-bacteria expressing either ARG1 or LUX. Before it solidified, a 14-gauge needle was placed inside the 8-gauge needle to form a hollow lumen within the gel. After the agarose-bacteria mixture solidified at room temperature for 10 min, the 14-gauge needle was removed. The hollow lumen was then filled with the agarose-bacteria mixture expressing the other imaging reporter (ARG1 or LUX). After it solidified, the complete cylindrical agarose gel was injected into the colon of the mouse with a PBS back-filled syringe. The same procedure was used with *E. coli* BL21 cells, except with the entire gel homogeneously composed of either ARG2- or GFP-expressing cells. Introduction of gel into the colon is a common preparatory protocol for gastrointestinal ultrasound (169, 170).

For imaging of *S. typhimurium* in tumors, we formed hindlimb ovarian tumor xenografts in SCID nude mice via subcutaneous injection of 5 x 10^7 OVCAR8 cells with matrigel.

After tumors grew to dimensions larger than approximately 6 mm (14 weeks), they were injected with ARG1-expressing *S. typhimurium* (50 µL, 3.2 x 10^9 cells/ml). The tumors were then imaged with ultrasound, with mice in a prone position with anesthesia, homeostasis and imaging parameters as described above. Our animal protocol specified that animals with total tumor volume exceeding 2 cm^3, or showing signs of distress as assessed by the veterinary team, be euthanized.

For luminescence imaging, mice were anaesthetized with 100 mg/kg ketamine and 10 mg/kg xylazine and imaged using a Bio-Rad ChemiDoc MP imager without illumination, no emission filter, and an integration time of 5 min. The image was thresholded and rendered in ImageJ, and superimposed on a brightfield image of the mouse using GIMP.

Image processing

MATLAB was used to process ultrasound images. Regions-of-interest (ROIs) were defined to capture the ultrasound signal from the phantom well, colon, or tumor region. All *in vitro* phantom experiments had the same ROI dimensions. For *in vivo* experiments ROIs were selected consistently to exclude edge effects from the colon wall or skin. Mean pixel intensity was calculated from each ROI, and pressure-sensitive ultrasound intensity was calculated by subtracting the mean pixel intensity of the collapsed image from the mean pixel intensity of the intact image. Images were pseudo-colored, with maximum and minimum levels adjusted for maximal contrast as indicated in accompanying color bars.

For the multiplexed imaging of ARG1 and ARG2, acoustic spectral unmixing was performed, using the methods described in (97). Briefly, a spatial averaging filter (kernel size 30 x 30 pixels or 750 x 750 µm) was applied to the three acquired images (before collapse, after collapse with 2.7 MPa and after collapse with 4.7 MPa) to reduce noise. Then, pixel-wise differences between the first and second image, and between the second and third image were calculated, and multiplied by the inverse of the collapse matrix, α, representing the expected fractional collapse of each ARG type at each pressure (α =

[0.7921, 0.5718; 0.2079, 0.4282]), to produce the unmixed pixel intensities corresponding to the contributions from ARG2 and ARG1.

Statistical analysis

For statistical significance testing, we used two-sided heteroscedastic t-tests with a significance level of type I error set at 0.05 for rejecting the null hypothesis. Sample sizes for all experiments, including animal experiments, were chosen on the basis of preliminary experiments to be adequate for statistical analysis.

Data and code availability

ARG1 and ARG2 plasmid sequences are included in Supplementary Information, and will be deposited to Addgene. All other materials and MATLAB code are available upon reasonable request.

4.6 Supplementary figures and tables

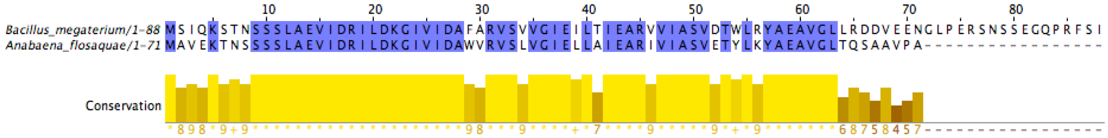

Figure 4-S1: Sequence homology of GvpA/B. Amino acid sequence alignment of the primary gas vesicle structural protein, GvpB from *B. megaterium* (the GvpA analog in this species) and GvpA from *A. flos-aquae.*

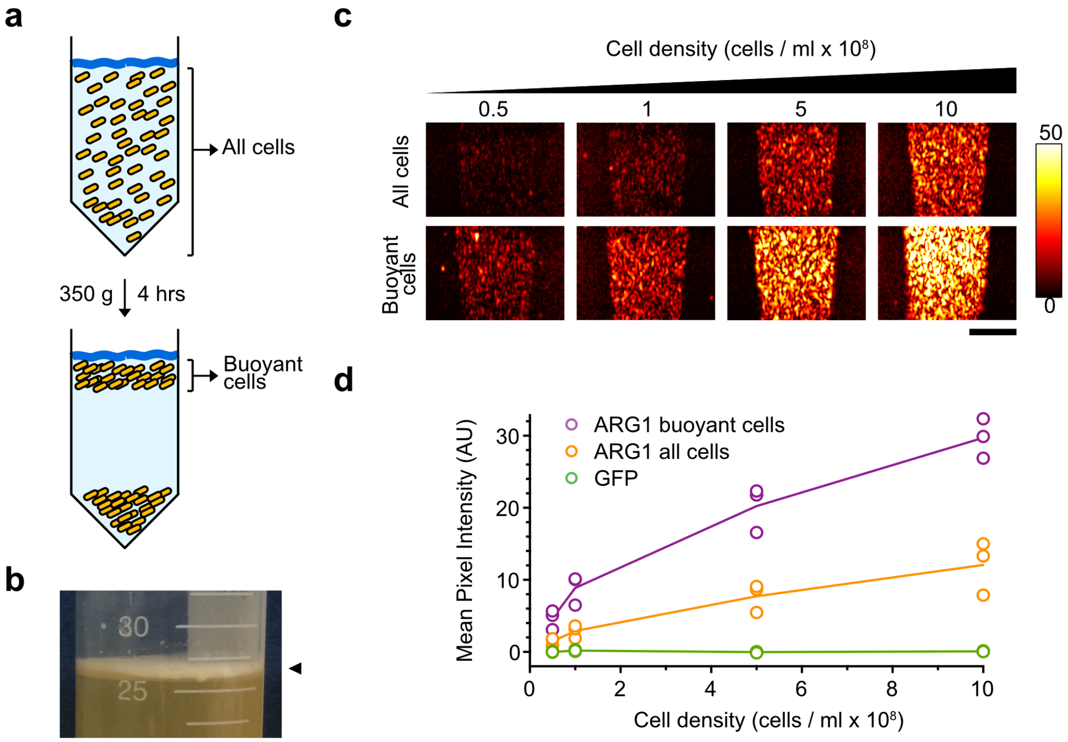

Figure 4-S2: Ultrasound contrast from buoyancy-enriched cells. (**a**) Diagram of centrifugation-assisted enrichment of buoyant cells. (**b**) Image of ARG1 *E. coli* culture 22 hours after induction and 4 hours of centrifugation at 350 g, showing the presence of buoyant cells. Arrow points to meniscus layer containing buoyant cells. Experiment repeated 3 times with similar results. (**c**) Ultrasound images of *E. coli* expressing ARG1 at various cellular concentrations, with and without buoyancy enrichment. Experiment was repeated 4 times with similar results. (**d**) Ultrasound contrast from *E. coli* expressing ARG1, with and without buoyant enrichment, and GFP at various cell densities. N=3 biological replicates; lines represent the mean.

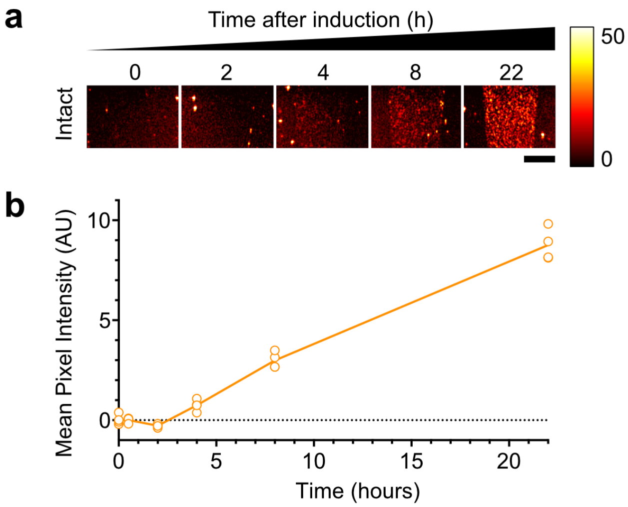

Figure 4-S3: Time course of acoustic reporter gene contrast after induction. (a) Ultrasound images of ARG1-expressing *E. coli* at various times after induction with IPTG. Experiment repeated 4 times with similar results. (**b**) Mean ultrasound contrast at each time point N=4 biological replicates; line represents the mean. Cell concentration was 5 x 10^8 cells/ml. Scale bar represents 2 mm.

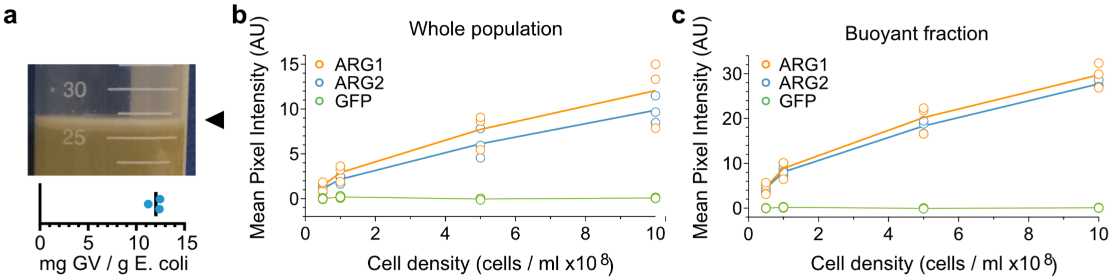

Figure 4-S4: Ultrasound contrast from cells expressing ARG1 and ARG2. (**a**) Top: image of ARG2 *E. coli* culture 22 hours after induction showing the presence of buoyant cells. Experiment repeated 3 times with similar results. Bottom: mass fraction of gas vesicles produced 22 hours after induction. N=3 biological replicates; line represents the mean. (**b**) Ultrasound contrast from the whole population of cells expressing ARG1, ARG2 or GFP. N=3 biological replicates; lines represent the mean. (**c**) Ultrasound contrast from the buoyancy-enriched population of cells expressing ARG1, ARG2 or GFP. N=3 biological replicates; lines represent the mean.

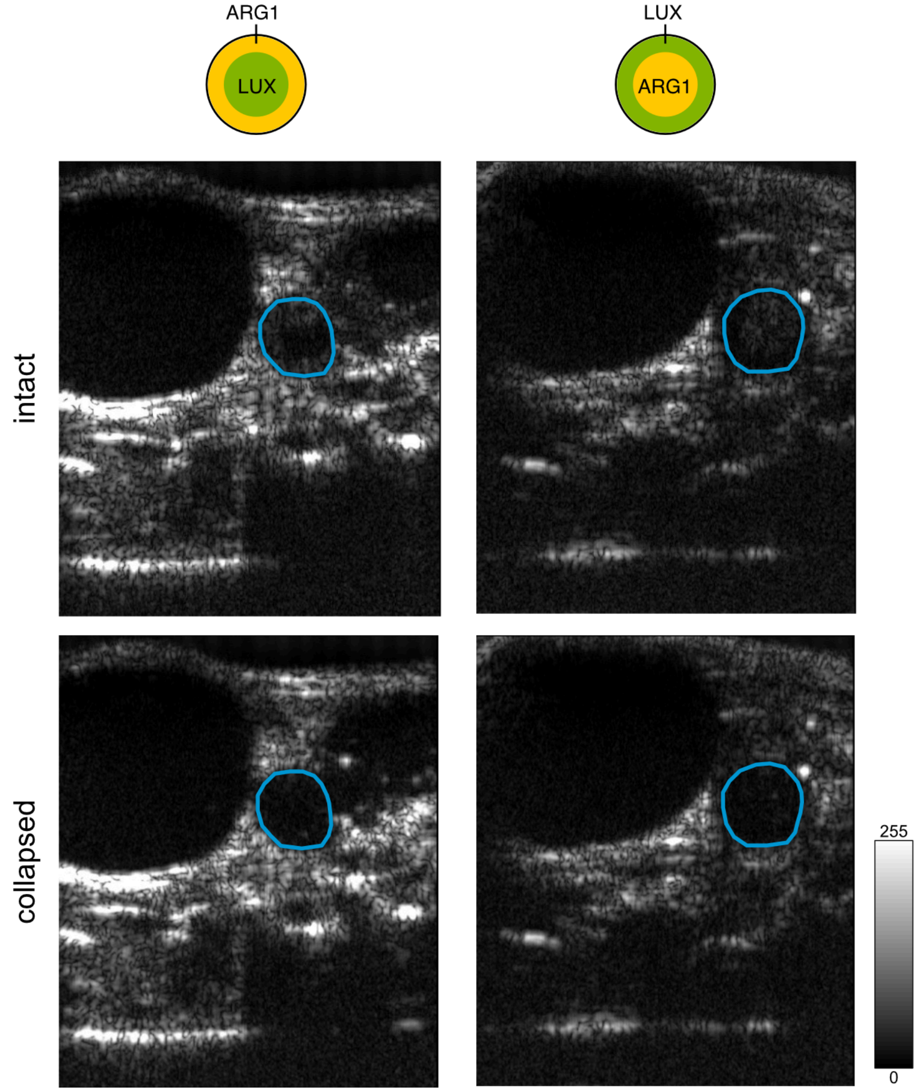

Figure 4-S5: Anatomical ultrasound images of acoustic bacteria in the GI tract. Raw images underlying the difference maps shown in **Figure 4-5, e and g**. The cyan outline identifies the colon region of interest for difference processing. N = 3 independent trials.

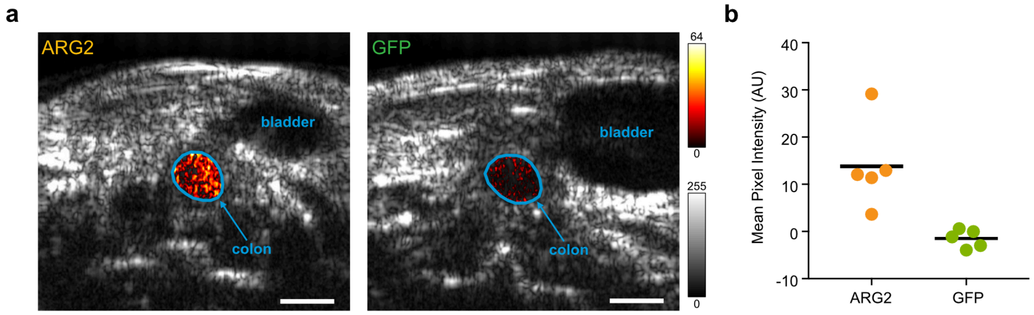

Figure 4-S6: Ultrasound imaging of ARG-expressing cells in the mouse colon. (**a**) Transverse ultrasound images of mice whose colon contains BL21 *E. coli* expressing either ARG2 or GFP at a final concentration of 10^9 cells/ml. A difference heat map of ultrasound contrast within the colon ROI before and after acoustic collapse is overlaid on a grayscale anatomical image. (**b**) Signal intensity in mice with *E. coli* expressing either ARG2 or GFP. N=5 biological replicates per sample. P-value = 0.02 using two-sided heteroscedastic t-test. Scale bar represents 2 mm.

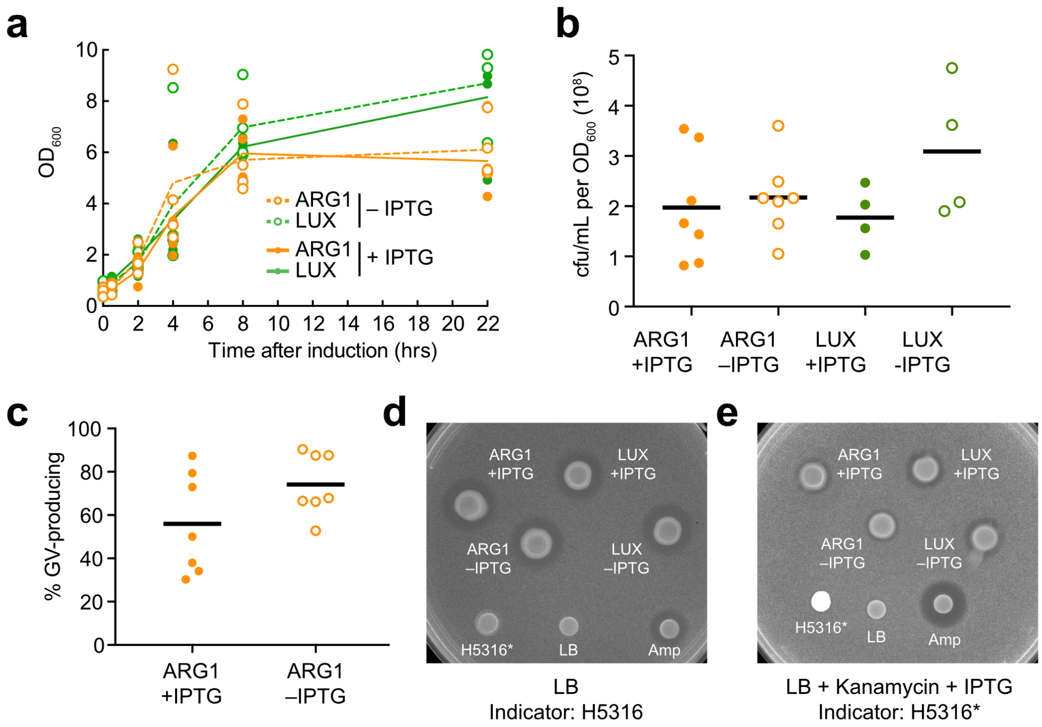

Figure 4-S7: Impact of ARG1 and LUX expression on *E. coli* Nissle 1917 (EcN) cell growth, viability and microcin release. (**a**) Optical density at 600 nm measured 0 to 22 hours after induction with 3 µM IPTG, or without induction, in EcN cells transformed with ARG1 or LUX. N=4 biological replicates per time point. Lines represent the mean. The p-

value comparing induced ARG1 and induced LUX values at 22 hours is 0.06. The p-value comparing uninduced ARG1 and induced LUX at 22 hours is 0.02. Comparisons at all other time points have p-values greater than 0.14. (**b**) Colony-forming units (cfu) per mL culture per OD_{600} after 22 hours of induction with 3 μM IPTG, or uninduced growth, of EcN cells transformed with ARG1 or LUX. All p-values greater than or equal to 0.22. N=7 biological replicates for ARG1 samples and N=4 biological replicates for LUX samples. Lines represent the mean. (**c**) Fraction of opaque, GV-producing colonies produced by plating ARG1-transformed EcN cells 22 hours after induction with 3 μM IPTG, or uninduced growth. Cells are plated on dual-layer IPTG induction plates, allowed to grow overnight at 30ºC and imaged. p-value=0.12. N=7 biological replicates. Lines represent the mean. (**d**) Left image: microcin release assay using a uniform layer of the indicator strain *E. coli* K12 H5316 in soft agar, after 17-hour incubation with filters containing microcin sources and controls, as indicated. EcN cells transformed with ARG1 or LUX were induced for 22 hours with 3 μM IPTG, or grown without induction, before spotting. H5316* indicates H5316 cells transformed with mWasabi and cultured for 22 hours as with EcN cells. All cells were washed before spotting to remove antibiotic. LB is LB media. Amp is 100 mg/ml ampicillin. Experiment was performed 4 times with similar results. (**e**) Results of the same experiment as in (d), but with the indicator strain comprising H5316* cells and the agar containing 50 μg/mL kanamycin, 3 μM IPTG and 50 μM desferal, to show that microcin release also occurs during transgene expression. Note that the H5316* spot appears bright because plate image is acquired with blue light transillumination, resulting in mWasabi fluorescence. Experiment was performed 4 times with similar results. All p-values were calculated using a two-sided heteroscedastic t-test.

Fraction of Cell Occupied by Gas	**Buoyant Force (fN)**
0%	-4.31
10%	0.43
20%	5.17
50%	19.40

Supplementary table 4-T1: Estimated buoyant force on ARG-expressing cells. This calculation assumes a wild-type *E. coli* cell density of 1.1 g/mL (171), a cellular volume, v, of 4.4 fL (172), and gravitational acceleration, g, of 9.8 m s^{-2}. The density of an ARG-expressing cell, ρ_{cell}, is calculated as 1.1 g /mL * $(1 - f)$, where f is the fraction of the volume occupied by the gas in gas vesicles. Buoyant force, F, is then calculated as $\boldsymbol{F} = (\boldsymbol{\rho_{media}} - \boldsymbol{\rho_{cell}})\boldsymbol{gv}$, where ρ_{media} is taken to be 1 g/mL. For comparison, the thrust force of *E. coli* flagellar propulsion is 570 fN (173).

C h a p t e r 5

ACOUSTIC BIOSENSORS FOR ULTRASONIC IMAGING OF ENZYME ACTIVITY

A. Lakshmanan, Z. Jin, S. P. Nety, D. Sawyer, A. L-Gosselin, D. Malounda, D. Maresca and M.G. Shapiro (2019). Acoustic biosensors for ultrasonic imaging of enzyme activity. (*manuscript in preparation*).

5.1 Introduction

Virtually every fundamental biological process in living organisms involves dynamic changes in the concentration or activity of specific molecules. Visualizing these changes within the context of intact tissues and organisms is critical to expand our understanding of basic biology and disease (174). A large repertoire of genetically encoded biosensors based on fluorescent proteins has been engineered to visualize specific molecular and cellular events (9, 11, 14, 15, 18, 19, 23). However, using such biosensors to study signaling taking place inside intact, living organisms is challenging due to the limited penetration of light in biological tissue. In contrast, non-invasive biomedical imaging technologies such as ultrasound are capable of imaging at depth with high spatial and temporal resolution (below 100 μm and 1 ms, respectively), and work in species ranging from small model organisms to humans (1, 32). However, ultrasound currently lacks the ability to visualize specific biomolecular processes due to the lack of biosensors that can dynamically report the activity of physiologically relevant molecules such as enzymes.

Here, we introduce biomolecular sensors for ultrasound based on gas vesicles (GVs), a unique class of air-filled protein nanostructures, which were recently established as nanoscale imaging agents and reporter genes for ultrasound (81, 175). GVs are expressed intracellularly in certain aquatic microbes as a means of regulating cellular buoyancy for optimal photosynthetic illumination (84). GVs comprise a 2 nm-thick protein shell enclosing an air compartment with a width of 45-250 nm and a length of several hundred nm (84, 85). The low density and high compressibility of GVs' air-filled core relative to surrounding aqueous media allows them to scatter sound waves and thereby produce ultrasound contrast (32). This capability has been demonstrated with GVs as purified injectable nanostructures and as acoustic reporter genes expressed heterologously in commensal bacteria (81, 97, 99, 175).

GVs are attractive candidates for the development of dynamic biosensors for ultrasound due to our ability to engineer their acoustic properties at the level of their constituent proteins (97, 98). In particular, although the formation of GVs is encoded by clusters of 8-14 genes, their protein shell is predominantly composed of the structural proteins GvpA and GvpC (85, 89-91, 102, 103) (**Fig. 5-1a**). In GVs derived from *Anabaena flos-aquae,* GvpA is a 7.4 kDa amphiphilic protein that forms the main structural backbone of the GV shell, while GvpC sits on the external surface of the GV to provide structural reinforcement (87, 88, 104, 176). GvpC contains five highly-conserved alpha-helical repeats of 33 amino acids, each of which binds across five GvpA monomers (63). Earlier work demonstrated that the engineering of GvpC enables tuning of the mechanical properties of GVs, including their ability to produce nonlinear ultrasound contrast (97). This contrast is readily detected against tissue background using amplitude modulation ultrasound pulse sequences (98, 101).

In this study, we hypothesized that we could develop molecular biosensors for ultrasound in the form of GVs that dynamically change their nonlinear ultrasound contrast in response to the activity of specific biomolecules. In particular, we set out to engineer variants of GvpC incorporating amino acid sequences recognized by specific proteases – an important class of enzymes underlying cellular signaling, homeostasis, disease processes and therapeutic mechanisms (177-180). Using this strategy, we created GV-based biosensors to visualize the activity of the model constitutively active TEV endopeptidase, the calcium-activated protease calpain, and the processive protease ClpXP. We tested the ability of acoustic biosensors to visualize enzymatic activity *in vitro*, in living engineered cells, and *in vivo* in the mouse gastrointestinal (GI) tract. The resulting technology establishes a connection between the deeply penetrant imaging capabilities of ultrasound and the dynamic activity of enzymes, and provides a strategy for developing acoustic biosensors for a broad range of molecular and cellular signals.

TEV endopeptidase was chosen for the first proof-of-concept experiment, as it is well-characterized and highly sequence-specific, making it a staple enzyme in molecular biology applications (181-183). Calpain was chosen for its physiological relevance in controlling cellular fate and function by influencing diverse processes including cell motility and fusion, signal transduction, gene expression, cell cycle progression, apoptosis and necrosis (184, 185). Besides being a temporal integrator and indicator of calcium levels in the cell, excessive calpain activation is associated with cell death and must be tightly controlled due to irreversible cleavage of substrates by the activated protease (186). The biological functions of calpain and its association with intracellular calcium signaling are of significant biomedical interest as biomarkers and potential therapeutic targets in a growing number of diseases including cancer, Alzheimer's Parkinson's, type-2 diabetes, myocardial infarction, pulmonary fibrosis, traumatic spinal cord and brain injury (187). Therefore, developing an acoustic sensor to non-invasively visualize calpain activation would enable early diagnosis and *in vivo* deep-tissue monitoring of cell-fate and disease pathologies. Our third candidate was the processive proteolytic complex ClpXP, an important member of the family of ATPases Associated with diverse cellular Activities or AAA+ proteases, whose main function is to degrade proteins in bacteria and eukaryotic organelles (188, 189). Protein degradation by ClpXP is critical for modulating cellular responses to the environment and is implicated in biological functions ranging from protein quality control and unfolded protein response to regulation of the circadian clock and temporal control of cell division (188, 190-194). Mitochondrial ClpXP is being increasingly studied for its role in regulating energy metabolism in the context of neurodegenerative diseases, cancer and aging (192, 193).

Although we had an established modular system for molecular engineering of Ana GVs based on addition of new, recombinantly-expressed GvpC variants to GVs stripped of their native GvpC (ΔGvpC), extending this platform to engineer dynamic GV sensors was a whole new challenge. The first challenge was in the design and screening of protease-sensitive GvpC variants. While NMR structural simulations have been used to predict the secondary structure of different GvpC regions, no high-resolution 3-D crystal structure or precise information about the higher-order organization of GvpC on the GV surface exists in the literature. This made it impossible to predict a priori the ideal location for inserting a protease recognition motif or tag, and its effect on the stability and functionality of the modified GvpC. Secondly, in order to build an effective GV sensor, the dynamic change in GV shell mechanics had to translate to an unambiguous difference in the acoustic response that could be clearly discerned during ultrasound imaging. Finally, we did not know if protease activity, especially in the case of the processive ClpXP complex, would entirely compromise the integrity of the shell structure leading to complete collapse of the GVs.

In this study, we establish the first dynamic biomolecular sensors for ultrasound imaging of protease activity by engineering Ana GVs to conditionally change their nonlinear contrast in response to the activity of three different types of proteases – the TEV endopeptidase, the calcium-activated calpain protease and the processive bacterial ClpXP protease. Genetic modification of the outer shell protein, GvpC, by incorporation of a protease recognition motif or degradation tag, enables its subsequent cleavage or degradation by the active protease. This dynamic weakening or removal of GvpC causes the GV shell to become less stiff, undergo nonlinear buckling in response to ultrasound, and produce enhanced signals under nonlinear ultrasound imaging using a custom cross-amplitude modulation sequence. Furthermore, we demonstrate dynamic sensing of proteolytic activity in *Escherichia coli* Nissle 1917 by constructing intracellular acoustic sensor genes, and controllably tune down their nonlinear acoustic contrast in response to circuit-driven gene expression. *E. coli* Nissle (ECN) is a probiotic strain with the capacity to colonize the mammalian gastrointestinal tract and an increasingly used chassis in synthetic biology for the development of microbial therapeutics (121, 145, 167). Given this context, we demonstrate the potential of these dynamic biomolecular reporters for *in vivo* ultrasound imaging applications by visualizing ECN cells expressing acoustic sensor genes inside the colon of live mice with high spatial resolution.

5.2 Results

5.2a Engineering an acoustic sensor of TEV endopeptidase activity

To build an acoustic sensor for Tobacco Etch Virus (TEV) endopeptidase, we engineered a GvpC variant containing a protease recognition motif ENLYFQ'G that could specifically be recognized and cleaved by the endopeptidase (**Fig. 5-1b**). Our hypothesis was that dynamic cleavage and/or subsequent dissociation of protease-sensitive GvpC would cause the GV shell to become less stiff, allowing it to undergo nonlinear buckling in response to ultrasound. This buckling would then lead to production of enhanced nonlinear signals under ultrasound imaging (**Fig. 5-1b**). Based on a semi-rational design strategy, the TEV recognition sequence was inserted with and without flexible linkers of different lengths into the repeat regions of Ana GvpC in substitution of the original GvpC sequence. The TEV-sensitive GvpC variants were expressed and purified in *E. coli* and re-added on the surface of ΔGvpC Ana GVs to engineer potential GV sensor candidates that had a TEV cleavage site on their outer surface.

Engineered GVs were incubated with active TEV protease and a heat-deactivated (dTEV) protease, and their hydrostatic collapse behavior was measured post incubation using pressurized absorbance spectroscopy. This technique measures the optical density of GVs (which scatter 500 nm light when intact) under increasing hydrostatic pressure and provides a quick assessment of GV shell mechanics: GVs that collapse at lower pressure also produce more nonlinear contrast. Using this approach, we identified an engineered GV variant that showed ~ 70 kPa reduction in the collapse pressure midpoint upon incubation with the active TEV protease (**Fig. 5-1c**). This GV variant (hereafter referred to as GV Sensor for TEV, or GVS_{TEV}) has the TEV cleavage site on repeat 2 of Ana GvpC, flanked by flexible GSGSGSG linkers on both sides.

TEV cleavage of the engineered GvpC on GVS_{TEV} is expected to produce N- and C-terminal fragments with molecular weights of approximately 9 and 14 kDa, respectively. Indeed, gel electrophoresis of GVS_{TEV} after exposure to active TEV resulted in a significant reduction in the intact GvpC band and the appearance of the two cleaved GvpC fragments (**Fig. 5-1d**). In addition, removal from solution of unbound fragments via buoyancy purification of the GVs resulted in a reduced band intensity for the N-terminal cleavage fragment, indicating its partial dissociation after cleavage (**Fig. 5-1d**). No changes in GvpC were observed after incubation with dTEV. Transmission electron microscopy (TEM) images showed intact GVs with similar appearance under both conditions, confirming that protease cleavage did not affect the structure of the core GvpA shell (**Fig. 5-1e**). Dynamic light scattering (DLS) measurements showed no significant difference in the hydrodynamic radius of the engineered GVs after incubation with dTEV and active TEV protease, confirming the retention of colloidal stability (**Fig. 5-1f**).

After confirming the desired mechanical and biochemical properties of GVS_{TEV}, we performed ultrasound imaging to visualize the effect of TEV protease on this biosensor's acoustic response. Nonlinear imaging was performed using a recently developed cross-amplitude modulation (x-AM) approach (101), while linear images were acquired using a conventional B-mode pulse sequence. As hypothesized, exposing the GVS_{TEV} samples to TEV protease produced a strong nonlinear acoustic response (maximal nonlinear contrast-to-noise ratio (CNR) enhancement of ~ 7 dB at 7.2V) (**Fig. 5-1g**). No similar nonlinear contrast was observed in controls exposed to dTEV, while as expected both samples produced similar linear scattering. Consistent with the pressure-dependent mechanics of the GV shell, the differential nonlinear acoustic response of GVS_{TEV} became evident at pressures above 5V, and kept increasing until 9V, at which point the GVs begin to collapse (**Fig. 5-1h**). As an additional control, we found that GVs with the wild-type GvpC sequence (GV_{WT}) showed no difference in their hydrostatic collapse pressure or enhancement of nonlinear acoustic signal in response to TEV protease (**Fig. 5-1, i-k**), and no GvpC cleavage was seen upon gel electrophoresis (**Fig. 5-S1**). These results establish GVS_{TEV} as an acoustic biosensor of the TEV protease enzyme.

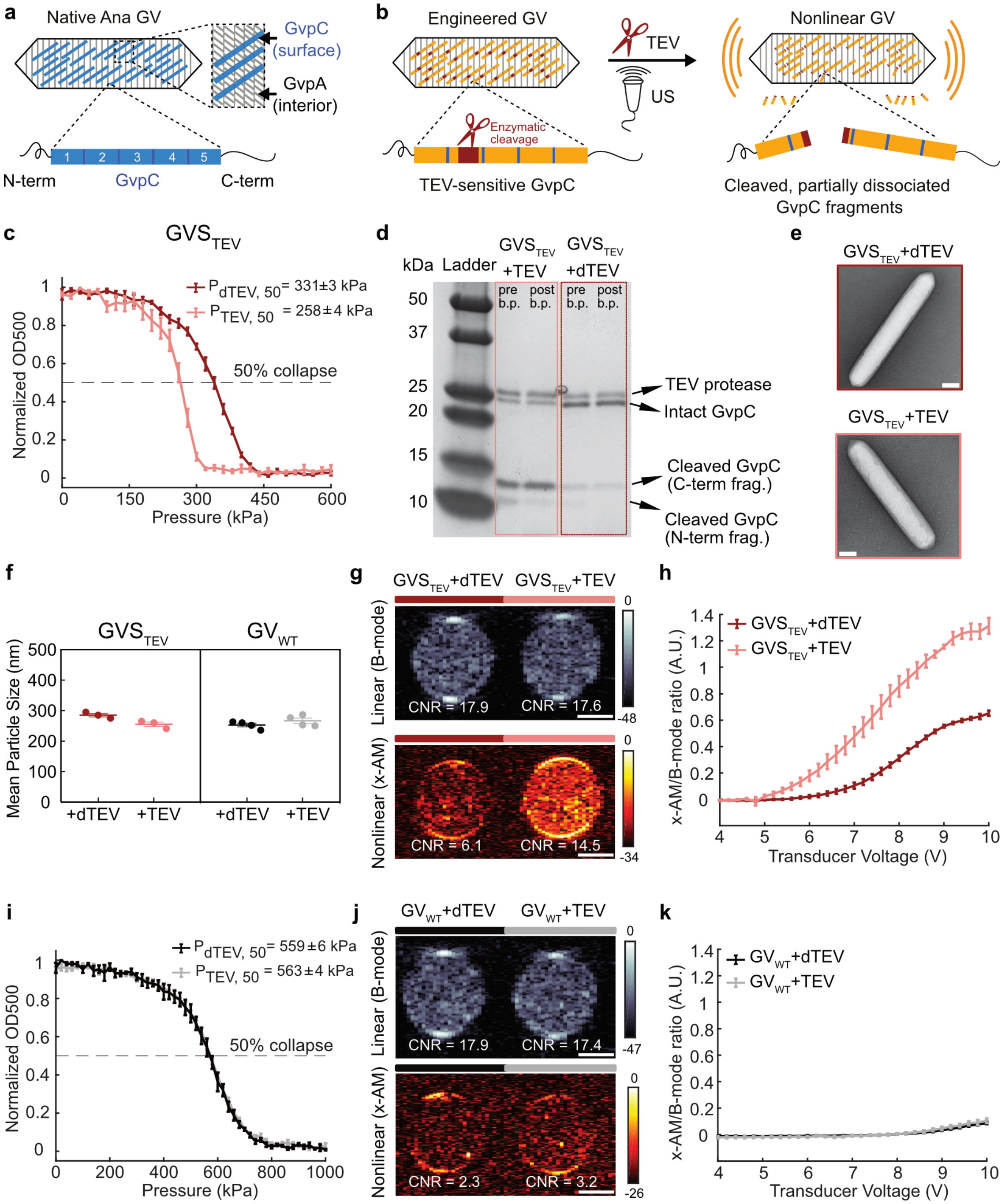

Figure 5-1: Engineering an acoustic sensor of TEV endopeptidase activity. (a) Schematic of a gas vesicle from *Anabaena flos-aquae* (Ana GV), with the structural backbone of its protein shell formed by GvpA ribs (gray) and the outer surface protein GvpC (blue) linking the GvpA ribs together to mechanically reinforce the structure. Each GvpC molecule is composed of five 33-amino acid repeats flanked by N-and C-terminal regions. (**b**) Schematic of a GV-based acoustic sensor of TEV endopeptidase activity. GVs

are engineered to have TEV-sensitive GvpC on the outer surface of their shell by incorporation of an enzyme recognition motif. Dynamic cleavage of the TEV-sensitive GvpC by the active endopeptidase causes weakening of the GV shell, leading to nonlinear buckling deformations and enhanced harmonic signals under ultrasound imaging (**c**) Normalized optical density (OD_{500nm}) measurements of the GV sensor of TEV (GVS_{TEV}) as a function of hydrostatic pressure after protease incubation. Heat-deactivated TEV (dTEV) is used as the negative control. Data points are fitted to a Boltzmann sigmoid function, and the legend shows the midpoint of hydrostatic collapse for each condition, along with the 95% confidence interval values (N≥3 independent trials). (**d**) SDS-PAGE analysis of OD_{500nm}-matched samples of GV_{TEV} incubated with dTEV and active TEV protease, before and after 2 rounds of buoyancy purification (pre and post b.p. respectively) (**e**) Representative TEM images of GVS_{TEV} after incubation with dTEV and active TEV protease. (**f**) DLS measurements of the average hydrodynamic radius of GVS_{TEV} and GV_{WT} samples after protease incubation (N≥3 biological replicates, individual dots represent each N and thick horizontal line indicates the mean) (**g**) Representative ultrasound images of agarose phantoms containing GVS_{TEV} incubated with TEV or dTEV protease at OD_{500nm} 2.2. The linear (B-mode) image was acquired at 1.6V and the nonlinear (x-AM) image showing the maximum difference in harmonic signal between the two samples was acquired at 7.2V. (**h**) Average ratio of x-AM to B-mode ultrasound signal as a function of transducer voltage for GVS_{TEV} after incubation with TEV and dTEV protease (N=3 independent biological replicates, with each N consisting of 2-3 technical replicates). (**i**) Hydrostatic collapse pressure measurements for engineered Ana GVs with WT-GvpC (GV_{WT}) after protease incubation (N≥3) (**j**) Representative ultrasound images of agarose phantoms containing GV_{WT} incubated with TEV or dTEV protease at OD_{500nm} 2.2. The B-mode image was acquired at 1.6V and the x-AM image at 9.2V. (**k**) Average ratio of x-AM to B-mode ultrasound signal as a function of transducer voltage for GV_{WT} after incubation with TEV and dTEV protease (N=3). For ultrasound images in (g) and (j), CNR stands for contrast-to-noise-ratio and color bars represent ultrasound signal intensity in the dB scale. Error bars indicate SEM. Scale bars in (e) represent 100 nm. Scale bars in (g) and (j) represent 1mm.

5.2b Engineering an acoustic sensor of calpain- a calcium activated protease

After validating our first acoustic biosensor using the model TEV protease, we examined the generalizability of our sensor design by engineering a GV sensor for a second endopeptidase. As our second target, we chose the calcium-dependent cysteine protease calpain, an endogenous mammalian enzyme with critical roles in a wide range of cell types (184, 185, 187). In mammals, the two most abundant isoforms of calpain found in almost all tissue and cell types are heterodimeric calpain-1 and -2, also known as μ-calpain and m-calpain respectively due to the micromolar and millimolar levels of Ca^{2+} required for their activation. We designed an acoustic sensor for μ-calpain by incorporating into GvpC an α-spectrin-derived sequence, QQEVYGMMPRD, that is cleaved by the active enzyme after the tyrosine residue (195). We hypothesized that cleavage of the engineered GvpC at this site would lead to weakening the GV shell and nonlinear ultrasound contrast (**Fig. 5-2a**). After generating several variants of GvpC in which the cleavage sequence was introduced, flanked by GSG or GSGSG linkers, into different sites within the second helical repeat region, we screened GVs containing these variants using pressurized absorbance spectroscopy in buffers with and without calpain and Ca^{2+}. This enabled us to identify a GV sensor for calpain (GVS_{calp}) that showed ~50 kPa decrease in collapse pressure only when both calpain and Ca^{2+} were present (**Fig. 5-2b**). Electrophoretic analysis confirmed cleavage and partial dissociation of the cleaved fragments from the GV surface (**Fig. 5-2c**), and TEM analysis of GVS_{calp} after incubation in buffer containing calpain and Ca^{2} confirmed the retained structural integrity of the GvpA shell (**Fig. 5-2d**).

Ultrasound imaging of GVS_{calp} revealed a robust nonlinear acoustic response from the GVS_{calp} when both calpain and calcium were present (**Fig. 5-2, e-g**), and not from negative controls lacking either or both of these analytes. A slight clustering tendency of GVS_{calp} nanostructures, which was attenuated by incubation with activated calpain (**Fig. 5-S2**), resulted in a slightly higher B-mode ultrasound signal for the negative controls. However, this did not significantly affect GVS_{calp}'s 7 dB nonlinear sensor contrast (**Fig. 5-2, e-g**). The relative nonlinear contrast of GVS_{calp} upon exposure to the active protease demonstrated a steep increase beyond 5.4V and leveled off at higher voltages due to GV collapse (**Fig. 5-2, h-j**). Additional control experiments performed on GVs with wild-type GvpC showed no proteolytic cleavage, change in GV collapse pressure or ultrasound response after incubation with calcium-activated calpain (**Fig. 5-S3**). These results show that acoustic biosensor designs can be generalized across multiple proteases, and can be used to sense the action of a conditionally active enzyme.

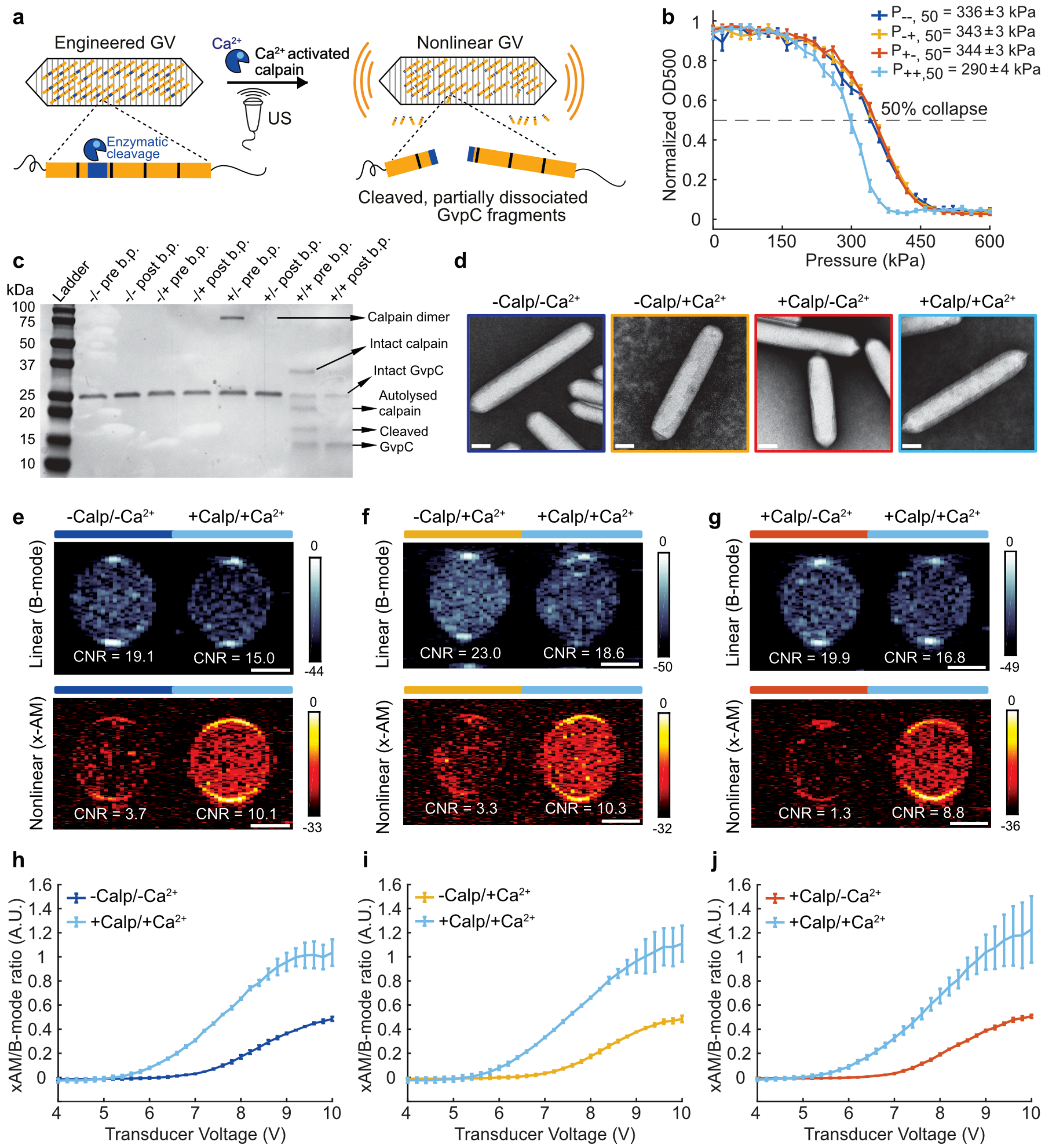

Figure 5-2: Engineering an acoustic sensor of calcium-activated calpain. (a) Schematic illustration of a GV sensor of calpain activity (GVS_{calp}). Engineered GVs have modified GvpC on their surface, with a protease recognition motif that can be specifically recognized and cleaved by calcium-activated calpain protease. Dynamic cleavage followed by partial dissociation of the calpain-sensitive GvpC reduces the GV shell stiffness, causing increased non-linear buckling and harmonic signals in response to ultrasound. (**b**) Hydrostatic collapse curves of GVS_{calp} after incubations in the presence (+) or absence (-) of calpain and/or calcium. Data points are fitted to a Boltzmann sigmoid function, and the legend shows the midpoint of hydrostatic collapse for each condition, along with the 95%

confidence interval values (N≥5 independent trials). (**c**) SDS-PAGE analysis of OD_{500nm}-matched samples of GVS_{calp} incubated in the presence (+) or absence (-) of calpain and/or calcium, before and after 2 rounds of buoyancy purification (pre and post b.p. respectively). (**d**) Representative TEM images of GVS_{calp} after incubations in the presence or absence of calpain and/or calcium. Scale bars represent 100 nm. (**e, f, g**) Representative ultrasound images of agarose phantoms containing GVS_{calp} incubated with and without calpain and/or calcium at OD_{500nm} 2.2. The B-mode images were taken at 1.6V for (e), (f) and (g) and the x-AM images corresponding to the maximum difference in non-linear contrast between the +calpain/+ calcium sample and the negative controls were taken at 7.2V for (e), (f) and at 7V for (g). CNR stands for contrast-to-noise-ratio and color bars represent ultrasound signal intensity in the dB scale. Scale bars represent 1 mm. (**h**, **i**, **j**) Average ratio of x-AM to B-mode ultrasound signal as a function of increasing transducer voltage for GVS_{calp} after incubation in the presence or absence of calpain and/or calcium (N=3 independent biological replicates, with each N consisting of 2 technical replicates). Error bars indicate SEM.

5.2c Building an acoustic sensor of processive proteolytic activity by ClpXP

In addition to endopeptidases, another important class of enzymes involved in cellular protein signaling and homeostasis is processive proteases, which unfold and degrade entire proteins starting from their termini. As a test case to determine whether GV-based biosensors could be developed for this class of enzymes, we selected ClpXP, a processive proteolytic complex from *Escherichia coli* comprising the unfoldase ClpX and the peptidase ClpP (188). ClpX forms hexameric rings that recognize and unfold protein substrates with terminal peptide sequences called degrons. The unfolded proteins are then fed into ClpP, a 14-meric chamber in which the peptidase degrades the proteins into small peptide fragments. We hypothesized that the addition of a degron to the C-terminus of GvpC would enable ClpXP to bind and degrade this protein, while leaving the underlying GvpA shell intact, and that the degradation of GvpC would result in the production of nonlinear ultrasound contrast (**Fig. 5-3a**).

To test this hypothesis, we appended the ssrA degradation tag, AANDENYALAA, via a short SG linker sequence, to the C-terminus of GvpC, resulting in a GV sensor of ClpXP, or GVS_{ClpXP} (**Fig. 5-3a**). To test the performance of this biosensor *in vitro*, we used a reconstituted cell-free transcription-translation system containing the purified ClpX protein and a ClpP plasmid in addition to any endogenous ClpXP present in the *E. coli*-derived extract. Gel electrophoresis performed after incubating GVS_{ClpXP} with this ClpXP system showed significant degradation of the engineered GvpC, compared to a negative control condition in which the extract was treated with a protease inhibitor (**Fig. 5-3b**). TEM images showed intact GVs under both conditions, confirming that GvpC degradation left the rest of the GV shell unaffected (**Fig. 5-3c**). Pressurized absorbance spectroscopy indicated a substantial weakening of the GV shell upon ClpX exposure, with the collapse pressure midpoint shifting by nearly 250 kPa (**Fig. 5-3d**). Ultrasound imaging experiments revealed a large, 17 dB enhancement in the nonlinear contrast produced by GVS_{ClpXP} at 7.8V in response to ClpXP activity (**Fig. 5-3, e-f**). Control GVs containing wild type GvpC showed no sensitivity to ClpXP activity (**Fig. 5-3, g-i**, **Fig. 5-S4**). These results established the ability of GV-based acoustic biosensors to visualize the activity of processive proteases, and show that GVS_{ClpXP} acts as a turn-on sensor of proteolysis, providing considerable advantages over turn-off sensors, whose loss of signal can be caused by poor expression or delivery in addition to the activity of their target enzyme.

5.2d Constructing intracellular acoustic sensor genes for dynamic monitoring of protease activity and circuit-driven gene expression

After demonstrating the performance of acoustic biosensors *in vitro*, we endeavored to show that they could also respond to enzymatic activity happening inside living cells. A hybrid cluster of genes incorporating GV genes from *A. flos-aquae* and another species was recently expressed in probiotic *E.Coli* Nissle 1917 cells as acoustic reporter genes (ARGs), allowing gene expression in these cells to be imaged with linear B-mode ultrasound (175). To test whether this original ARG construct (ARG_{WT}) could be converted into a fully genetically encoded acoustic sensor of ClpXP (ASG_{ClpXP}), we swapped the wild type GvpC in the ARG gene cluster with the modified GvpC of GVS_{ClpXP} (**Fig. 5-4a**), and transformed it into Nissle cells, which natively express ClpXP. As hypothesized, pressurized absorbance spectroscopy on cells expressing ASG_{ClpXP} revealed a reduction in the hydrostatic collapse pressure midpoint of ~ 160 kPa relative to cells expressing ARG_{WT} (**Fig. 5-4b**). In ultrasound imaging, cells expressing ASG_{ClpXP} showed an enhancement in nonlinear contrast of approximately 13 dB (**Fig. 5-4c**) compared to ARG controls, with the linear B-mode signal being similar. The nonlinear response of $\mathrm{ASG_{ClpXP}}$ expressing cells was strongest beyond 12.5V (**Fig. 5-4d**, **Fig. 5-S5**).

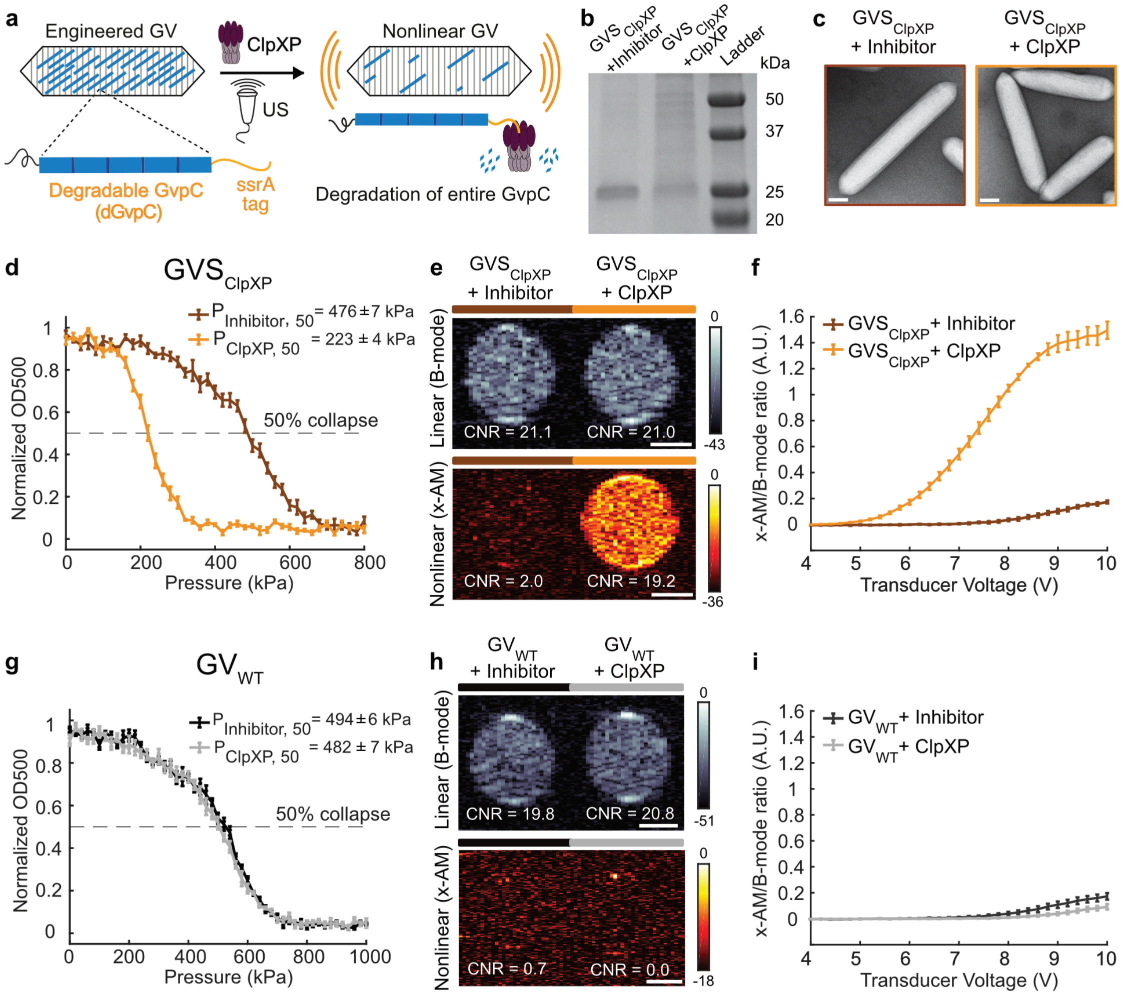

Figure 5-3: Engineering an acoustic sensor of processive proteolysis by ClpXP. (**a**) Schematic of a GV sensor of ClpXP activity ($\mathrm{GVS_{ClpXP}}$). Ana GVs are engineered to have a degradable version of GvpC (dGVpC), by appending a ssrA tag to its C-terminus. This enables dGvpC recognition and degradation by the ClpXP proteolytic complex, weakening the GV shell and leading to an enhanced non-linear acoustic response. (**b**) SDS-PAGE analysis of $\mathrm{OD_{500nm}}$-matched $\mathrm{GVS_{ClpXP}}$ samples incubated in a reconstituted cell-free transcription-translation (TX-TL) system, containing a protease inhibitor cocktail or ClpXP. (**c**) Representative TEM images of $\mathrm{GVS_{ClpXP}}$ after incubations in the presence of a protease inhibitor or ClpXP. (**d**) Normalized optical density ($\mathrm{OD_{500nm}}$) measurements of $\mathrm{GVS_{ClpXP}}$ as a function of hydrostatic pressure after protease incubation. Data points are

fitted to a Boltzmann sigmoid function, and the legend shows the midpoint of hydrostatic collapse for each condition, along with the 95% confidence interval values (N=5). (**e**) Representative ultrasound images of agarose phantoms containing $\mathrm{GVS}_{\mathrm{ClpXP}}$ incubated with the inhibitor cocktail or active ClpXP at $\mathrm{OD}_{500\mathrm{nm}}$ 2.2. (**f**) Average x-AM/B-mode ratio as a function of ultrasound transducer voltage for $\mathrm{GVS}_{\mathrm{ClpXP}}$ after incubation with the protease inhibitor or active ClpXP. (**g**) Hydrostatic collapse pressure measurements for engineered Ana GVs with WT-GvpC ($\mathrm{GV}_{\mathrm{WT}}$) after protease incubation (N=3) (**h**) Representative ultrasound images of agarose phantoms containing $\mathrm{GV}_{\mathrm{WT}}$ incubated with the inhibitor cocktail or active ClpXP at $\mathrm{OD}_{500\mathrm{nm}}$ 2.2. (**i**) Average ratio of x-AM to B-mode acoustic signal as a function of transducer voltage for $\mathrm{GV}_{\mathrm{WT}}$ after incubation with the inhibitor cocktail or ClpXP protease. For ultrasound images in (e) and (h), CNR stands for contrast-to-noise-ratio and color bars represent ultrasound signal intensity in the dB scale. The B-mode images were acquired at 1.6V and the x-AM images showing maximal difference in the non-linear CNR between the GV samples with inhibitor and ClpXP were acquired at 7.8V. For (f) and (i), N=3 independent biological replicates, with each N having 3 technical replicates. Error bars indicate SEM. Scale bars in (c) represent 100 nm. Scale bars in (e) and (h) represent 1mm.

One of the main applications of reporter genes in cells is to monitor the dynamic activity of natural or synthetic gene circuits (196-199). To test whether our acoustic sensors could be used to track the output of a synthetic gene circuit, we co-transformed Nissle cells with $\mathrm{ASG}_{\mathrm{ClpXP}}$ under the transcriptional control of a T5 promoter and a Lac operator, and a separate wild-type GvpC gene controlled by the an anhydrotetracycline (aTc)-dependent promoter (**Fig. 5-4e**). We hypothesized that induction of the gene circuit with aTc would result in the production of non-degradable wild-type GvpC, which would take the place of any degraded engineered GvpC on $\mathrm{ASG}_{\mathrm{ClpXP}}$ GVs, stiffen the GV shell and reduce the nonlinear scattering of the acoustic sensor (**Fig. 5-4e**). Indeed, when we induced the cells with just IPTG to form $\mathrm{ASG}_{\mathrm{ClpXP}}$, we observed strong nonlinear contrast. However, when aTc was added to the cultures after IPTG induction, nonlinear acoustic contrast was reduced by ~ 10 dB (**Fig. 5-4, f-g**, **Fig. 5-S5**). These results demonstrate that our developed biosensors can be utilized as acoustic sensor genes inside living cells, and operate within the context of engineered genetic circuits.

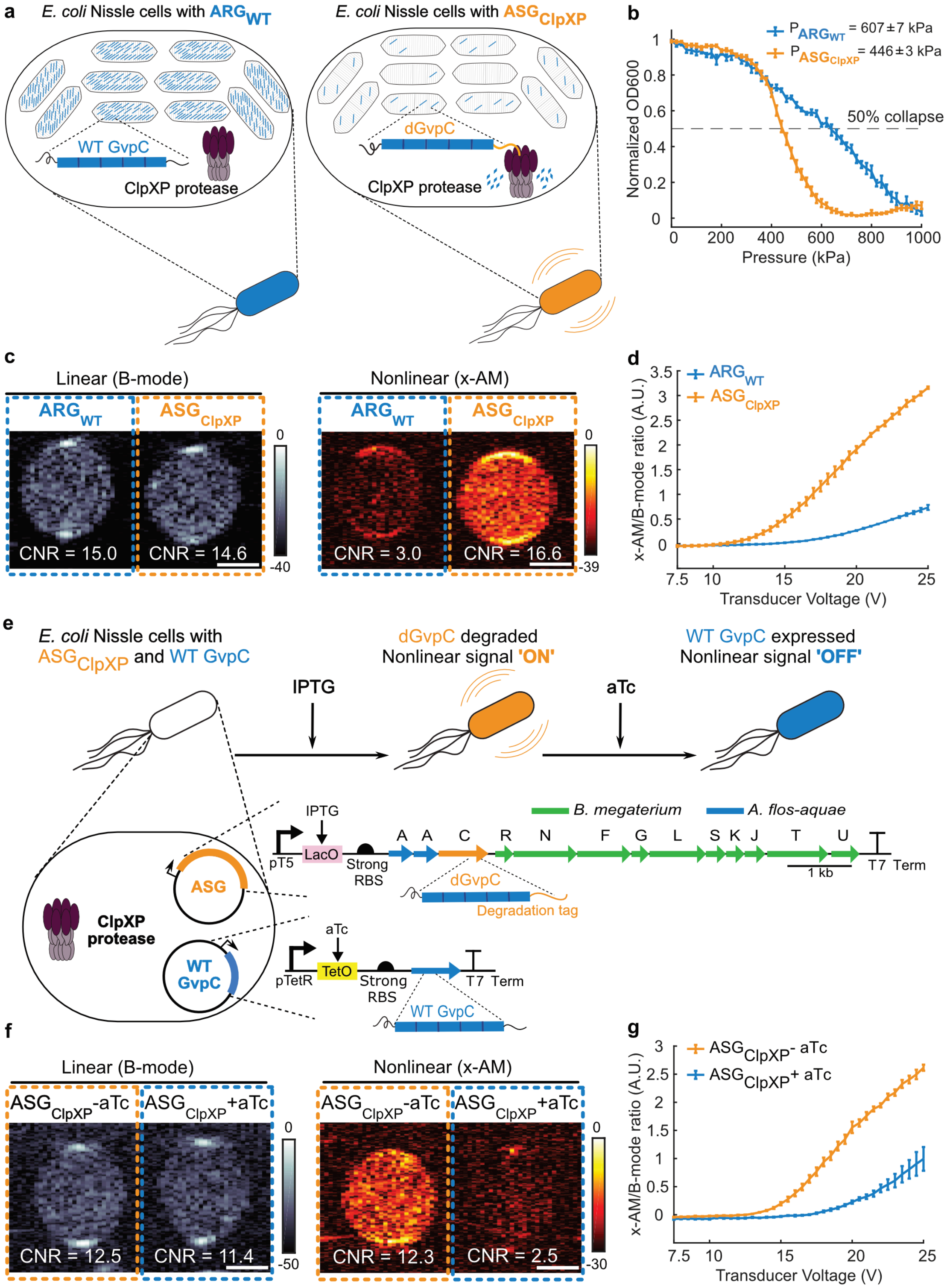

Figure 5-4: Constructing intracellular acoustic sensor genes for dynamic monitoring of protease activity and circuit-driven gene expression. (a) Schematic of *E. Coli* Nissle

cells expressing the original acoustic reporter gene construct (ARG_{WT}) containing WT GvpC or the acoustic sensor gene construct for ClpXP (ASG_{ClpXP}) containing a degradable version of GvpC (dGvpC), which can be processed by the proteolytic activity of intracellular ClpXP. Proteolytic activity causes a decrease in the shell stiffness of GVs expressed by $ASG_{ClpXP,}$ enhancing their non-linear acoustic response and leading to increased harmonic signals from Nissle cells under ultrasound imaging. (**b**) Normalized optical density of cells expressing either ARG_{WT} or ASG_{ClpXP} at 600 nm, as a function of applied hydrostatic pressure. Data points are fitted to a Boltzmann sigmoid function, and the legend shows the midpoint of hydrostatic collapse for each cell type, along with the 95% confidence interval values (N≥3). (**c**) Representative ultrasound images of Nissle cells expressing either ARG_{WT} or ASG_{ClpXP} at OD_{600nm} 1.5 (N=3 independent biological replicates, with each N having 3 technical replicates). (**d**) Average x-AM/B-mode ratio as a function of ultrasound transducer voltage for Nissle cells expressing either ARG_{WT} or ASG_{ClpXP}. (**e**) Schematic of pT5-LacO driven ASG_{ClpXP} and pTet-TetO driven WT GvpC gene circuits, co-transformed into Nissle cells, for dynamic tuning of non-linear acoustic signals from the intracellular GV sensors in response to circuit-driven gene expression. (**f**) Representative ultrasound images of Nissle cells (OD_{600nm} 1) expressing ASG_{ClpXP}, with or without aTc induction. (**g**) Average x-AM/B-mode ratio as a function of ultrasound transducer voltage for Nissle cells expressing ASG_{ClpXP}, with and without aTc induction (N=5). For ultrasound images in (c) and (f), CNR stands for contrast-to-noise-ratio and color bars represent ultrasound signal intensity in the dB scale. The B-mode images were acquired at 1.6V and the x-AM images showing maximal difference in the non-linear CNR were acquired at 17.5V for (c) and at 21V for (f). Error bars indicate SEM. Scale bars in (c) and (f) represent 1 mm.

5.2e Ultrasound imaging of bacteria expressing acoustic sensor genes in vivo

Finally, after establishing the basic principles of acoustic biosensor engineering *in vitro* and demonstrating their performance *in cellulo*, we assessed the ability of our sensor constructs to produce ultrasound contrast detectable within a biologically relevant anatomic location *in vivo*. In particular, increasing appreciation of the role played by the mammalian microbiome in health and disease, and the development of engineered probiotic microbes targeting the GI system, have made microbial imaging in the mammalian GI tract a topic of paramount importance (115-129). This anatomical site is an excellent target for ultrasound imaging due to its location deep inside the animal. However, detecting engineered bacteria using conventional linear B-mode imaging of the colon is challenging due to high background signal from endogenous linear scatterers in the tissue. We hypothesized that we could address this challenge by taking advantage of the strong nonlinear response of acoustic biosensors in response to cleavage of their GvpC by ClpXP, and that we could distinguish cells engineered to express ASG_{ClpXP} from background tissue and from cells expressing wild-type linear ARGs *in vivo*.

To test this hypothesis, we co-injected Nissle cells expressing ASG_{ClpXP} into the mouse colon, distributing them along the lumen wall, together with cells expressing ARG_{WT}, distributed in the lumen center (**Fig. 5-5a**). Using nonlinear x-AM imaging, we could clearly visualize the unique *in vivo* contrast generated by ASG-expressing cells, telling them apart with high spatial accuracy as a bright ring of contrast lining the colon periphery (**Fig. 5-5b, Fig. 5-S6**). Nonlinear scattering from the background tissue and ARG_{WT} cells in the center of the lumen was substantially weaker. A comparison of ultrasound images acquired before and after acoustic collapse of the GVs using a high-pressure pulse from the transducer, confirmed that the bright ring of nonlinear signal was emanating from GV-containing cells **(Fig. 5-5b)**. Independent experiments using fresh cell preparations across different mice showed a consistent difference in the nonlinear contrast between the inner and outer ring (**Fig. 5-5c**, **Fig. 5-S6)**. These results demonstrate the ability of acoustic biosensors to be visualized with high spatial resolution inside living cells in deep tissue.

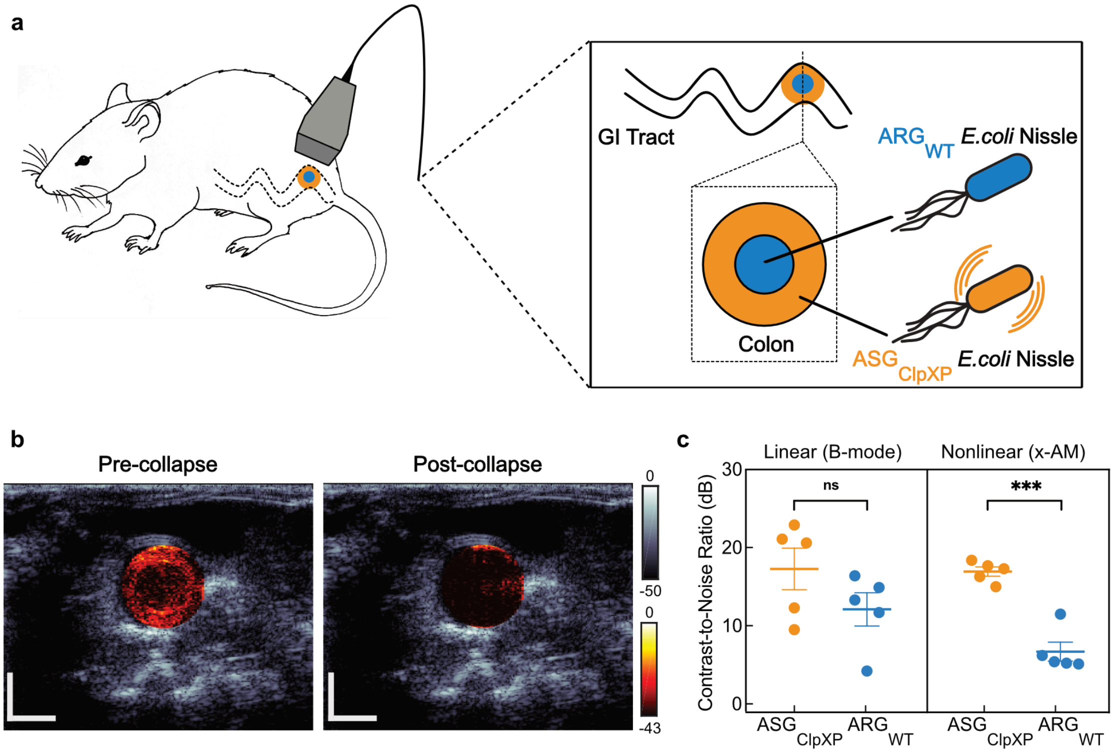

Figure 5-5: Ultrasound imaging of bacteria expressing acoustic sensor genes in the gastrointestinal tract of mice. (**a**) Schematic illustrating the *in vivo* ultrasound imaging experiment, after co-injection of probiotic *E. coli* Nissle (ECN) expressing the wild-type acoustic reporter genes (ARG$_{WT}$) or the acoustic sensor gene construct for ClpXP (ASG$_{ClpXP}$) into the GI tract of mice. (**b**) Transverse ultrasound image of a mouse, whose colon contains ECN expressing ARG$_{WT}$ at the center of the lumen and ECN expressing ASG$_{ClpXP}$ at the periphery of the lumen. Cells were injected at a final concentration of 1.5 * 10^9 cells/mL. Linear (B-mode) anatomical images were acquired at 7.4V and nonlinear (x-AM) images of the colon were acquired at 20V by an ultrasound transducer before and after acoustic collapse, and superimposed on each other to form the composite image displayed in the figure. B-mode signal is displayed using the bone colormap and x-AM signal is shown using the hot colormap. Color bars represent B-mode and x-AM ultrasound signal intensity in the dB scale. Horizontal and vertical scale bars represent 2 mm. (**c**) B-mode and x-AM contrast-to-noise ratio (CNR) *in vivo*, for ECN expressing ARG$_{WT}$ or ASG$_{ClpXP}$. N = 5 independent replicates, individual dots represent each N and the thick horizontal line indicates the mean. P = 0.0003 for the x-AM signal from ECN expressing ASG$_{ClpXP}$ versus the ARG$_{WT}$ control. Error bars indicate SEM.

5.3 Conclusion and Outlook

Our results establish a paradigm for visualizing molecular and cellular activity non-invasively using acoustic biosensors. Just as early fluorescent biosensors connected molecular recognition motifs to the nanoscale arrangement and resonant energy transfer between fluorophores, our paradigm connects recognition sequences to the nanoscale mechanics and nonlinear acoustic scattering of GVs. This connection is enabled by the dependence of the buckling mechanics of GVs on the reinforcing protein GvpC, and the ability to incorporate internal and terminal peptide sequences that allow this protein to interact with other biomolecules. Following in the footsteps of early work on fluorescent biosensors (200, 201), we focused our initial sensor development on proteases due to their relatively compact recognition motifs, the large impact on protein structure expected from cleavage, and the importance of this class of enzymes in biology. Our ability to build GV-based biosensors for three different proteases demonstrates the modularity of this paradigm. In future studies, the design strategy presented here could be extended to building acoustic sensors for other physiologically relevant enzymes, ions or other molecules that interact with specific recognition motifs.

Significant scope exists for further optimizing the design of acoustic biosensors and their imaging with ultrasound. While all three of our protease sensors produced detectable nonlinear contrast, the change exhibited by $\mathrm{GVS}_{\mathrm{ClpXP}}$ was significantly larger than for the other two constructs. This difference is consistent with $\mathrm{GVS}_{\mathrm{ClpXP}}$'s larger shift in hydrostatic collapse pressure upon exposure to its target enzyme, indicating a bigger change in the GV shell stiffness. This is not surprising for an enzyme that processively degrades GvpC, and whose recognition motif can be incorporated outside the main GV-binding region of GvpC. Endopeptidase sensors could be optimized to reach similar performance by incorporating more than one cleavage site within the GvpC sequence and tuning the linkers connecting these sites to the rest of GvpC, to enable stronger binding and stiffening in their uncleaved configuration. However, even in their current form our biosensors were easily detectable at GV concentrations of 250 pM, or GvpC concentrations of approximately 450 nM. Another limitation, shared with most other protease biosensors, is that proteolysis is irreversible, such that each sensor molecule visualizes activity only once. This limitation is alleviated in genetically encoded biosensors because cells can make more of the intact sensor. For GV-based sensors, this could be achieved by re-expressing only the engineered GvpC, thus reducing the metabolic burden of GV formation.

In this study, we detected the activation of our biosensors using nonlinear x-AM ultrasound, taking the ratio of contrast in this mode to linear B-mode scattering as a metric of sensor response. This serves as a ratiometric signal, advantageous for quantification in scenarios where the sensor concentration may vary. In addition, each sensor had a characteristic response profile under varying acoustic pressure, reflecting its unique mechanical properties. While the optimum detection pressure was different for each sensor, they could all operate over a range of several hundred kPa, reducing the need for precise calibration of the pressure reached at every point in a tissue.

In addition to characterizing the performance of acoustic biosensors in reconstituted *in vitro* systems, we demonstrated the transferability of this basic technology *in cellulo* by constructing a fully genetically encoded version of $\text{GVS}_{\text{ClpXP}}$ and connecting it to a synthetic gene circuit, and *in vivo* by demonstrating the ability to image intracellular signals from engineered probiotic bacteria located in the mouse GI tract. Future work is needed to extend the use of acoustic biosensors beyond these proofs-of-concept into specific biological applications. With further engineering and expression in a wider range of cell types, acoustic biosensors promise to take dynamic imaging of molecular and cellular function to new depths.

5.4 Methods

Design and cloning of genetic constructs

All gene sequences codon optimized for *E.Coli* expression were inserted into their plasmid backbones via Gibson Assembly or KLD Mutagenesis using enzymes from New England Biolabs and custom primers from Integrated DNA Technologies. The protease recognition sequences for Tobacco Etch Virus (TEV) protease and μ-Calpain, flanked by flexible linkers, were introduced by substitution-insertion into the second repeat of the wild-type *Anabaena flos-aquae* (Ana) GvpC sequence in a pET28a expression vector (Novagen) driven by a T7 promoter and lac operator. The ssrA degradation tag for the ClpXP bacterial proteasome was appended to the C-terminus of Ana GvpC using a short flexible linker. The acoustic sensor gene for intracellular protease sensing of ClpXP was constructed by modification of the acoustic reporter gene cluster ARG1 (175) by insertion of the ssrA degradation tag to the C-terminal end of GvpC using a linker sequence. For expression in *E.coli* Nissle, the pET28a T7 promoter was replaced by the T5 promotor. For dynamic regulation of intracellular sensing, the wild-type GvpC sequence was cloned into a modified pTARA backbone under a pTEt promoter and tet operator. The complete list and features of plasmids used in this study are given in **Supplementary table 5-T1**. Plasmid constructs were cloned into NEB Turbo *E. Coli* (New England Biolabs) and sequence-validated.

Gas Vesicle expression, purification and quantification

Gas vesicles (GVs) for *in vitro* biochemical assays with proteases were harvested and purified from confluent *Ana* cultures using protocols described in Chapter 2 and Appendix A. Briefly, Ana cells were grown in Gorham's media supplemented with BG-11 solution (Sigma) and 10 mM sodium bicarbonate at 25°C, 1% CO_2 and 100 rpm shaking, under a 14h light cycle and 10h dark cycle. Confluent cultures were transferred to sterile separating funnels and left undisturbed for 2-3 days to allow buoyant *Ana* cells expressing GVs to float to the top. Hypertonic lysis with 10% Solulyse (Genlantis) and 500 mM sorbitol was used to harvest the Ana GVs. Purified GVs were obtained through 3-4 rounds of centrifugally assisted floatation, with removal of the subnatant and resuspension in 1x Phosphate Buffered Saline (PBS, Corning) after each round.

For expression of acoustic reporter/sensor genes (AR/SGs) in bacteria, *E. Coli* Nissle *1917* cells (Ardeypharm GmbH) were made electrocompetent and transformed with the genetic constructs. After electroporation, cells were rescued in SOC media supplemented with 2% glucose for 1h at 37°C. Transformed cells were grown for 12-16 hours in 5 mL of LB medium supplemented with 50 μg/mL kanamycin and 2% glucose. Large-scale cultures for expression were prepared by a 1:100 dilution of the starter culture in LB medium containing 50 μg/mL kanamycin and 0.2% glucose. Cells were grown at 37°C to an OD_{600nm} of 0.2-0.3, then induced with 3μM Isopropyl β-D-1-thiogalactopyranoside (IPTG) and allowed to grow for 22 hrs at 30°C. Buoyant *E.Coli* Nissle cells expressing GVs were isolated from the rest of the culture by centrifugally assisted floatation in 50 mL conical tubes at 300g for 3-4 hrs, with a liquid column height less than 10 cm to prevent GV collapse by hydrostatic pressure.

Ana GV concentration was determined OD measurements at 500 nm using a Nanodrop (Thermo Fisher Scientific), using the resuspension buffer or pre-collapsed GVs as the blank. Buoyant cells expressing GVs were quantified using a pressure-sensitive OD measurement at 600 nm using the Nanodrop.

Bacterial expression and purification of GvpC variants

For expression of Ana GvpC variants, plasmids were transformed into chemically competent BL21(DE3) cells (Invitrogen) and grown overnight for 14-16 h at 37°C in 5 mL starter cultures in LB medium with 50 μg/mL kanamycin. Starter cultures were diluted 1:250 in Terrific Broth (Sigma) and allowed to grow at 37°C (250 rpm shaking) to reach an OD_{600nm} of 0.4-0.7. Protein expression was induced by addition of 1 mM IPTG and the cultures were transferred to 30°C. Cells were harvested by centrifugation at 5500g after 6-

8 hours. For the GvpC-ssrA variant, expression was carried out at 25°C for 8 hours to reduce the effect of protease degradation and obtain sufficient protein yield.

GvpC expressed as inclusion bodies in E. coli, was purified by lysing the cells at room temperature using Solulyse (Genlantis), supplemented with lysozyme (400 μg/mL) and DNAseI (10 μg/mL). Inclusion body pellets were isolated by centrifugation at 27,000g for 15 mins and then resuspended in a solubilization buffer comprising 20 mM Tris-HCl buffer with 500 mM NaCl and 6 M urea (pH: 8.0), before incubation with Ni-NTA resin (Qiagen) for 2 h at 4°C. The wash and elution buffers were of the same composition as the solubilization buffer, but with 20mM and 250 mM imidazole respectively. The concentration of the purified protein was assayed using Bradford Reagent (Sigma). Purified GvpC variants were verified to be >95% pure by SDS-PAGE analysis.

Preparation of gas vesicles for *in vitro* protease assays

Engineered GVs having protease-sensitive or wild-type GvpC was prepared using the urea stripping and GvpC re-addition protocols detailed in Appendix A. Briefly, Ana GVs were stripped of their native outer layer of GvpC by treatment with 6M urea solution buffered with 100 mM Tris- HCl (pH:8-8.5). Two rounds of centrifugally assisted floatation with removal of the subnatant liquid after each round were performed to ensure complete removal of native GvpC. Recombinant Ana GvpC variants purified from inclusion bodies were then added to the stripped Ana GVs in 6M urea a 2-3x molar excess concentration determined after accounting for 1:25 binding ratio of GvpC: GvpA. For a twofold stoichiometric excess of GvpC relative to binding sites on an average Ana GV, the nmol of recombinant GvpC to be added to stripped GVs was calculated according to the formula: 2* OD * 198 nM * volume of GVs (in liters). The exact volume of recombinant GvpC to be added was then determined by considering its molar mass and concentration. The mixture of stripped GVs (OD_{500nm} = 1.5-2) and recombinant GvpC in 6 M urea buffer was loaded into dialysis pouches made of regenerated cellulose membrane with a 6-8 kDa M.W. cutoff (Spectrum Labs). The GvpC was allowed to slowly refold onto the surface of the stripped GVs by dialysis in large buckets containing 4L of PBS for > 12h at 4°C. Dialyzed

GV samples were subjected to two or more rounds of centrifugally assisted floatation at 300g for 3-4h to remove any excess unbound GvpC. Engineered GVs were resuspended in PBS after subnatant removal and quantified using pressure-sensitive OD measurements at 500 nm using a Nanodrop.

Pressurized Absorbance Spectroscopy

Purified, engineered Ana GVs were diluted in PBS to an OD_{500nm} ~ 0.2-0.4 and 400 μL of the diluted sample was loaded into a flow-through quartz cuvette with a pathlength of 1 cm (Hellma Analytics). Buoyant *Nissle* cells expressing GVs were diluted to an OD_{600nm} of ~ 1 in PBS for measurements. A 1.5-MPa nitrogen gas source was used to apply hydrostatic pressure in the cuvette through a single valve pressure controller (PC series, Alicat Scientific), while a microspectrometer (STS-VIS, Ocean Optics) measured the optical density of the sample at 500 nm (for Ana GVs) or 600nm (for Nissle cells). The hydrostatic pressure was increased from 0 to 1 MPa in 20kPa increments with a 7-s equilibration period at each pressure before measurement of the optical density. Each set of optical density measurements was normalized by scaling to the Min-Max measurement value, and the data was fitted using the Boltzmann sigmoid function $\mathrm{f(p)} = \left(1 + \mathrm{e}^{(\mathrm{P}-\mathrm{P_c})/\Delta\mathrm{P}}\right)^{-1}$, with the midpoint of normalized optical density change $\mathrm{P_c}$ as well as the 95% confidence intervals (rounded to the nearest integer) reported in the figures.

TEM sample preparation and imaging

Freshly diluted samples of engineered Ana GVs (OD_{500nm} ~ 0.3) in 10 mM HEPES buffer containing 150 mM NaCl (pH 8), or buoyant *Nissle* cells diluted to OD_{600nm} ~ 1 in water was used for TEM measurements. 2 μL of the diluted sample was added to Formvar/carbon 200 mesh grids (Ted Pella) that were rendered hydrophilic by glow discharging (Emitek K100X). For engineered Ana GVs, 2% uranyl acetate was added for negative staining. Images were acquired using the FEI Tecnai T12 LaB6 120kV TEM equipped with a Gatan Ultrascan 2k X 2k CCD and 'Leginon' automated data collection software suite.

Dynamic Light Scattering (DLS) measurements

Engineered Ana GVs were diluted to an OD_{500nm} ~ 0.2 in PBS or 10 mM HEPES buffer with 150 mM NaCl (pH 8). 150-200 μL of the sample was loaded into a disposable cuvette (Eppendorf UVette®) and the particle size was measured using the ZetaPALS particle sizing software (Brookhaven instruments) with an angle of 90 ° and refractive index of 1.33.

In vitro protease assays

For *in vitro* endpoint biochemical assays with the Tobacco Etch Virus (TEV) endopeptidase, recombinant TEV protease (R&D Systems) was incubated (25% v/v fraction) with engineered Ana GVs resuspended in PBS (final OD_{500nm} in reaction mixture = 5-6) at 30°C for 14-16h. Engineered GVs with WT GvpC and TEV protease heat-inactivated at 80°C for 20-30 mins were used as the controls.

For *in vitro* endpoint biochemical assays with the calcium-activated protease Calpain, recombinant μ-calpain (Millipore Sigma) was incubated in a 10% v/v fraction with engineered Ana GVs (resuspended in PBS), in a reaction mixture containing 50 mM Tris-HCl, 50 mM NaCl, 5 mM 2-mercaptoethanol, 1 mM EDTA and 1 mM EGTA and 5 mM Ca^{2+} (pH: 7.5). The final concentration of engineered GVs in the reaction mixture was OD_{500nm} ~ 6 and the protease assay was carried out at 25°C for 14-16h. Negative controls included the same reaction mixture without calpain, without calcium and without calpain and calcium. Engineered GVs with WT-GvpC were used as additional negative controls for comparison.

For *in vitro* biochemical assays with the ClpXP bacterial proteasome, a reconstituted cell-free transcription-translation (TX-TL) system adapted for ClpXP degradation assays (gift from Dr. Zachary Sun in Prof. Richard Murray's lab at Caltech) was used. Briefly, cell-free extract was prepared by lysis of ExpressIQ *E.coli* cells (New England Biolabs), and mixed in a 44% v/v ratio with an energy source buffer, resulting in a master mix of extract and buffer comprising: 9.9 mg/mL protein, 1.5 mM each amino acid except leucine, 1.25 mM leucine, 9.5 mM Mg-glutamate, 95 mM K-glutamate, 0.33 mM DTT, 50 mM HEPES, 1.5 mM ATP and GTP, 0.9 mM CTP and UTP, 0.2 mg/mL tRNA, 0.26 mM CoA, 0.33 mM NAD, 0.75 mM cAMP, 0.068 mM folinic acid, 1 mM spermidine, 30 mM 3-PGA and 2% PEG-8000. For purified ClpX protein, a monomeric N-terminal deletion variant Flag-ClpXdeltaNLinkedHexamer-His6 (Addgene ID: 22143) was used. Post Ni-NTA purification, active fractions of ClpX hexamers with sizes above 250 kDa were isolated using a Supradex 2010/300 column, flash frozen at a concentration of 1.95 μM and stored at -80°C in a storage buffer consisting of: 50 mM Tris-Cl (pH 7.5), 100 mM NaCl, 1mM DTT, 1 mM EDTA and 2% DMSO. The final reaction mixture was prepared as follows: 75% v/v fraction of the master mix, 10% v/v of purified ClpX, 1nm of the purified pBEST-ClpP plasmid and engineered Ana GVs (concentration of OD_{500nm} = 2.5-2.7 in the reaction mixture). The mixture was made up to the final volume using ultrapure H_2O. The reaction was allowed to proceed at 30°C for 14-16 h. As a negative control, a protease inhibitor cocktail mixture (SIGMA*FAST*^{TM}, Millipore Sigma) was added at 1.65x concentration. For this, a 10x solution of the inhibitor was prepared fresh before each incubation by dissolving the cocktail tablets in PBS and premixed with the cell-free extract at room temperature for 30 mins before addition to the reaction mixture.

Dynamic sensing of circuit-driven gene expression in *E. Coli* Nissle

Electrocompetent *E. coli* Nissle cells were co-transformed with the pET expression plasmid (Lac-driven) containing the acoustic sensor gene cluster for ClpXP and a modified pTARA plasmid (Tet-driven) containing the WT Ana GvpC gene. Electroporated cells were rescued in SOC media supplemented with 2% glucose for 2h at 37°C. Transformed cells were grown overnight in 5 mL LB medium supplemented with 50 μg/mL kanamycin, 50 μg/mL chloramphenicol and 2% glucose. Starter cultures were diluted 1:100 in LB medium with 50 μg/mL kanamycin, 50 μg/mL chloramphenicol and 0.2% glucose and allowed to grow at 37°C to reach an OD_{600nm} of 0.2-0.3. Acoustic sensor gene expression was induced with 3μM IPTG and the bacterial culture was transferred to 30°C incubator with 250 rpm shaking for 1.5-2h. The culture was then split into two halves of equal volume, and one half was induced with 50 ng/mL aTc for expression of WT GvpC. Cultures with and without aTc induction were allowed to grow for an additional 20 h at 30°C. Cultures were then spun down at 300g in a refrigerated centrifuge at 4°C for 3-4 hrs in 50 mL conical tubes to isolate buoyant cells expressing GVs from the rest of the culture. The liquid column height was maintained at less than 10 cm while spinning, to prevent GV collapse by hydrostatic pressure.

In vitro **ultrasound imaging**

Imaging phantoms were prepared by melting 1% agarose (w/v) in PBS and casting wells using a custom 3-D printed template mold (containing a 2-by-2 grid of cylindrical wells with 2 mm diameter and 1mm spacing between the outer radii in the bulk material). Ana GV samples from *in vitro* assays or buoyant Nissle cells expressing GVs were mixed 1:1 with 1% molten agarose solution at 42°C and quickly loaded before solidification into the phantom wells. All samples and their controls were OD matched using the Nanodrop prior to phantom loading, with the final concentration being OD_{500nm} = 2.2 for Ana GVs and OD_{600nm}= 1.0-1.5 for buoyant Nissle cells. Wells not containing sample were filled with plain 1% agarose. Hydrostatic collapse at 1.4 MPa was used to determine that the contribution to light scattering from GVs inside the cells was similar for those expressing the acoustic sensor gene and its wild-type counterpart. The phantom was placed in a custom holder on top of an acoustic absorber material and immersed in PBS to acoustically couple the phantom to the ultrasound imaging transducer.

Imaging was performed using a Verasonics Vantage programmable ultrasound scanning system and a L22-14v 128-element linear array Verasonics transducer, with a specified pitch of 0.1 mm, an elevation focus of 8 mm, an elevation aperture of 1.5mm and a center frequency of 18.5 MHz with 67% -6 dB bandwidth. Linear imaging was performed using a conventional B-mode sequence with a 128-ray-lines protocol. For each acquisition, a single pulse was transmitted with an aperture of 40 elements. For nonlinear image acquisition, a custom cross-amplitude modulation (x-AM) sequence detailed in (101) with an x-AM angle (θ) of 19.5° and an aperture of 65 elements were used. Both B-mode and x-AM sequences were programmed to operate close to the center frequency of the transducer (15.625 MHz) and the center of the sample wells were aligned to the set transmit focus of 5 mm. Each image was an average of 50 accumulations. B-mode images were acquired at a transmit voltage of 1.6V and a custom, automated voltage ramp imaging script (programmed in MATLAB) was used to sequentially toggle between B-mode and x-AM acquisitions. The script acquired x-AM signals at each specified voltage step immediately followed by a B-mode acquisition at 1.6V, before another x-AM acquisition at the next voltage step. For engineered Ana GVs subjected to *in vitro* protease assays, an x-AM voltage ramp sequence from 4V to 10V in 0.2V increments was used. For Nissle cells expressing GVs, an x-AM voltage ramp sequence from 7.5 to 25V in 0.5V increments was used. Samples were subjected to complete collapse at 25V with the B-mode sequence for 10 seconds, and the subsequent B-mode image acquired at 1.6V and x-AM image acquired at the highest voltage of the voltage ramp sequence was used as the blank for data processing. Each image was an average of 50 accumulations.

***In vivo* ultrasound imaging**

All *in vivo* experiments were performed on C57BL/6J male mice, aged 14–27 weeks, under a protocol approved by the Institutional Animal Care and Use Committee of the California Institute of Technology. No randomization or blinding were necessary in this study. Ultrasound imaging was performed as follows. Mice were anesthetized with 1–2% isoflurane, maintained at 37 °C on a heating pad, depilated over the imaged region, and imaged using an L22-14v transducer. For imaging of *E. coli* in the gastrointestinal tract, mice were placed in a supine position, with the ultrasound transducer positioned on the lower abdomen, transverse to the colon such that the transmit focus of 5 mm was close to the center of the colon lumen. Prior to imaging, buoyancy-enriched *E. coli* Nissle 1917 expressing ARG_{WT} or ASG_{ClpXP} were mixed in a 1:1 ratio with 4% agarose in PBS at 42 °C, for a final bacterial concentration of $1.5*10^9$ cells ml^{-1}. An 8-gauge needle was filled with the mixture of agarose and bacteria. Before it solidified, a 14-gauge needle was placed inside the 8-gauge needle to form a hollow lumen within the gel. After the agarose–bacteria mixture solidified at room temperature for 10 min, the 14-gauge needle was removed. The hollow lumen was then filled with the agarose–bacteria mixture expressing the other imaging reporter. After it solidified, the complete cylindrical agarose gel was injected into the colon of the mouse with a PBS back-filled syringe. For the colon imaging, B-mode images were acquired at 1.9V and x-AM images were acquired at 20V, with other parameters being the same as those used for *in vitro* imaging. B-mode anatomical imaging was performed at 7.4V using the 'L22-14v WideBeamSC' script provided by Verasonics.

Image processing and data analysis

All *in vitro* and *in vivo* ultrasound images were processed using MATLAB. Regions of interest (ROIs) were manually defined so as to adequately capture the signals from each sample well or region of the colon. The sample ROI dimensions (1.2 mm X 1.2 mm square) were the same for all *in vitro* phantom experiments. The noise ROI was manually selected from the background for each pair of sample wells. For the *in vivo* experiments, circular ROIs were manually defined to avoid edge effects from the skin or colon wall. For each ROI, the mean pixel intensity was calculated, and the pressure-sensitive ultrasound intensity ($\Delta I = I_{\text{intact}} - I_{\text{collapsed}}$) was calculated by subtracting the mean pixel intensity of the collapsed image from the mean pixel intensity of the intact image. The Contrast-to-Noise Ratio (CNR) was calculated for each sample well by taking the mean intensity of the sample ROI over the mean intensity of the noise ROI. The x-AM by B-mode ratio at a specific voltage was calculated with the following formula:

$$\frac{\Delta \mathrm{I}_{\mathrm{xAM}}(\mathrm{V})}{\Delta \mathrm{I}_{\mathrm{B-mode}}(\mathrm{V})}$$

where $\Delta \mathrm{I}_{\mathrm{xAM}}(\mathrm{V})$ is the pressure-sensitive nonlinear ultrasound intensity acquired by the x-AM sequence at a certain voltage V, and $\Delta \mathrm{I}_{\mathrm{B-mode}}(\mathrm{V})$ is the pressure-sensitive linear ultrasound intensity of the B-mode acquisitions at 1.6 V following the x-AM acquisitions at the voltage V. All images were pseudo-colored (bone colormap for B-mode images, hot colormap for x-AM images), with the maximum and minimum levels adjusted for maximal contrast, as indicated in the accompanying color bars.

Statistical analysis and replicates

Data is plotted as the mean ± standard error of mean (SEM). Sample size is N =3 biological replicates in all *in vitro* experiments unless otherwise stated. For each biological replicate, there were technical replicates to accommodate for technical variabilities e.g. sample loading and pipetting. SEM was calculated by taking the values for the biological replicates, which are the mean values of their technical replicates respectively. The numbers of biological replicates and technical replicates were chosen based on preliminary experiments, such that they would be sufficient to report significant differences in mean values. Individual data for each replicate is given in Supplementary Figs. X in the form of scatter plots. P values, for determining the statistical significance for the *in vivo* data, were calculated using a two-tailed unpaired Welch's t-test.

5.5 Supplementary figures and tables

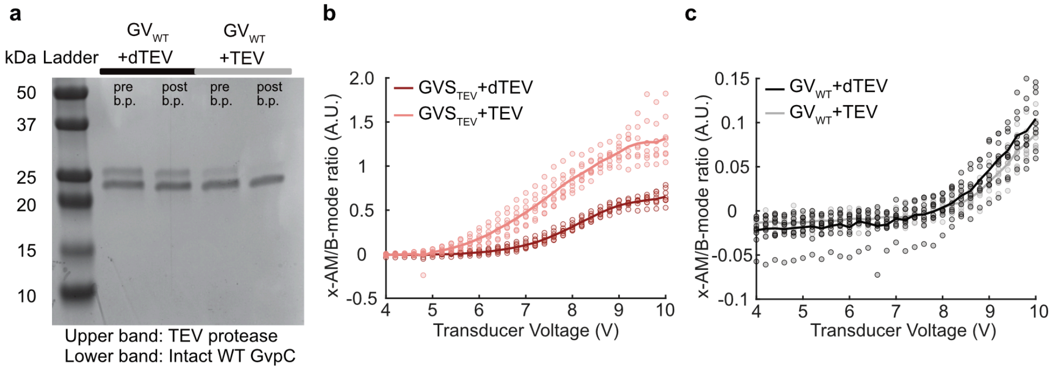

Figure 5-S1: Engineering an acoustic sensor of TEV endopeptidase activity. (**a**) SDS-PAGE analysis of OD_{500nm}-matched samples of GV_{WT} incubated with dTEV and TEV protease, before and after two rounds of buoyancy purification (pre and post b.p. respectively). (**b, c**) Scatter plots showing the ratio of nonlinear (x-AM) to linear (B-mode) ultrasound signal as a function of transducer voltage for all the replicate samples used in the x-AM voltage ramp imaging experiments for GVS_{TEV} (b) and GV_{WT} (c). Total number of replicates is 8 for GV_{TEV} and 9 for GV_{WT}. Solid line represents the mean of all the replicates.

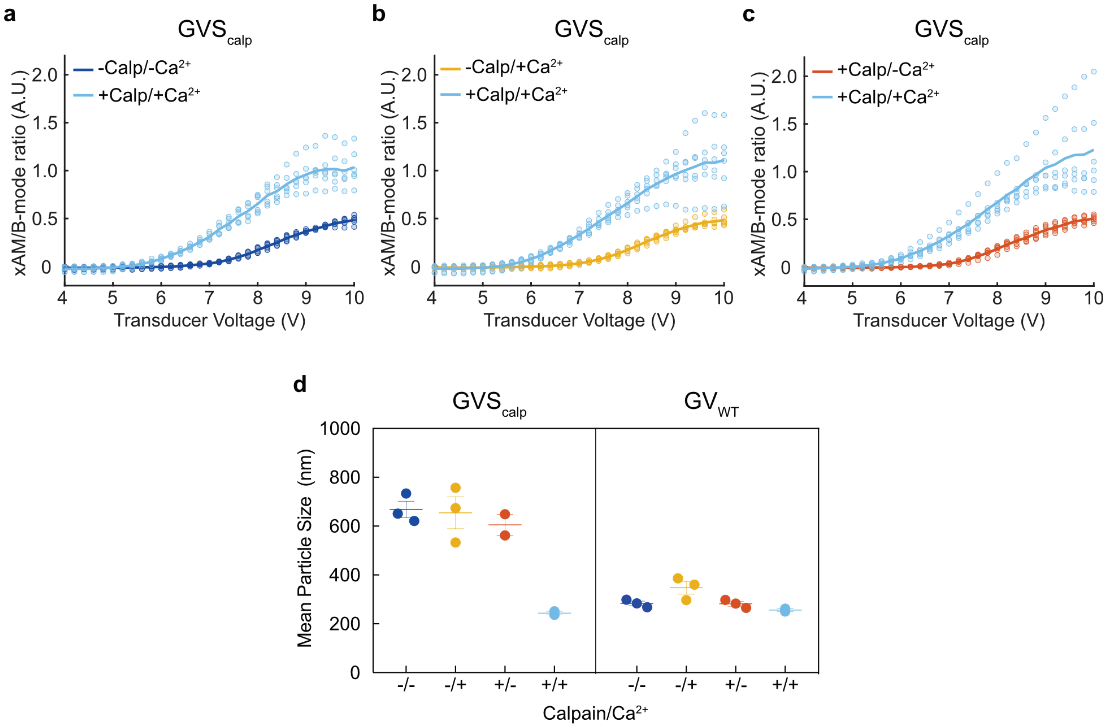

Figure 5-S2: Engineering an acoustic sensor of calpain activity. (**a**, **b**, **c**) Scatter plots showing the ratio of x-AM to B-mode ultrasound signal as a function of increasing transducer voltage for all the GVS$_{\text{calp}}$ replicate samples after incubation in the presence or absence of calpain and/or calcium. Total number of replicates is 6 for GVS$_{\text{calp}}$. (**d**) DLS measurements showing the average hydrodynamic radius of GVS$_{\text{calp}}$ and GV$_{\text{WT}}$ samples after calpain/calcium incubations (N ≥ 2 biological replicates, individual dots represent each N and horizontal line indicates the mean, error bars indicate SEM).

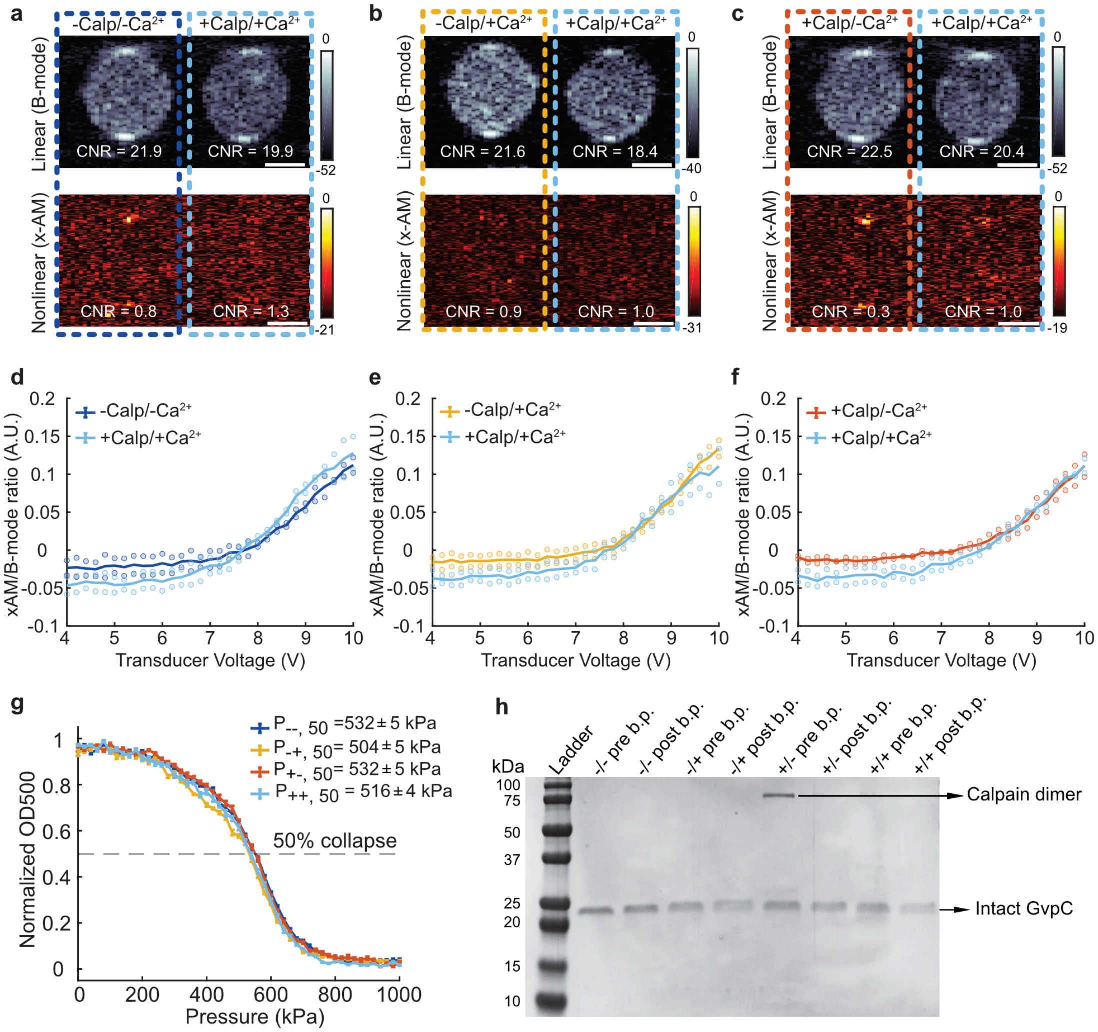

Figure 5-S3: Characterization of GV$_{WT}$ sample with calpain protease. (**a**, **b**, **c**) Representative ultrasound images of agarose phantoms containing GV$_{WT}$ incubated with and without calpain and/or calcium at OD$_{500nm}$ 2.2. The B-mode images were taken at 1.6V for **a**, **b** and **c** and the x-AM images corresponding to the maximum difference in non-linear contrast between the +calpain/+ calcium sample and the negative controls were taken at 7.2V for (a) and (b) and at 7V for (c). CNR stands for contrast-to-noise-ratio and color bars represent ultrasound signal intensity in the dB scale. Scale bars represent 1 mm. (**d**, **e**, **f**) Scatter plots showing the ratio of x-AM to B-mode ultrasound signal as a function of increasing transducer voltage for GV$_{WT}$ after incubation in the presence or absence of calpain and/or calcium (N=2). (**g**) Hydrostatic collapse curves of GV$_{WT}$ after incubations in the presence (+) or absence (-) of calpain and/or calcium. Data points are fitted to a Boltzmann sigmoid function, and the legend shows the midpoint of hydrostatic collapse for each condition, along with the 95% confidence interval values (N≥5) (**h**) SDS-PAGE analysis of OD$_{500nm}$-matched samples of GV$_{WT}$ incubated in the presence (+) or

absence (-) of calpain/calcium, before and after 2 rounds of buoyancy purification (pre and post b.p. respectively).

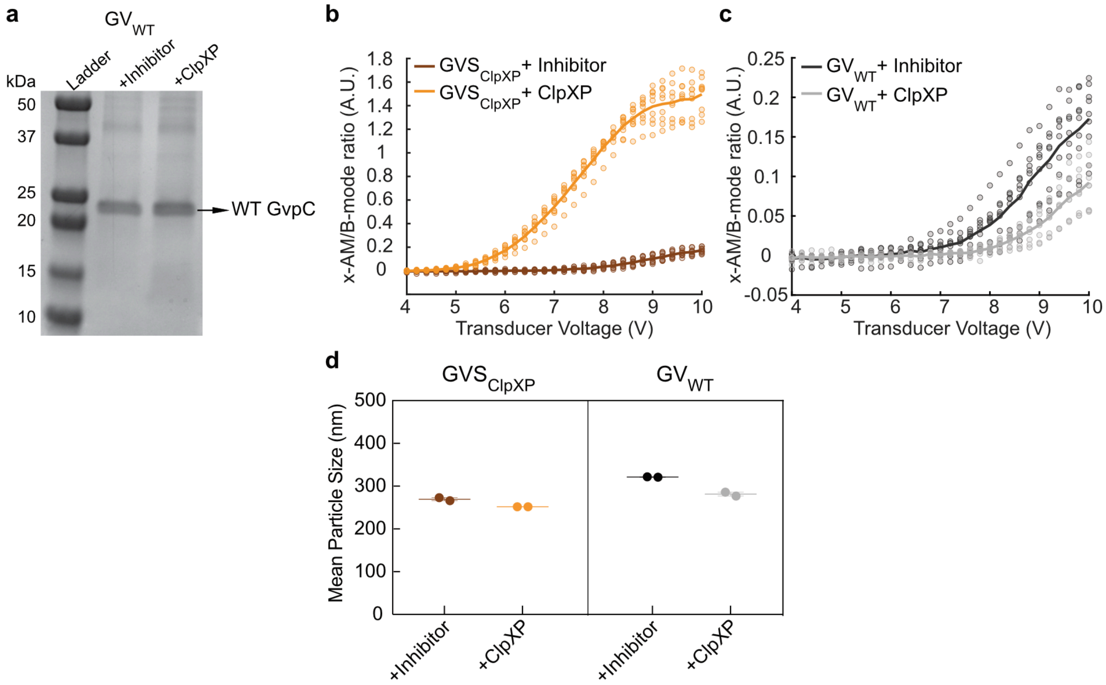

Figure 5-S4: Engineering an acoustic sensor of ClpXP proteolytic activity. (**a**) SDS-PAGE analysis of OD_{500nm}-matched GV_{WT} samples incubated in a reconstituted cell-free transcription-translation (TX-TL) system containing a protease inhibitor cocktail or ClpXP. (**b**, **c**) Scatter plots showing the ratio of x-AM to B-mode acoustic signal as a function of transducer voltage for all the replicate samples used in the x-AM voltage ramp experiments for GVS_{ClpXP} (b) and GV_{WT} (c). Total number of replicates is 9 for GVS_{ClpXP} GV_{WT}. (**d**) DLS measurements showing the average hydrodynamic radius of GVS_{ClpXP} and GV_{WT} samples after incubations with protease inhibitor or ClpXP (N = 2 biological replicates, individual dots represent each N and horizontal line indicates the mean, error bars indicate SEM)

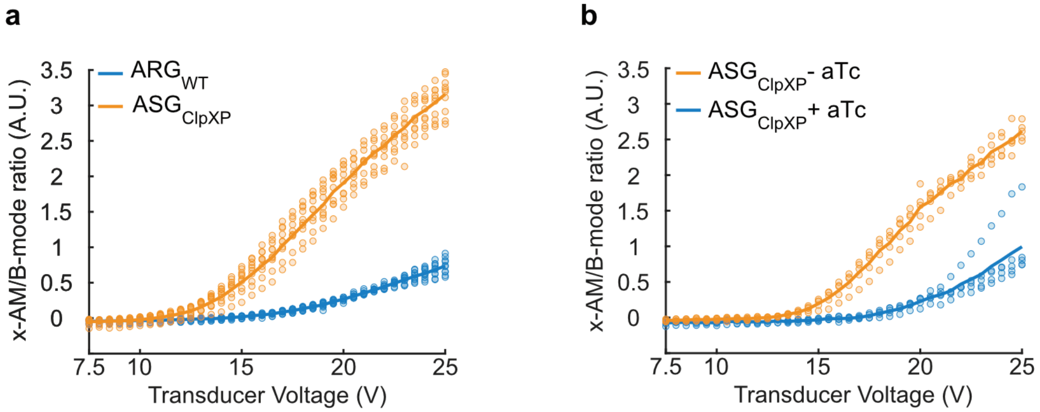

Figure 5-S5: Constructing intracellular ASGs for dynamic monitoring of protease activity and circuit-driven gene expression. (**a**, **b**) Scatter plots showing the ratio of x-AM to B-mode acoustic signal as a function of transducer voltage for all the replicate samples used in the x-AM voltage ramp experiments for Nissle cells expressing either ARG$_{\text{WT}}$ or ASG$_{\text{ClpXP}}$ (a) and Nissle cells expressing ASG$_{\text{ClpXP}}$, with or without aTc induction (b). Total number of replicates is 9 for (a) and 5 for (b).

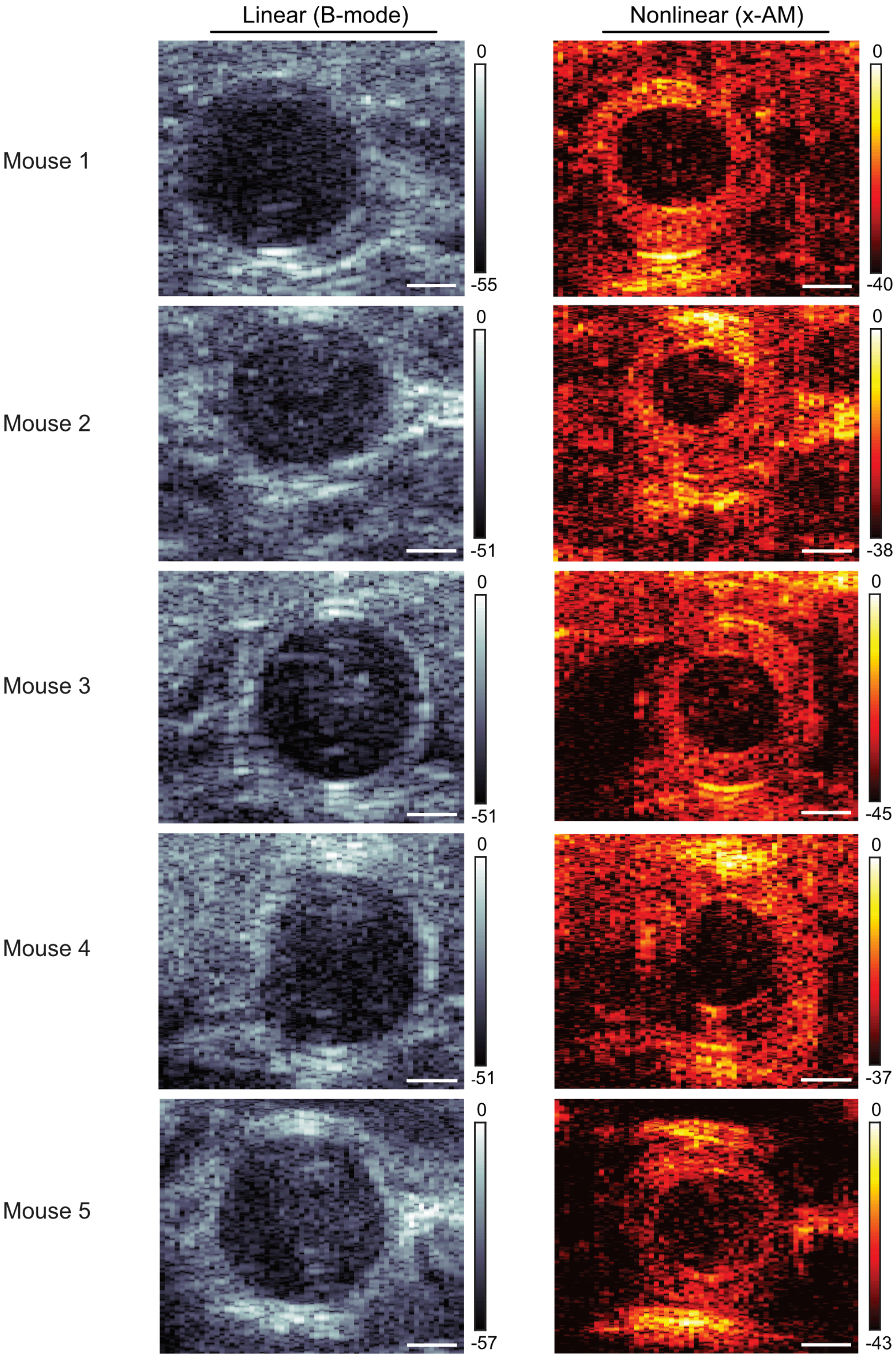

Figure 5-S6: Ultrasound imaging of ASGs in the GI tract of mice. Transverse ultrasound images of the colon for all mice used in the *in vivo* imaging experiments. *E.Coli* Nissle (ECN) cells expressing ARG_{WT} were at the center of the lumen and ECN expressing ASG_{ClpXP} were at the periphery of the lumen. Cells were injected at a final concentration of 1.5 * 10^9 cells/mL. Linear (B-mode) images were acquired at 1.9V and nonlinear (x-

AM) images of the colon were acquired at 20V. B-mode signal is displayed using the bone colormap and x-AM signal is shown using the hot colormap. Color bars represent B-mode and x-AM ultrasound signal intensity in the dB scale. Scale bars represent 1 mm.

Description/purpose of genetic construct	Plasmid Backbone	Transcriptional regulators	Output gene product(s)	Insertions/Tags (including linkers)	Resistance
WT Ana GvpC used as control for TEV/calpain sensor	pET28a	pT7, LacO	WT C-His Ana GvpC	SLE-His6 at C-terminus	Kanamycin
WT Ana GvpC used as control for ClpXP sensor	pET28a	pT7, LacO	WT N-His-Ana-GvpC	G-His6-SG at N-terminus	Kanamycin
Ana GvpC with TEV cleavage site	pET26b	pT7, LacO	C-His Ana GvpC with TEV cleavage site	SLE-His6 at C-terminus, GSGSGSG-ENLYFQG-SGSGSG in GvpC repeat 2	Kanamycin
Ana GvpC with calpain cleavage site	pET28a	pT7, LacO	C-His Ana GvpC with calpain cleavage site	SLE-His6 at C-terminus, GSGSG-QQEVYGMMPRD-GSGSG in GvpC repeat 2	Kanamycin
Ana GvpC with ssrA degradation tag	pET28a	pT7, LacO	N-His Ana GvpC with ssrA degradation tag	G-His6-SG at N-terminus, SG-AANDENYALAA at C-terminus	Kanamycin
ClpP plasmid for use in cell-free TX-TL system	pBEST	OR2-OR1-Pr	ClpP		Ampicillin
Original acoustic reporter gene construct (ARGWT)	pET28a	pT5, LacO	Ana GvpA, WT Ana GvpC, Mega GvpR-U		Kanamycin
Acoustic sensor gene for ClpXP (ASGClpXP)	pET28a	pT5, LacO	Ana GvpA, dGvpC, Mega GvpR-U	SG-AANDENYALAA at C-terminus	Kanamycin
WT Ana GvpC under Tet promoter	pTARA	pTet,TetO	WT Ana GvpC		Chloramphenicol

Supplementary table 5-T1: List and features of genetic constructs.

Chapter 6

ENGINEERING ACOUSTIC SENSORS WITH REVERSIBLE DYNAMICS FOR MOLECULAR ULTRASOUND IMAGING OF CALCIUM

6.1 Introduction

Understanding the neural circuits underlying human perception, cognition and behavior, and deciphering the pathological basis of neurological and psychiatric disease, is one of the biggest challenges in modern biology and medicine. Tackling this complex problem requires the development of tools and technologies to precisely observe neuronal activity (10, 18). Such tools should ideally provide high cellular and molecular specificity, with the ability to non-invasively cover large sections of the mammalian brain. An important molecular target for directly monitoring neuronal activity is calcium, as organellar and cytosolic free Ca^{2+} concentrations are among the most dynamic and important intracellular signals of neuronal activity and communication (19, 202, 203). The flux of calcium ions regulates processes ranging from neurotransmitter release, synaptic plasticity and memory formation to gene and protein regulation, cellular transport and cell death (204). Altered calcium flux and signaling is observed in many neurodegenerative disorders such as Alzheimer's and Parkinson's (205), as well as epilepsy (206), and psychiatric conditions such as bipolar disorder and schizophrenia (207). In addition, basal calcium concentration of 50-100 nM in resting state neurons can increase 10-100 fold during peak activity (202), providing a broad dynamic range for sensing.

Optical methods to visualize changes in neuronal calcium currently based on chemical or genetically encoded fluorescent indicators provide some of the most sensitive and spatiotemporally resolved measurements of neural activity (10, 11, 208). However, these approaches are fairly invasive, and typically require either dissection or surgery to provide optical access due to the poor penetration of light into deeper layers of tissue.

In contrast, ultrasound has good penetration depth and whole-organism access, but has been limited to imaging brain anatomy and neurovascular blood flow, as an indirect readout for cellular and molecular activity (209, 210). This is mainly due to the lack genetically-encodable acoustic reporters for direct visualization of molecular targets such as calcium. This limitation was partially addressed in Chapter 5, by engineering genetically encoded acoustic sensors of calcium-triggered calpain activity using gas vesicles (GVs). However, these calcium sensors rely on the irreversible enzymatic cleavage of GvpC for modulating the GV shell mechanics and nonlinear acoustic response, necessitating GV or GvpC re-expression over the timescale of a few hours for repeated sensing. For real-time monitoring of calcium transients that recur over shorter time-scales, it is desirable to have an acoustic sensor where the GV shell mechanics is dynamically modulated without irreversibly altering the GvpC sensing element.

Here, we describe how we have successfully engineered and characterized such an acoustic sensor, which relies on a temporary and reversible change in the conformation of GvpC to change the GV shell mechanics and produce an observable ultrasound signal upon molecular sensing of calcium. We conceptually designed our reversible acoustic sensor of calcium to harness the allosteric interaction between Ca^{2+}-activated calmodulin and its target peptide (referred to hereafter as calmodulin binding peptide or CBP), thereby building on the knowledge of almost two decades of engineering efforts for genetically encoded optical calcium indicators (19, 22, 23, 202, 203, 211-213). Calmodulin (CaM) is an extremely well-conserved, ubiquitously expressed protein consisting of 148 amino acids (~16.7 kDa), with a very high binding affinity and specificity for calcium (214-218). Each CaM molecule binds to 4 Ca^{2+} ions through its EF-hand motifs, with the C-terminal and N-terminal binding motifs having different Ca^{2+}-binding affinities (219-221). Ca^{2+} binding to inactive apocalmodulin causes it to undergo a conformational change, resulting in an exposition of hydrophobic patches on its surface that enable it to bind to a large variety of different target proteins with high affinity (214-218, 222). In contrast to the high degree of conservation of calmodulin throughout evolution, there is little homology in the primary structure of CBPs and calmodulin target sites (215, 223). Around 30 proteins have been identified with high binding affinity to CaM (Kd ~ nM), with CBPs identified from their calmodulin binding regions (214, 215, 222, 224-230). The common feature of these CBPs is the presence of an amphipathic helix of ~ 20 amino acids, containing 2-4 hydrophobic anchor residues often flanked by basic residues. The molecular interaction between Ca^{2+}-activated CaM and the one of its most well-known CBPs, i.e. M13 from skeletal muscle myosin light chain kinase, has been extensively characterized (231-234). **Figure 6-S1** shows the structure of inactive apocalmodulin, active CaM and the CaM-M13 peptide complex, which highlights the conformational changes that occur at each step.

In this chapter, we demonstrate the ability to engineer GVs that show a completely reversible dynamic change in their shell mechanics in the presence of calcium, which can be acoustically distinguished. Furthermore, we verify that these sensors are highly sensitive to calcium, with three variants showing unique response profiles spanning physiologically relevant intracellular calcium concentrations. These acoustic calcium sensors represent the next generation of biomolecular tools that give new molecular information content to ultrasound, thereby taking functional molecular imaging to new depths in biological tissue.

6.2 Results

6.2a Screening and identification of GvpC variants for engineering an allosteric calcium sensor using GVs

To engineer an allosteric calcium sensor using GVs, we constructed GvpC variants that were truncated to have only the first 3 out of 5 repeats in the wild-type sequence, with a calmodulin binding peptide (CBP) inserted in repeat 2 (**Fig. 6-1a**). Our hypothesis was that in the presence of calcium, activated calmodulin would change its conformation and bind to the CBP, thereby causing a conformational change of the engineered GvpC sequence. This would result in partial unfolding or detachment of GvpC from the GV surface, making the GV shell less stiff and allowing it to undergo increased nonlinear buckling deformations in response to ultrasound (**Fig. 6-1b**). Conversely, a decrease in calcium concentration would lead to unbinding of calmodulin from the CBP, dynamic reversal of the GvpC conformation to its original state, and turning off of nonlinear ultrasound contrast.

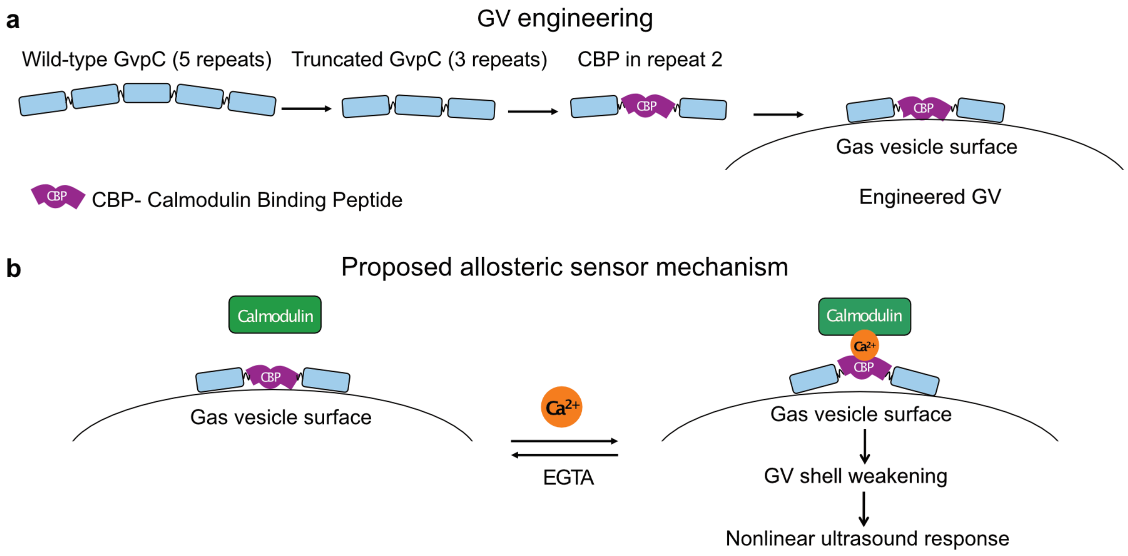

Figure 6-1: Engineering acoustic biomolecules for dynamic molecular imaging of calcium. (**a**) Schematic of the optimized GV engineering approach for dynamic imaging of calcium ions (Ca^{2+}). The wild-type GvpC from *Anabaena flos-aquae* (Ana GvpC) containing 5 repeats is modified to truncated version with 3 repeats along with insertion of a calmodulin binding peptide (CBP) in repeat 2. The recombinant GvpC is re-added to ΔGvpC Ana GVs to form an engineered GV that exposes CBPs on its outer surface. (**b**) Illustration of the proposed mechanism by which reversible acoustic sensing of calcium is achieved, based on allosteric binding of Ca^{2+}-bound calmodulin to the CBP on the engineered GV surface. Binding of calmodulin to the CBP leads to a conformational change of the GvpC, weakening its association with the GV shell and increasing the nonlinear response to ultrasound. Addition of a chelating agent such as EGTA leads to sequestering of the Ca^{2+} bound to the calmodulin, causing it to unbind from the CBP and allowing the GvpC to revert to its original state. This lowers the nonlinear acoustic response from engineered GVs to that observed in the Ca^{2+}-free state.

Based on this working hypothesis, we designed, cloned, expressed and screened ~ 30 Ana GvpC variants containing different CBPs on a ΔGvpC Ana GV backbone **(Fig. 6-2, a-b, Supplementary table 6-T1**). The hydrostatic collapse behavior of engineered GVs was measured after re-addition of CBP-containing GvpC and after incubations with or without Ca^{2+} and CaM using pressurized absorbance spectroscopy. This technique measures the optical density of GVs (which scatter 500 nm light when intact) under increasing hydrostatic pressure and provides a quick assessment of GV shell mechanics: GVs that collapse at lower pressure also produce more nonlinear ultrasound contrast. The truncated GvpC variant with three repeats (WT_{1-3}), used for insertion of different CBPs, was selected after preliminary rounds of screening with the CBP sequence from smooth muscle myosin light chain kinase (smMLCK) used in GCaMP (**Supplementary table 6-T2**). This peptide (CBP13) was inserted at different positions within the truncated or wild-type GvpC with or without flexible linker sequences of different lengths. Addition of even a short flexible G4S linker (Flsh) abrogated the ability of the GvpC variant to strengthen the GV shell (**Fig. 6-2c**). Designs with two serine residues spanning the CBP13 peptide did better in terms of strengthening the GVs, but did not show an appreciable calcium-dependent change in hydrostatic collapse (**Fig. 6-2d**). Initial designs also included two copies of CBP13 in different repeats of the wild-type GvpC sequence (CBP13-08 and 13-09, **Supplementary table 6-T2**). We observed that insertion of multiple CBP peptides greatly reduced their ability to strengthen the GV shell, thus reducing the dynamic range that could be potentially achieved for our acoustic sensor (**Fig. 6-2c**). We also observed that the truncated WT_{1-3} GvpC was able to strengthen the GVs to almost 90% of the level achieved by the wild-type sequence (**Fig 6-2, a,c**). Hence, we decided to go with the truncated GvpC for our sensor design, as it would enable more peptides to be displayed on the surface of each GV compared to the wild-type sequence, allowing greater modulation of the GV shell by activated calmodulin and a bigger change in the nonlinear ultrasound response. Using the truncated GvpC backbone, we inserted other calmodulin binding peptides (CBPs) in repeat 2. This strategy enabled us to identify two variants CBP1 and CBP2, that showed sufficient GV strengthening capacity, as well as a significant decrease in hydrostatic collapse of >150 kPa in the presence of Ca^{2+} and CaM (**Fig. 6-2, a-b**). CBP1 and CBP2 had calmodulin binding domains from skeletal muscle myosin light chain kinase and CaMKI respectively, and were chosen for further evaluation as discussed in the following sections.

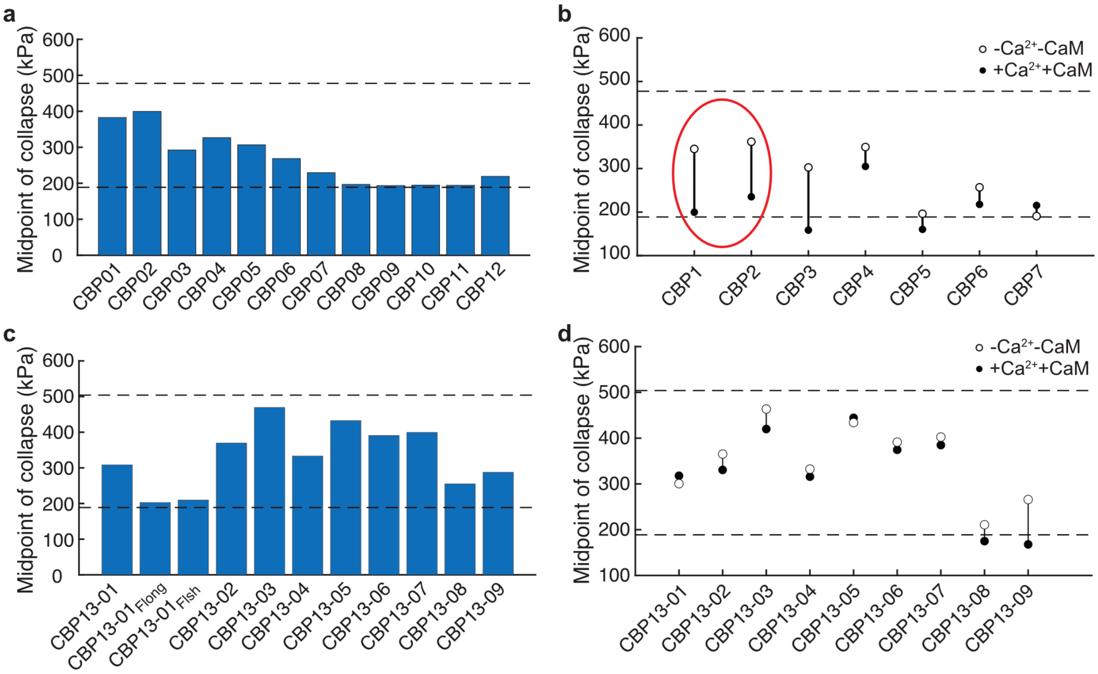

Figure 6-2: Screening of CBP-GvpC candidates for engineering allosteric sensors for dynamic acoustic imaging of calcium. (**a**) Screening of truncated GvpC variants containing different CBPs in their repeat 2 region, for their ability to strengthen ΔGvpC Ana GVs. (**b**) Screening of the best-performing variants in A in the presence and absence of calcium (Ca^{2+}) and calmodulin (CaM), for identifying those that show the maximum calcium-dependent change in collapse pressure. Lower and upper dashed lines in (a) and (b) indicate the average midpoint of collapse for ΔGvpC GVs and WT_{1-3} GVs (having the truncated GvpC with 3 repeats) respectively. (**c**) Screening of CBP13, for its ability to bind to and strengthen ΔGvpC Ana GVs. Variants include short flexible (flsh) and long flexible (flong) linker sequences flanking CBP13, as well as insertion of one or two copies of CBP at different positions on truncated or WT Ana GvpC. (**d**) Screening of the best-performing variants in (c) in the presence and absence of calcium (Ca^{2+}) and calmodulin (CaM), for identifying those that show the maximum calcium-dependent change in collapse pressure. Lower and upper dashed lines in A and B indicate the average midpoint of collapse for ΔGvpC Ana GVs and WT GVs (having the WT-GvpC with 5 repeats) respectively. Red oval indicates the two variants i.e. CBP1 and 2, that were chosen from all the screening experiments for further evaluation. For (a) to (d), the normalized optical density measurements at 500 nm (OD_{500nm}) are taken as a function of applied hydrostatic pressure for engineered GVs containing the GvpC variants. Midpoint of hydrostatic collapse is plotted for each variant by curve-fitting data points to a Boltzmann sigmoid function.

6.2b Evaluating calcium-specific response of engineered GV sensors

Engineered GVs containing GvpC with CBP1 and 2 were incubated in the presence or absence of 50 μM Ca^{2+} and CaM (in 5x molar excess to GvpC). Pressurized absorbance spectroscopy revealed that these engineered GVs showed a reproducible and substantial decrease in the midpoint of hydrostatic collapse of ~150 kPa, only when both Ca^{2+} and CaM were present (**Fig. 6-3, a-b**). In comparison, WT_{1-3} GvpC used as the negative control, did not show any change in hydrostatic collapse pressure upon addition of Ca^{2+} and CaM (**Fig. 6-3c**). Additionally, the calcium-dependent binding of CaM to the engineered GVs was evaluated by subjecting the incubated samples to four stringent rounds of washing by centrifugally-assisted buoyancy purification and removal of subnatant after each round, followed by running the concentrated GV samples on a denaturing polyacrylamide gel (SDS-PAGE). A band at ~16 kDa corresponding to calmodulin was only observed when Ca^{2+} was present, confirming the calcium-dependent CaM-CBP interaction (**Fig. 6-3d**).

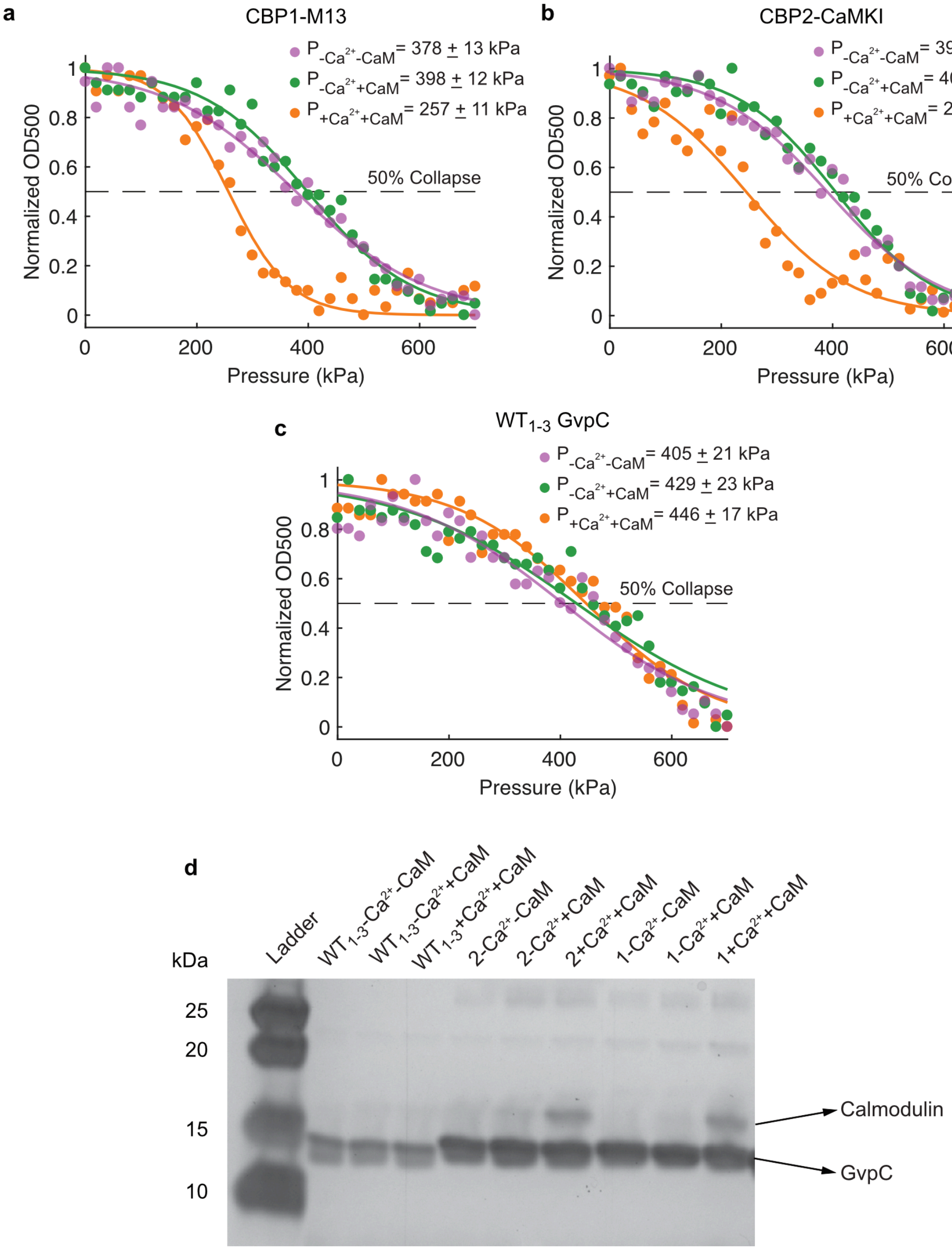

Figure 6-3: Calcium-specific response of engineered GVs. (**a, b, c**) Normalized optical density measurements at 500 nm (OD_{500nm}) as a function of applied hydrostatic pressure for engineered GVs incubated in the presence (+) or absence (-) of calmodulin and/or calcium, with their GvpC containing CBP1- the M13 peptide from skeletal muscle myosin light chain kinase (a), CBP2- a calmodulin binding peptide from CaMKI (b), or WT_{1-3} used as the negative control (c). Data points are fitted to a Boltzmann sigmoid function, and the legend shows the midpoint of hydrostatic collapse for each condition, along with the 95%

confidence interval values. (**d**) SDS-PAGE analysis of engineered GVs (with CBP1, CBP2 or WT$_{1-3}$ GvpC) incubated in the presence (+) or absence (-) of calmodulin and/or calcium, after four rounds of centrifugally-assisted buoyancy purification.

6.2c Testing reversibility of calcium-dependent change in GV shell mechanics

Engineered GVs containing truncated GvpC with CBP1 or 2 were further characterized for reversibility in the sensor dynamics. This was done by incubating the GVs in the presence or absence of Ca^{2+} and CaM, and subsequently adding an excess of EGTA to sample containing calcium to sequester the divalent Ca^{2+} ions in the solution. This would lead to unbinding of CaM from the CBP-GvpC and allow it to revert back to its original confirmation, thereby re-strengthening the GV shell and causing a rebound of the collapse pressure midpoint towards the value observed in the absence of calcium. Indeed, we observed that EGTA addition to GV samples incubated with Ca^{2+} and CaM led to an almost complete recovery of the hydrostatic collapse profile, close to that observed in the absence of calcium (**Fig. 6-4, a-b**).

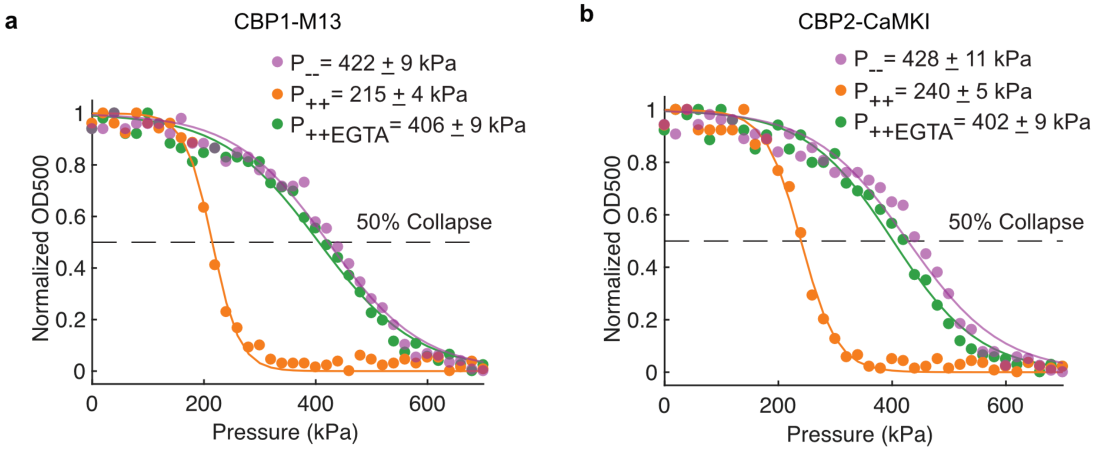

-- : without Ca^{2+} and calmodulin, ++ : with Ca^{2+} and calmodulin, ++EGTA: after addition of EGTA (Ca^{2+} chelator) to the ++ sample

Figure 6-4: Reversibility of calcium-dependent change in GV shell mechanics. (**a, b**) Hydrostatic collapse profiles of engineered GVs with GvpC containing CBP-1 (a) or CBP2 (b), after incubations in the presence (+) or absence (-) of calmodulin (CaM) and calcium, as well as after addition of a Ca^{2+}- chelator (EGTA) to the sample with Ca^{2+} and CaM. Data points are fitted to a Boltzmann sigmoid function, and the legend shows the midpoint of hydrostatic collapse for each condition, along with the 95% confidence interval values.

6.2d Acoustic characterization of engineered GVs with reversible dynamics for calcium imaging

Next, we wanted to determine if the changes observed in the GV shell mechanics during hydrostatic collapse measurements would translate to a robust and discernable difference in the nonlinear ultrasound response. For this purpose, engineered GVs containing CBP 1 or 2 in their GvpC sequence were incubated in the presence or absence of Ca^{2+} and CaM, matched to similar optical densities (OD_{500nm}), and loaded into agarose phantoms for ultrasound imaging. Additional GV samples were loaded after incubations with both Ca^{2+} and CaM, followed by EGTA addition to reverse the calcium-dependent decrease in GV shell stiffness. Nonlinear imaging was performed using a recently established custom cross-amplitude modulation (x-AM) technique (101), while linear images were acquired using a conventional B-mode pulse sequence.

As expected based on collapse pressure results, GV samples incubated with both Ca^{2+} and CaM produced a strong increase nonlinear ultrasound contrast of over 10 dB in comparison to the negative controls without Ca^{2+} and/or CaM, for similar levels of linear signal across all samples (**Fig. 6-5, a-b**). Furthermore, the nonlinear contrast enhancement disappeared upon addition of EGTA for both CBP1 and 2 containing GVs, confirming the reversible dynamics of the genetically encoded acoustic calcium sensor (**Fig. 6-5, a-b**). Consistent with the pressure-dependent nonlinear buckling response of the GV shell, the differential nonlinear contrast from GVs with Ca^{2+} and CaM was confirmed by x-AM voltage ramp imaging experiments. x-AM images were taken at increasing voltages, immediately followed by a B-mode image at 1.6V after each x-AM voltage step. The nonlinear signal normalized to the linear GV signal showed a steep increase as a function of transducer voltage for both tested variants with Ca^{2+} and CaM beyond 4V, which levelled off beyond 8.5V owing to GV collapse at higher voltages (**Fig. 6-5, c-d**). In contrast, the nonlinear acoustic response from samples with EGTA was in the baseline range observed for the negative controls at all imaging voltages. Interestingly, the $-Ca^{2+}$ +CaM GV samples showed a marginally higher nonlinear buckling response compared to the other negative controls. A possible explanation for this would be the diffusion of negligible amounts of calcium from the + Ca^{2+} sample wells during the imaging session, or low-levels of non-specific binding of CaM to the engineered GVs.

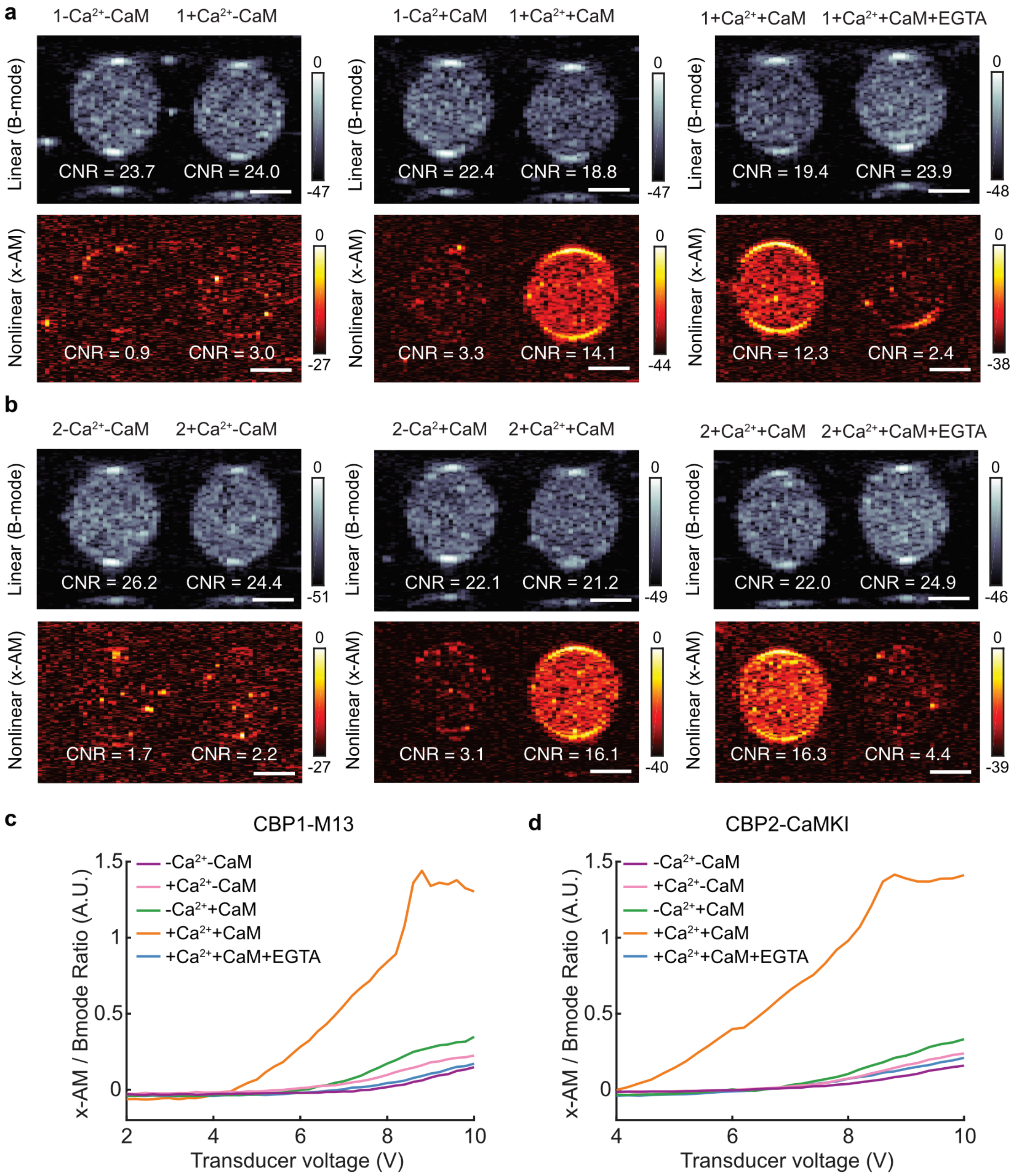

Figure 6-5: Acoustic characterization of engineered GVs with reversible dynamics for calcium imaging. (**a, b**) Representative ultrasound images of agarose phantoms containing

engineered GVs with CBP1 (A) or CBP2 (B), incubated in the presence (+) or absence (-) of calcium (Ca^{2+}), calmodulin (CaM) and/or EGTA at OD_{500nm} 2.2. The linear (B-mode) images were acquired at 1.6V for (a) and (b) and the nonlinear (x-AM) images were acquired at 6.2V for (a) and at 6.8V for (b). CNR stands for contrast-to-noise-ratio and color bars represent ultrasound signal intensity in the dB scale. Scale bars represent 1 mm. (**c, d**) Ratio of x-AM to B-mode ultrasound signal as a function of increasing transducer voltage for engineered GVs with CBP1 (c) or CBP2 (d), after incubation in the presence or absence of calcium (Ca^{2+}), calmodulin (CaM) and/or EGTA.

6.2e Determining sensitivity thresholds for allosteric calcium sensors

Following the promising ultrasound imaging results for the reversible acoustic calcium sensor, we examined the effect of calcium concentration on the hydrostatic collapse of these engineered GV variants. As intracellular calcium transients typically range from 100 nM to ~ 10s of μM in neurons (202), we performed a titration of calcium concentrations from 100 nM-100 μM, using a Tris buffer containing EDTA and EGTA to ensure no free Ca^{2+} at the zero baseline concentration. $CaCl_2$ stock solution was spiked in, such that the final [Ca^{2+}], added in excess of the chelators present in the reaction buffer, is as shown in **Figure 6-6**. Both engineered GV variants showed a calcium dose-dependent response, with a different sensitivity threshold for each variant. Engineered GVs with CBP1-GvpC displayed a calcium-dependent collapse pressure reduction in the low μM range, with a saturation of response between 10-100 μM (**Fig. 6-6a**). In contrast, GVs with CBP2-GvpC had a higher threshold for calcium response, with a sharp drop in collapse pressure observed ~10 μM (**Fig. 6-6b**). These results establish the ability of these engineered acoustic sensors to non-invasively image physiologically relevant changes in intracellular calcium. Future work will include additional characterization, by carefully titrating free calcium concentrations in the reaction mixture down to the sub-micromolar range, to determine the minimum limit of detection of the sensors.

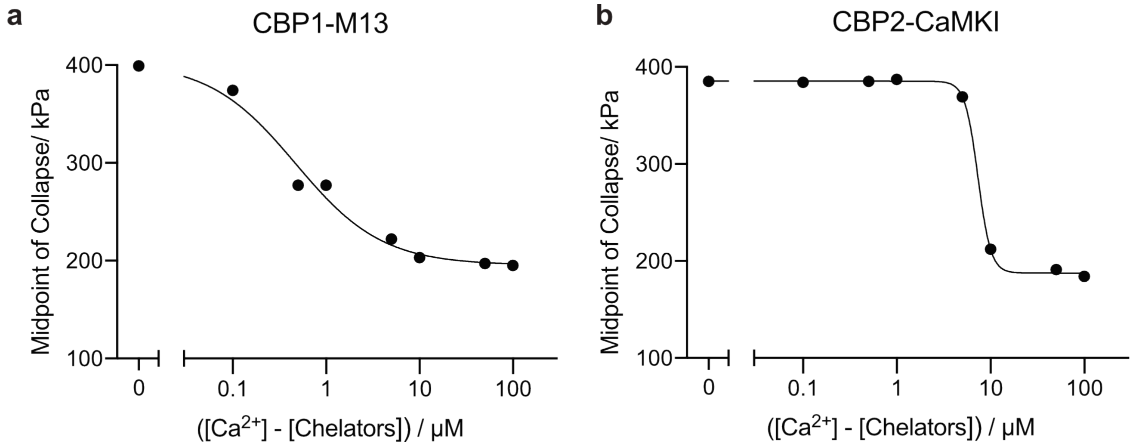

Figure 6-6: Effect of calcium concentration on the collapse of engineered GVs. (**a, b**) Midpoint of hydrostatic collapse as a function of calcium concentration (amount added in excess of chelators / µm) for engineered GVs with CBP1 (a) or CBP2 (b), after incubations in the presence of calmodulin and calcium. The midpoint of collapse corresponds to a 50% reduction in the optical density of the GV sample at 500 nm (OD_{500nm}). Midpoints are calculated based on curve-fitting of data points to a Boltzmann sigmoid function.

6.3 Conclusion and Outlook

The results of this study demonstrate, for the first time, the feasibility of constructing a genetically encoded calcium sensor with reversible dynamics for ultrasound. This approach opens up myriad opportunities for non-invasive functional molecular imaging at significant depths within biological tissues and intact organisms. To achieve this result, we leveraged the allosteric interaction between Ca^{2+}-activated calmodulin and its target peptides, to reversibly modulate the nanoscale mechanics and nonlinear acoustic response of GVs. By screening a wide variety of CBPs in different configurations within wild-type and truncated Ana GvpC, we were able to identify and engineer multiple GV sensors that display a calcium-specific change in acoustic response, with a sensitivity and dynamic range spanning physiologically relevant Ca^{2+} concentrations in the low µM range.

The two best-performing CBPs identified in this study, i.e. CBP1 and CBP2, come from skeletal muscle myosin light chain kinase (sk-MLCK) and calmodulin-dependent protein kinase (CaMKI) (**Supplementary table 6-T1**). Both these CBPs are able to provide a significant calcium-triggered enhancement in nonlinear acoustic contrast of more than 10 dB, which is fully reversible upon removal of free Ca^{2+} using a chelator such as EGTA. Interestingly, engineered GVs containing CBP1 and CBP2 show different sensitivity thresholds for calcium, which is likely correlated with the differential binding affinities of these CBPs on the GV surface to Ca^{2+}-activated calmodulin. The Ca^{2+}-activation of CaM and its subsequent binding to its target peptide depends on many factors, including the local molecular context and proximity of the CBP to the CaM, the concentration of calcium and calmodulin, and the 3-D structural conformation and accessibility of the CBP sequence for the interaction with CaM (214-216, 224, 231). Furthermore, some calmodulin binding peptides have been shown to have much lower CaM affinities within the parent protein, compared to the isolated peptide sequence. For example, the K_d of the CaM-kinase complex is reported to be 30 nM, compared with ~ 1pM for the CaM-CBP2 complex (224). In contrast, similar apparent K_d values of ~ 1 nM have been reported for CaM-CBP1 and CaM-skMLCK (217, 218, 234). In our engineered acoustic sensors, CBP1 and CBP2 are not present in isolated form on the GVs, but inserted into a GvpC backbone. This might explain why CBP1-GvpC responds to lower levels of free Ca^{2+} compared to CBP2-GvpC, even though CBP2 in its isolated form seems to have a higher binding affinity for activated CaM. The calcium titration experiments also show that it is possible to tune the sensitivity of the acoustic calcium sensor by changing the CBP sequence on the GvpC.

The design and engineering approach presented here could be extended to build GV sensors for other physiologically important molecules and targets other than calcium. While we use exogenously supplied calmodulin for proof-of-concept testing and validation of these reversible allosteric calcium sensors *in vitro*, we anticipate eventually expressing these genetically encodable acoustic calcium sensors inside mammalian cells that have endogenous calmodulin, typically in the μM range (218, 235). While the levels of endogenous calmodulin should be sufficient for allosterically actuating the GV sensor to observe a nonlinear acoustic response, alternate strategies include transient overexpression of calmodulin in the target cells to be imaged or genetic engineering of GVs to incorporate CaM as a fusion to GvpC, in order to have all the sensor components attached to the GV shell backbone. As a starting point for this, we used a truncated GvpC variant containing just the first repeat region and fused M13 and CaM to its N-terminus and C-terminus respectively, similar to the design strategy used for GCaMP and its derivatives (**Fig. 6-S2, a-b**). While the single repeat GvpC was able to bind to and strengthen ΔGvpC Ana GVs, fusion of both M13 and CaM abrogated its ability to bind to the GV surface (**Fig. 6-S2c**). Follow-up work could evaluate fusions of M13 and CaM to GvpC variants containing more repeats, such as WT_{1-3} or WT-GvpC, using appropriate linkers to allow the engineered variant to bind to and strengthen GVs.

The dynamic change in nonlinear response of greater than 10 dB observed for these reversible GV sensors should enable robust detection for *in vivo* imaging applications. However, there is scope for further improving this by directed evolution and genetic engineering of GVs with higher collapse pressure thresholds in the ‘off’ or ‘no Ca^{2+}’ state. This will enable screening of variants that provide an even higher calcium-triggered change in collapse pressure, paving the way for more sensitive sensors that respond to more subtle changes in calcium concentration from baseline levels.

Future work will include more detailed characterization of the promising sensor variants identified in this study, including the exact molecular mechanics underlying their actuation, and kinetic assays to determine the sensor response rate. Since these acoustic sensors show fully reversible dynamics that involve non-destructive deformations of the GV shell, they could potentially be used for temporal monitoring of calcium oscillations or recurring changes in calcium flux. *In vivo* model systems such as *Xenopus* oocytes would be a great platform to further evaluate the performance of optimized sensor variants and perform single cell acoustic calcium imaging. The large size of the oocyte would allow engineered GVs and purified CaM or their encoding DNA/mRNA to be microinjected without adversely affecting cell function (236). Calcium waves or oscillations can also be induced in *Xenopus* oocytes under various conditions (236).

This study establishes the foundation to engineer nanoscale acoustic biomolecules for dynamic and functional non-invasive imaging of biologically relevant targets, such as calcium. The development of genetically encoded calcium indicators such as GCaMP provided optical imaging with new tools to track functional connectivity and activity patterns of cells within transparent model systems and optically-accessible tissues. Similarly, we anticipate that our newly developed acoustic sensors will endow ultrasound with superior capabilities for functional cellular and molecular sensing *in vivo*, paving the way for a deeper understanding and monitoring of fundamental physiology, neural circuitry and disease processes in living organisms.

6.4 Methods

Design and cloning of genetic constructs

All GvpC gene sequences codon optimized for *E.Coli* expression were inserted into a pET plasmid via Gibson Assembly or KLD Mutagenesis using enzymes from New England Biolabs and custom primers from Integrated DNA Technologies. The wild-type GvpC sequence was first truncated to form $WT_{1\text{-}3}$ GvpC containing 3 repeats. This was used as the template for KLD mutagenesis, in order to insert the calmodulin binding peptides (CBPs) in repeat 2 by substitution-insertion. Plasmid constructs were cloned into NEB Turbo *E. Coli* (New England Biolabs) for amplification, purified and sequence-validated before use.

Sample buffer preparation

To avoid precipitation of free calcium in the solution as calcium phosphate, a phosphate-free Tris buffer containing 20 mM Tris-HCl and 150 mM NaCl (pH 7.3) was used for all the experimental procedures in this study, including dilution and preparation of engineered GVs, *in vitro* biochemical assays and agarose phantom preparation for ultrasound imaging.

Preparation of engineered GVs

Gas vesicles from *Anabaena flos-aquae* (Ana GVs) were expressed, purified, stripped of their native GvpC and quantified using pressure-sensitive OD at 500 nm (OD_{500nm}) using the protocols described in Chapters 2, 3 and Appendix A. CBP-containing GvpC variants were expressed in BL21(DE3), purified from inclusion bodies and quantified according to earlier described procedures (237). Recombinant GvpC was added to stripped Ana GVs (pre-diluted to OD_{500nm} of 1.1 in 6M urea) in a 3x molar excess determined after accounting for 1:25 binding ratio of GvpC:GvpA, as described earlier. The only difference in the GvpC re-addition protocol to the ΔGvpC GVs was the use of Tris buffer for dialysis instead of PBS. Engineered GVs were purified using centrifugally-assisted floatation at 300g for 3-4h to remove excess unbound GvpC and resuspended in Tris buffer before quantification.

Pressurized absorbance spectroscopy

GVs were diluted in Tris buffer to an OD_{500nm} ~ 0.2-0.3 and 400 μL of the diluted sample was loaded into a flow-through quartz cuvette with a pathlength of 1 cm (Hellma Analytics). A 1.5-MPa nitrogen gas source was used to apply hydrostatic pressure in the cuvette through a single valve pressure controller (PC series, Alicat Scientific), while a microspectrometer (STS-VIS, Ocean Optics) measured the optical density of the sample at 500 nm. The hydrostatic pressure was increased from 0 to 700 kPa in 20kPa increments with a 7-s equilibration period at each pressure before measurement of the optical density. Each set of optical density measurements was normalized by scaling to the Min-Max measurement value, and the data was fitted using the Boltzmann sigmoid function $f(p) = \left(1 + e^{(P-P_c)/\Delta P}\right)^{-1}$, with the midpoint of normalized optical density change P_c as well as the 95% confidence intervals (rounded to the nearest integer) reported in the figures.

Denaturing polyacrylamide gel electrophoresis (SDS-PAGE)

Purified GVs were matched to similar optical densities and mixed 1:1 with 2x Laemmli buffer (Bio-Rad), containing SDS and 2-mercaptoethanol. The samples were then boiled at 95°C for 5 minutes and loaded into a pre-made polyacrylamide gel (Bio-Rad) immersed in 1x Tris-Glycine-SDS Buffer (Bio-Rad). 10 uL of Precision Plus Protein™ Dual Color Standards (Bio-Rad) was loaded as the ladder. Denaturing gel electrophoresis was performed at 120V for 55 minutes, after which the gel was washed in DI water for 15 minutes to remove excess SDS and stained for 1 hour in a rocker-shaker using the SimplyBlue SafeStain (Invitrogen). The gel was allowed to de-stain overnight in DI water, before imaging using a Bio-Rad ChemiDoc^{TM} imaging system.

***In vitro* biochemical assays**

Recombinant human calmodulin (Enzo Life Sciences) supplied as a lyophilized powder was dissolved in Tris buffer to a concentration of 1 mg/mL and used for all the biochemical assays. Calcium chloride (Sigma) was prepared as a 500 mM stock solution and diluted as necessary in Tris buffer for the incubation experiments. EGTA was prepared as a 100 mM stock solution in water, and the pH was adjusted to 7.3 using NaOH.

For the screening experiments in Fig. 6-2, engineered GVs at $OD_{500nm} = 0.4$ were incubated for 6 hours at room temperature in the absence or presence of mM levels of Ca^{2+} (to guarantee calcium saturation) and calmodulin in 2-10 molar excess of the amount of CBP-GvpC in the incubation mixture. 1 mM EDTA and EGTA were added to the Tris buffer to ensure that the baseline Ca^{2+} levels were 0, before spiking in calcium such that the final concentration of free Ca^{2+} was between 1-5 mM.

For hydrostatic collapse and SDS-PAGE assays in Fig. 6-3 and Fig 6-S3, GVs at $OD_{500nm} =$ 0.4 were incubated for 5 hours at room temperature in the presence or absence of 50 μM Ca^{2+} and calmodulin in 5x molar excess of the amount of CBP-GvpC in the reaction mixture. For the SDS-PAGE analysis, incubated GVs were subjected to four rounds of centrifugally-assisted buoyancy purification, with subnatant removal after each round to get rid of excess or free calmodulin that is unbound or non-specifically bound to the GVs. For the ++ samples, GV resuspension was done in the presence of 50 μM Ca^{2+} after each round of purification, in order to maintain the same calcium concentration used for the incubations. GVs were subsequently concentrated to a small volume of 5-10 uL and OD_{500nm}-matched before mixing with 2x Laemmli buffer for gel electrophoresis.

For reversibility assays in Fig. 6-4, GVs at OD_{500nm} = 0.8 were incubated for 5 hours at room temperature in the presence or absence of 50 μM Ca^{2+} and calmodulin in 3x molar excess of the amount of CBP-GvpC in the incubation mixture. For testing reversibility of calcium-dependent changes to GV shell mechanics, 2.5 mM EGTA was subsequently added to the ++ sample and incubation was allowed to continue for an additional 3 hours before collapse pressure measurements.

For the ultrasound imaging experiments in Fig. 6-5, GVs at OD_{500nm} = 2.5 were incubated for 5 hours at room temperature in the presence or absence of 100 μM Ca^{2+} and calmodulin in 3x molar excess of the amount of CBP-GvpC in the incubation mixture. For testing reversibility of calcium-dependent changes to GV acoustic response, 5 mM EGTA was subsequently added to the ++ sample and incubation was allowed to proceed for an additional 3 hours before concentrating the GVs, OD-matching and loading into the agarose phantoms.

For the calcium titration experiments in Fig. 6-6, GVs at OD_{500nm} = 0.4 were incubated for 5 hours at room temperature in the presence of varying concentrations of Ca^{2+} (0 - 100 μM) and calmodulin in 10x molar excess of the concentration of CBP-GvpC in the incubation mixture. 250 μM EDTA and EGTA were added to the Tris buffer to ensure that the free Ca^{2+} levels were 0, before spiking in calcium such that the final concentration of free Ca^{2+} was between 0-100 μM.

***In vitro* ultrasound imaging**

Imaging phantoms were prepared by melting 1% agarose (w/v) in Tris buffer and casting wells using a custom 3-D printed template mold (containing a 2-by-2 grid of cylindrical wells with 2 mm diameter and 1mm spacing between the outer radii in the bulk material). GV samples were matched to OD_{500nm} = 4.4 after *in vitro* incubations, mixed 1:1 with 1% molten agarose in Tris at 42°C and quickly loaded before solidification into the phantom wells. Wells not containing sample were filled with plain 1% agarose. The phantom was placed in a custom holder on top of an acoustic absorber material and immersed in PBS to acoustically couple the phantom to the ultrasound imaging transducer.

Imaging was performed using a Verasonics Vantage programmable ultrasound scanning system and a L22-14v 128-element linear array Verasonics transducer, with a specified pitch of 0.1 mm, an elevation focus of 8 mm, an elevation aperture of 1.5mm and a center frequency of 18.5 MHz with 67% -6 dB bandwidth. Linear imaging was performed using a conventional B-mode sequence with a 128-ray-lines protocol. For each acquisition, a single pulse was transmitted with an aperture of 40 elements. For nonlinear image acquisition, a custom cross-amplitude modulation (x-AM) sequence detailed in (101) with an x-AM angle (θ) of 19.5° and an aperture of 65 elements were used. Both B-mode and x-AM sequences were programmed to operate close to the center frequency of the transducer (15.625 MHz) and the center of the sample wells were aligned to the set transmit focus of 5 mm. Each image was an average of 50 accumulations. B-mode images were acquired at a transmit voltage of 1.6V and a custom, automated voltage ramp imaging script (programmed in MATLAB) was used to sequentially toggle between B-mode and x-AM acquisitions. The script acquired x-AM signals at each specified voltage step immediately followed by a B-mode acquisition at 1.6V, before another x-AM acquisition at the next voltage step. An x-AM voltage ramp sequence starting at 2V or 4V and ending at 10V in 0.2V increments was used. Samples were subjected to complete collapse at 25V with the B-mode sequence for 10 seconds, and the subsequent B-mode image acquired at 1.6V and x-AM image acquired at the highest voltage of the voltage ramp sequence was used as the blank for data processing.

Image processing and data analysis

Ultrasound images were processed using MATLAB. Regions of interest (ROIs) were manually defined so as to adequately capture the signals from each sample well or region of the colon. The sample ROI dimensions (1.2 mm X 1.2 mm square) were the same for all *in vitro* phantom experiments. The noise ROI was manually selected from the background for each pair of sample wells. For each ROI, the mean pixel intensity was calculated, and the pressure-sensitive ultrasound intensity ($\Delta I = I_{\text{intact}} - I_{\text{collapsed}}$) was calculated by subtracting the mean pixel intensity of the collapsed image from the mean pixel intensity of the intact image. The Contrast-to-Noise Ratio (CNR) was calculated for each sample well by taking the mean intensity of the sample ROI over the mean intensity of the noise ROI. The x-AM by B-mode ratio at a specific voltage was calculated with the following formula:

$$\frac{\Delta \mathrm{I}_{\mathrm{xAM}}(\mathrm{V})}{\Delta \mathrm{I}_{\mathrm{B-mode}}(\mathrm{V})}$$

where $\Delta \mathrm{I}_{\mathrm{xAM}}(\mathrm{V})$ is the pressure-sensitive nonlinear ultrasound intensity acquired by the x-AM sequence at a certain voltage V, and $\Delta \mathrm{I}_{\mathrm{B-mode}}(\mathrm{V})$ is the pressure-sensitive linear ultrasound intensity of the B-mode acquisitions at 1.6 V following the x-AM acquisitions at the voltage V. All images were pseudo-colored (bone colormap for B-mode images, hot colormap for x-AM images), with the maximum and minimum levels adjusted for maximal contrast, as indicated in the accompanying color bars.

6.5 Supplementary figures and tables

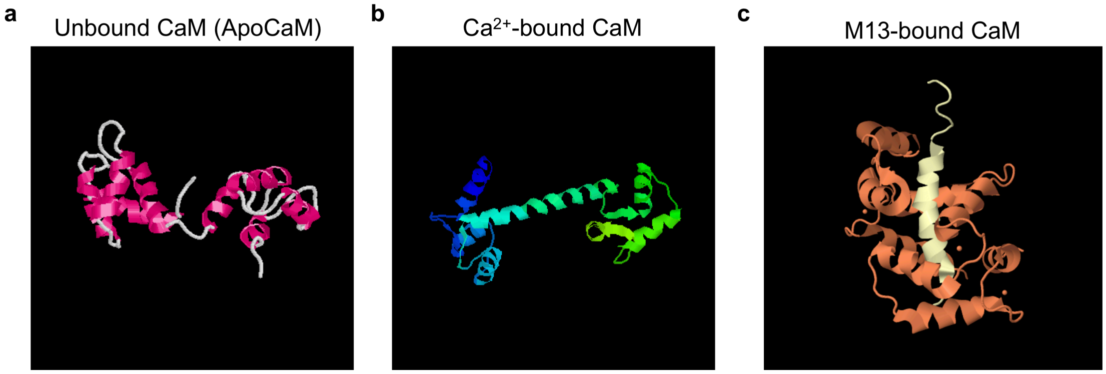

Figure 6-S1: Illustration of the allosteric interactions of calmodulin. (**a**) 3-D conformational model of unbound calmodulin (CaM) or apocalmodulin (**b**) 3-D conformational model of Ca^{2+}-bound calmodulin. (**c**) 3-D conformational model of Ca^{2+}-activated CaM bound to its target peptide M13. Structures are from the RCSB Protein Data Bank, rendered in PyMOL.

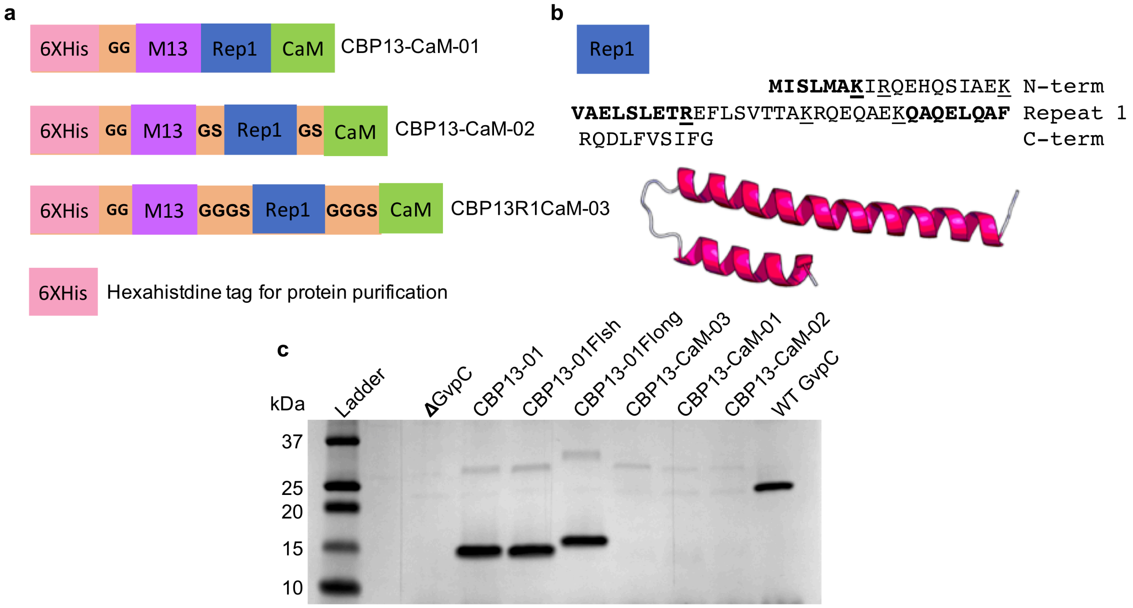

Figure 6-S2: Initial screening of CBP-GvpC variants. (**a**) Illustration of first-generation designs containing M13 and CaM, fused to the N-and C-terminus of a single-repeat GvpC (Rep1) respectively. (**b**) Sequence information for Rep1, along with its α-helical structure predicted by the Raptor-X prediction algorithm. (**c**) SDS-PAGE analysis of the binding ability of CBP13-GvpC variants to the surface of stripped Ana GVs. All GV variants were at OD_{500} ~ 10 and mixed with equal volume of 2x Laemmli buffer prior to loading.

Name	CBP Sequence	Parent protein/mutant version	Start position in Repeat 2
CBP01	RWKKNFIAVSAANRFKKIS	Skeletal muscle myosin light chain kinase (skMLCK)	9
CBP02	KSKWKQAFNATAVVRHMRK	Calmodulin dependent protein kinase I (CaMKI)	9
CBP03	RWKKAFIAVSAANRFK	Truncated N5A mutant of CBP1	11
CBP04	RWKKAFIAVSAANRFKKIS	N5A mutant of CBP1	9
CBP05	RRKLKGAILTTMLATR	Calmodulin dependent protein kinase II (CaMKII)	9
CBP06	RRKLKAAVKAVVASSRLGS	Calspermin	9
CBP07	KKRFSFKKSFKLSGFSFKK	MARCKS (Myristoylated alanine-rich C-kinase substrate)	9
CBP08	KEVIRNKIRAIGKMARVFS	Calcineurin	9
CBP09	INLKALAALAKKIL	Mastoparan	11
CBP10	INWKGIAAMAKKLL	MastoparanX	11
CBP11	GAVLKVLTTGLPALISWIK	Melittin	9
CBP12	RFLLKRGLRNKRIGHFLF	PI3-alpha (Phosphoinositide 3-kinase-alpha subunit)	10
CBP13	SSRRKWNKTGHAVRAIGRLSS	Smooth muscle myosin light chain kinase (smMLCK)	5

Supplementary table 6-T1: Details of different calmodulin binding peptides. The sequence information for CBP-GvpC variants shown in Figure 6-2, a-b. The exact sequence and its starting amino acid position in repeat 2 of truncated WT_{1-3} GvpC (with the first 3 repeats, N-and C-terminal regions) is also mentioned in the table. The underlined residues in the CBP sequence are the hydrophobic anchor residues important for binding to Ca^{2+}-activated calmodulin.

Name	Inserted Sequence	Truncated (T) or wild-type (W) GvpC	Start Position/ Repeat (R#)
CBP13-01	SSRRKWNKTGHAVRAIGRLSS	T	5/R2
CBP13-01Flong	GGGGSGGGGSSRRKWNKTGHAVRAIGRLSSGGGGSGGGGS	T	Between R1 &R3
CBP13-01Flsh	GGGGSSRRKWNKTGHAVRAIGRLSSGGGGS	T	3/R2
CBP13-02	RRKWNKTGHAVRAIGRL	T	7/R2
CBP13-03	RRKWNKTGHAVRAIGRL	T	11/R2
CBP13-04	RRKWNKTGHAVRAIGRLSS	T	7/R2
CBP13-05	RRKWNKTGHAVRAIGRL	T	9/R2
CBP13-06	SSRRKWNKTGHAVRAIGRLSS	W	5/R2
CBP13-07	SSRRKWNKTGHAVRAIGRLSS	W	5/R3
CBP13-08	SSRRKWNKTGHAVRAIGRLSS	W	5/R2 and 5/R4
CBP13-09	SSRRKWNKTGHAVRAIGRLSS	W	5/R3 and 5/R5

Supplementary table 6-T2: Details of the CBP13-GvpC variants. Sequence information for M13-GvpC variants shown in Figure 6-2, c-d. The exact insert sequence (with or without flanking linkers) and starting amino acid position in the truncated WT_{1-3} GvpC (T) or wild-type GvpC sequence (W) is mentioned in the table. CBP13 is calmodulin binding peptide sequence from smooth muscle myosin light chain kinase (smMLCK) used in all versions of GCaMP.

BIBLIOGRAPHY

1. Piraner, DI, et al. (2017) Going Deeper: Biomolecular Tools for Acoustic and Magnetic Imaging and Control of Cellular Function. *Biochemistry*, 56(39): p. 5202-5209.
2. Gilad, AA and Shapiro, MG (2017) Molecular Imaging in Synthetic Biology, and Synthetic Biology in Molecular Imaging. *Molecular Imaging and Biology*, 19(3): p. 373-378.
3. Gradinaru, V, et al. (2010) Molecular and cellular approaches for diversifying and extending optogenetics. *Cell*, 141(1): p. 154-165.
4. James, ML and Gambhir, SS (2012) A molecular imaging primer: modalities, imaging agents, and applications. *Physiological Reviews*, 92(2): p. 897-965.
5. Margolis, DJ, et al. (2007) Molecular imaging techniques in body imaging. *Radiology*, 245(2): p. 333-356.
6. Mukherjee, A, et al. (2017) Biomolecular MRI reporters: evolution of new mechanisms. *Progress in Nuclear Magnetic Resonance Spectroscopy*, 102: p. 32-42.
7. Pysz, MA, Gambhir, SS, and Willmann, JK (2010) Molecular imaging: current status and emerging strategies. *Clinical Radiology*, 65(7): p. 500-516.
8. Wu, M and Shu, J (2018) Multimodal Molecular Imaging: Current Status and Future Directions. *Contrast Media & Molecular Imaging*, 2018: p. 1-12.
9. Lin, C-W, Jao, CY, and Ting, AY (2004) Genetically encoded fluorescent reporters of histone methylation in living cells. *Journal of the American Chemical Society*, 126(19): p. 5982-5983.
10. Looger, LL and Griesbeck, O (2012) Genetically encoded neural activity indicators. *Current Opinion in Neurobiology*, 22(1): p. 18-23.
11. Mutoh, H, Akemann, Wefvr, and Knöpfel, T (2012) Genetically engineered fluorescent voltage reporters. *ACS Chemical Neuroscience*, 3(8): p. 585-592.
12. Massoud, TF and Gambhir, SS (2003) Molecular imaging in living subjects: seeing fundamental biological processes in a new light. *Genes & Development*, 17(5): p. 545-580.
13. Du, W, et al. (2006) Optical molecular imaging for systems biology: from molecule to organism. *Analytical and Bioanalytical Chemistry*, 386(3): p. 444-457.
14. Baker, B, et al. (2008) Genetically encoded fluorescent sensors of membrane potential. *Brain Cell Biology*, 36(1-4): p. 53-67.
15. Deuschle, K, et al. (2005) Construction and optimization of a family of genetically encoded metabolite sensors by semirational protein engineering. *Protein Science*, 14(9): p. 2304-2314.
16. Ting, AY, et al. (2001) Genetically encoded fluorescent reporters of protein tyrosine kinase activities in living cells. *Proceedings of the National Academy of Sciences*, 98(26): p. 15003-15008.

17. Johnson, I (1998) Fluorescent probes for living cells. *The Histochemical Journal*, 30(3): p. 123-140.
18. Lin, MZ and Schnitzer, MJ (2016) Genetically encoded indicators of neuronal activity. *Nature Neuroscience*, 19(9): p. 1142-1153.
19. Miyawaki, A, et al. (1997) Fluorescent indicators for Ca2+ based on green fluorescent proteins and calmodulin. *Nature*, 388(6645): p. 882-887.
20. Griesbeck, O (2004) Fluorescent proteins as sensors for cellular functions. *Current Opinion in Neurobiology*, 14(5): p. 636-641.
21. Miyawaki, A (2005) Innovations in the imaging of brain functions using fluorescent proteins. *Neuron*, 48(2): p. 189-199.
22. Akerboom, J, et al. (2012) Optimization of a GCaMP calcium indicator for neural activity imaging. *Journal of Neuroscience*, 32(40): p. 13819-13840.
23. Whitaker, M (2010) Genetically Encoded probes for measurement of intracellular calcium. *Methods in Cell Biology*, 99: p. 153-182.
24. Dictenberg, J (2012) Genetic encoding of fluorescent RNA ensures a bright future for visualizing nucleic acid dynamics. *Trends in Biotechnology*, 30(12): p. 621-626.
25. Dobrucki, LW and Sinusas, AJ (2010) PET and SPECT in cardiovascular molecular imaging. *Nature Reviews Cardiology*, 7(1): p. 38-47.
26. Histed, SN, et al. (2012) Review of functional/anatomic imaging in oncology. *Nuclear medicine communications*, 33(4): p. 349-361.
27. Mick, CG, et al. (2014) Molecular imaging in oncology: 18F-sodium fluoride PET imaging of osseous metastatic disease. *American Journal of Roentgenology*, 203(2): p. 263-271.
28. Tai, YF and Piccini, P (2004) Applications of positron emission tomography (PET) in neurology. *Journal of Neurology, Neurosurgery & Psychiatry*, 75(5): p. 669-676.
29. Van Dort, ME, Rehemtulla, A, and Ross, BD (2008) PET and SPECT imaging of tumor biology: new approaches towards oncology drug discovery and development. *Current Computer-Aided Drug Design*, 4(1): p. 46-53.
30. Delbeke, D and Martin, WH (2004) Metabolic imaging with FDG: a primer. *The Cancer Journal*, 10(4): p. 201-213.
31. Dickerson, BC (2007) Advances in functional magnetic resonance imaging: technology and clinical applications. *Neurotherapeutics*, 4(3): p. 360-370.
32. Maresca, D, et al. (2018) Biomolecular Ultrasound and Sonogenetics. *Annual Review of Chemical and Biomolecular Engineering*, 9: p. 229-252.
33. Szabo, TL (2004) Diagnostic ultrasound imaging: inside out. Academic Press.
34. Azhari, H (2010) Basics of biomedical ultrasound for engineers. John Wiley & Sons.
35. Cobbold, RS (2006) Foundations of biomedical ultrasound. Oxford University Press.
36. Liang, H-D, Noble, JA, and Wells, PNT (2011) Recent advances in biomedical ultrasonic imaging techniques. *Interface Focus*, 1(4): p. 475-476.
37. Powers, J and Kremkau, F (2011) Medical ultrasound systems. *Interface Focus*, 1(4): p. 477-489.
38. Foster, FS, et al. (2000) Advances in ultrasound biomicroscopy. *Ultrasound in Medicine & Biology*, 26(1): p. 1-27.

39. Errico, C, et al. (2015) Ultrafast ultrasound localization microscopy for deep super-resolution vascular imaging. *Nature*, 527(7579): p. 499-502.
40. Evans, DH, Jensen, JA, and Nielsen, MB (2011) Ultrasonic colour Doppler imaging. *Interface Focus*, 1(4): p. 490-502.
41. Rubin, JM, et al. (1994) Power Doppler US: a potentially useful alternative to mean frequency-based color Doppler US. *Radiology*, 190(3): p. 853-856.
42. Tanter, M and Fink, M (2014) Ultrafast imaging in biomedical ultrasound. *IEEE Transactions on Ultrasonics, Ferroelectrics, and Frequency Control*, 61(1): p. 102-119.
43. Mace, E, et al. (2013) Functional ultrasound imaging of the brain: theory and basic principles. *IEEE Transactions on Ultrasonics, Ferroelectrics, and Frequency Control*, 60(3): p. 492-506.
44. Mace, E, et al. (2011) Functional ultrasound imaging of the brain. *Nature Methods*, 8(8): p. 662-664.
45. Lin, F, et al. (2017) 3-D Ultrasound Localization Microscopy for Identifying Microvascular Morphology Features of Tumor Angiogenesis at a Resolution Beyond the Diffraction Limit of Conventional Ultrasound. *Theranostics*, 7(1): p. 196-204.
46. Ferrara, K, Pollard, R, and Borden, M (2007) Ultrasound microbubble contrast agents: fundamentals and application to gene and drug delivery. *Annual Review of Biomedical Engineering*, 9: p. 415-447.
47. Paefgen, V, Doleschel, D, and Kiessling, F (2015) Evolution of contrast agents for ultrasound imaging and ultrasound-mediated drug delivery. *Frontiers in Pharmacology*, 6(197): p. 1-16.
48. Unnikrishnan, S and Klibanov, AL (2012) Microbubbles as ultrasound contrast agents for molecular imaging: preparation and application. *American Journal of Roentgenology*, 199(2): p. 292-299.
49. Frinking, PJA, et al. (2000) Ultrasound contrast imaging: current and new potential methods. *Ultrasound in Medicine & Biology*, 26(6): p. 965-975.
50. Mor-Avi, V, et al. (2001) Combined assessment of myocardial perfusion and regional left ventricular function by analysis of contrast-enhanced power modulation images. *Circulation*, 104(3): p. 352-7.
51. Simpson, DH, Chin, CT, and Burns, PN (1999) Pulse inversion Doppler: a new method for detecting nonlinear echoes from microbubble contrast agents. *IEEE Transactions on Ultrasonics, Ferroelectrics and Frequency Control*, 46(2): p. 372-382.
52. Gramiak, R, Shah, PM, and Kramer, DH (1969) Ultrasound cardiography - contrast studies in anatomy and function. *Radiology*, 92(5): p. 939-948.
53. Cosgrove, D and Harvey, C (2009) Clinical uses of microbubbles in diagnosis and treatment. *Medical and Biological Engineering and Computing*, 47(8): p. 813-826.
54. Qin, S, Caskey, CF, and Ferrara, KW (2009) Ultrasound contrast microbubbles in imaging and therapy: physical principles and engineering. *Physics in Medicine & Biology*, 54(6): p. R27-R57.
55. Blomley, MJK, et al. (2001) Microbubble contrast agents: a new era in ultrasound. *British Medical Journal*, 322(7296): p. 1222-1225.

56. Lee, H, et al. (2017) Microbubbles used for contrast enhanced ultrasound and theragnosis: a review of principles to applications. *Biomedical Engineering Letters*, 7(2): p. 59-69.
57. Stride, E and Saffari, N (2003) Microbubble ultrasound contrast agents: a review. *Proceedings of the Institution of Mechanical Engineers, Part H: Journal of Engineering in Medicine*, 217(6): p. 429-447.
58. Sirsi, S and Borden, M (2009) Microbubble Compositions, Properties and Biomedical Applications. *Bubble Science Engineering and Technology*, 1(1-2): p. 3-17.
59. Stride, E and Edirisinghe, M (2009) Novel preparation techniques for controlling microbubble uniformity: a comparison. *Medical & Biological Engineering & Computing*, 47(8): p. 883-892.
60. Lindner, JR (2004) Microbubbles in medical imaging: current applications and future directions. *Nature Reviews Drug Discovery*, 3(6): p. 527-533.
61. Ellegala, DB, et al. (2003) Imaging tumor angiogenesis with contrast ultrasound and microbubbles targeted to αvβ3. *Circulation*, 108(3): p. 336-341.
62. Kaufmann, BA and Lindner, JR (2007) Molecular imaging with targeted contrast ultrasound. *Current Opinion in Biotechnology*, 18(1): p. 11-16.
63. Buchholz, BEE, Hayes, PK, and Walsby, AE (1993) The Distribution of the Outer Gas Vesicle Protein, Gvpc, on the Anabaena Gas Vesicle, and Its Ratio to Gvpa. *Journal of General Microbiology*, 139: p. 2353-2363.
64. Wang, S, Hossack, JA, and Klibanov, AL (2018) Targeting of microbubbles: contrast agents for ultrasound molecular imaging. *Journal of Drug Targeting*, 26(5-6): p. 420-434.
65. Burns, PN, et al. (1994) Harmonic power mode Doppler using microbubble contrast agents: an improved method for small vessel flow imaging. *Proceedings of IEEE Ultrasonics Symposium*, 3: p. 1547-1550.
66. Desailly, Y, et al. (2013) Sono-activated ultrasound localization microscopy. *Applied Physics Letters*, 103(17): p. 174107(1-4).
67. Errico, C, et al. (2016) Transcranial functional ultrasound imaging of the brain using microbubble-enhanced ultrasensitive Doppler. *NeuroImage*, 124: p. 752-761.
68. Simpson, DH, Burns, PN, and Averkiou, MA (2001) Techniques for perfusion imaging with microbubble contrast agents. *IEEE Transactions on Ultrasonics, Ferroelectrics, and Frequency Control*, 48(6): p. 1483-1494.
69. Willmann, JrK, et al. (2008) US imaging of tumor angiogenesis with microbubbles targeted to vascular endothelial growth factor receptor type 2 in mice. *Radiology*, 246(2): p. 508-518.
70. Tang, MX, et al. (2011) Quantitative contrast-enhanced ultrasound imaging: a review of sources of variability. *Interface Focus*, 1(4): p. 520-539.
71. Astafyeva, K, et al. (2015) Perfluorocarbon nanodroplets stabilized by fluorinated surfactants: characterization and potentiality as theranostic agents. *Journal of Materials Chemistry B*, 3(14): p. 2892-2907.
72. Hannah, AS, et al. (2014) Photoacoustic and ultrasound imaging using dual contrast perfluorocarbon nanodroplets triggered by laser pulses at 1064 nm. *Biomedical Optics Express*, 5(9): p. 3042-3052.

73. Oeffinger, BE and Wheatley, MA (2004) Development and characterization of a nano-scale contrast agent. *Ultrasonics*, 42(1-9): p. 343-347.
74. Perera, R, et al. (2019) Bubble Trouble: Conquering Microbubble Limitations in Contrast Enhanced Ultrasound Imaging by Nature-Inspired Ultrastable Echogenic Nanobubbles. *BioRxiv*: p. 633578.
75. Rapoport, N (2012) Phase-shift, stimuli-responsive perfluorocarbon nanodroplets for drug delivery to cancer. *Wiley Interdisciplinary Reviews: Nanomedicine and Nanobiotechnology*, 4(5): p. 492-510.
76. Santiesteban, DY, et al. (2017) Copper sulfide perfluorocarbon nanodroplets as clinically relevant photoacoustic/ultrasound imaging agents. *Nano Letters*, 17(10): p. 5984-5989.
77. Xu, JS, et al. (2010) Synthesizing and binding dual-mode poly (lactic-co-glycolic acid)(PLGA) nanobubbles for cancer targeting and imaging. *Biomaterials*, 31(7): p. 1716-1722.
78. Yin, T, et al. (2012) Nanobubbles for enhanced ultrasound imaging of tumors. *International Journal of Nanomedicine*, 7: p. 895-904.
79. Kanai, A and Miyata, H (2001) Direct numerical simulation of wall turbulent flows with microbubbles. *International Journal for Numerical Methods in Fluids*, 35(5): p. 593-615.
80. Murai, Y, et al. (2006) Turbulent shear stress profiles in a bubbly channel flow assessed by particle tracking velocimetry. *Experiments in Fluids*, 41(2): p. 343.
81. Shapiro, MG, et al. (2014) Biogenic gas nanostructures as ultrasonic molecular reporters. *Nature Nanotechnology*, 9(4): p. 311-316.
82. Bowen, C and Jensen, T (1965) Blue-green algae: fine structure of the gas vacuoles. *Science*, 147(3664): p. 1460-1462.
83. Klebahn, H (1895) Gasvakuolen, ein Bestandteil der Zellen der wasserblutenbildenden Phycochromaceen. *Flora (Jena)*, 80: p. 241-282.
84. Walsby, AE (1994) Gas vesicles. *Microbiological Reviews*, 58(1): p. 94-144.
85. Pfeifer, F (2012) Distribution, formation and regulation of gas vesicles. *Nature Reviews Microbiology*, 10(10): p. 705-715.
86. Ezzeldin, HM, Klauda, JB, and Solares, SD (2012) Modeling of the major gas vesicle protein, GvpA: from protein sequence to vesicle wall structure. *Journal of Structural Biology*, 179(1): p. 18-28.
87. Hayes, P, Buchholz, B, and Walsby, A (1992) Gas vesicles are strengthened by the outer-surface protein, GvpC. *Archives of Microbiology*, 157(3): p. 229-234.
88. Walsby, AE and Hayes, PK (1989) Gas Vesicle Proteins. *Biochemical Journal*, 264(2): p. 313-322.
89. Offner, S, Wanner, G, and Pfeifer, F (1996) Functional studies of the gvpACNO operon of Halobacterium salinarium reveal that the GvpC protein shapes gas vesicles. *Journal of Bacteriology*, 178(7): p. 2071-2078.
90. Offner, S, et al. (1998) Structural characteristics of halobacterial gas vesicles. *Microbiology-Uk*, 144: p. 1331-1342.
91. Strunk, T, et al. (2011) Structural model of the gas vesicle protein GvpA and analysis of GvpA mutants in vivo. *Molecular Microbiology*, 81(1): p. 56-68.

92. Dunbar, CE, et al. (2018) Gene therapy comes of age. *Science*, 359(6372): p. eaan4672(1-10).
93. Schön, C, Biel, M, and Michalakis, S (2015) Retinal gene delivery by adeno-associated virus (AAV) vectors: Strategies and applications. *European Journal of Pharmaceutics and Biopharmaceutics*, 95: p. 343-352.
94. Tavlaridou, S, et al. (2013) Effect of an overproduction of accessory Gvp proteins on gas vesicle formation in Haloferax volcanii. *Extremophiles*, 17(2): p. 277-287.
95. Shapiro, MG, et al. (2014) Genetically encoded reporters for hyperpolarized xenon magnetic resonance imaging. *Nature Chemistry*, 6(7): p. 629-634.
96. Cherin, E, et al. (2017) Acoustic Behavior of Halobacterium salinarum Gas Vesicles in the High-Frequency Range: Experiments and Modeling. *Ultrasound in Medicine & Biology*, 43(5): p. 1016-1030.
97. Lakshmanan, A, et al. (2016) Molecular Engineering of Acoustic Protein Nanostructures. *ACS Nano*, 10(8): p. 7314-7322.
98. Maresca, D, et al. (2017) Nonlinear ultrasound imaging of nanoscale acoustic biomolecules. *Applied Physics Letters*, 110(7): p. 073704(1-5).
99. Farhadi, A, et al. (2018) Recombinantly Expressed Gas Vesicles as Nanoscale Contrast Agents for Ultrasound and Hyperpolarized MRI. *AIChE Journal*, 64(8): p. 2927-2933.
100. Simon, RD (1981) Morphology and protein composition of gas vesicles from wild type and gas vacuole defective strains of Halobacterium salinarium strain 5. *Microbiology*, 125(1): p. 103-111.
101. Maresca, D, et al. (2018) Nonlinear X-Wave Ultrasound Imaging of Acoustic Biomolecules. *Physical Review X*, 8(4): p. 041002(1-12).
102. Kinsman, R and Hayes, P (1997) Genes encoding proteins homologous to halobacterial Gvps N, J, K, F & L are located downstream of gvpC in the cyanobacterium Anabaena flos-aquae. *DNA Sequence*, 7(2): p. 97-106.
103. Hayes, PK and Powell, RS (1995) The Gvpa/C Cluster of Anabaena-Flos-Aquae Has Multiple Copies of a Gene Encoding Gvpa. *Archives of Microbiology*, 164(1): p. 50-57.
104. Kinsman, R, Walsby, AE, and Hayes, PK (1995) GvpCs with reduced numbers of repeating sequence elements bind to and strengthen cyanobacterial gas vesicles. *Molecular Microbiology*, 17(1): p. 147-154.
105. DasSarma, S, et al. (2013) An improved genetic system for bioengineering buoyant gas vesicle nanoparticles from Haloarchaea. *BMC Biotechnology*, 13(112): p. 1-10.
106. Sremac, M and Stuart, ES (2008) Recombinant gas vesicles from Halobacterium sp. displaying SIV peptides demonstrate biotechnology potential as a pathogen peptide delivery vehicle. *BMC Biotechnology*, 8(9): p. 1-14.
107. Walsby, A, Revsbech, N, and Griffel, D (1992) The gas permeability coefficient of the cyanobacterial gas vesicle wall. *Microbiology*, 138(4): p. 837-845.
108. Burns, PN (1996) Harmonic imaging with ultrasound contrast agents. *Clinical Radiology*, 51: p. 50-55.
109. Maresca, D, et al. (2014) Imaging microvasculature with contrast-enhanced ultraharmonic ultrasound. *Ultrasound in Medicine & Biology*, 40(6): p. 1318-1328.

110. Blanco, E, Shen, H, and Ferrari, M (2015) Principles of nanoparticle design for overcoming biological barriers to drug delivery. *Nature Biotechnology*, 33(9): p. 941-951.

111. Ruoslahti, E (1996) RGD and other recognition sequences for integrins. *Annual Review of Cell and Developmental Biology*, 12: p. 697-715.

112. Rodriguez, PL, et al. (2013) Minimal "Self" Peptides That Inhibit Phagocytic Clearance and Enhance Delivery of Nanoparticles. *Science*, 339(6122): p. 971-975.

113. Brock, R (2014) The Uptake of Arginine-Rich Cell-Penetrating Peptides: Putting the Puzzle Together. *Bioconjugate Chemistry*, 25(5): p. 863-868.

114. Zakeri, B, et al. (2012) Peptide tag forming a rapid covalent bond to a protein, through engineering a bacterial adhesin. *Proceedings of the National Academy of Sciences*, 109(12): p. E690-E697.

115. Round, JL and Mazmanian, SK (2009) The gut microbiota shapes intestinal immune responses during health and disease. *Nature Reviews Immunology*, 9(5): p. 313-323.

116. Yurist-Doutsch, S, et al. (2014) Gastrointestinal Microbiota-Mediated Control of Enteric Pathogens. *Annual Review of Genetics*, 48: p. 361-382.

117. Belkaid, Y and Hand, TW (2014) Role of the Microbiota in Immunity and Inflammation. *Cell*, 157(1): p. 121-141.

118. Wang, Y and Kasper, LH (2014) The role of microbiome in central nervous system disorders. *Brain Behavior and Immunity*, 38: p. 1-12.

119. Sampson, TR, et al. (2016) Gut Microbiota Regulate Motor Deficits and Neuroinflammation in a Model of Parkinson's Disease. *Cell*, 167(6): p. 1469-1480.

120. Courbet, A, et al. (2015) Detection of pathological biomarkers in human clinical samples via amplifying genetic switches and logic gates. *Science Translational Medicine*, 7(289): p. 289ra83(1-10).

121. Danino, T, et al. (2015) Programmable probiotics for detection of cancer in urine. *Science Translational Medicine*, 7(289): p. 289ra84(1-11).

122. Kotula, JW, et al. (2014) Programmable bacteria detect and record an environmental signal in the mammalian gut. *Proceedings of the National Academy of Sciences of the United States of America*, 111(13): p. 4838-4843.

123. Archer, EJ, Robinson, AB, and Suel, GM (2012) Engineered E. coli That Detect and Respond to Gut Inflammation through Nitric Oxide Sensing. *ACS Synthetic Biology*, 1(10): p. 451-457.

124. Steidler, L, et al. (2000) Treatment of murine colitis by Lactococcus lactis secreting interleukin-10. *Science*, 289(5483): p. 1352-1355.

125. Claesen, J and Fischbach, MA (2015) Synthetic Microbes As Drug Delivery Systems. *ACS Synthetic Biology*, 4(4): p. 358-364.

126. Wells, JM and Mercenier, A (2008) Mucosal delivery of therapeutic and prophylactic molecules using lactic acid bacteria. *Nature Reviews Microbiology*, 6(5): p. 349-362.

127. Din, MO, et al. (2016) Synchronized cycles of bacterial lysis for in vivo delivery. *Nature*, 536(7614): p. 81-85.

128. Fischbach, MA, Bluestone, JA, and Lim, WA (2013) Cell-Based Therapeutics: The Next Pillar of Medicine. *Science Translational Medicine*, 5(179): p. 179ps7(1-6).

129. Riglar, DT, et al. (2017) Engineered bacteria can function in the mammalian gut long-term as live diagnostics of inflammation. *Nature Biotechnology*, 35(7): p. 653-658.

130. Mowat, AM and Agace, WW (2014) Regional specialization within the intestinal immune system. *Nature Reviews Immunology*, 14(10): p. 667-685.

131. Donaldson, GP, Lee, SM, and Mazmanian, SK (2016) Gut biogeography of the bacterial microbiota. *Nature Reviews Microbiology*, 14(1): p. 20-32.

132. Derrien, M and Vlieg, JETV (2015) Fate, activity, and impact of ingested bacteria within the human gut microbiota. *Trends in Microbiology*, 23(6): p. 354-366.

133. Foucault, ML, et al. (2010) In Vivo Bioluminescence Imaging for the Study of Intestinal Colonization by Escherichia coli in Mice. *Applied and Environmental Microbiology*, 76(1): p. 264-274.

134. Daniel, C, et al. (2013) Bioluminescence Imaging Study of Spatial and Temporal Persistence of Lactobacillus plantarum and Lactococcus lactis in Living Mice. *Applied and Environmental Microbiology*, 79(4): p. 1086-1094.

135. Chu, J, et al. (2016) A bright cyan-excitable orange fluorescent protein facilitates dual-emission microscopy and enhances bioluminescence imaging in vivo. *Nature Biotechnology*, 34(7): p. 760-767.

136. Smith-Bindman, R, et al. (2012) Use of diagnostic imaging studies and associated radiation exposure for patients enrolled in large integrated health care systems, 1996-2010. *Journal of the American Medical Association*, 307(22): p. 2400-2409.

137. Foster, FS, et al. (1993) Principles and applications of ultrasound backscatter microscopy. *IEEE Transactions on Ultrasonics, Ferroelectrics, and Frequency Control*, 40(5): p. 608-617.

138. Li, N and Cannon, MC (1998) Gas vesicle genes identified in Bacillus megaterium and functional expression in Escherichia coli. *Journal of Bacteriology*, 180(9): p. 2450-2458.

139. Braat, H, et al. (2006) A phase I trial with Transgenic bacteria expressing interleukin-10 in Crohn's disease. *Clinical Gastroenterology and Hepatology*, 4(6): p. 754-759.

140. Daniel, C, et al. (2011) Recombinant lactic acid bacteria as mucosal biotherapeutic agents. *Trends in Biotechnology*, 29(10): p. 499-508.

141. Gorbach, SL (1996) Microbiology of the Gastrointestinal Tract, in *Medical Microbiology*, Baron, S, Editor: Galveston (TX).

142. Sprinzak, D and Elowitz, MB (2005) Reconstruction of genetic circuits. *Nature*, 438(7067): p. 443-448.

143. Klumpp, S and Hwa, T (2014) Bacterial growth: global effects on gene expression, growth feedback and proteome partition. *Current Opinion in Biotechnology*, 28: p. 96-102.

144. Reits, EA and Neefjes, JJ (2001) From fixed to FRAP: measuring protein mobility and activity in living cells. *Nature Cell Biology*, 3(6): p. E145-E147.

145. Sonnenborn, U and Schulze, J (2009) The non-pathogenic Escherichia coli strain Nissle 1917–features of a versatile probiotic. *Microbial Ecology in Health and Disease*, 21(3-4): p. 122-158.

146. Chen, ZY, et al. (2014) Incorporation of therapeutically modified bacteria into gut microbiota inhibits obesity. *Journal of Clinical Investigation*, 124(8): p. 3391-3406.
147. Francis, KP, et al. (2000) Monitoring Bioluminescent Staphylococcus aureusInfections in Living Mice Using a Novel luxABCDEConstruct. *Infection and immunity*, 68(6): p. 3594-3600.
148. Borkowski, O, et al. (2016) Overloaded and stressed: whole-cell considerations for bacterial synthetic biology. *Current Opinion in Microbiology*, 33: p. 123-130.
149. Sleight, SC and Sauro, HM (2013) Visualization of evolutionary stability dynamics and competitive fitness of Escherichia coli engineered with randomized multigene circuits. *ACS Synthetic Biology*, 2(9): p. 519-528.
150. Patzer, S, et al. (2003) The colicin G, H and X determinants encode microcins M and H47, which might utilize the catecholate siderophore receptors FepA, Cir, Fiu and IroN. *Microbiology*, 149(9): p. 2557-2570.
151. Danino, T, et al. (2012) In Vivo Gene Expression Dynamics of Tumor-Targeted Bacteria. *ACS Synthetic Biology*, 1(10): p. 465-470.
152. Romero, PA and Arnold, FH (2009) Exploring protein fitness landscapes by directed evolution. *Nature Reviews Molecular Cell Biology*, 10(12): p. 866-876.
153. Shaner, NC, et al. (2008) Improving the photostability of bright monomeric orange and red fluorescent proteins. *Nature Methods*, 5(6): p. 545-551.
154. Shaner, NC, et al. (2004) Improved monomeric red, orange and yellow fluorescent proteins derived from Discosoma sp red fluorescent protein. *Nature Biotechnology*, 22(12): p. 1567-1572.
155. Couture, O, et al. (2009) Ultrafast Imaging of Ultrasound Contrast Agents. *Ultrasound in Medicine and Biology*, 35(11): p. 1908-1916.
156. Couture, O, Fink, M, and Tanter, M (2012) Ultrasound Contrast Plane Wave Imaging. *IEEE Transactions on Ultrasonics Ferroelectrics and Frequency Control*, 59(12): p. 2676-2683.
157. Widdel, F and Pfennig, N (1981) Sporulation and further nutritional characteristics of Desulfotomaculum acetoxidans. *Archives of Microbiology*, 129(5): p. 401-402.
158. Datsenko, KA and Wanner, BL (2000) One-step inactivation of chromosomal genes in Escherichia coli K-12 using PCR products. *Proceedings of the National Academy of Sciences*, 97(12): p. 6640-6645.
159. Choi, K-H, et al. (2005) A Tn7-based broad-range bacterial cloning and expression system. *Nature Methods*, 2(6): p. 443-448.
160. Gerdes, K (1988) The parB (hok/sok) locus of plasmid R1: a general purpose plasmid stabilization system. *Bio/Technology*, 6(12): p. 1402-1405.
161. Derman, AI, et al. (2009) Phylogenetic analysis identifies many uncharacterized actin-like proteins (Alps) in bacteria: regulated polymerization, dynamic instability and treadmilling in Alp7A. *Molecular Microbiology*, 73(4): p. 534-552.
162. Krumholz, A, et al. (2014) Multicontrast photoacoustic in vivo imaging using near-infrared fluorescent proteins. *Scientific Reports*, 4(3939): p. 1-7.

163. Berlec, A, et al. (2015) In vivo imaging of Lactococcus lactis, Lactobacillus plantarum and Escherichia coli expressing infrared fluorescent protein in mice. *Microbial Cell Factories*, 14(181): p. 1-14.
164. Hong, G, Antaris, AL, and Dai, H (2017) Near-infrared fluorophores for biomedical imaging. *Nature Biomedical Engineering*, 1(0010): p. 1-22.
165. Yao, J, et al. (2016) Multi-scale photoacoustic tomography using reversibly switchable bacterial phytochrome as a near-infrared photochromic probe. *Nature Methods*, 13(1): p. 67-73.
166. Shaner, NC, et al. (2013) A bright monomeric green fluorescent protein derived from Branchiostoma lanceolatum. *Nature Methods*, 10(5): p. 407-409.
167. Blum-Oehler, G, et al. (2003) Development of strain-specific PCR reactions for the detection of the probiotic Escherichia coli strain Nissle 1917 in fecal samples. *Research in Microbiology*, 154(1): p. 59-66.
168. Schindelin, J, et al. (2012) Fiji: an open-source platform for biological-image analysis. *Nature Methods*, 9(7): p. 676-682.
169. Wang, HJ, et al. (2013) Molecular Imaging of Inflammation in Inflammatory Bowel Disease with a Clinically Translatable Dual-Selectin-targeted US Contrast Agent: Comparison with FDG PET/CT in a Mouse Model. *Radiology*, 267(3): p. 818-829.
170. Freeling, JL and Rezvani, K (2016) Assessment of murine colorectal cancer by micro-ultrasound using three dimensional reconstruction and non-linear contrast imaging. *Molecular Therapy-Methods & Clinical Development*, 3(16070): p. 1-11.
171. Baldwin, WW, et al. (1995) Buoyant density of Escherichia coli is determined solely by the osmolarity of the culture medium. *Archives of Microbiology*, 164(2): p. 155-157.
172. Volkmer, B and Heinemann, M (2011) Condition-dependent cell volume and concentration of Escherichia coli to facilitate data conversion for systems biology modeling. *PloS One*, 6(7): p. e23126(1-6).
173. Chattopadhyay, S, et al. (2006) Swimming efficiency of bacterium Escherichiacoli. *Proceedings of the National Academy of Sciences*, 103(37): p. 13712-13717.
174. Eckert, MA, et al. (2013) Novel molecular and nanosensors for in vivo sensing. *Theranostics*, 3(8): p. 583-594.
175. Bourdeau, RW, et al. (2018) Acoustic reporter genes for noninvasive imaging of microorganisms in mammalian hosts. *Nature*, 553(7686): p. 86-90.
176. Dunton, PG and Walsby, AE (2005) The diameter and critical collapse pressure of gas vesicles in Microcystis are correlated with GvpCs of different length. *FEMS Microbiology Letters*, 247(1): p. 37-43.
177. Chowdhury, D and Lieberman, J (2008) Death by a thousand cuts: granzyme pathways of programmed cell death. *Annual Review of Immunology*, 26: p. 389-420.
178. Krem, MM and Di Cera, E (2002) Evolution of enzyme cascades from embryonic development to blood coagulation. *Trends in Biochemical Sciences*, 27(2): p. 67-74.
179. Pogson, M, Georgiou, G, and Iverson, BL (2009) Engineering next generation proteases. *Current Opinion in Biotechnology*, 20(4): p. 390-397.

180. Sjöberg, AP, Trouw, LA, and Blom, AM (2009) Complement activation and inhibition: a delicate balance. *Trends in Immunology*, 30(2): p. 83-90.
181. Kapust, RB, et al. (2001) Tobacco etch virus protease: mechanism of autolysis and rational design of stable mutants with wild-type catalytic proficiency. *Protein Engineering*, 14(12): p. 993-1000.
182. Phan, J, et al. (2002) Structural basis for the substrate specificity of tobacco etch virus protease. *Journal of Biological Chemistry*, 277(52): p. 50564-50572.
183. Parks, TD, et al. (1994) Release of proteins and peptides from fusion proteins using a recombinant plant virus proteinase. *Analytical Biochemistry*, 216(2): p. 413-417.
184. Goll, DE, et al. (2003) The calpain system. *Physiological Reviews*, 83(3): p. 731-801.
185. Ono, Y and Sorimachi, H (2012) Calpains—an elaborate proteolytic system. *Biochimica et Biophysica Acta (BBA)-Proteins and Proteomics*, 1824(1): p. 224-236.
186. Harwood, SM, Yaqoob, MM, and Allen, DA (2005) Caspase and calpain function in cell death: bridging the gap between apoptosis and necrosis. *Annals of Clinical Biochemistry*, 42(6): p. 415-431.
187. Ono, Y, Saido, TC, and Sorimachi, H (2016) Calpain research for drug discovery: challenges and potential. *Nature Reviews Drug Discovery*, 15(12): p. 854-876.
188. Baker, TA and Sauer, RT (2012) ClpXP, an ATP-powered unfolding and protein-degradation machine. *Biochimica et Biophysica Acta (BBA)-Molecular Cell Research*, 1823(1): p. 15-28.
189. Culp, E and Wright, GD (2017) Bacterial proteases, untapped antimicrobial drug targets. *The Journal of Antibiotics*, 70(4): p. 366-377.
190. Al-Furoukh, N, et al. (2015) ClpX stimulates the mitochondrial unfolded protein response (UPRmt) in mammalian cells. *Biochimica et Biophysica Acta (BBA)-Molecular Cell Research*, 1853(10): p. 2580-2591.
191. Cohen, SE, McKnight, BM, and Golden, SS (2018) Roles for ClpXP in regulating the circadian clock in Synechococcus elongatus. *Proceedings of the National Academy of Sciences*, 115(33): p. E7805-E7813.
192. Fischer, F, Langer, JD, and Osiewacz, HD (2015) Identification of potential mitochondrial CLPXP protease interactors and substrates suggests its central role in energy metabolism. *Scientific Reports*, 5(18375): p. 1-13.
193. Seo, JH, et al. (2016) The mitochondrial unfoldase-peptidase complex ClpXP controls bioenergetics stress and metastasis. *PLoS Biology*, 14(7): p. e1002507(1-21).
194. Truscott, KN, Bezawork-Geleta, A, and Dougan, DA (2011) Unfolded protein responses in bacteria and mitochondria: a central role for the ClpXP machine. *IUBMB Life*, 63(11): p. 955-963.
195. Suzuki, S, et al. (2014) Development of an artificial calcium-dependent transcription factor to detect sustained intracellular calcium elevation. *ACS Synthetic Biology*, 3(10): p. 717-722.
196. Elowitz, MB and Leibler, S (2000) A synthetic oscillatory network of transcriptional regulators. *Nature*, 403(6767): p. 335-338.

197. Gardner, TS, Cantor, CR, and Collins, JJ (2000) Construction of a genetic toggle switch in Escherichia coli. *Nature*, 403(6767): p. 339-342.
198. Khalil, AS and Collins, JJ (2010) Synthetic biology: applications come of age. *Nature Reviews Genetics*, 11(5): p. 367-379.
199. Tigges, M, et al. (2009) A tunable synthetic mammalian oscillator. *Nature*, 457(7227): p. 309-312.
200. Heim, R and Tsien, RY (1996) Engineering green fluorescent protein for improved brightness, longer wavelengths and fluorescence resonance energy transfer. *Current Biology*, 6(2): p. 178-182.
201. Mitra, RD, Silva, CM, and Youvan, DC (1996) Fluorescence resonance energy transfer between blue-emitting and red-shifted excitation derivatives of the green fluorescent protein. *Gene*, 173(1): p. 13-17.
202. Grienberger, C and Konnerth, A (2012) Imaging calcium in neurons. *Neuron*, 73(5): p. 862-885.
203. Hires, SA, Tian, L, and Looger, LL (2008) Reporting neural activity with genetically encoded calcium indicators. *Brain Cell Biology*, 36(1-4): p. 69-86.
204. Burgoyne, RD (2007) Neuronal calcium sensor proteins: generating diversity in neuronal Ca2+ signalling. *Nature Reviews Neuroscience*, 8(3): p. 182-193.
205. Bezprozvanny, I (2009) Calcium signaling and neurodegenerative diseases. *Trends in Molecular Medicine*, 15(3): p. 89-100.
206. Steinlein, OK (2014) Calcium signaling and epilepsy. *Cell and Tissue Research*, 357(2): p. 385-393.
207. Berridge, MJ (2014) Calcium signalling and psychiatric disease: bipolar disorder and schizophrenia. *Cell and Tissue Research*, 357(2): p. 477-492.
208. Tian, L, et al. (2009) Imaging neural activity in worms, flies and mice with improved GCaMP calcium indicators. *Nature Methods*, 6(12): p. 875-881.
209. Kircher, MF, Gambhir, SS, and Grimm, J (2011) Noninvasive cell-tracking methods. *Nature Reviews Clinical Oncology*, 8(11): p. 677-688.
210. van Raaij, ME, et al. (2011) Functional micro-ultrasound imaging of rodent cerebral hemodynamics. *NeuroImage*, 58(1): p. 100-108.
211. Koldenkova, VP and Nagai, T (2013) Genetically encoded Ca2+ indicators: Properties and evaluation. *Biochimica et Biophysica Acta (BBA)-Molecular Cell Research*, 1833(7): p. 1787-1797.
212. Akerboom, J, et al. (2013) Genetically encoded calcium indicators for multi-color neural activity imaging and combination with optogenetics. *Frontiers in Molecular Neuroscience*, 6(2): p. 1-29.
213. Dana, H, et al. (2018) High-performance GFP-based calcium indicators for imaging activity in neuronal populations and microcompartments. *BioRxiv*: p. 434589.
214. Bayley, PM, Findlay, WA, and Martin, SR (1996) Target recognition by calmodulin: dissecting the kinetics and affinity of interaction using short peptide sequences. *Protein Science*, 5(7): p. 1215-1228.
215. Hultschig, C, Hecht, H-J, and Frank, R (2004) Systematic delineation of a calmodulin peptide interaction. *Journal of Molecular Biology*, 343(3): p. 559-568.

216. Park, HY, et al. (2008) Conformational changes of calmodulin upon Ca2+ binding studied with a microfluidic mixer. *Proceedings of the National Academy of Sciences*, 105(2): p. 542-547.
217. Persechini, A, Yano, K, and Stemmer, PM (2000) Ca2+ binding and energy coupling in the calmodulin-myosin light chain kinase complex. *Journal of Biological Chemistry*, 275(6): p. 4199-4204.
218. Wu, X and Bers, DM (2007) Free and bound intracellular calmodulin measurements in cardiac myocytes. *Cell Calcium*, 41(4): p. 353-364.
219. Yáñez, M, Gil-Longo, J, and Campos-Toimil, M (2012) Calcium binding proteins, in *Calcium Signaling*, Islam, M, Editor, Advances in Experimental Medicine and Biology, Springer. p. 461-482.
220. Halling, DB, et al. (2016) Conserved properties of individual Ca2+-binding sites in calmodulin. *Proceedings of the National Academy of Sciences*, 113(9): p. E1216-E1225.
221. Lakowski, TM, et al. (2007) Calcium-induced folding of a fragment of calmodulin composed of EF-hands 2 and 3. *Protein Science*, 16(6): p. 1119-1132.
222. Crivici, A and Ikura, M (1995) Molecular and structural basis of target recognition by calmodulin. *Annual Review of Biophysics and Biomolecular Structure*, 24(1): p. 85-116.
223. Tidow, H and Nissen, P (2013) Structural diversity of calmodulin binding to its target sites. *The FEBS Journal*, 280(21): p. 5551-5565.
224. Clapperton, JA, et al. (2002) Structure of the complex of calmodulin with the target sequence of calmodulin-dependent protein kinase I: studies of the kinase activation mechanism. *Biochemistry*, 41(50): p. 14669-14679.
225. Evans, TIA and Shea, MA (2009) Energetics of calmodulin domain interactions with the calmodulin binding domain of CaMKII. *Proteins: Structure, Function, and Bioinformatics*, 76(1): p. 47-61.
226. Fischer, R, Julsgart, J, and Berchtold, MW (1998) High affinity calmodulin target sequence in the signalling molecule PI 3-kinase. *FEBS Letters*, 425(1): p. 175-177.
227. Graff, JM, et al. (1989) Phosphorylation-regulated calmodulin binding to a prominent cellular substrate for protein kinase C. *Journal of Biological Chemistry*, 264(36): p. 21818-21823.
228. Hubbard, MJ and Klee, CB (1987) Calmodulin binding by calcineurin. Ligand-induced renaturation of protein immobilized on nitrocellulose. *Journal of Biological Chemistry*, 262(31): p. 15062-15070.
229. Malencik, DA and Anderson, SR (1983) High affinity binding of the mastoparans by calmodulin. *Biochemical and Biophysical Research Communications*, 114(1): p. 50-56.
230. Medvedeva, MV, et al. (1996) Interaction of proteolytic fragments of calmodulin with caldesmon and calponin. *Biochemical Journal*, 315(3): p. 1021-1026.
231. Ikura, M, et al. (1992) Solution structure of calmodulin and its complex with a myosin light chain kinase fragment. *Cell Calcium*, 13(6-7): p. 391-400.
232. Martin, SR, et al. (1996) Spectroscopic characterization of a high-affinity calmodulin− target peptide hybrid molecule. *Biochemistry*, 35(11): p. 3508-3517.

233. Sekharudu, CY and Sundaralingam, M (1993) A model for the calmodulin—peptide complex based on the troponin C crystal packing and its similarity to the NMR structure of the calmodulin—myosin light chain kinase peptide complex. *Protein Science*, 2(4): p. 620-625.

234. Blumenthal, DK and Stull, JT (1980) Activation of skeletal muscle myosin light chain kinase by calcium (2+) and calmodulin. *Biochemistry*, 19(24): p. 5608-5614.

235. Maier, LS, et al. (2006) Dynamic changes in free Ca-calmodulin levels in adult cardiac myocytes. *Journal of Molecular and Cellular Cardiology*, 41(3): p. 451-458.

236. Marin, M (2012) Calcium signaling in Xenopus oocyte, in *Calcium Signaling*, Islam, M, Editor, Advances in Experimental Medicine and Biology, Springer. p. 1073-1094.

237. Lakshmanan, A, et al. (2017) Preparation of biogenic gas vesicle nanostructures for use as contrast agents for ultrasound and MRI. *Nature Protocols*, 12(10): p. 2050-2080.

238. Smith, R and Peat, A (1967) Growth and gas-vacuole development in vegetative cells of Anabaena flos-aquae. *Archives of Microbiology*, 58(2): p. 117-126.

APPENDIX A

DETAILED EXPERIMENTAL PROTOCOLS

REAGENT SETUP

G625 growth medium for *Anabaena flos-aquae (*Ana*)* (4 L): 5.84 mM $NaNO_3$, 224 µM KH_2PO_4, 304 µM $MgSO_4.7H_2O$, 208 µM $Na_2SiO_3.9H_2O$, 189 µM Na_2CO_3, 10 mM $NaHCO_3$, 245 µM $CaCl_2$, 31 µM citric acid and 3 µM EDTA. Separately, add 24 mg of ferric ammonium citrate to 1 mL of ultrapure water (in a 1.5 mL micro-centrifuge tube). Heat in a 42°C water-bath for 10-15 min to dissolve before adding to the media in the Nalgene 4L beaker. Adjust to pH 8.0 with HCl. Filter sterilize using a 0.22 µm bottle-top filter. G625 growth media prepared using this method is stable for at least 6 months if stored in a cool, dry place at room temperature under sterile conditions. Since the iron sediments, make sure that the bottle is swirled each time before use.

Carolina growth medium for *Halobacteria salinarum-NRC1* (Halo) (1 L): 4.278 M NaCl, 81 mM $MgSO_4.7H_2O$, 10 mM Trisodium citrate dihydrate, 27 mM KCl, 5g/L casein hydrolysate and 3g/L yeast extract. Adjust pH to 7.2 with NaOH and autoclave at 121˚C and 18 psi for 30 minutes. Autoclaved media can be stored for at least 6 months under sterile conditions at room temperature.

TMC lysis buffer for Halo GVs: 10 mM Tris-HCl, 2.5 mM $MgCl_2$ and 2mM $CaCl_2$, pH 7.5. Store indefinitely.

Sorbitol lysis buffer for Ana GVs: 1M D-Sorbitol in distilled water. Store indefinitely.

Terrific Broth (TB): Add 47.6 g of TB powder and 8 mL glycerol to 1L of distilled water. Autoclave at 121°C for 15 m. Autoclaved media can be stored for at least 6 months under sterile conditions at room temperature.

Luria-Bertani (LB) Broth: Add 25 g of LB powder to 1 L of distilled water. Autoclave at 121°C for 15 m. Autoclaved media can be stored for at least 6 months under sterile conditions at room temperature.

Kanamycin stock solution: 50 mg/mL in distilled water.

Ampicillin stock solution: 100 mg/mL in distilled water.

Chloramphenicol stock solution: 25 mg/mL in ethanol.

IPTG inducer stock solution: 1M IPTG in distilled water.

GV stripping buffer (Round 1): 10M urea, 100mM Tris-HCl, pH 8.0-8.5.

GV stripping buffer (Round 2): 6M urea, 60mM Tris-HCl, pH 8.0-8.5.

TGS buffer: 1:9 (v/v) dilution of 10X TGS stock in DI H_2O.

Inclusion body solubilization buffer: 6M urea, 20mM Tris-HCl, 500mM NaCl, pH 8.0.

Inclusion body wash buffer: 6M urea, 20mM Tris-HCl, 500mM NaCl, 20mM imidazole, pH 8.0.

Inclusion body elution buffer: 6M urea, 20mM Tris-HCl, 500mM NaCl, 250mM imidazole, pH 8.0.

Soluble protein wash buffer: 50mM NaH_2PO_4, 300mM NaCl, 20mM imidazole, 1mM 2-mercaptoethanol, pH 8.0.

Soluble protein elution buffer: 50mM NaH_2PO_4, 300mM NaCl, 250mM imidazole, pH 8.0.

Antibiotic stocks and IPTG solution are at 1000x concentration and should be filter-sterilized after preparation and stored at -20°C. IPTG is light-sensitive and should be stored in the dark at -20°C. Lysis buffers and stock solutions for media preparation should be filtered (0.22 μm filter) and stored at room temperature. All protein purification buffers (wash and elution buffers) should be filter-sterilized and stored at 4°C.It is not advisable to use urea buffers more than a week old for protein purification. GV stripping buffers should be freshly prepared before each use.

Ultrasound gel preparation for imaging experiments: Take a 30 mL luer-lok syringe, remove the piston and place the syringe with the tip facing down in a 50 mL falcon tube. Fill the syringe with ultrasound gel before loading the falcon tube into a table top centrifuge. Spin at 2500g for 30 minutes to ensure that there are no air bubbles in the gel and keep at room temperature. It is advisable to prepare the gel on the same day of the experiment, as longer storage may lead to drying if the syringe is not sealed tightly.

EQUIPMENT SETUP

Cleaning and sterilization of glassware: Clean and sterilize all glassware by autoclaving and fully dry them before use.

Setting up the apparatus for pressurized absorbance spectroscopy: The setup used to conduct pressurized absorbance spectroscopy is illustrated in **Fig. 2-2** and includes the following components: (i) computer equipped with MATLAB to run the collapse pressure scripts, (ii) compressed N_2 tank with control valves and a regulator, (iii) pressure controller, (iv) flow-through quartz cuvette, (v) UV-Vis spectrometer equipped with a light source and cuvette holder.

Couple the pressure controller to the gas tank via a stainless-steel gas connector, to the computer via a USB port, and to the flow-through cuvette via plastic cannulae. Connect the Ecovis Krypton light source of the UV-Vis spectrometer to a power supply, allowing light to pass through the sample in the quartz cuvette. The transmitted light then passes through an optical fiber connector into the OceanOptics STS microspectrometer. The spectrometer is connected to the computer and controlled by a MATLAB script, which also interfaces with the pressure controller. An equilibration time of 7 seconds at each pressure step and a final collapse pressure of 1400 kPa (for blanking) is hard-coded into the script and kept constant for all measurements. Before acquiring sample measurements, the system is calibrated by recording the spectra for full transmission (using the cuvette loaded with PBS or buffer of choice) and zero transmission (by turning the cuvette 90° so that no light passes through).

CAUTION Ensure that the compressed nitrogen tank is transported and stored safely. Cylinders should be secured and stored upright in a cool dry area protected from combustible materials. The gas valve seal must always be in place. When not in use, keep all the cylinder and regulator valves shut and the pressure controller and spectrometer powered off.

Setting up the Verasonics imaging station and imaging parameters: The Verasonics imaging system and setup for *in vitro* and *in vivo* experiments is shown in **Fig. 2-3, a-b** and comprises the following components: (i) computer, (ii) ultrasound probe, (iii) translatable probe clamp equipped with three independent motors that move in the x, y and z directions with µm-level precision (iv) fixed phantom holder and (v) Verasonics scripts running on MATLAB software. Adapt the setup for *in vivo* imaging by replacing the phantom holder with a mouse mounting platform equipped with a heating pad, anesthesia equipment and nose-cone for the animal and a manually translatable probe clamp.

CRITICAL Make sure that the probe is well coupled to the sample and that the transducer array of the probe is immersed in liquid or covered with ultrasound gel before transmitting ultrasound.

Setting up the syringe pump: Gas vesicle injections are administered as a bolus using a syringe pump (shown in **Fig. 2-3b**). The following settings are used for each injection: (i) syringe diameter - 3.55 mm (inner diameter of a BD 1/2cc Tuberculin Syringe); (ii) injection rate - 300 µL/min to 500 µL/min; and (iii) injection volume – 50 µL.

PROCEDURE:

Production and purification of gas vesicles (GVs):

1| Gas vesicles can be produced natively in cyanobacterial (Ana GVs) or haloarchaeal (Halo GVs) hosts. In addition, they can be heterologously expressed in *E. coli* (Mega GVs). To produce and purify Ana, Halo or Mega GVs, follow steps in Option A, B, or C respectively.

(A) Producing and purifying Ana GVs ● TIMING 4.5 weeks

(i) **Making Ana starter cultures (Steps i-iv: ● TIMING 2 wks)** Open the seal of the primary culture tube of *Anabaena flos-aquae* (as received from CCAP, UK), and loosen the screw cap to allow aeration of the culture. Let the tube stand upright and undisturbed for 2 days in a cool (room temperature i.e. (18-25 °C)), dry place with access to ambient light. Viable Ana cells producing GVs will float to the top of the tube, forming a dark green layer.

(ii) Take a pre-sterilized Pyrex glass culture tube. Aliquot 9 mL of G625 growth media into the tube in the presence of a flame to ensure sterility. Add 0.2 mL of 50x BG-11 cyanobacteria freshwater solution. Swirl a few times to ensure complete mixing.

(iii) Gently transfer 0.8 mL of the floating green cells from the primary culture to the G625 media in the culture tube to make a total volume of 10 mL. Swirl gently to disperse the cells. The culture should have just a hint of green at this stage.

(iv) Transfer the starter culture to the shaker incubator (shown in **Fig. 2-1, b**) and allow it to grow at 25°C, 100 rpm and 1% CO_2 with cycles of 14 hours of light illumination and 10 hours in the dark until the cells form a dense, floating green layer that is clearly visible at the top of the liquid phase. This growth typically takes around 1-2 weeks. Note that the doubling time of *Anabaena flos-aquae* during exponential phase is ~ 56.5 hours(238), so depending on the number of viable cells in the starter culture, it will take 1-2 weeks to produce enough floating green cells that have the ability to produce GVs. Viable cells typically form the dense layer at the top and dead cells sink to the bottom of the tube.

(v) **Sub-culturing Ana for GV production (Steps v-vi: ● TIMING 2 wk)** Aliquot 200-250 mL of G625 media into an autoclaved 1L Erlenmeyer flask (use a bunsen burner flame or a laminar hood to provide a sterile environment to avoid contamination). Add 1x final concentration of BG-11 freshwater solution (4-5 mL of the 50x stock) just before inoculation with Ana starter culture. Swirl to mix components.

(vi) Inoculate 2 mL of the green, floating layer of the starter culture per flask and grow cells in the incubator at 25°C, 100 rpm, 1% CO2, 14 h light and 10 h dark cycle until they become confluent (as shown in **Fig. 2-1, b-c**). This should take ~ 2 weeks, with the exact time depending on the number of viable cells inoculated.

(vii) **Harvesting Ana GVs (Steps vii-xi: ● TIMING 1 d)** Pour the confluent culture from the flask into a separatory funnel (pre-sterilized with stopcork in place), allowing it to stand undisturbed on a metal ring stand for 12-16 hours until the GV-producing *Ana* cells separate from the spent media to form a compact green layer at the top **(Fig. 2-1e)**.

(viii) Carefully remove most of the spent media by opening the stopcork at the bottom of the funnel and retain only the green fraction at the top along with ~30 ml of media.

(ix) Using a 25 mL serological pipet, gently resuspend the cells and transfer to a 50 mL tube.

(x) Use 10 mL of fresh G625 growth media to collect cells sticking to the walls of the funnel. Each flask should be reconstituted to ~ 50 mL of concentrated cell suspension.

(xi) Split the suspension into two falcon tubes and add equal volume of 1M sorbitol (final concentration is 500 mM) and 10% (vol/vol) of Solulyse (i.e. 5.5 mL in 55 mL) to achieve hypertonic lysis. Place the tubes in a rotatory shaker at 4°C for 6-8 hours. Green lysates will have a milky tinge post-lysis due to the presence of GVs.

CRITICAL STEP We have observed that GVs become structurally compromised by certain detergents and surfactants used routinely for cell lysis such as BugBuster (EMD Millipore), Triton-X and sodium dodecyl sulfate. It is therefore advisable to thoroughly characterize the effect of any new detergent on GV structure and integrity using techniques such as TEM and pressure absorbance spectroscopy before using them for ultrasound and MRI.

(xii) **Isolation and purification of Ana GVs from lysate (Steps xii-xvii: ● TIMING 2-3 d)** Transfer 35 mL of cell lysate to a 50 mL tube and centrifuge at 350g, 8°C for ~24 hours in a table-top centrifuge, preferably equipped with a swinging bucket rotor.

(xiii) Slowly remove as much as possible of the green subnatant liquid and cell pellet using a 25 mL serological pipet, without disturbing the white GV layer on top.

(xiv) For the second and third round of centrifugation (350g, 8°C), resuspend the white supernatant layer containing GVs in 25 mL of sterile 1x PBS (Corning). During each resuspension step, gently wash the inner walls of the falcon tube with fresh PBS to recover GVs sticking to the sides. The green subnatant should progressively become clearer with each spin. The second and third rounds of centrifugation are shorter than the first, with the endpoint being when all the GVs rise to the top of the tube.

(xv) For the final spin, resuspend GVs in 10-12 mL of PBS (total volume can be varied depending on GV yield) and aliquot them into 2 mL tubes. Spin in a microcentrifuge at 350g for 4 hrs at 4-8°C.

CRITICAL STEP Do not fill the tube to the brim, as GVs will get stuck to the lid of the tube when they float to the top during centrifugation.

(xvi) Using a 21.5 G flat needle attached to a 3 mL syringe, maintain the angle of the microcentrifuge tube and slowly insert the needle through the GV film to the bottom. Collect most of the subnatant, and slowly take out the needle. Some GV loss will occur at this step. This is OK as long as most of the GVs do not get sucked up into the syringe.

(xvii) Resuspend the purified GVs in ~ 6-8 mL of PBS (exact volume of added PBS can be varied and is determined by how concentrated the GV solution needs to be for the end application) and aliquot the milky white GV solution (**Fig. 2-1j**) into screw-top vials or microcentrifuge tubes.

▪ **PAUSE POINT** The Ana GVs aliquoted into tubes can be stored for up to a year at 4°C.

CRITICAL STEP Avoid freezing and subjecting the tube to shocks, such as dropping to the ground or snapping the cap, as this may collapse the GVs.

(B) Producing and purifying Halo GVs ● TIMING 3.5 weeks

(i) **Growing Halo cultures for GV production (Steps i-iii: ● TIMING 2 wks)** Aliquot 250 mL of Carolina growth medium in to an autoclaved 1L Erlenmeyer flask under sterile conditions.

(ii) Inoculate Halo cultures using one of the following methods. (1) Using a sterile pipette tip or toothpick, scrape a small amount of pink culture from the agar plate to add to the flask as inoculum. (2) Use one to two brine crystals containing Halo for inoculation. (3) Inoculate 2.5 mL from a healthy pink liquid starter culture into 250 mL of fresh growth medium (1:100).

(iii) Grow the culture in an incubator at 42˚C with 100 rpm shaking. Depending on the health of the parent culture, it may take ~ 2 weeks for the inoculated culture to become confluent. Confluency is determined by the color and turbidity of cultures as shown in **Fig. 2-1d**.

(iv) **Harvesting Halo GVs (Steps iv-vi: ● TIMING 1 wk)** Gently pour the culture from the flask into a separatory funnel (pre-sterilized with stopcork in place). Allow the culture to remain undisturbed until a visible ring is formed at the top **(Fig. 2-1f)**. This typically takes 4-6 days.

(v) Remove as much of the spent media as possible by opening the stopcork, retaining only the buoyant layer of milky-pink cells for lysis. The retained volume is~10-20 mL and a lot of cells stick to the sides of the funnel.

(vi) Using equal volume (10-20 mL) of TMC lysis buffer (pH 7.5), gently wash the cells stuck on the sides of the funnel and retrieve as many cells as possible. The volume of TMC buffer used might be varied depending on the cell density to achieve efficient hypo-osmotic lysis. However, note that if too much buffer is used in this step, the number of 2 mL aliquots will proportionately increase for the next step, thus increasing sample processing time.

(vii) **Isolation and purification of Halo GVs from lysate (Steps vii-xi: ● TIMING 2 d)** Aliquot ~1.6 mL of cells in 2 mL tubes and spin in a microcentrifuge at 300g for 4 hours at 8˚C.

CRITICAL STEP Close the tubes gently; the pressure wave caused from snapping the lid will collapse a large number of Halo GVs.

(viii) At the top of the tube, a mixed layer of Halo GVs (white) and unlysed Halo cells (milky-pink) will be visible. Using a blunt end 18.5 or 21.5G needle, aspirate the pellet at the bottom of the tubes as well as the pink cell lysate.

CRITICAL STEP Take care to limit the amount of floating Halo cells and Halo GVs (white) that are aspirated in to the syringe.

(ix) Transfer the GVs and unlysed Halo cells to fresh tubes and bring to 1.6 mL with 1x PBS. Centrifuge tubes at 300 g for 4 hours at 8˚C.

(x) Repeat steps viii and ix. After each step, the amount of milky-pink buoyant cells will reduce and white Halo GVs will increase. Continue with centrifugally-assisted floatation until all the cells have lysed and there is no evidence of pink cell lysate in the subnatant.

(xi) Resuspend the purified GVs in PBS and aliquot the milky white GV solution (**Figure 2j**) into screw top vials or microcentrifuge tubes.

▪ **PAUSE POINT** The aliquoted Halo GVs can be stored for up to one year at 4°C.

CRITICAL STEP Avoid freezing and subjecting the tube to mechanical shocks, such as dropping to the ground or snapping the cap, as this may collapse the GVs.

(C) Producing and purifying Mega GVs ● TIMING 4 d

(i) **Heterologous expression of Mega GVs in *E. coli* (Steps i-iv: ● TIMING 2 d)** Transform 50 µL chemically competent Rosetta^{TM} 2(DE3) pLysS cells using > 1 ng of pST39 plasmid containing the pNL29 Mega GV gene cluster[11] by mixing the two components in a 1.5 mL tube and incubating on ice for 30 minutes. Heat shock the tube in a 42 °C water bath for 45 seconds, and put the tube back on ice for a minute. Add 500µL of SOC outgrowth medium and incubate in a shaker at 37°C and 250 rpm for 1 hour.

(ii) Prepare 3 mL of LB broth containing 1x Ampicillin (100 µg/mL), 1x Chloramphenicol (25 µg/mL) and 1% (wt/vol) glucose in a glass culture tube. Resuspend 300 µL of the transformed *E. coli* in the broth. Grow the culture in a shaker-incubator at 37°C and 250 rpm until OD_{600} reaches 0.4 – 0.6. Make 100 µL aliquots of the culture in sterile tubes, and mix with 100 µL of 50% sterile glycerol. Freeze the tubes at -80°C as *E. coli* glycerol stocks.

▪ **PAUSE POINT** The glycerol stocks can be stored at –80°C and used for up to 3 months. Note that while using glycerol stocks is convenient, the GV yield is reduced when using frozen stocks, so we recommend fresh overnight transformations for best results.

(iii) Resuspend a tube of the aliquoted glycerol stock in 3 mL LB broth containing 1x Ampicillin, 1x Chloramphenicol and 1% (wt/vol) glucose. Grow the *E. coli* culture to saturation (OD_{600} > 4). For fresh transformations, aliquot 500 uL of the transformed *E. Coli* from Step (i) into 5 mL of LB broth containing 1x Ampicillin, 1x Chloramphenicol and 1% (wt/vol) glucose. Allow it to grow overnight until the culture reaches saturation (~ 16 hours).

(iv) Prepare 100 mL LB broth containing 1x Ampicillin, 1x Chloramphenicol and 0.2% (wt/vol) glucose, and inoculate 1 mL of the saturated *E. coli* culture into the broth. Grow at 37°C for ~ 2 hours until OD_{600} reaches 0.4 to 0.6. Induce the culture by adding 20 µM IPTG (final concentration), and grow at 30°C for an additional 16-24 hours.

(v) **Harvesting and purifying Mega GVs from *E. coli* cultures (Steps v-x: ● TIMING 2 d)** Split the culture equally into three 50 ml Falcon tubes and spin for 1 hour at 500g and 25°C.

CRITICAL STEP Avoid higher speeds because they may cause collapse of GVs.

(vi) Insert a 10mL syringe with needle to > 1 cm below the surface of the solution and withdraw the clear liquid component of the solution. Withdraw the liquid slowly to preserve the thin layer of cells floating at the top of the solution, as well as the pellet at the bottom, both of which contain Mega GVs.

(vii) To lyse the cells, add 4 ml SoluLyse-Tris reagent per 50 ml of *E. coli* culture, 250 µg/ml lysozyme and 10 µg/ml DNAseI. Rotate the tubes for 10 minutes at room temperature and then aliquot 1.5 mL of the solution to 2 mL tubes. Spin samples for 4 hours at 800 g and 8°C. Mix the floating GV layer gently with supernatant and transfer to a clean tube.

(viii) Spin the samples for 4 h at 800g. Use a 3 mL syringe to remove the bottom fraction, which sometimes includes a small pellet. Gently resuspend GVs in 1 mL of PBS. Repeat the spin and wash steps 3 times.

CRITICAL STEP Be aware that GVs are susceptible to desiccation and resuspend GVs immediately after withdrawing the liquid.

(ix) Mega GVs are natively clustered. To uncluster them, GV-containing solution is mixed with 10 M urea in a 2:3 ratio to achieve 6 M final urea concentration, and the resulting solution is gently rotated for 30 min.

(x) Dialyze GVs overnight in 6-8 kDa MWCO tubing against 4L of PBS. This step can be omitted for experiments with no stringent requirements for buffer conditions. The white layer of unclustered GVs at the top of the liquid phase after buoyancy purification, as well as the re-suspended milky-white solution of Mega GVs in PBS is shown in **Fig. 2-1, i-j**.

▪ **PAUSE POINT** Mega GVs can be stored for up to one year at 4°C .

CRITICAL STEP Avoid freezing and subjecting the tube to mechanical shocks, such as dropping to the ground or snapping the cap, as this may collapse the GVs.

Quantification of GVs by measuring pressure-sensitive optical density ● TIMING 15 m

2| Determine the concentration of a solution of gas vesicles by measuring its pressure-sensitive optical density at 500 nm ($OD_{500,ps}$) using a NanoDrop 2000 Spectrophotometer. Load 2 µL of sample on the pedestal for each measurement. Collapsed gas vesicles in the same buffer are used as a blank for measurements. Prepare collapsed GVs by sonication in a water bath until the solution turns completely clear or by manual collapse in a capped syringe. For manual collapse, remove the plunger from a 12 mL Luer-Lock syringe closed with a tip cap and place 5-10 µL of gas vesicle solution at the bottom of the syringe.

Making sure that the tip cap is screwed on tight, replace the plunger and push down until there is significant resistance. The increase in pressure will collapse the gas vesicles, turning the milky white solution clear. A shortcut for quick measurements of GV concentration is to blank with the GV resuspension buffer. For most samples, this will give an OD reading that is very close to that measured when using collapsed GVs as a blank. However, for some samples containing GVs that are fluorescent, it is necessary to use the collapsed GVs as the blank.

! CAUTION Before doing manual collapse, ensure that the tip-cap on the syringe is facing away from you and securely fastened, as pressurization of the syringe may cause ejection of the cap, resulting in potential injury to the user. Wear protective eyewear and clothing.

CRITICAL STEP It is important to ensure that the GVs are homogenously re-suspended in solution just before measurements. For each sample, take the average $OD_{500,ps}$ value after multiple measurements (n>=3) to ensure precision and accuracy.

Quantification of GV protein concentration ● TIMING 15 m

3| Measure the protein concentrations using the Pierce 660nm protein assay to obtain relationships between optical density and protein content for the GV solutions. The protein concentrations to OD relationships that we have determined for Ana, Halo and Mega GVs are given in **Table 2-T4**.

Chemical functionalization of GVs ● TIMING 2 d

CRITICAL Purified Ana, Halo and Mega GVs contain lysine residues on the surface that can be used to chemically conjugate a variety of moieties such as polyethylene glycol, fluorophores and biotin using an amine-reactive coupling group such as N-hydroxysuccinimide ester.

4| Measure the concentration of purified GVs using the OD relationships in Table 2.

5| Aliquot the NHS-moiety in anhydrous DMSO at 100x of the required molar concentration for the amine-NHS reaction. For Alexa-488-NHS conjugation to Ana GVs, aliquot 5 µl of the 10 mM stock solution of the dye pre-prepared in anhydrous-DMSO.

CRITICAL STEP Ensure that the NHS-moiety solution does not contain detergents or surfactants that might affect the integrity and properties of GVs.

6| Adjust the concentration and volume of GVs to the desired amount and ensure that the buffer is free of amines (avoid Tris buffer). For Alexa-488-NHS conjugation to Ana GVs, bring Ana GVs to OD1 in 1 mL of PBS at pH 7.4.

CRITICAL STEP If GVs were previously in a buffer containing free amines or PBS with pH less than 7, ensure complete buffer exchange with PBS at pH 7 – 9 before proceeding with the amine-NHS reaction.

7|Add 10^5 molar excess of the NHS-moiety to GVs, keeping the DMSO concentration at 0.5% or less of the total reaction volume. For Alexa-488-NHS conjugation to Ana GVs, add 5 µl of the 10 mM Alexa-488-NHS in DMSO to 1 mL of Ana GV solution. Based on the average number of gvpA and gvpC protein monomers that make up Ana GVs, approximately 50,000 lysine residues are present for every Ana GV. One can tune the molar ratio of the two reactants (NHS-moiety : GV) to achieve the desired reaction efficiency.

8| Allow the reaction to proceed for 4 hours at room temperature under gentle rotation.

9| Quench the unreacted NHS-moieties using Tris-HCl buffer at pH 8 to a final concentration of 10 mM for 20 minutes at room temperature under gentle rotation

10| Add the whole reaction to dialysis tubes (6-8 kDa cutoff) and dialyze against a 4000x volume excess of PBS at 4˚C for 8 hours. Replace the buffer and allow dialysis to continue for an additional 8 hours.

CRITICAL STEP If NHS-moiety is not amenable to dialysis, repeated rounds of centrifugally-assisted purification is an alternative method to remove excess reactants and/or for buffer exchange.

▪ **PAUSE POINT** Chemically functionalized GVs can be stored in PBS buffer for up to one year at 4˚C -.

Genetic modification and functionalization of Ana GVs ● TIMING 3 days

The outer scaffold protein of Ana GVs, gas vesicle protein C (GvpC), can be removed and replaced with genetically modified recombinant versions as a molecular handle for GV mechanical modification and functionalization. This procedure comprises stripping native GvpC off Ana GVs (Steps 11-19), preparing recombinant GvpC (Steps 20-38) and re-adding this GvpC onto ΔGvpC Ana GVs via dialysis (Steps 39-41). In addition, GVs functionalized with GvpC fused to the SpyTag peptide enable convenient downstream covalent functionalization with proteins fused to the SpyCatcher moiety (Steps 42-45).

11| Preparation of ΔGvpC GVs (Steps 11-19: ● TIMING **12 h**) Dilute purified Ana GVs in PBS such that $OD_{500,ps}$ <10.

12| Prepare 3:2 (vol/vol) mix of GV stripping buffer (10M urea in 100mM Tris buffer) and GV solution in PBS. Pipet 1.7 mL into 2 mL microcentrifuge tubes.

13| Centrifuge at 300g for 4 hours, or until the subnatant is completely clear. Remove the clear subnatant with a syringe using a 21G flat needle. Retain the milky white supernatant in the tube. Resuspend the GV-containing supernatant in GV stripping Buffer (Round 2 i.e. 6M urea, 60mM Tris-HCl). Repeat this step 1 time.

14| Confirm GvpC removal by performing SDS-PAGE. Incubate a 1:1 (vol/vol) mix of GVs in 2x Laemmli buffer (containing 5% (vol/vol) 2-mercaptoethanol) at 95°C for 5 m. Centrifuge briefly to collect condensate.

15| Assemble the electrophoresis cell with the comb and tape removed from the polyacrylamide gels. Fill the inner chamber completely with 200 mL 1x TGS buffer. Ensure that the cell is not leaking fluid. Fill the outer chamber up to mark with 600 mL 1x TGS buffer.

16| Load the protein ladder and samples in the gel using gel-loading tips. GVs should be at $OD_{500} > 3$ prior to the 1:1 dilution. If purified proteins are being run on the same gel for comparison, load > 100 ng.

CRITICAL STEP In order to prevent contamination between wells, do not exceed the maximum recommended volume per well.

17| Connect electrophoresis cell to power supply and run the gel for 55 m at 120V.

18| Recover the gel by disassembling the electrophoresis cell and the gel cassette. Incubate the gel in a holder with DI H_2O for 10 m, then stain for 1 h with 10 mL SimplyBlue^{TM} SafeStain. De-stain the gel for at least 1 h with 10 mL DI H_2O.

19| Image the gel using a Coomassie imaging protocol using the gel imaging system to visualize protein bands. The GvpC band at approximately 25 kDa should be missing.

▪ **PAUSE POINT** Store the ΔGvpC GVs in urea buffer at 4°C for no more than 1 week. When preparing ΔGvpC GVs for long term storage without any further genetic functionalization or recombinant GvpC addition (steps 39-45), we recommend dialyzing the GV solution against PBS in order to completely remove the urea.

20| Preparation of recombinant GvpC (Steps 20-38): ● **TIMING 1 d**) Transform > 1 ng pure plasmid encoding recombinant GvpC with a C-terminal hexahistidine tag into BL21 (DE3) competent cells and grow culture in terrific broth with 50 µg/ml kanamycin overnight.

21| Dilute 500 µL of the starter culture 1:1 with 50% glycerol in water and store at -80°C (for upto one year for best results). Future starter cultures can be grown from aliquots of this glycerol stock instead of fresh transformations.

22| Dilute starter culture 1:250 in terrific broth with 50 µg/ml kanamycin and grow to OD_{600}~0.4-0.7 with shaking (250 rpm) at 37ºC. Induce at a final concentration of 1mM IPTG. Grow culture for 6-12 h at 30ºC with shaking.

CRITICAL STEP Frozen IPTG stocks should be thawed fully and vortexed to mix contents before use.

23| Pellet the cells in ultracentrifuge tubes at 5,500g for 15 min at 4°C and discard the supernatant.

▪ **PAUSE POINT** Cell pellets can be stored at -20°C for up to one year. Protein extraction is typically more effective with frozen cells.

24| Resuspend the pellets in 10 mL Solulyse with 10 µg/mL DNAse. Rotate at room temperature for 10 min.

25| Centrifuge at 20,000g for 15 m at 4°C to clear the lysate and discard the supernatant.

26| Resuspend the pellet in 10mL Solulyse and lysozyme (0.25 mg/mL). Rotate at room temperature for 10 m.

27| Add 5mL Solulyse and vortex. Centrifuge at 20,000g for 20 m at 4°C and discard the supernatant.

28| Thoroughly resuspend the pellet in 5 mL of inclusion body solubilization buffer.

29| Centrifuge at 20,000g for 20 m at 4°C.

30| Add 1.5mL Ni-NTA slurry to the supernatant, incubate at 4°C with shaking (60 rpm) for 2 h or more.

31| Pour into a polyprep column and collect all the flow-through, wash and elutions in the next steps. Collecting all fractions is good practice for troubleshooting and analyzing purification steps using SDS-PAGE.

32| Wash with 10 column volumes of inclusion body wash buffer.

33| Elute with 2 column volumes of inclusion body elution buffer.

34| To quantify the eluted protein using the Bradford assay, prepare a standard curve of bovine serum albumin (BSA) at a final concentrations of 100, 250, 500, 750, 1000 and 1500 µg/mL in 60 µL of 3x diluted inclusion body elution buffer in PBS. Prepare dilutions of eluted protein 1:2 in PBS with a final volume 60 µL. Prepare a negative control of 3x diluted inclusion body elution buffer in PBS.

35| To 25 µL of the sample and BSA standards, add 1 mL of Bradford reagent, vortex and incubate at room temperature for 5-10 m. Prepare all samples in duplicate.

36| Blank the spectrophotometer with a negative control sample and measure the OD_{595}.

37| Measure the OD_{595} of the standard curve samples. Plot the OD_{595} versus the concentration, and compute linear regression fit.

38| Measure the OD_{595} of the eluted protein samples. Use the linear fit from Step 37 to compute the unknown concentrations, and multiply by 3 (dilution factor) to obtain concentration of stock elution solution.

▪ **PAUSE POINT** Store the elutions separately at 4°C for up to 3 months. Elution 1 has > 80% of collected pure protein and is used for the subsequent experiments. Elution 2 is more dilute and is typically stored as backup or for running protein controls for SDS-PAGE.

39| Preparation of GVs with recombinant GvpC (Steps 39-41: ● **TIMING 1 d**) Add recombinant GvpC to ΔGvpC GVs according to the formulation: 2 * OD * 198 nM * volume (in L) of GVs = nmol recombinant GvpC. This provides a 2-fold stoichiometric excess of GvpC relative to binding sites on an average Ana GV, assuming a 1:25 molar ratio of GvpC : GvpA binding based on previous work (63). The exact volume of recombinant GvpC to be added is calculated based on the molar mass of the particular variant and the concentration of eluted GvpC (measured by Bradford according to steps 34-38). For truncated GvpC variants with a lower GV binding affinity, a higher stoichiometric excess may be added to promote attachment of GvpC to the GV surface. However, note that adding too much excess of GvpC might lead to protein aggregation during dialysis.

40| Soak the dialysis tubing in PBS for 5 minutes. Add samples (GVs + recombinant GvpC) into dialysis tubing and clip both sides. Dialyze in 4L PBS with stirring on low speed for at least 12 h.

CRITICAL STEP The length of dialysis tubing used for each sample depends on the total volume of the dialysate, which is determined by the amount of engineered GVs required for the end application. The type of dialysis tubing used (molecular weight cutoff) can change depending on the GvpC variant, as truncated variants may have a much lower molecular weight.

41| Transfer the dialysate into 2-mL centrifuge tubes and spin at 300g for 3 hours, or until subnatant is clear. Remove subnatant with syringe with a 21.5G flat needle. Retain the milky white supernatant in the tube. Resuspend GVs in PBS. Repeat this centrifugation step one time.

▪ **PAUSE POINT** Store at 4°C for up to 3 months. **NOTE:** Since different GvpC variants have different binding affinities to the GvpA shell, it is advisable to check the hydrostatic collapse profile of the stored GV variant before use in imaging experiments, to ensure that there is no dissociation of recombinant GvpC from the GV surface during storage

42| Preparation of SpyCatcher-functionalized GVs (Steps 42-45: ● **TIMING 5 h**) Prepare Ana GVs with GvpC fused to SpyTag peptide using Steps 39-41.

43| Mix SpyTag-functionalized GVs with SpyCatcher-fused proteins according to the formulation: 2 * OD * 395 nM * volume (in L) of SpyTag GVs= nmol SpyCatcher-fused protein. This results in a 2-fold excess of SpyCatcher to SpyTag in the reaction, based on the stoichiometry described in Step 39. Note that the SpyCatcher-mNeonGreen (SC-mNG) fusion protein used in our published work (97) is expressed separately in *E.Coli* following procedures in Steps 20-23 and using the plasmid containing SC-mNG (details in the reagents section). SC-mNG is expressed as a soluble protein and hexahistidine-tagged, enabling purification using the same Ni-NTA slurry used for recombinant GvpC purification. Unlike GvpC inclusion bodies, soluble proteins are in the supernatant after cell lysis with Solulyse/DNAse (Step 24), allowing direct incubation of the supernatant with the slurry (Step 30). Wash and elution (Steps 31-33) are performed with soluble protein wash buffer and soluble protein elution buffer respectively, and the protein is desalted into PBS using PD10 desalting columns. Protein quantification is done using the Pierce or Bradford assay before use.

44| Incubate 1 hour or more at room temperature.

45| Centrifuge at 300 g for 3 hours or until subnatant is clear. Remove clear subnatant with syringe with 21.5G needle. Retain milky white supernatant in the tube. Resuspend supernatant in PBS. Repeat this centrifugation step one time.

▪ **PAUSE POINT** Store at 4°C for up to 3 months.

GV Characterization

46| To characterize the purified GVs, follow the procedure in A to determine the critical collapse pressure of GVs using pressurized absorbance spectroscopy. Follow option B for DLS measurements and option C for preparing the GV specimens for TEM.

(A) Determining critical collapse of GVs with pressurized absorbance spectroscopy ● TIMING 40m

(i) Before acquiring measurements, connect the spectrophotometer to a power supply for 30 m to allow it to warm up.

(ii) Run the Alicat_startup script to initialize the pressure controller.

(iii) Blank the spectrophotometer with a cuvette filled with PBS or GV resuspension buffer and run OceanOptics_startup_FullTrans to save the data.

(iv) Establish a zero-transmission baseline with the opaque side of cuvette blocking the light path using the OceanOptics_startup_NoTrans script.

(v) Fill cuvette with intact GV sample ($OD_{500nm} = 0.2$ in PBS) and fasten the cannulae securely. To assist loading, use elongated gel-loading micropipette tips.

(vi) Open the N_2 tank valve, pressure regulator, and pressure controller valve.

(vii) Run the Collapse_script to measure the $OD_{500,ps}$ under increasing hydrostatic pressure (0 kPa – 1.4 MPa in 20-kPa increments).

(viii) Between these measurements, rinse the cuvette with DI H_2O, 70% ethanol and acetone to ensure that cuvette is completely clean and dry before adding the next sample.

(ix) After measurements, close gas the valves and turn off the spectrophotometer.

(B) Preparation of GV specimens for dynamic light scattering (DLS) ● TIMING 5 m

(i) Dilute the GV samples to $OD_{500,ps} = 0.2$ in PBS.

(ii) Measure the particle size on ZetaPALS instrument with an angle of 90° and refractive index 1.33.

(C) Preparation of GV samples for transmission electron-microscopy (TEM) ● TIMING 30 m

(i) Buffer-exchange the purified GVs in 10 mM HEPES buffer with 150 mM NaCl or an alternative non-phosphate containing buffer via centrifugally-assisted floatation (same procedure as used for GV isolation) at 8°C and 300g. Replace the subnatant with equal volume 10 mM HEPES buffer with 150 mM NaCl. Repeat 3 times. The aim of this step is to prevent phosphate in the PBS from causing unwanted precipitation of the uranyl acetate stain used downstream in step (vi). Therefore, if the GV solution is very concentrated, direct dilution of the GV sample into the above-mentioned HEPES buffer to a final OD of 0.2 would be a quicker alternative.

(ii) Dilute the GVs to a final OD of 0.2.

(iii) Spin 2% Uranyl acetate solution in a benchtop centrifuge at 14,000xg for 5 minutes to pellet any precipitate.

(iv) Charge Formvar TEM grids using the glow discharge system with 15 mA current for 1 minute.

CRITICAL STEP Gently handle the TEM grids and avoid contact of the tweezer tip with the center of the grid to prevent bending and damage to the grids.

(v) Place 2 µl of well-mixed GV solution on the charged Formvar TEM grids for 3 minutes. The sample should be placed on the carbon side of the grid; avoid placing sample on the copper side. For convenience, we use PELCO reverse, anti-capillary tweezers to hold the TEM grid while adding sample and negative stain.

(vi) Add 5 µl of 2% uranyl acetate to the GV solution on the TEM grid for 30 seconds.

(vii) Using a Whatman filter paper, wick the solution by gently touching the edge of the grid. For consistent results, leave a thin film of sample on the grids and leave to air dry.

(viii) Image the grids using TEM.

Ultrasound imaging of GVs *in vitro* in agarose phantoms

Steps 47-63 describe the application of GVs as contrast agents for ultrasound.

47| Agarose phantom preparation and sample loading (Steps 47-55: ● **TIMING** **3 h**) Make a 250 mL solution of 1% (wt/vol) agarose in PBS and microwave for 3 minutes to ensure dissolution. Ensure that the lid is loosely fastened and swirl the bottle at 1 min intervals to prevent the agarose from settling.

48| Fasten the lid and put the bottle in a water bath at 50-55°C for at least 30-45 min to allow the solution to equilibrate to the bath temperature.

49| Fill the Nalgene plastic holder (L 12.5 cm x W 8 cm, 300 mL) with 150 mL of molten 1% agarose in PBS. Keep the remaining agarose solution in the water bath for sample loading.

50| Immerse the multi-well phantom mold on top of the agarose solution.
CRITICAL STEP Remove any small air bubbles with a syringe needle and lower the mold gently onto the surface of the agarose, maintaining a small angle to allow any air trapped on the interface between the agarose and mold to escape.

51| Let the agarose phantom solidify at room temperature for 1 h.

52| Carefully take out the multi-well phantom mold without disturbing the agarose beneath.

53| Prepare the GV samples and controls at 2x of the final desired concentration.

54| Prepare a 1:1 mixture of the 1% agarose in PBS with the GVs or polystyrene beads.

Make sure the 1% agarose in PBS is equilibrated to a temperature of 50-55°C before and during the mixing with GVs or polystyrene beads. Just prior to mixing with the agarose, place the GV or polystyrene sample for 10-15 seconds in a 50°C water bath to warm the sample. This allows proper mixing of agarose with the sample and provides enough time to load the sample into the well before the agarose solidifies.

CRITICAL STEP Do not heat the GV samples to temperatures above 50°C. GV collapse has been observed even for a 10-20 sec incubation at 65°C or above.

55| Pipette the mixture into the phantom well. The volume of mixture pipetted depends on the dimensions of the well, typically 50-100 µL.

56| Phantom imaging (Steps 56-62: ●TIMING 1 h) Place the ultrasound acoustic absorber at the bottom of the phantom holder to prevent multiple ultrasound wave reflections during the measurement

57| Immerse the phantom in water or 1X PBS.

58| Perform ultrasound imaging on the Verasonics L11-4v or L22-14v ray-line example scripts using the following parameters: set the transmit frequency is to 4.5 MHz, set the number of cycles of the transmitted ultrasound pulse to 3, the F-number to 3, the voltage to 2.5 and the persistence to 90. These parameters can be adjusted by the user in the Verasonics MATLAB script defining the ultrasound pulse sequence, and operated via the VSX GUI. Perform the collapse using a high-power pulse at 25V.

59| Perform ultrasound imaging at the fundamental frequency with the L22-14v: the transmit frequency is set to 11.5 MHz, the number of cycles of the transmitted ultrasound pulse is set to 6, the F-number to 2, and the voltage to 3V. Those parameters are adjusted in the script and operated via the VSX GUI.

60| Perform ultrasound imaging at the second harmonic frequency with the L11-4v transducer: echoes at the second harmonic frequency are displayed using a 2 MHz wide band pass filter centered around 9 MHz. Other parameters are identical to the fundamental imaging mode and adjusted in the script. Second harmonic imaging is operated as an option via the VSX GUI. Note that we have recently developed new amplitude modulation strategies that can also be used for highly selective non-linear imaging of native and engineered GVs (98, 101).

61| Obtain acoustic multiplexing images by using GVs at OD 1 and a transmit frequency of 6.25 MHz and at 1.6V on the L11-4v, with a 4 cycle pulse, transmit focus of 20 mm, F-number of 2 and persistence of 90. To collapse the GVs, increase the acoustic pressure by lowering the F-number to 0.1 and gradually ramping up the voltage. At each collapse step, the transducer is translated in the y and z planes using the Velmex motors to ensure homogenous collapse over the entire well and field of view.

62| Save the ultrasound images for subsequent processing as .fig images (MATLAB format) directly from the MATLAB figure panel.

Ultrasound imaging of GVs *in vivo*

63| GVs can be used as contrast agents for *in vivo* ultrasound imaging. The section below describes the steps for imaging injected GVs in mice using the Verasonics system. Any experiments involving live mice must conform to relevant Institutional and National regulations. All animal experiments reported in this article received approval from the Institutional Animal Care and Use Committees of the California Institute of Technology or the Sunnybrook Research Institute.

GV imaging *in vivo* using the Verasonics ultrasound system ●TIMING 45 m

(i) Place the mouse in the induction chamber with isoflurane 3-4%, room air at 2 liters/min with the vacuum on for isoflurane removal.

(ii) When the animal is unresponsive to toe pinch, move the animal to the heat pad and nose cone for continued anesthesia and place it on the supine position. Reduce the isoflurane to 2% and apply eye lubricant to both eyes to avoid drying. Use NAIR™ and cotton swabs to depilate the abdominal area and wash thoroughly with saline to avoid any burns on the skin.

(iii) Prepare the catheter using 10 cm of PE10 plastic tubing and a 30 G needle. With a razor blade, cut the plastic at the bottom of the needle to allow the blunt end to be free. Push this end into the PE10 plastic tubing.

!CAUTION Follow safe practices and wear proper PPE while handling sharp needles.

(iv) Fill the catheter with saline using a 30 G syringe. Confirm that there is no leaking from the catheter. Remove the saline-filled syringe before the next step. Failure to fill the tubing with liquid to remove the air from the catheter can lead to a gas embolism and death of the animal.

(v) To insert the catheter into the tail-vein, place the mouse on its side for a better view of the lateral tail vein, clean the tail with an alcohol swab. Using the dominant hand to hold the catheter, use the other hand to hold the tail between your thumb and index finger. Insert the bevel needle through the skin and into the vein at a flat angle and advance it for several mm. If the needle is inserted correctly, blood should backflow through the catheter.

(vi) Secure the position of the catheter in the tail vein with tissue adhesive glue and use the 30G syringe filled with saline to flush the blood from the catheter.

CRITICAL STEP The flow of saline should be smooth, confirming proper positioning of the needle tip in the tail vein. Excessive pressure to achieve flow may indicate improper positioning of catheter or clotting of blood.

(vii) To perform ultrasound imaging, slowly adjust the mouse to a supine position and apply ultrasound gel on the depilated area. Place the transducer on the gel.

CRITICAL STEP Make sure that there are no air gaps and that the gel is completely coupled to the transducer.

(viii) Open the Verasonics L11-4v ray-line example script in MATLAB. The transmit frequency is set to 4.5 MHz with the L11-4v transducer. Position the transducer to see the Inferior vena cava (IVC) for vascular imaging. Keep the voltage at 2.5V, 3-cycle pulse, F-number 3 and persistence 20. Other imaging scripts can also be used here

CRITCAL STEP Ensure that the region of interest in the mouse aligns with the focus of the transducer to acquire optimal images.

(ix) Remix the gas vesicles thoroughly by gently pipetting up and down, then aliquot 100 µL of solution of $OD_{500,ps}$ ~ 25 into a 1.5 mL micro-centrifuge tube.

CRITCAL STEP Gas vesicles must be mixed thoroughly each time before an injection, they are buoyant and will float up to the top of the tube. Make sure to inject immediately after remixing.

(x) Carefully load a 30 G tuberculin syringe with the GV solution, making sure there are no air bubbles. Do not tap as this may collapse the GVs. Replace the saline-filled syringe at the end of the catheter and secure it to the syringe pump.

(xi) Fill the catheter line with GVs at a rate of 5 µL/s.

(xii) Inject 50 µL of GVs into the tail vein at a rate of 5 µL/s and record the ultrasound signal appearing in the IVC and liver.

CRITCAL STEP The total amount of injected saline and sample should be monitored and within the approved safety guidelines to prevent adverse effects on the animal caused by blood dilution.

(xiii) Perform imaging using B-mode or harmonic filtering as described in steps 58-60 for *in vitro* specimens.

(xiv) At the end of the imaging session, turn off the isoflurane and remove the mouse from the nosecone. Wait for the animal to completely recover from the anesthesia before returning it back to the cage.

TROUBLESHOOTING TABLE

Step No.	Problem	Possible Reason	Solution
1A(iv), 1A(vi) 1B(iii)	Cultures growing too slowly	Not enough viable cells	Increase the amount of starter inoculum.
1A(iv), 1A(vi) 1B(iii)	Cell death	Contamination	Start fresh from primary cultures and follow sterile procedures.
		Incubator conditions (aeration, pH, temperature and lighting) not optimal	Loosen the cap/foil to allow aeration, monitor CO_2 levels. For Ana cultures, ensure temperature inside incubator does not increase during light cycle due to heat from the lamps and confirm proper exposure of the cultures to light.
1A(vii)-(xi), 1B(iv)-(vi)	Poor GV yield	Cultures not confluent	Allow cultures to grow for a few more days. Confluency is determined by the color and turbidity of the cultures as described in the procedure and shown in Figure 2
1A(xi), 1B(vi)		Incomplete lysis	Dilute the concentrated cell suspension with lysis buffer and/or allow lysis to proceed longer.

1A(vii)-(xi),1 B(iv)-(vi)		Collapse of GVs	Make sure the cultures are not subjected to agitation above 100 rpm and handle flasks gently while transporting and placing on hard surfaces.
1A(x), 1B(vi)		Inefficient retrieval of buoyant cells from the separatory funnel	Thoroughly wash the inner walls of the funnel with media/buffer to retrieve the buoyant cells sticking to the sides (especially for Halo).
1A(xii)	Incomplete separation of GVs from lysate/subnatant	Lysate is too dense, requiring longer spins for GVs to float to the top	Increase time of centrifugation and/or dilute lysate with PBS prior to spin
1A(xii), 1C(v)	Collapse of GVs during spins	Hydrostatic Pressure on GVs greater than critical collapse pressure	Aliquot suspensions into more tubes to reduce height of the column (volume in a single falcon tube should not exceed 40 mL).
1A(xv), 1B(vii)		Pressurization of tubes while opening and closing	Ensure microcentrifuge tubes are closed very gently. The caps of such tubes should not make a snap sound when closed.
8	NHS-amine reaction did not work	NHS will hydrolyze in the presence of water/moisture.	Ensure DMSO used for storage is anhydrous. Limit exposure to ambient moisture. Store in a desiccated environment.
4-10	GVs aggregate after reaction with NHS-moiety	Conjugation of moieties on the GVs destabilizes the protein.	Conjugate fewer moieties on the GV surface by reducing the concentration of NHS-moiety and/or reaction time.
		Presence of surfactants in the reactant sample.	Purify the NHS-moieties using chromatography or other methods.

9, 10	Subsequent reaction using NHS-moiety conjugated GVs does not work.	Presence of excess NHS-moieties in solution.	Repeat dialysis until excess NHS-moieties are below level of detection.
11-19	Incomplete GvpC stripping	GV concentration is too high for efficient removal of GvpC	Dilute native Ana GVs in PBS to an OD ~ 5 before adding 10 M urea buffer.
20-38	Low or no GvpC yield	Low expression of GvpC variant	Check plasmid for mutations, prepare fresh transformations and try reducing temperature and increasing duration of expression.
		Poor binding to the Ni column	Ensure column is charged and increase incubation time with resin or add more resin.
		Inefficient retrieval of inclusion bodies	Ensure that inclusion pellets are not lost during repeated rounds of centrifugation and resuspension
39-41	Incomplete GvpC re-addition	GV concentration is too high for re-addition reaction to go to completion	Reduce GV OD_{500} during GvpC re-addition. Confirm re-addition by SDS-PAGE and Coomassie staining.
		GvpC concentration is too low	Inaccurate quantification of GvpC eluate.
39-41	Protein precipitation is seen after re-addition	Excess unbound GvpC forms precipitates in PBS.	Reduce stoichiometric excess factor of GvpC during re-addition.
42-45	No fluorescence from SpyCatcher-GFP-labeled GVs	Incomplete SpyTag functionalization	Confirm GvpC-SpyTag re-addition using SDS-PAGE.
		Incomplete SpyTag-SpyCatcher reaction	Increase excess factor of SpyCatcher during reaction and/or increase reaction time.

46A	Collapse curves are inconsistent or noisy	Incomplete collapse	Make sure that there are no air leaks in the connectors or bubbles in the sample
		Presence of detergents and/or incomplete GvpC addition	Always run control GV samples such as ΔGvpC and GvpC_{WT} to ensure that the re-addition was done under proper conditions and corroborate with SDS-PAGE results.
46C	Too much black background on TEM grid	GV sample contains contaminants or phosphate-containing molecules	Using dialysis or centrifugally-assisted purification to resuspend GVs in 10 mM HEPES with 150 mM NaCl buffer.
		Uranyl acetate precipitate present in solution	Avoid extended exposure to ambient light. Uranyl acetate will precipitate when exposed to light and UV.
46C	Too many or too few GVs on the TEM grid	Incorrect GV OD measurement	Measure GV OD and double check the dilution calculation.
		GVs were not given adequate time to adhere on charged grids.	Excessive wicking can cause too many GVs to come off grids. Reduce how much solution is being wicked off.
47-62	Only the top of the GV sample for *in vitro* ultrasound phantoms shows contrast	The concentration of GVs is too high.	Lower the concentration of GVs.
47-62	The signal from GVs and polystyrene beads is very different.	The concentration of GVs or polystyrene beads is too high or too low.	Matching of GVs' concentration to concentration of beads.
63	Weak or no signal after injection	IVC not in the image	Move the transducer to find the optimal location in the IVC and try to align the imaging

		target with the natural focus of the transducer
	GVs collapsed prior to or during injection	Check that there is no pressure when injecting through the catheter by manually injecting a small volume of saline with a 30G syringe. If you feel pressure, readjust the catheter into the tail vein and ensure that there are no blocks, allowing the saline to flow smoothly
	Transmit power set too high	Ensure that transmit power does not generate an acoustic pressure on the GVs that exceeds the critical collapse pressure